The Dissertation Committee for Akarsh Simha certifies that this is the approved version of the following dissertation:

Brownian Motion in Liquids: Theory and Experiment

Committee:

Philip J. Morrison, Supervisor

Mark G. Raizen, Co-Supervisor

Irene M. Gamba

Richard D. Hazeltine

C. Wendell Horton, Jr.

Brownian Motion in Liquids: Theory and Experiment

by

Akarsh Simha,

Dissertation
Presented to the Faculty of the Graduate School of
The University of Texas at Austin
in Partial Fulfillment
of the Requirements
for the degree of
Doctor of Philosophy

The University of Texas at Austin
August, 2017

Dedicated to my mother Sheela, my father Pradeep, my brother Utkarsh,
and to all my teachers and mentors,
without whose guidance and support this endeavor would have been impossible.

Acknowledgments

There are so many people to thank, that I do not know where to begin—for everyone starting from high-school teachers, college professors to my advisers, and the friends and mentors I have found along this course—have made a contribution to this endeavor.

Foremost, I want to express my deep gratitude to my adviser Prof. Philip J. Morrison, who has been a source of inspiration, knowledge and support through this endeavor. Prof. Morrison's excellent teaching and vast knowledge of the subject, which I was fortunate to experience in a graduate course on fluid mechanics that he taught, inspired me to do theoretical work. Ever since, his breadth of knowledge of classical physics and applied mathematics has been a source of enduring learning, for which I am very grateful. Prof. Morrison has always provided an environment that every researcher craves for, but is very hard to come by — in him I have found an adviser that encouraged me to pursue whatever sparked my interest, and yet, someone to go to for advice and support whenever I'm stuck, at which stage he would usually suggest a solution or a very apt reference.

I first started working with my co-adviser Prof. Mark G. Raizen as an almost fresh graduate student, with no experimental background. Yet, he gave me an opportunity to touch the equipment in his lab, and was patient enough to let the Pauli effect (which thankfully wasn't very strong) wear off. While I was still learning the ropes of not just experimental work, but also of life as an adult, his caring nature and support were extremely valuable. I have never hesitated to go to him for advice. Mark is an exceptional PI, and working as part of his research group was an extremely rewarding experience.

Prof. Jean-Luc Thiffeault (U. Wisconsin) was instrumental in pointing me to several key pieces of literature and providing feedback on my ideas. My discussions with him were very helpful in learning about low Reynolds number hydrodynamics.

I am thankful to my other thesis committee members, Prof. Irene Gamba, Prof. Richard Hazeltine, and Prof. Wendell Horton, along with my advisers for reading this tome and providing me with valuable feedback. I thank Prof. Gamba for being very supportive in her capacity as a teacher, and also for going out of her way to be present

at my dissertation defense. I learned a lot in the PDE class I took with her. Excellent teachers Prof. Mike Downer and Prof. Thomas Chen enriched my knowledge, as did discussions with Prof. E. C. G. Sudarshan and Prof. G. Bhamathi both in class and outside. Prof. Lawrence Shepley's sense of humor and encouragement for the Whizkey seminar will be sorely missed.

During my first exposure to experimental work, I had the fortune of working with Tongcang Li and Simon Kheifets. Despite the brevity of my overlap with Tongcang, I learned a lot from him. For the next few years, I worked with Simon on measuring instantaneous velocity in liquid. Simon is an exceptionally talented experimentalist, with a strong understanding of the fundamentals, and an aptitude for theory. He was instrumental in the arduous task of managing an extremely challenging experiment, and finding us direction where I could see none. To his mentorship, I owe whatever experimental skill I possess. Kevin Melin joined us in the final days of this challenging experiment, and made valuable contributions.

Jianyong Mo has been a close colleague and a friend, especially through the latter half of grad school. Jianyong took over the Brownian motion experiment in 2014, and rapidly mastered the domain. His exceptional work ethic and dogged determination have been a source of inspiration, and his eye for detail has helped time and again in our collaboration. In addition to being an excellent experimentalist, his aptitude for theory was instrumental in verifying some of the tedious calculations of drag coefficients and reaction field tensors. Some of the figures in this dissertation are taken from the dissertations and other work of Simon Kheifets and Jianyong Mo. They have been attributed to their author, and have been used with permission.

Able undergraduate students Camilo Perez, Jimmy Kennington, Will Plusnick and William Watson contributed to the experiments on Brownian motion. I appreciate the mentorship of Jack Clifford at the physics machine shop in helping me make some of the parts for the experiment. When working in Raizen's lab, I had the opportunity of interacting with very many dedicated, knowledgeable and pleasant fellow students, who contributed to my exposure and made me feel very welcome, including David Medellin, Kirsten Viering, Tom Mazur, Isaac Chavez, Georgios Stratis, Jamie Gardner, Erik Anciaux, Karl Burkhardt, Yu Lu, Daniel Raimi-Zlatic, Tharon Morrison, David Riegler, and Adam Libson. I would like to particularly thank my first boss Dr. Rob Clark for introducing me to the Raizen lab (and also to his crazy side), Kevin Melin for his uplifting snarky sense of humor and the many discussions on our shared

technological interests, Will Plusnick for being instrumental in keeping me inebriated during our many discussions about software and technology, and David Riegler for all the piano inspiration and wisdom – especially that Fantaisie-Impromptu fingering.

Matt Ervin has been extremely helpful in navigating the administrative matters in the department, and also a lot of fun to talk to. Marybeth Cassias, Rachael Salge and Olga Vera helped us with navigating administrative matters during my tenure in the Raizen lab. Cathy Rapinett orchestrated administrative matters during my association with the Morrison group. To all of them, I am thankful.

The theoretical work presented herein was supported financially by a Graduate Continuing Fellowship from the University of Texas at Austin, and the experimental work by the Robert A. Welch Foundation and the Sid W. Richardson Foundation. During part of the theoretical work, I also enjoyed the hospitality of the WHOI Geophysical Fluid Dynamics program, and the Numerical Plasma Physics Division of the Max Planck IPP, Garching, Germany, which I warmly acknowledge.

Siva Swaminathan and Akila Kesavasamy have been very helpful in reviewing parts of this dissertation, and helping me polish my defense presentation to the point of putting up with my inane questions about color contrast.

I enjoyed several excellent discussions on physics, as well as a lot of good food, with fellow members of the Morrison group,[1] ex-Morrisonians, members of the Whizkey seminar, and fellow physics grad students—in particular with George Miloshevich, Santiago Benavides, Manasvi Lingam, Tim Magee, Siva Swaminathan, Jeffrey Heninger, Elliot Persico, Matt Klimek, Mingsy Chua, Nick Bhattacharya, Eric Horsley, and Jay Hathaway—which enriched my knowledge as well as taste-buds. The enthusiasm of Santi, Nick, Eric and Jay, who were then undergrads, kept me from ever becoming too jaded.

One of the most memorable experiences of graduate school was doing homework together in the graduate lounge. The "Fluid Mechanics homework group", which aided in my half-complete assignment submissions to Prof. Morrison, consisted of Frank Lee, Justin Feng, and Darius Bunandar. Even outside of "fluids" and the associated Tom & Jerry screenings, Frank has been fun to talk to and "BS" with on pointless things. While Justin has an exceptional talent for communicating complicated General Relativity concepts in pictures, he also has an exceptional sense of

[1]Technically, this should be the Morrison monoid, because although we have an identity, are associative with one another, we do not have inverses to the best of my knowledge.

humor. Working on heavy assignments at 3 AM has a tendency to bring out the best—arguably also the worst—forms of humor – and Justin, Frank and I were party to this effect together.

Karthik Subramanian's gift of excellent Ethiopian Yirgacheffe coffee beans have been crucial to the final stages of this work. The coffee machine co-operative at NMPP, Garching was also of particular help. Several open-source software packages, particularly Emacs, ack, and TikZ have saved a lot of frustration. Bouldin Creek Café's great food, and flexibility with off-menu orders of the "Hippie Shake", have kept me going during this process.

I cannot ignore my high school and undergraduate teachers, and the people at the Bangalore planetarium, who contributed to the foundation in physics that made me feel prepared entering grad school. In particular, I wish to thank Dr. Shobha Vasuki, R. Sudhamani, Saroja Appana, H. R. Madhusudan, Dr. B. S. Shylaja, Prof. S. Lakshmi Bala, Prof. Suresh Govindarajan, Prof. Arul Lakshminarayan and Prof. Spenta Wadia.

Performance in one's professional life hinges on a stable personal life. During my graduate school, I have enjoyed deep personal friendships with Siva Swaminathan, Akila Kesavasamy, Prakash Mohan, Shravan Gowrishankar and Vishaal Sapuram. Akila and Siva have been an important source of support. Prof. Suresh Govindarajan, Kumar Appaiah, Hemant Hariyani, Jimi Lowrey and Pranesh Srinivasan have been friends and mentors in many capacities. To them, I am thankful. Throughout my life, I have enjoyed the enduring love and support of my family, without which I would not be writing this.

Brownian Motion in Liquids: Theory and Experiment

Publication No. _____

Akarsh Simha, Ph.D.
The University of Texas at Austin, 2017

Supervisor: Philip J. Morrison
Co-Supervisor: Mark G. Raizen

Since the theoretical work of Einstein [1905] and Von Smoluchowski [1906], and the experiments of Perrin [1909], Brownian motion at long time-scales has been extensively studied for over a century. Short time-scale aspects of Brownian motion are however becoming increasingly relevant, as technology attempts to make smaller and faster devices. The subject matter of this dissertation is the study of short time-scale (typically $\sim \mu$s) aspects of Brownian motion of microscopic particles in liquids, where the dynamics of the fluid medium are significant.

We detail two recent experiments probing this regime: an experiment [Kheifets *et al.*, 2014] that measured the hydrodynamic instantaneous velocity of a dielectric particle in liquid medium and confirmed theories of Brownian motion based on hydrodynamics up to sub-microsecond time-scales, and a subsequent experiment [Mo *et al.*, 2015*a*] that verified the Maxwell-Boltzmann distribution of velocities well into the tails.

In a liquid medium, the presence of a boundary near a particle has a significant impact on the characteristics of its Brownian motion, owing to the hydrodynamic coupling between the bounding walls and the particle. However, exact solutions to the hydrodynamic equations are not known even for the common situation of a flat wall. An approximate theory was developed by Felderhof [2005], using a point-particle approximation. Despite agreement with previous experiments, that work results in a drag coefficient with a spurious dependence on the particle's density. In this work, we describe a modification [Simha *et al.*, 2017] to the point-particle approximation that

resolves this inconsistency. Moreover, Felderhof's approximation scheme neglects the size of the particle not only in comparison to the distance of the bounding wall, but also to the skin-depth of rotational flow it generates in the fluid. Since this skin-depth depends on the time-scale of the motion, it is not obvious that such an approximation scheme works at all time-scales. We use the formalism of boundary integral equations to set up a perturbative framework, and obtain the point-particle framework through a series of systematic approximations. This derivation explains why the theory works so well at all time-scales. An alternative calculation for a simple case of a no-slip sphere near a full-slip wall is presented, with results indicating that the point-particle approximation may not capture all non-perturbative terms.

We then discuss an experiment [Mo *et al.*, 2015*b*] that probed the effects of a boundary on Brownian motion at short time-scales. The experiment agrees very well with the point-particle theory, demonstrating that the boundary significantly impacts Brownian motion down to a certain time-scale, and that the effects are diminished at shorter time-scales. Such effects allude to the possibility of using Brownian motion as a probe of the local environment.

Contents

List of Figures

List of Abbreviations

BTG	Barium Titanate Glass
EOU	Einstein-Ornstein-Uhlenbeck
FFT	Fast Fourier Transform
GLE	Generalized Langevin Equation
GWN	Gaussian White Noise
LTI	Linear And Time-Invariant
MSD	Mean-squared Displacement
NA	Numerical Aperture
OU	Ornstein-Uhlenbeck
PACF	Position Auto-correlation Function
PBS	Polarizing Beam Splitter
PPA	Point-Particle Approximation
PSD	Power Spectral Density
RMS	Root Mean Square
SDE	Stochastic Differential Equation
SNR	Signal To Noise Ratio
VACF	Velocity Auto-correlation Function

List of Symbols

ω	Frequency
ρ_p	Density of particle
ρ_f	Density of fluid
c	Speed of sound in the fluid
η	Dynamic shear viscosity of the fluid
m_p	Mass of particle
m_f	Mass of fluid displaced by particle
m^*	Effective (virtual) mass of the particle coupled to the fluid
$\boldsymbol{u}$	Velocity of particle
$\boldsymbol{v}$	Velocity of fluid
P	Pressure
ν	Kinematic shear viscosity of the fluid η/ρ_f
α	The complex wave-number / inverse skin-depth of vorticity $\sqrt{-\mathrm{i}\omega\rho_f/\eta}$, $\Re[\alpha] > 0$
a	Radius of spherical particle
$\boldsymbol{\sigma}$	Hydrodynamic stress tensor
γ_s	Steady Stokes drag coefficient on a sphere, $6\pi\eta a$
$\gamma_0(\omega)$	Unsteady Stokes drag coefficient on a sphere, $\gamma_s(1+\delta+\delta^2/9)$
$\tilde{\gamma}_0$	A quantity defined to be $\gamma_s(1+\delta+\delta^2/3)$
$\boldsymbol{\gamma}$	Tensor of drag coefficients
h	Distance from the center of particle to the wall
ϵ	Ratio of radius of sphere to distance to the wall a/h
δ	The non-dimensional product $\alpha a = \sqrt{-\mathrm{i}\omega\tau_f}$
$\mathfrak{v}$	The non-dimensional product $\alpha h = \sqrt{-\mathrm{i}\omega\tau_w}$
τ_f	Time-scale of vorticity diffusion over particle size $\rho_f a^2/\eta$
τ_w	Time-scale of vorticity diffusion over particle-wall distance $\rho_f h^2/\eta$

τ_k	Time-scale of over-damped harmonic trap γ^{steady}/K
τ_p	Momentum relaxation time-scale m^*/γ_s
τ_v	Decorrelation time-scale of VACF $\pi\tau_p^2/(4\tau_f)$
τ_c	Time-scale of fluid compressibility a/c
$\boldsymbol{S}_\xi(\omega)$	For general ξ, this represents the PSD of ξ
$\boldsymbol{C}_\xi(t)$	For stationary random process ξ, this represents the auto-correlation function of ξ
$\boldsymbol{Y}$	Admittance of the particle coupled to the fluid
$\boldsymbol{Y}_K$	Admittance of the particle coupled to the fluid and a harmonic trap
$\boldsymbol{K}$	Matrix of stiffness coefficients of harmonic trap
$\boldsymbol{F}_{\text{th}}$	Thermal (Langevin) force acting on the particle
$\boldsymbol{F}_{\text{ext}}$	External force applied to the particle
$\boldsymbol{F}_\omega^{\text{drag}}$	Drag force acting on the particle
$\boldsymbol{F}_\omega^{\text{ind}}$	Induced force that replaces the particle
T	Absolute temperature
μ	Ratio of refractive indices of particle to medium
n_p	Refractive index of particle
n_f	Refractive index of fluid
$\mathfrak{c}$	Speed of light in vacuum
k_B	Boltzmann's constant
$\boldsymbol{G}^0$	Unsteady Oseen tensor (fundamental solution of the unsteady Stokes equations)
$\boldsymbol{G}$	Any Green's function of the unsteady Stokes equations
$\boldsymbol{T}^0$	Stress tensor corresponding to $\boldsymbol{G}^0$
$\boldsymbol{R}$	The reaction-field tensor

Chapter One: Introduction

1.1 What does "Brownian motion" mean in this dissertation?

Brownian motion means different things to different people. The word "*Standard Brownian Motion*" usually refers to the *Wiener process* W_t, which may be loosely thought of as the integral of white noise.

However, in this dissertation, the primary subject of interest will be physical Brownian motion – the motion of a colloidal particle (a particle of the order of a few hundred nanometers to a few microns in size) suspended in a fluid. Specifically, the fluid will be a Newtonian liquid for the most part, and the particle will be a non-porous solid. Since physical particles have mass, their velocities cannot undergo sudden changes unless an infinite force is applied. The Wiener process is not differentiable, and therefore only models physical Brownian motion well at long time-scales. This dissertation will particularly explore theory that models, and experiments that probe short time-scale aspects of Brownian motion. In particular, hydrodynamic theories of Brownian motion, i.e. theories that correctly account for the behavior of the fluid environment, will form the central theme of this dissertation.

1.2 Brief history of Brownian motion

This section will only briefly explore the history of Brownian motion. There are several articles [see e.g. Bian *et al.*, 2016; Hänggi & Marchesoni, 2005] that go into more detail. A collection of historic articles, and articles on the history of Brownian motion may be found as of this writing on Prof. Peter Hänggi's website [Hänggi].

Although Brownian motion is named for Robert Brown, it was probably first described by Jan Ingenhousz [Van der Pas, 1971], a Dutch scientist, in 1785. Ingenhousz was observing the evaporation of liquids under a microscope, and noted that for example, finely ground charcoal introduced into a droplet of alcohol would be observed

to execute a "confused, continuous and violent motion".[1] Robert Brown's independent discovery appears in a 1828 article [Brown, 1828], wherein they observe pollen particles of about 1/4000 to 1/5000 inch in length immersed in water "very evidently in motion", which they claimed neither originated from currents in the fluid or from gradual evaporation. Brown also reports repeating the experiment after killing the plants, and observing the motion nevertheless.

Einstein [1905] gave a theoretical explanation of Brownian motion, based on thermodynamics and the Stokes law. Einstein explained the motion using statistical mechanics and the result of Stokes [1851] for the friction on a spherical particle in steady flow. Einstein's theory ignores the effects of the mass of the particle. Soon after, Von Smoluchowski [1906] gave an alternate explanation in terms of a random walk. Langevin [1908] used Smoluchowski's random walk to recover Einstein's result through the use of the now famous Langevin equation.[2] Incidentally, Langevin does note that the use of the Stokes drag formula does not account for the inertia of the fluid. Perrin [1909] performed experiments verifying Einstein's theory, which led to the measurement of Avagadro's number and thus proved the existence of molecules. This work won Perrin the Nobel Prize in Physics in 1926.

Uhlenbeck & Ornstein [1930] improved the model of Langevin by including the effects of the mass of the particle. The resulting random process (which describes the velocity of the Brownian particle) has come to be known as the Ornstein-Uhlenbeck process. However, computer simulations of liquid argon by Rahman [1964, 1966] showed a power law behavior for the velocity auto-correlation function at long time-scales, as opposed to the exponential decay expected from the Ornstein-Uhlenbeck model. Motivated by the fluid dynamic behavior seen in the computer simulations, Zwanzig & Bixon [1970], and Widom [1971] developed improved models of Brownian motion in liquids, which account for fluid dynamic "memory" effects that may be explained using the unsteady Stokes equations. Such models, often referred to as "Hydrodynamic theories" of Brownian motion, will form the primary theme of this dissertation. Stokes [1851] had already derived the result for the hydrodynamic friction on an oscillating spherical particle. The same result in the time-domain was analyzed by Boussinesq [1885] and Basset [1888], and the resulting force, which appears as a convolution integral over the past velocities of the particle, is known as the Boussinesq-Basset

[1] A translation of the description of Jan Ingenhousz is available in the cited reference.

[2] A translation of the work of Langevin has been presented by Lemons & Gythiel [1997]

force, or sometimes simply as the Basset force. These results form the fluid dynamic aspects of the hydrodynamic theory of Brownian motion.

1.3 Brownian motion at short time-scales

Microscopic and nanoscopic systems are gaining relevance as we continue to improve access to these scales through advanced microscopy and push the boundaries of technology to make devices smaller and faster. At these scales, the impact of thermal fluctuations is significant, and thus Brownian motion becomes ubiquitous. For example, micro-organisms and cell organelles suffer the incessant effect of thermal fluctuations, as do components of Micro-electro-mechanical systems (MEMS) and tips of atomic force microscopes [Clarke *et al.*, 2006]. Optical tweezers, which are gaining popularity as instrumentation to study microscopic objects especially in the context of biophysics, may be used to hold particles, but these particles are subject to incessant Brownian motion within the confines of the optical trap.

As we push the boundaries of technology further, the study of Brownian motion at short time-scales becomes increasingly important. The exploration of short time-scale Brownian motion has opened a window into the experimental study of statistical mechanics [see e.g. Mo *et al.*, 2015*a*; Kheifets *et al.*, 2014; Franosch *et al.*, 2011], and aids in better calibrating optical tweezers [Berg-Sørensen & Flyvbjerg, 2004; Grimm *et al.*, 2012]. It may provide a tool to measure the viscoelastic properties of complex fluids [Felderhof, 2009*a*] and to probe the nature of boundary conditions on surfaces [Lauga & Squires, 2005; Mo *et al.*, 2017]. One of the key advantages of measurements in short time-scales, is that mechanical noise usually drops with frequency, whereby artifacts induced by such noise may be circumvented, and the measurements may be shot-noise limited [see e.g. Kheifets *et al.*, 2014].

The long time-scale regime of Brownian motion is characterized by diffusive behavior – the Root Mean Square (RMS) displacement of the particle over a time period t grows like $\sqrt{t}$. This may be explained by a random walk model – the variance of the sum of independent and identically distributed Gaussian random variables grows linearly with the number of variables added, so the standard deviation grows like the square root of the number of steps taken. However, any physical particle has inertia, and therefore at short time-scales, the particle must have a well-defined velocity and

a displacement that grows linearly with t. This short time-scale regime of Brownian motion is called the *ballistic regime*.

For over a century, the ballistic regime of Brownian motion has eluded observation until recent experiments by Blum *et al.* [2006] and Huang *et al.* [2011]. The theory of Uhlenbeck & Ornstein [1930] models well the transition from diffusive to ballistic Brownian motion in a rare fluid like a gas. In the Einstein-Ornstein-Uhlenbeck (EOU) model of Brownian motion, the velocity decorrelates exponentially over a certain time-scale τ_p, known as the *momentum relaxation time* or the *Smoluchowski time*. This time-scale roughly marks the transition from the ballistic regime into the diffusive regime.

In denser fluids like liquids, the transition is much more complicated, since hydrodynamics plays a key role. Hydrodynamic theories of Brownian motion, which model the relaxation of the fluid environment after perturbation by the motion of the particle, become important when the timescale of relaxation of the fluid, τ_f, is comparable to or larger than the timescale of decorrelation of the velocity of the particle[3] τ_p. One can show that for a spherical particle in a Newtonian fluid, the ratio of these timescales is given by

$$\frac{\tau_p}{\tau_f} = \frac{2}{9}\,\frac{\rho_p}{\rho_f}, \tag{1.1}$$

where ρ_p denotes the density of the particle and ρ_f denotes the density of the fluid environment. For glass particles ($\rho_p \approx 2.0$ g/cm^3) in air at STP ($\rho_f \approx 0.001$ g/cm^3), there is a very large separation between these two timescales, $\tau_p \approx 400\tau_f$, whereby the EOU theory works well. However, for glass particles in water ($\rho_f \approx 1.0$ g/cm^3), there is very little separation between time-scales, $\tau_p \approx 2\tau_f$, and the hydrodynamic effects become very significant.

The hydrodynamic theories of Zwanzig & Bixon [1970] and Widom [1971] model the fluid environment using the regime of unsteady Stokes flow (see Chapter 3). This regime accounts for the non-instantaneous diffusion of shear stress in the fluid environment, as the particle moves about. The predictions of these theories for Brownian motion have been successfully verified by experiments [Franosch *et al.*, 2011; Huang *et al.*, 2011; Kheifets *et al.*, 2014] over a large range of time-scales.

In most of these theories, the fluid is assumed to be incompressible, which is a good approximation for liquids. The effects of compressibility become relevant on a

[3]These time-scales will be defined precisely at a later stage.

time-scale $\tau_c := L/c$ where L denotes some measure of the size of the particle, and c is the speed of sound in the fluid. For micron-sized particles in water, this time-scale is of the order of a nano-second, which is much smaller than the time-scales τ_f or τ_p for the same system. The regime of compressible Brownian motion is as yet out of reach of experiment, although there are some proposals [Mo, 2015, Chap. 9].

The hydrodynamic theories show that the Brownian particle is sensitive to its fluid environment. For example, the presence of walls in the vicinity of the particle alters its Brownian motion in a significant manner [Mo *et al.*, 2015*b*], as do the boundary conditions on these walls [Mo *et al.*, 2017]. Non-Newtonian behavior of the fluid environment would also alter the nature of Brownian motion [Felderhof, 2009*a*]. This brings up the possibility of using Brownian motion as a probe of the local fluid environment.

1.4 Organizational summary of this dissertation

This dissertation is organized as follows: In Chapter 2, we review well-known results pertaining to the statistical description of Brownian motion. We provide an overview of the various theories mentioned in this Introduction, and define various quantities that we use to characterize Brownian motion. In Chapter 3, we review well-known material pertaining to low Reynolds number hydrodynamics. We develop the basic framework used to calculate drag coefficients that enter the hydrodynamic theories of Brownian motion, and review various formulations of solutions to the unsteady Stokes equations that are relevant to this work. Chapter 4 discusses the well-known hydrodynamic theory of a spherical Brownian particle in an unbounded fluid medium.

In Chapter 5 we describe the ingredients of an experimental setup that may be used to probe Brownian motion in liquids at short time-scales. The experimental setup uses optical tweezers to confine spherical dielectric particles in liquid media, and back-focal-plane detection, using a novel split-beam detector, to track the displacement of the particle along one dimension. We describe in detail the methods of trapping a Brownian particle, detecting and recording its motion, and data analysis, based on the experimental setup developed in the Raizen Lab at the University of Texas at Austin.

In Chapter 6, we detail aspects of published experimental results pertaining to

Brownian motion in bulk liquid. We describe the measurement of hydrodynamic instantaneous velocity in liquid [Kheifets *et al.*, 2014], and the subsequent verification of Maxwell-Boltzmann statistics [Mo *et al.*, 2015*a*]. We begin with a description of the experimental challenges involved in these measurements, and then detail the results. The experiments achieve a shot-noise limited position resolution under 3 fm/$\sqrt{\text{Hz}}$, over a large bandwidth. The hydrodynamic instantaneous velocity is observed to follow a modified equipartition theorem, which accounts for the kinetic energy of the fluid displaced by the moving particle. Statistics of the thermal force acting on the particle, recovered from the experimental data using the theoretical results for the admittance, are seen to agree with the predictions of the fluctuation-dissipation theorem. This result may be interpreted as a verification of the fluctuation-dissipation theorem under the assumption that the hydrodynamic theory (Chapter 4) is correct.

In Chapter 7, we describe a theoretical approximation framework that may be used to calculate the drag force on a particle oscillating in a viscous fluid medium in the presence of other boundaries [Simha *et al.*, 2017]. The presence of boundaries near a spherical particle, except in special cases, produces a problem of reduced symmetry, which typically renders impossible the exact solution of the unsteady Stokes equations. Using a novel point-particle approximation, Felderhof [2005, 2006*a*, 2012] has developed theoretical predictions for the Brownian motion of a particle in the presence of boundaries. Some of the results have shown excellent agreement with experiments [Jeney *et al.*, 2008]. However, Felderhof's framework results in drag coefficients that depend on the particle's density, whereas the problem of calculating the drag force can be formulated without any reference to the particle's density. Moreover, the results for the effective mass of the particle inferred from the RMS velocity predicted by Felderhof [2005] do not agree with well-known results obtained through potential flow calculations. We present a modification of Felderhof's framework that resolves these inconsistencies. The difference produced by this resolution is not significant enough to be detected by previous experiments. A second concern with the point-particle framework is that it is not obvious that such an approximation works at short time-scales. This is because the approximation appears to neglect the particle's size in comparison to the skin-depth of rotational flow it generates, the latter depending on the time-scale of motion. To address this issue, the modified point-particle framework is derived through a series of systematic approximations performed in a general formalism of boundary integral equations. The formalization

of the point-particle approximation provides an explanation for why it works so well over a large range of time-scales.

In Chapter 8, an alternate calculation using the method of reflections is presented for the special case of a full-slip flat wall, and the results of the modified point-particle approximation are compared against the method of reflections. The comparison shows that although there are differences in the actual expressions, they agree in all asymptotic limits. The differences in the expressions indicate that the modified point-particle approximation may not capture all non-perturbative terms. In investigating the asymptotic limits, we also observe that the modifications to the point-particle approximation result in the expected effective mass. We also present a numerical comparison of drag coefficients, which shows that the effects of our modification to the point-particle approximation become significant when the relative density between the particle and the fluid is large.

In Chapter 9, we apply the theoretical ideas developed in the previous chapters to the problem of Brownian motion. We show that while there are no experimentally discernible differences between the predictions from the method of reflections and from the modified point-particle approximation, the differences produced by the modification themselves are of great significance to systems of metallic micro-/nano-particles in liquids. The low-frequency expansion of the power spectral density of the thermal force shows that the force in the perpendicular direction, and also in the parallel direction in case of a no-slip wall, becomes less colored at low frequencies in the presence of a wall. We also provide well-known expressions for hindered diffusion that are relevant to the work presented in the next chapter.

In Chapter 10, we detail aspects of published experimental results [Mo *et al.*, 2015*b*] pertaining to Brownian motion in a liquid in the vicinity of boundaries. The experimental results show that the (no-slip) boundary has a significant effect on Brownian motion, and the differences are especially discern-able in the VACF. The differences become insignificant only when the distance between the particle and the wall is about an order of magnitude larger the diameter of the particle. We show that fitting the VACF provides a reliable method to measure the distance to the wall. The experimental measurements also demonstrate that the thermal force loses color at low frequencies in the presence of the wall.

Excepting the first three introductory chapters, the author contributed in either an experimental or theoretical capacity to the work described in the remaining chapters.

Chapter Two: Preliminaries: Statistical mechanics of Brownian Motion

This chapter reviews well-known results that form prerequisites for the description and analysis of Brownian motion.

2.1 Describing Brownian Motion through a Langevin equation

Langevin [1908] introduced a description of the long time-scale aspects of Brownian motion through what has now come to be known as the Langevin equation. Many a time, the phrase "a Langevin equation" is used to describe any stochastic differential equation, not just the specific one that Langevin wrote down.

A Stochastic Differential Equation (SDE) relates a random process to other random processes. A simple example is the equation

$$\dot{x}(t) = -\gamma x(t) + \sigma\eta(t), \tag{2.1}$$

where $x(t)$ is the stochastic process that the equation is to be solved for, $\eta(t)$ represents Gaussian White Noise (GWN), and γ and σ are some constants. For each time instant t, Gaussian white noise $\eta(t)$ is a Gaussian random variable that is independent from the realization of η at any other time instant, with zero mean and with an indefinite variance such that integrating it over a short interval δt produces a finite variance[1] of δt. For each realization of the white noise process $\eta(t)$, the equation describes a corresponding realization of the desired process $x(t)$.

Gaussian white noise is a mathematically bizarre object, and therefore, care is required in analyzing SDEs. Formal mathematical frameworks to handle SDEs were introduced by Itô and Stratonovich[2]. In this work, we shall be content with the use of an informal framework using Fourier / Laplace transforms to solve the SDEs.

[1] This loose statement is better described by $\mathrm{d}W_t\,\mathrm{d}W_t = \mathrm{d}t$.

[2] The author finds a useful reference on this subject in the lecture notes from the Woods Hole Geophysical Fluid Dynamics school, 2015.

This informal framework is somewhat similar to Stratonovich calculus, since we take Fourier transforms without trepidation, pretending that the transforms exists; we may be able to formalize this procedure by using a low-pass filtered white noise to compute the power spectra, and then take the limit as the bandwidth goes to infinity.

The auto-correlation function of a random process $\xi(t)$ may be defined through

$$C_\xi(t,\, t') := \langle \xi(t)\xi(t') \rangle, \tag{2.2}$$

where $\langle \quad \rangle$ denotes averaging over the ensemble of realizations of ξ. If the process $\xi(t)$ is stationary, i.e. the statistics are invariant under translations of the origin of time, the auto-correlation function only depends on the difference in arguments, i.e. $C_\xi(t,\, t') = C_\xi(t - t')$ for stationary processes. GWN is stationary, and *uncorrelated* (sometimes also called δ-correlated), i.e.

$$\langle \eta(t)\eta(t') \rangle = \delta(t - t') \tag{2.3}$$

Specifically in the context of equilibrium Brownian motion, consider a particle of mass m suspended in a viscous fluid (at low Reynolds number). Phenomenologically, the random collisions of fluid molecules with the particle may be thought of as producing two effects: a deterministic effective drag force $\boldsymbol{F}_{\text{drag}} = -\gamma \boldsymbol{v}$ that may be obtained through macroscopic models of fluid dynamics, and a random force $\boldsymbol{F}_{\text{th}}$ that models the random effects of the collisions. The latter force is usually referred to as the "thermal force" or the "Langevin force." In this context, we shall assume it to be a Gaussian white noise process and write $\boldsymbol{F}_{\text{th}} = \boldsymbol{\sigma}\eta(t)$, an assumption that will be justified later. We may apply Newton's second law and write

$$m\, \frac{\mathrm{d}\boldsymbol{u}}{\mathrm{d}t} = -\gamma \boldsymbol{u}(t) + \boldsymbol{\sigma}\eta(t), \tag{2.4}$$

for the velocity $\boldsymbol{u}(t)$ of the particle. The above is an example of a Langevin equation that describes Brownian motion. In particular, the above equation produces the Einstein-Ornstein-Uhlenbeck theory of Brownian motion, and describes Brownian motion in a rare fluid such as a gas. The stochastic process $u(t)$ is an example of an Ornstein-Uhlenbeck (OU) process[3] [Uhlenbeck & Ornstein, 1930]. The OU process may be thought of as low-pass-filtered white noise (figure 2.3).

[3]In the spirit of football rivalries, the author wishes to point out that we would rather call this the "u_t process".

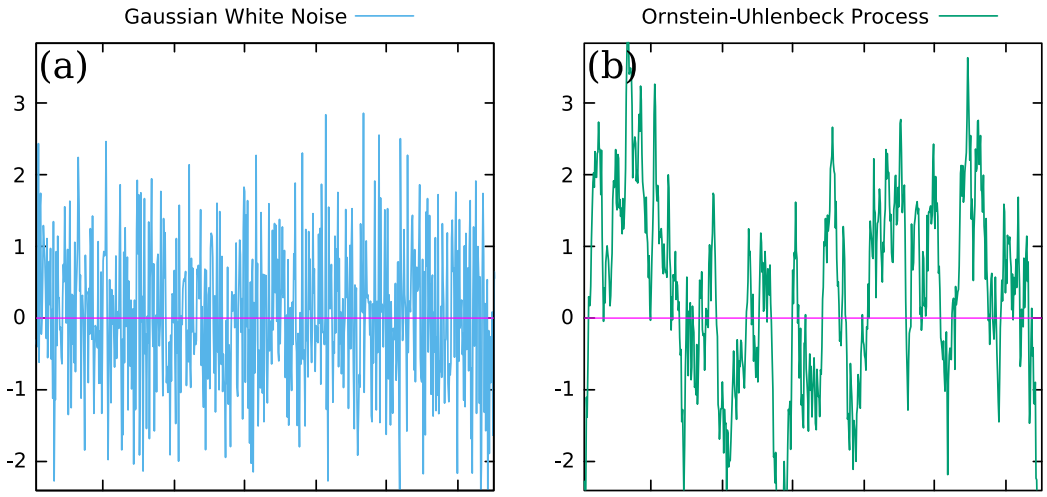

Figure 2.1: (a) A (discrete) realization of Gaussian White Noise with unit variance at each time-step. (b) The realization of an OU process described by (2.4) (in one dimension) with $\gamma/m = 0.03$ and $\sigma/m = 0.005$ that corresponds to the GWN realization shown in (a). The SDE was solved by numerical integration using the Euler-Maruyama scheme.

Figure 2.1 (b) shows an example realization of the Ornstein-Uhlenbeck process described by (2.4) (in one dimension) for $\gamma/m = 0.03$ and $\sigma/m = 0.005$ obtained by integration of the SDE using the Euler-Maruyama scheme. The realization of (discretized) Gaussian white noise that was integrated is shown in sub-figure (a).

Figure 2.2 compares the displacement obtained by integrating an Ornstein-Uhlenbeck process against the Wiener process computed from the same realization of Gaussian White Noise. The integral of the OU process does not have cusps, unlike the Wiener process. As stated in the Introduction, the Wiener process does not model physical Brownian motion well at short time-scales, since its derivative is not well-defined.

2.2 The Einstein-Ornstein-Uhlenbeck theory

We shall now proceed to solve the equation (2.4). Completing the description by determining σ, we will obtain the EOU theory of Brownian motion. For simplicity, we shall hereafter consider one dimension instead of all three until we encounter an anisotropic geometry.

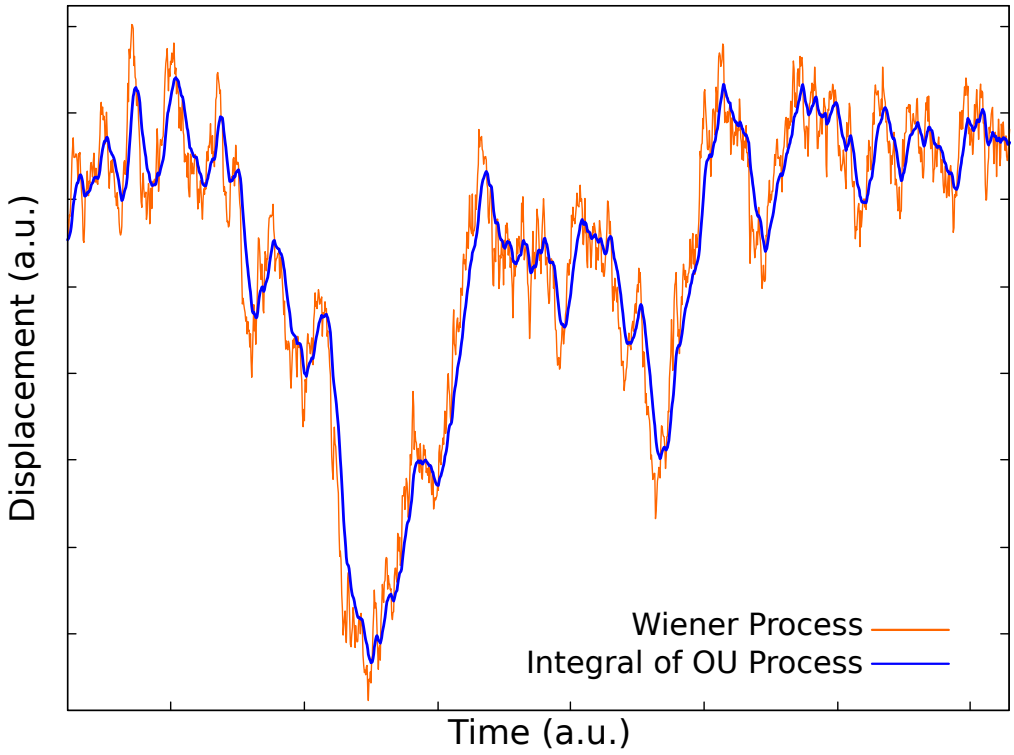

Figure 2.2: The plot compares the integral of a realization of an OU process described by described by (2.4) (in one dimension) with $\gamma/m = 0.1$ and $\sigma/m = 0.1$ against the Wiener process computed from the same realization of Gaussian White Noise. The plot shows that the displacement calculated from the OU process has no cusps, unlike the Wiener process.

To find the statistics of $u(t)$, we use Fourier transforms.[4] We will denote the Fourier transform of $u(t)$ by $\check{u}(\omega)$ (or simply $u(\omega)$ or u_ω wherever the ambiguity does not hinder understanding), and use the convention

$$\check{u}(\omega) := \int \mathrm{d}t\, \mathrm{e}^{\mathrm{i}\omega t}\, u(t), \qquad u(t) = \int \frac{\mathrm{d}\omega}{2\pi}\, \mathrm{e}^{-\mathrm{i}\omega t}\, \check{u}(\omega). \tag{2.5}$$

We may therefore readily write[5]

$$[-\mathrm{i}\omega m + \gamma]\, \check{u}(\omega) = \sigma \check{\eta}(\omega), \tag{2.6}$$

[4]Since we are describing thermal equilibrium, we do not have an origin in time or initial conditions. Thus, Fourier transforms are naturally suited over Laplace transforms. If one wanted to model the relaxation from a known initial state (possibly the result of a thermal fluctuation in equilibrium, or a specially prepared non-equilibrium state) to thermal equilibrium, Laplace transforms would be more suitable [see e.g. Balakrishnan, 2008].

[5]We have ignored issues of the existence and convergence of the Fourier transforms.

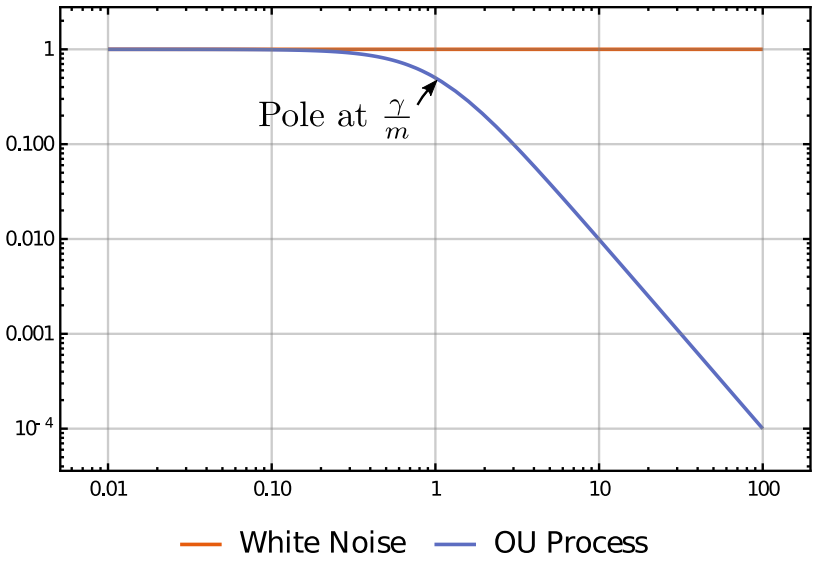

Figure 2.3: A comparison of the flat PSD of Gaussian White Noise with the PSD of the OU process u. The latter has a pole at γ/m which causes a fall off $\sim 1/\omega^2$. The power spectral densities have been normalized to 1. The x-axis represents frequency in units of γ/m.

and consequently determine the Power Spectral Density (PSD) S_u of u to be

$$S_u(\omega) = \frac{\sigma^2}{\omega^2 m^2 + \gamma^2} S_\eta(\omega), \tag{2.7}$$

where we have used the fact that power spectra[6] $S_\xi \propto |\check{\xi}^2(\omega)|$ and assumed that γ is real. The power spectrum $S_u(\omega)$ is compared to the flat power spectrum of GWN in figure 2.3.

The Wiener-Khinchin theorem[7] states that for a stationary[8] process, auto-correlation functions and power spectra form a Fourier transform pair, i.e.

$$S_\xi(\omega) = \int_{-\infty}^{\infty} \mathrm{d}t \; C_\xi(t) \; \mathrm{e}^{-\mathrm{i}\omega t}. \tag{2.8}$$

We may use this to find the velocity auto-correlation function (VACF) from (2.7). Noting that $S_\eta = 1$ (given that it is Gaussian white noise) and using the convolution

[6]The random processes considered here are typically not in $L^2(\mathbb{R})$, whereby the precise definition of the power spectrum is through the limit $S_\xi(\omega) := \lim_{T\to\infty} \frac{1}{T} \left| \int_{-T/2}^{T/2} \mathrm{d}t \; \mathrm{e}^{\mathrm{i}\omega t} \xi(t) \right|^2$. However, any experimentally relevant signal is recorded only for finite time, whereby in practice it is sufficient to note that $S_\xi \propto |\check{\xi}^2(\omega)|$ for many purposes.

[7]It must be noted that this is a non-trivial theorem, as it involves convergence issues etc.

[8]The general result applies not only to stationary, but wide-sense stationary stochastic processes.

theorem, we find that

$$C_u(t) = \frac{\sigma^2}{m^2} \int_{-\infty}^{\infty} \mathrm{d}t' \; \mathrm{e}^{-\gamma|t-t'|/m} \; C_\eta(t'). \tag{2.9}$$

From the assumption that $\eta(t)$ is Gaussian White Noise, we have $C_\eta(t') = \delta(t')$, whereby we may write

$$C_u(t) = \frac{\sigma^2}{2m\gamma} \mathrm{e}^{-\gamma|t|/m}. \tag{2.10}$$

The above result may also be obtained by multiplying (2.4) by $u(t')$ where t' is some instant of time, and then making a causality argument about $\langle u(t)\eta(t')\rangle$, but we will prefer the method using Fourier transforms for future purposes.

Defining the mean-squared displacement (MSD) through

$$\mathrm{MSD}(\tau) := \left\langle [x(t+\tau) - x(t)]^2 \right\rangle, \tag{2.11}$$

wherein the non-dependence on t arises from the assumption of stationarity, we find that it may also be written as

$$\begin{aligned} \mathrm{MSD}(\tau) &= 2\left[\left\langle x^2 \right\rangle - C_x(\tau)\right] \\ &= 2\left[C_x(0) - C_x(\tau)\right]. \end{aligned} \tag{2.12}$$

As can be seen by noting the linearity of ensemble averages (so that we can pull derivatives out of averages) and using stationarity (which tells us that C_x and C_u are functions of $t - t'$), the position auto-correlation function satisfies

$$-\frac{\mathrm{d}^2}{\mathrm{d}t^2} C_x(t) = C_u(t), \tag{2.13}$$

whereby we have

$$C_x(t) = \frac{\sigma^2}{2m\gamma} \left[At + B - \left(\frac{m}{\gamma}\right)^2 \mathrm{e}^{-\gamma t/m} \right] \qquad (t > 0). \tag{2.14}$$

To determine coefficient A, we need to make a few observations. For any stationary random process $\xi(t)$, $C_\xi(t) := \langle \xi(t+t_0)\xi(t_0)\rangle$ (where t_0 may be any instant of time by time-translation symmetry) is necessarily an even function of t, for $C_\xi(-t) = \langle \xi(-t+t_0)\xi(t_0)\rangle = \langle \xi(t_0')\xi(t_0'+t)\rangle = C_\xi(t)$, where we chose $t_0' = t_0 - t$. This is mirrored by the explicit form of $C_u(t)$, and also by the fact that the power spectrum is a purely real quantity. Therefore, the derivative of an auto-correlation function $\mathrm{d}C_\xi/\mathrm{d}t$

is necessarily an odd function of time. Therefore, we must either have $\dot{C}_x(0) = 0$ or $\dot{C}_x(0)$ undefined (as is the case with $\dot{C}_u(0)$). However, since $C_u(t)$ is a continuous function, $\dot{C}_x(t)$ has continuous derivative, and therefore we must have $\dot{C}_x(0) = 0$. We may now use this to determine A. The result is

$$A = -\frac{m}{\gamma}. \tag{2.15}$$

From the fact that $C_x(t)$ must be even, we have

$$C_x(t) = \frac{\sigma^2}{2m\gamma}\left[-\frac{m}{\gamma}|t| + B - \left(\frac{m}{\gamma}\right)^2 \mathrm{e}^{-\gamma|t|/m}\right]. \tag{2.16}$$

Using (2.12), we now have

$$\mathrm{MSD}(t) = \frac{\sigma^2}{m\gamma}\left[\frac{m}{\gamma}t + \left(\frac{m}{\gamma}\right)^2 \left(\mathrm{e}^{-\gamma t/m} - 1\right)\right] \qquad (t > 0). \tag{2.17}$$

The long-time behavior of the MSD for a Brownian particle typically scales like $\mathrm{MSD}(t) \sim 2Dt$ where D is called the diffusion constant. We mentioned this earlier in the Introduction as a characteristic feature of the diffusive regime. From this we may identify the diffusion constant to be $\sigma^2/(2\gamma^2)$.

So far, we have solved the SDE for the OU process and computed various statistical quantities such as correlation functions and power spectra without any further physical input. We now task ourselves with determining the strength of the Langevin force σ, which requires a physical input. In thermal equilibrium, the average energy of the Brownian particle must remain constant. This means that the energy input into the particle by the thermal fluctuations through the Langevin force must match the energy removed from it by the viscous dissipation. Thus, the condition of thermal equilibrium must provide a way to connect σ to γ, a fact expressed by the *fluctuation-dissipation theorem*. The connection is particularly easy to obtain in this case: we may use the equipartition theorem $\langle v^2 \rangle = k_B T/m$ to fix $C_u(0) = k_B T/m$ and therefore obtain $\sigma^2 = 2k_B T\gamma$.

With this value for σ, we may write

$$\begin{aligned} C_u(t) &= \frac{k_B T}{m}\mathrm{e}^{-|t|/\tau_p}, \\ \mathrm{MSD}(t) &= \frac{2k_B T\tau_p^2}{m}\left[\frac{t}{\tau_p} + \left(\mathrm{e}^{-t/\tau_p} - 1\right)\right] \qquad (t > 0), \\ D &= \frac{k_B T}{\gamma}, \end{aligned} \tag{2.18}$$

where we have defined the momentum relaxation time,

$$\tau_p = \frac{m}{\gamma}. \tag{2.19}$$

From the form of the MSD, it is clear that the momentum relaxation time τ_p is the timescale associated with the transition from ballistic to diffusive Brownian motion. For $t \ll \tau_p$, we expand the exponential term to second order in a Taylor expansion, and we see that the term of order t cancels, leaving the term of order t^2 behind. The resulting asymptotic form,

$$\mathrm{MSD}(t) \sim \frac{k_B T}{m} t^2 \qquad t \to 0, \tag{2.20}$$

is equivalent to ballistic motion with velocity $v_{\mathrm{eq}} = \sqrt{k_B T/m}$. For large time-scales $t \gg \tau_p$, the exponential transients have decayed, and what remains is the diffusive behavior $\mathrm{MSD}(t) \sim 2Dt$.

2.3 The Hydrodynamic Theory

A hydrodynamic explanation of Brownian motion in a dense fluid was inspired by the computer simulations of Rahman [1964, 1966], and was provided first (to the best of the author's knowledge) by Alder & Wainwright [1970]. A more comprehensive theory was then derived by Zwanzig & Bixon [1970].

Notably, it was observed first in the computer simulations that the VACF showed a power-law decay, specifically $C_u(t) \sim t^{-3/2}$ in the long time limit, instead of the exponential behavior predicted by the EOU theory. This long-time power-law tail is explained well if one includes the effects due to the finite time that the fluid environment takes to relax to a change in the particle's velocity.

Generally speaking, if the finite time taken by the fluid to relax is to be accounted for, the drag force must take the form of a memory kernel integrated against the past velocities of the particle. As a specific example, the force exerted by a viscous fluid on an accelerating spherical particle is given by [Basset, 1888; Franosch *et al.*, 2011]

$$F_{\mathrm{drag}}(t) = -\left[\frac{m_f}{2}\dot{u}(t) + 6\pi\eta a\left(u(t) + \sqrt{\frac{\tau_f}{\pi}}\int_{-\infty}^{t}\frac{\dot{u}(t')}{\sqrt{t-t'}}\,\mathrm{d}t'\right)\right], \tag{2.21}$$

where η is the coefficient of viscosity of the fluid, a is the radius of the spherical particle, $\tau_f := a^2\rho_f/\eta$ is the time-scale over which the fluid relaxes (see Chapter 3 for details), and $m_f := \frac{4}{3}\pi\rho_f a^3$ is the mass of fluid displaced by the particle.[9]

The most general form of the viscous dissipation under the conditions that the fluid have a linear, time-translation invariant and causal response is given by convolution with a memory kernel $\boldsymbol{\zeta}(t)$ (which could in general be a tensor), whereby we may write the equation of motion as

$$m\,\frac{\mathrm{d}\boldsymbol{u}(t)}{\mathrm{d}t} = -\int_{-\infty}^{t} \boldsymbol{\zeta}(t-t')\cdot\boldsymbol{u}(t')\,\mathrm{d}t' + \boldsymbol{F}_{\mathrm{th}}(t). \tag{2.22}$$

Such an equation is typically called a Generalized Langevin Equation (GLE), and it turns out that in this case, the Langevin force $\boldsymbol{F}_{\mathrm{th}}$ can no longer be assumed to be white-noise. We will say more about this in Section 2.4. While we have written the above equation in a causal form, when working in frequency domain to describe equilibrium (which has time reversal symmetry), it is usually convenient to ignore causality. In frequency domain, we may write the GLE as

$$[-\mathrm{i}\omega m\mathbb{1} + \boldsymbol{\gamma}(\omega)]\cdot\check{\boldsymbol{u}}(\omega) = \check{\boldsymbol{F}}_{\mathrm{th}}(\omega), \tag{2.23}$$

which is much easier to deal with than the time-domain form owing to the replacement of the convolution by multiplication. $\boldsymbol{\gamma}(\omega)$ is a tensor of drag coefficients for oscillations at frequency ω, i.e. the drag force experienced by a particle oscillating in the fluid with velocity $\boldsymbol{u}\,\mathrm{e}^{-\mathrm{i}\omega t}$ is $\boldsymbol{\gamma}(\omega)\cdot\boldsymbol{u}(\omega)\,\mathrm{e}^{-\mathrm{i}\omega t}$. $\boldsymbol{\zeta}(t)$ would correspond to the inverse Fourier-Laplace transform of $\boldsymbol{\gamma}(\omega)$ computed with an appropriate Bromwich contour to impose causality.

In linear response theory, it is assumed that the system responds to thermal fluctuations as it would to an external force $\boldsymbol{F}_{\mathrm{ext}}$ [Balakrishnan, 2008]. Introducing the mechanical admittance $\boldsymbol{Y}(\omega)$ (also called mobility),

$$\check{\boldsymbol{u}}(\omega) = \boldsymbol{Y}(\omega)\cdot\check{\boldsymbol{F}}_{\mathrm{ext}}(\omega), \tag{2.24}$$

which could in general be a tensor as indicated above, we may write the GLE of (2.23) as

$$\check{\boldsymbol{u}}(\omega) = \boldsymbol{Y}(\omega)\cdot\check{\boldsymbol{F}}_{\mathrm{th}}(\omega), \tag{2.25}$$

[9] On a side note, the author wishes to point out that the Basset force has a structure similar to a fractal derivative with half-integer order. See Saichev & Woyczynski [2013] for more. The fractal relaxation is probably one way to understand the origin of Faddeeva functions in the solution of Clercx & Schram [1992].

with the form of the admittance given by

$$\boldsymbol{Y}(\omega) = \left[-\mathrm{i}m\omega\mathbb{1} + \boldsymbol{\gamma}(\omega)\right]^{-1}. \tag{2.26}$$

The admittance provides a convenient way to connect up the "macroscopic" description of dynamics of a particle in a liquid under an external force, with the thermal fluctuations represented through the Langevin force, to obtain a description of Brownian motion. The fluctuation-dissipation theorem, or alternately a Green-Kubo relation, may be used to determine equilibrium Brownian dynamics once the admittance is known.

The connection between the VACF and admittance may be made through the Green-Kubo relation

$$\boldsymbol{Y}(\omega) = \frac{1}{k_B T}\int_0^\infty \mathrm{e}^{\mathrm{i}\omega t}\,\boldsymbol{C}_u(t)\,\mathrm{d}t, \tag{2.27}$$

from which, we may deduce (using the even and real nature of the auto-correlation and the Wiener-Khinchin theorem) that

$$\Re[\boldsymbol{Y}(\omega)] = \frac{1}{2k_B T}\boldsymbol{S}_u(\omega). \tag{2.28}$$

Thus, we have the following computationally useful expressions for the various statistical properties of Brownian motion [Franosch & Jeney, 2009]:

$$\begin{aligned}
\boldsymbol{S}_u(\omega) &= 2k_B T\ \Re[\boldsymbol{Y}(\omega)],\\
\boldsymbol{S}_x(\omega) &= \boldsymbol{S}_u(\omega)/\omega^2,\\
\boldsymbol{C}_u(t) &= \frac{2k_B T}{\pi}\int_0^\infty \mathrm{d}\omega\ \cos(\omega t)\,\Re[\boldsymbol{Y}(\omega)],\\
\boldsymbol{C}_x(t) &= \frac{2k_B T}{\pi}\int_0^\infty \mathrm{d}\omega\ \cos(\omega t)\,\frac{\Re[\boldsymbol{Y}(\omega)]}{\omega^2}.
\end{aligned} \tag{2.29}$$

The expressions for the auto-correlation functions are obtained by noting that the admittance must be conjugate-even,[10] whereby the power-spectra are even functions of frequency. Therefore, one may replace the inverse Fourier transform in the Wiener-Khinchin theorem by an cosine transform.

For the case of a sphere in bulk fluid, $\gamma(\omega)$ takes the form [Stokes, 1851; Landau & Lifshitz, 1987]

$$\gamma(\omega) = 6\pi\eta a\left[1 + \sqrt{-\mathrm{i}\omega\tau_f} + (-\mathrm{i}\omega\tau_f)/9\right]. \tag{2.30}$$

[10] i.e. that $\boldsymbol{Y}^*(-\omega) = \boldsymbol{Y}(\omega)$, as can be deduced from (2.27) upon noting that $\boldsymbol{C}_u$ is real

For this case, the inverse cosine transforms in (2.29) may be computed in closed-form and the results expressed in terms of Faddeeva functions. See Clercx & Schram [1992] for details. In most other cases, the cosine transforms need to be evaluated numerically. Special quadrature algorithms for oscillatory functions, such as the Filon-Trapezoid rule [Tuck, 1967] used by [Franosch & Jeney, 2009], are recommended.

2.4 Fluctuation-Dissipation Theorem from the Green-Kubo relation

It is evident that it is not possible to determine the statistics of the Langevin force $\boldsymbol{F}_{\text{th}}$ in the GLE, in the same way that we did for the EOU theory. This is because the equipartition theorem only gives us (assuming decoupled dimensions, so we may consider only one dimension),

$$\langle v^2 \rangle = \frac{k_B T}{m} = \int_{-\infty}^{\infty} \frac{\mathrm{d}\omega}{2\pi} \, |Y(\omega)|^2 S_F(\omega). \tag{2.31}$$

If $S_F(\omega)$ did not have a dependence on ω, one could determine the magnitude of its constant value from the above condition alone, as we did earlier. However, for the GLE, no assumptions of this nature can be made on the Langevin force, whereby we must find another way of computing its statistics.

Using the Green-Kubo relation (which may be derived from the GLE; see Balakrishnan [1979]) provides a way. Combining the first of (2.29) with (2.25),[11]

$$S_u(\omega) = |Y(\omega)|^2 S_F(\omega) = 2k_B T \, \Re[Y(\omega)], \tag{2.32}$$

we see that

$$S_F(\omega) = 2k_B T \, \Re[1/Y(\omega)]. \tag{2.33}$$

If the only resistive force acting on the particle is the viscous dissipation of the fluid, we note that $\Re[1/Y(\omega)] = \Re[\gamma(\omega)]$ since the other terms are pure imaginary. Thus, we obtain the power spectral density of the Langevin force as,

$$S_F(\omega) = 2k_B T \, \Re[\gamma(\omega)]. \tag{2.34}$$

[11] Once again, we assume that $\boldsymbol{Y}$ is diagonal, and we may consider one dimension. Otherwise, we transform to that basis.

This is the result of the fluctuation-dissipation theorem for the GLE. Since $\Re[\gamma(\omega)]$ is generally not constant, the thermal fluctuations are necessarily modeled by colored noise. Specifically in the context of a sphere in unbounded Newtonian fluid, we have $\Re[\gamma(\omega)] = 6\pi\eta a(1 + \sqrt{\omega\tau_f/2})$, so the thermal force has a higher strength at high frequencies. This unphysical result, we believe, is resolved by including the effects of fluid compressibility.

2.5 Inclusion of a Harmonic Restoring Force

In many practical applications, the Brownian particle is constrained in motion by some sort of mechanism. For example, in optical tweezers, the radiation pressure produces a potential well that traps the particle. In general, most sorts of confinement could be approximated by a harmonic restoring force. Therefore, it becomes useful to include the effects of a harmonic restoring force.

The force being given by $\boldsymbol{F}_{\text{trap}}(t) = -\boldsymbol{K} \cdot \boldsymbol{x}(t)$, where $\boldsymbol{K}$ is a tensor of stiffness constants for the trap, we may write it in frequency domain as $\check{\boldsymbol{F}}_{\text{trap}}(\omega) = \boldsymbol{K} \cdot \check{\boldsymbol{u}}(\omega)/(\mathrm{i}\omega)$ and add this to the GLE in equation (2.23) to obtain

$$[-\mathrm{i}\omega m\mathbb{1} + \boldsymbol{\gamma}(\omega) - \boldsymbol{K}/(\mathrm{i}\omega)] \cdot \check{\boldsymbol{u}}(\omega) = \check{\boldsymbol{F}}_{\text{th}}(\omega), \tag{2.35}$$

which implies that we may introduce the effects of the harmonic trap into the admittance as

$$\boldsymbol{Y}_K(\omega) = [-\mathrm{i}m\omega\mathbb{1} + \boldsymbol{\gamma}(\omega) - \boldsymbol{K}/(\mathrm{i}\omega)]^{-1}. \tag{2.36}$$

Chapter Three: Preliminaries: Unsteady Stokes Flow

In Chapter 2, we defined and described how to compute various statistical properties characterizing Brownian motion of a particle in a medium. The medium's effect on the particle was broken into two parts, the fluctuating Langevin force $\boldsymbol{F}_{\text{th}}$, and the viscous dissipation $\boldsymbol{\gamma}(\omega)$. The fluctuation-dissipation theorem provides a way to connect the statistics of the thermal force to the drag coefficient $\boldsymbol{\gamma}$. Alternately, everything can be computed once the admittance is known, which again hinges on knowing the drag coefficient $\boldsymbol{\gamma}$.

In this chapter, we will develop the fluid mechanical preliminaries necessary to calculate the drag coefficients. The assumption throughout shall be that the medium is an incompressible Newtonian fluid at low Reynolds numbers in local thermal equilibrium. The unsteady Stokes equations are used to describe this regime of fluid mechanics. We will describe the calculation for the simple case of a sphere, as well as describe various tools to handle problems of unsteady Stokes flow.

The material in sections 3.4, 3.6, 3.7 is largely lifted from the introductory sections of a draft of an article [Simha *et al.*, 2017] that the author of this dissertation has co-authored with Dr. Jianyong Mo and Prof. Philip J. Morrison.[1]

3.1 Steady and Unsteady Stokes Flows

We begin by considering the Navier-Stokes equations

$$\rho_f(\boldsymbol{r},\,t)\left[\frac{\partial}{\partial t}\,\boldsymbol{v}(\boldsymbol{r},\,t)+\boldsymbol{v}(\boldsymbol{r},\,t)\cdot\boldsymbol{\nabla}\boldsymbol{v}(\boldsymbol{r},\,t)\right]=-\boldsymbol{\nabla}P(\boldsymbol{r},\,t)+\eta\Delta\boldsymbol{v}(\boldsymbol{r},\,t)$$
$$+\left(\eta_b+\frac{1}{3}\eta\right)\boldsymbol{\nabla}(\boldsymbol{\nabla}\cdot\boldsymbol{v}(\boldsymbol{r},\,t)), \qquad (3.1)$$
$$\frac{\partial}{\partial t}\,\rho_f(\boldsymbol{r},\,t)+\boldsymbol{\nabla}\cdot[\rho_f(\boldsymbol{r},\,t)\,\boldsymbol{v}(\boldsymbol{r},\,t)]=0,$$

[1] A. Simha, J. Mo, and P. J. Morrison, "Unsteady Stokes flow near boundaries: the point-particle approximation and the method of reflections." Submitted for review to the *Journal of Fluid Mechanics* in July 2017. Much of the text of this work was authored and typeset by A. Simha, with many helpful suggestions from P. J. Morrison and J. Mo.

where $\rho_f(\boldsymbol{r},\, t)$ represents the density of the fluid, $P(\boldsymbol{r},\, t)$ is the pressure, $\boldsymbol{v}(\boldsymbol{r},\, t)$ is the velocity field, η is the dynamic shear viscosity of the fluid, and η_b is the bulk viscosity of the fluid. These equations would need to be supplemented with an equation of state of the specific fluid under consideration in order to relate the pressure and the density. The Navier-Stokes equations have been known to describe a viscous compressible fluid very well.

If we assume that the fluid is incompressible,[2] the Navier-Stokes equations are simplified to

$$\begin{gathered}\rho_f \left[\frac{\partial}{\partial t}\,\boldsymbol{v}(\boldsymbol{r},\, t) + \boldsymbol{v}(\boldsymbol{r},\, t)\cdot\boldsymbol{\nabla}\boldsymbol{v}(\boldsymbol{r},\, t)\right] = -\boldsymbol{\nabla}P(\boldsymbol{r},\, t) + \eta\Delta\boldsymbol{v}(\boldsymbol{r},\, t), \\ \boldsymbol{\nabla}\cdot\boldsymbol{v}(\boldsymbol{r},\, t) = 0.\end{gathered} \tag{3.2}$$

A fluid may be regarded as incompressible when (i) the typical velocity scale of flow u is negligible compared to the speed of sound c in the fluid, i.e. $u \ll c$, and when (ii) the length scale L in the problem and time scale τ are such that the time-scale $\tau_c := L/c$ is much smaller than τ, i.e. $L/c \ll \tau$ [see e.g. Landau & Lifshitz, 1987, §10]. We shall comment further on this at a later stage.

We may non-dimensionalize the equation and estimate the size of various terms, by introducing a length scale L, a velocity scale u, and a time-scale τ. For the problems we wish to consider, it is necessary to allow τ to be different from L/u. For example, the length-scale could model the dimensions of the container of the fluid, or the size of a particle under consideration; the velocity scale could be the typical size of the velocity on the boundaries; the time-scale could correspond to the time of variation of these boundary conditions. There are multiple choices for non-dimensionalization of the pressure, for example $\rho_f u^2$ and $\rho_f uL/\tau$. We proceed with the latter choice. The equations then take the form

$$\begin{gathered}\rho_f \left[\frac{u}{\tau}\frac{\partial\bar{\boldsymbol{v}}}{\partial\bar{t}} + \frac{u^2}{L}\bar{\boldsymbol{v}}\cdot\bar{\boldsymbol{\nabla}}\bar{\boldsymbol{v}}\right] = -\frac{\rho_f u}{\tau}\bar{\boldsymbol{\nabla}}\bar{P} + \eta\frac{u}{L^2}\bar{\Delta}\bar{\boldsymbol{v}}, \\ \bar{\boldsymbol{\nabla}}\cdot\bar{\boldsymbol{v}} = 0,\end{gathered} \tag{3.3}$$

where the bars on top of various quantities represent their appropriately non-dimensionalized versions.

To make further approximations, we wish to compare the ratios of sizes of various terms. Dividing all terms by the size of the viscous term, we may rewrite the first of

[2] and that there are no other reasons (e.g. salinity variations) for the density of the fluid to vary

the above as

$$\frac{\rho_f L^2}{\eta\tau}\frac{\partial \bar{\boldsymbol{v}}}{\partial \bar{t}} + \frac{\rho_f u L}{\eta}\bar{\boldsymbol{v}}\cdot\bar{\boldsymbol{\nabla}}\bar{\boldsymbol{v}} = -\frac{\rho_f L^2}{\eta\tau}\bar{\boldsymbol{\nabla}}\bar{P} + \bar{\Delta}\bar{\boldsymbol{v}}, \tag{3.4}$$

where we may identify the Reynolds number $\mathrm{Re} := \rho_f L u/\eta$ as the ratio of the advective term to the viscous term. We shall later show that the time-scale $\tau_f := \rho_f L^2/\eta$ plays an important role, and we shall refer to this in this work as the *vorticity-diffusion timescale*. We hence see that the non-dimensional equation depends on the Reynolds number and the ratio of time-scales τ/τ_f as

$$\frac{\tau_f}{\tau}\frac{\partial \bar{\boldsymbol{v}}}{\partial \bar{t}} + \mathrm{Re}\;\bar{\boldsymbol{v}}\cdot\bar{\boldsymbol{\nabla}}\bar{\boldsymbol{v}} = -\frac{\tau_f}{\tau}\bar{\boldsymbol{\nabla}}\bar{P} + \bar{\Delta}\bar{\boldsymbol{v}}. \tag{3.5}$$

As is well known, a tremendous simplification results when the Reynolds number is small – we may drop the non-linear advective term[3] and the system reduces to the *unsteady Stokes equations*, which may also be called the transient Stokes equations or the linearized incompressible Navier-Stokes equations. Evidently, in the dimensionful form, these equations are

$$\begin{aligned} \rho_f\frac{\partial}{\partial t}\boldsymbol{v}(\boldsymbol{r},\,t) &= -\boldsymbol{\nabla}P(\boldsymbol{r},\,t) + \eta\Delta\boldsymbol{v}(\boldsymbol{r},\,t), \\ \boldsymbol{\nabla}\cdot\boldsymbol{v}(\boldsymbol{r},\,t) &= 0. \end{aligned} \tag{3.6}$$

These equations shall form the central theme of this work.

A further approximation may be made if τ/τ_f is large, so that the time-scale τ_f over which the fluid relaxes is much shorter than the time-scale τ over which boundary conditions change. Despite τ/τ_f being small, the pressure term cannot be neglected as it enforces the $\boldsymbol{\nabla}\cdot\boldsymbol{v} = 0$ constraint. This leads to the equations,

$$\begin{aligned} -\boldsymbol{\nabla}P(\boldsymbol{r},\,t) + \eta\Delta\boldsymbol{v}(\boldsymbol{r},\,t) &= 0, \\ \boldsymbol{\nabla}\cdot\boldsymbol{v}(\boldsymbol{r},\,t) &= 0, \end{aligned} \tag{3.7}$$

which are the celebrated Stokes equations.

For over 150 years, Stokes flow has been used very effectively to explain the motion of particles in low Reynolds number situations, because in these situations, the fluid may be imagined to be very syrupy whence the particle motion is generally not very fast. However, with recent technological progress, such fast motion can become relevant in the context of micro- and nano- scale particles in typical liquids. As a

[3]Although, however, in some situations, it must be retained to the Oseen approximation.

result, the regime of unsteady Stokes flow has become important. Some examples of this were mentioned in the Introduction (Chapter 1).

Whereas both the steady and the unsteady Stokes equations are linear, rendering them significantly easier to solve than the full Navier-Stokes equations, unsteady Stokes problems are in general harder to solve in situations with reduced symmetry. Loosely speaking, while the steady Stokes equations may be reduced to the Laplace equation, where Fourier analysis (in time) works, the unsteady Stokes equations transform into the Helmholtz equation. There are many coordinate systems where the Laplace equation may be separated, but the Helmholtz equation cannot be. Similarly, in 2-dimensional problems, the Laplace equation[4] may yield to techniques of complex analysis and conformal mapping whereas the Helmholtz equation generally does not. A few analytically tractable cases include a sphere moving in an infinite fluid, an infinitely long cylinder moving in an infinite fluid, and the oscillations of an infinite plane wall.

3.2 The anatomy of unsteady Stokes flow

Taking the divergence of the first of (3.6) and using the second equation gives us an equation for the pressure,

$$\Delta P(\boldsymbol{r}, \omega) = 0, \tag{3.8}$$

and taking the curl of the first equation gives us an equation for the vorticity $\boldsymbol{\Omega} := \boldsymbol{\nabla} \times \boldsymbol{v}$,

$$\frac{\partial \boldsymbol{\Omega}}{\partial t} = \frac{\eta}{\rho_f} \boldsymbol{\Omega}. \tag{3.9}$$

The latter equation is simply the diffusion equation for the vorticity, with diffusion coefficient $\nu := \eta/\rho_f$. This quantity ν is often called the kinematic viscosity, and is useful in the analysis of incompressible fluids. This provides the interpretation of $\tau_f = L^2/\nu$ as the time-scale over which vorticity diffuses over a region of size L.

The unsteady Stokes equations may be simplified by Fourier transformation[5] in

[4] In 2-D problems, the steady Stokes equations may be specifically reduced to the biharmonic equation by the use of a stream-function. A similar situation occurs in axi-symmetric situations which admit a Stokes stream-function.

[5] Our convention was specified in equation (2.5).

time,

$$\begin{aligned} -\mathrm{i}\omega\rho_f\ \check{\boldsymbol{v}}(\boldsymbol{r},\,\omega) &= -\boldsymbol{\nabla}\check{P}(\boldsymbol{r},\,\omega) + \eta\Delta\check{\boldsymbol{v}}(\boldsymbol{r},\,\omega), \\ \boldsymbol{\nabla}\cdot\check{\boldsymbol{v}}(\boldsymbol{r},\,\omega) &= 0, \end{aligned} \tag{3.10}$$

so that the equations for pressure and vorticity become

$$\begin{aligned} \Delta\check{P}(\boldsymbol{r},\,\omega) &= 0, \\ \alpha^2\check{\boldsymbol{\Omega}} - \Delta\check{\boldsymbol{\Omega}} &= 0, \end{aligned} \tag{3.11}$$

where we have defined $\alpha := \sqrt{-\mathrm{i}\omega\rho_f/\eta}$. Since this quantity is important for the most part of this work, we shall establish a consistent convention for the branch of the complex square-root by choosing $\Re[\alpha] > 0$. The former is a Laplace equation, and the latter is a Helmholtz equation with complex wavenumber.

If we consider a Helmholtz decomposition of the velocity field and think of the pressure as related to a scalar potential and the vorticity as related to a vector potential[6], the above two equations are reminiscent of Coulomb-gauge electrodynamics. There is one important difference, which is that the vector equation is really a diffusion equation, whereby the wavenumber is complex with real and imaginary parts of equal magnitude.

Thus, we may form the following interpretation – if we have a disturbance produced in the fluid at some point, there are two kinds of phenomena that propagate: the longitudinal pressure wave, and the transverse "vorticity wave"[7]. In our approximation, the pressure satisfies a Laplace equation, whereby the disturbances propagate instantaneously. Of course, this is unphysical, and the issue is resolved by accounting for the compressibility of the fluid – the waves are then simply longitudinal sound waves. As we mentioned earlier, this suggests that the fluid may be considered incompressible as long as the time-scale of interest τ is sufficiently long compared to the time taken by sound to travel the length scales in the problem, i.e. when $\tau \gg \tau_c := L/c$ where c denotes the speed of sound in the fluid. As may be intuited, the linearized compressible Navier-Stokes may be separated into two wave equations in a similar manner – one for the sound and one for the vorticity – both of which in general have

[6] As is evident, this correspondence is not exact – the pressure and vorticity are related to the scalar and vector potentials for the velocity field through integral / differential operators. But these operators are scalar operators and the solenoidal and irrotational parts are not coupled, whereby there is a rough analogy between the two pairs of objects.

[7] To the best of the author's knowledge, there is no standard term for this wave in the literature. "Shear wave" might be an alternative term.

complex wavenumber (the former due to the damping of sound by bulk viscosity). We shall focus on incompressible fluids in this work; a detailed analysis of compressible Brownian motion may be found in the work of Chow & Hermans [1973].

We now return to our previous note on the complex nature of $\alpha = |\alpha|(1-\mathrm{i})/\sqrt{2}$. As is typical for the Helmholtz equation, this implies that (in one dimension) the vorticity has solutions that behave as $\mathrm{e}^{\alpha x}$ and $\mathrm{e}^{-\alpha x}$. The former solution grows at infinity, so if we were seeking a fundamental solution, one may imagine a behavior of the form $\mathrm{e}^{-\alpha|x|}$ in one dimension and $\mathrm{e}^{-\alpha r}/r$ in three dimensions. Thus, the equality of magnitudes of real and imaginary parts of α implies that the vorticity has a skin depth that equals the wavelength [see e.g. Landau & Lifshitz, 1987, §24]. So one can hardly call them waves given how rapidly they decay. In this work, we sometimes refer to α as the complex skin-depth, or as a complex-wavenumber, since neither phenomenon is stronger than the other.

3.3 Solving the unsteady Stokes equations

In this section, we outline the typical procedure for solving the unsteady Stokes equations.

The boundary conditions for the unsteady Stokes equations are typically specified in terms of the velocity and its derivatives. For example, the no-slip boundary condition entails that the fluid velocity match the interface velocity, so there is no penetration or slippage of the fluid on the interface. The full-slip or free-slip boundary condition demands that the component of fluid velocity normal to the interface match the interface's velocity, but the shear stress transferred tangential to the boundary vanish, i.e. the normal derivatives of the tangential components of fluid velocity vanish. There is also the more general partial slip boundary condition which is specified as a mixture of the above cases, but we shall not concern ourselves with this case in this work.

The pressure is therefore unspecified and may be thought of as a degree of freedom that allows us to impose $\boldsymbol{\nabla}\boldsymbol{\cdot}\boldsymbol{v} = 0$. The typical procedure to solve the unsteady Stokes equations involves first the determination of the pressure by solving the Laplace equation (3.8), leaving the coefficients undetermined, as we are not given boundary conditions for the pressure. The result then is plugged into the first of (3.10), which

may be re-written as

$$\left[\alpha^2 - \Delta\right] \check{\boldsymbol{v}} = -\frac{1}{\eta} \boldsymbol{\nabla} \check{P}. \tag{3.12}$$

The known pressure (up to undetermined coefficients) is treated as a source for the Helmholtz equation (with complex wavenumber α). Solving the Helmholtz equation results in additional undetermined coefficients in the complementary function. The undetermined coefficients are then determined by applying boundary conditions. In an unbounded fluid medium, the velocity is typically either assumed to become zero, or attain a constant value at infinity, depending on whether there is a quiescent background flow or not.[8]

If there are body forces applied to the fluid, the divergence of the body force fields appears as a source in the equation for the pressure (so that we have a Poisson equation), and the body forces also appear as an additional source in the equation for the velocity.

3.4 Calculating unsteady drag coefficients

The drag coefficients calculated using steady Stokes flows, including for example the Stokes law $\boldsymbol{F}_s = -6\pi\eta a \boldsymbol{u}$ for a spherical particle of radius a, assume that the velocity $\boldsymbol{u}$ of the particle remains constant in time, i.e. the particle is not accelerating. If the particle has a changing velocity, but the timescale of change in velocity τ is much larger than the timescale of vorticity diffusion τ_f (as defined in Section 3.1), steady Stokes flow still provides a good approximation. However, if one wishes to study the motion of a particle on time-scales comparable to, or shorter than τ_f, unsteady Stokes flow must be used to calculate the drag force.

Throughout this work, we will use the term "drag" to colloquially refer to the net force exerted by the fluid on the particle. This includes both reactive (e.g. added mass) and resistive (e.g. viscous dissipation) effects.

Consider a small rigid body S (the "particle") of arbitrary shape immersed in a fluid bounded (partially or completely) by surface(s) W. In the regime of usefulness of unsteady Stokes flow in determining particle dynamics, the particle has a changing velocity $\boldsymbol{u}(t)$. To avoid having the problem of a moving boundary on which we need to impose boundary conditions, we assume that the excursions of the particle from

[8] Of course, these are not the only two cases.

a central location $\boldsymbol{r}_0$ are much smaller than the size of the particle itself, and that the Fourier components of the displacement decay as quick as or faster than $1/\omega$. A detailed argument may be found in Landau & Lifshitz [1987, §24]. See also Zwanzig & Bixon [1970]; Mazur & Bedeaux [1974] and appendix A. Then, we may pretend that the boundary of the particle itself does not change position, but the velocity boundary condition on that boundary changes. Physically, this is indeed the case in the applications we consider here such as optical tweezers, since the particle is confined by the trap. This assumption simplifies the problem tremendously as it results in a purely linear problem.

Given that the problem is linear, we may Fourier decompose the velocity $\boldsymbol{u}(t)$ into Fourier components $\boldsymbol{u}_\omega$, and consider the problem of finding the drag on the body S performing small translational oscillations in an arbitrary direction at arbitrary[9] frequency ω in an incompressible fluid of dynamic shear viscosity η and density ρ_f.

To find the drag force, we must solve the unsteady incompressible Stokes equations (3.10), subject to some combination of no-slip or full-slip boundary conditions[10] on ∂S and W. For simplicity, we shall use abbreviated notation, $\boldsymbol{v}_\omega$ for $\check{\boldsymbol{v}}(\boldsymbol{r},\omega)$ etc. Once the solutions for $\boldsymbol{v}_\omega$ and P_ω have been computed, one may compute the drag force on the body as

$$\boldsymbol{F}_\omega^{\text{drag}} = \oint_{\partial S} \mathrm{d}^2 x \;\; \boldsymbol{\sigma} \cdot \hat{\boldsymbol{n}}, \tag{3.13}$$

where $\boldsymbol{\sigma}$ is the stress tensor having components $\sigma_{ij}(\boldsymbol{r};\omega) = P_\omega \delta_{ij} + \eta(\partial_i v_{\omega j} + \partial_j v_{\omega i})$ and $\hat{\boldsymbol{n}}$ is the outward unit normal to the surface ∂S. Since the system is linear in the low Reynolds number regime, the drag force $\boldsymbol{F}_\omega^{\text{drag}}$ is a linear response to the velocity $\boldsymbol{u}_\omega$ of the body, whereby it should be possible to write

$$\boldsymbol{F}_\omega^{\text{drag}} = -\boldsymbol{\gamma}(\boldsymbol{r}_0;\omega) \cdot \boldsymbol{u}_\omega, \tag{3.14}$$

where $\boldsymbol{\gamma}(\boldsymbol{r}_0;\omega)$ is a tensor of drag coefficients. Here, we have explicitly indicated that the drag coefficients may depend on the mean position $\boldsymbol{r}_0$ of the body, although we will drop this in the future to simplify notation.

We remark that the setup of this problem to compute the drag coefficient made no reference to the density of the body itself, and the effects of the body on the fluid were captured through the boundary conditions at ∂S.

[9] It is assumed however that the frequency is not high enough that the compressibility of the fluid becomes important

[10] We shall restrict ourselves to these special cases in this work.

In general, analytically solving these equations in situations where the configuration of S and W does not possess sufficient symmetry poses difficulties as noted before, as separable eigenfunction expansions may not exist. Even for the simple case of a sphere for S and a single plane wall W, the Helmholtz equation (with complex wavenumber) in (3.10) is not separable in a coordinate system that is suitable for the symmetry of the boundaries. Thus, it is natural to consider approximation techniques. The point-particle approximation [Felderhof, 2005], matched asymptotic expansions [O'Neill & Stewartson, 1967], and the method of reflections [see e.g. Happel & Brenner, 1965][11] are some approximation techniques to resort to.

3.5 Singularity solutions of the unsteady Stokes equations

In electrostatics, the fundamental singularity solution of the Laplace operator, i.e. the solution to

$$\Delta\Phi(\boldsymbol{r}) = \delta(\boldsymbol{r}), \tag{3.15}$$

given by

$$\Phi(\boldsymbol{r}) = -\frac{1}{4\pi|\boldsymbol{r}|}, \tag{3.16}$$

plays an important role in solving more general problems, for one may therefore write the solution to the Poisson equation

$$\Delta\phi(\boldsymbol{r}) = \rho(\boldsymbol{r}), \tag{3.17}$$

as a convolution of the source with the singularity solution

$$\phi(\boldsymbol{r}) = \int \mathrm{d}^3 r' \, \frac{-1}{4\pi|\boldsymbol{r}-\boldsymbol{r}'|}\rho(\boldsymbol{r}'). \tag{3.18}$$

This is of course well-known.

In the above, Φ represents the solution to a point-charge or monopole singularity. One may also consider solutions to higher-order singularities such as the dipole $\boldsymbol{\nabla}\delta(\boldsymbol{r})$, the quadrupole $\boldsymbol{\nabla}\boldsymbol{\nabla}\delta(\boldsymbol{r})$ etc. These solutions are simply given by $\boldsymbol{\nabla}\Phi$, $\boldsymbol{\nabla}\boldsymbol{\nabla}\Phi$ etc. These singularity solutions allow the use of the multipole expansion – we may formally

[11] Happel & Brenner [1965] only describe the case of steady Stokes flows.

expand the kernel $\Phi(\boldsymbol{r}-\boldsymbol{r}')$ in (3.18) in a Taylor-like series about an origin $\boldsymbol{r}_0$ and write

$$\Phi(\boldsymbol{r}-\boldsymbol{r}') = \Phi(\boldsymbol{r}-\boldsymbol{r}_0) + (\boldsymbol{r}'-\boldsymbol{r}_0)\cdot\boldsymbol{\nabla}\Phi(\boldsymbol{r}-\boldsymbol{r}_0) + \ldots, \tag{3.19}$$

and therefore obtain

$$\phi(\boldsymbol{r}) = \Phi(\boldsymbol{r}-\boldsymbol{r}_0)\int \mathrm{d}^3r'\ \rho(\boldsymbol{r}') + \boldsymbol{\nabla}\Phi(\boldsymbol{r}-\boldsymbol{r}_0)\cdot\int \mathrm{d}^3r'\ \rho(\boldsymbol{r}')\,(\boldsymbol{r}'-\boldsymbol{r}_0) + \ldots, \tag{3.20}$$

which is the multipole expansion, the term $\int \mathrm{d}^3r'\ \rho(\boldsymbol{r}')\,(\boldsymbol{r}'-\boldsymbol{r}_0)$ being the dipole moment, etc.

The unsteady Stokes equations are linear and elliptic,[12] so singularity solutions provide similarly powerful techniques to construct solutions. Singularity solutions of, and their applications to the solution of unsteady Stokes equations are well-known and discussed, for example, in textbooks by Pozrikidis [1992]; Guazzelli & Morris [2011]; Kim & Karrila [2013]. In this section, we shall provide a brief introduction to make this work self-contained and establish some conventions. For simplicity, we shall work in frequency domain.

The first difference between the Poisson equation of electrostatics, and the unsteady Stokes equations, is that the latter are vector equations. Therefore, the simplest singularity is a vector-valued one, representing a unit point force (oscillating at frequency ω) applied to the fluid. The resulting fundamental singularity solution for the velocity field forms a rank-2 tensor $\boldsymbol{G}^0(\boldsymbol{r};\,\omega)$ with components G^0_{ij}, and the corresponding solution for the pressure forms a vector $\boldsymbol{P}^0(\boldsymbol{r};\,\omega)$ with components P^0_j. $\boldsymbol{G}^0$ and $\boldsymbol{P}^0$ are solutions to

$$\Delta G^0_{ij}(\boldsymbol{r}-\boldsymbol{r}';\omega) - \alpha^2 G^0_{ij}(\boldsymbol{r}-\boldsymbol{r}';\omega) - \frac{1}{\eta}\partial_i P^0_j(\boldsymbol{r}-\boldsymbol{r}';\omega) = \delta_{ij}\delta(\boldsymbol{r}-\boldsymbol{r}'), \tag{3.21}$$

$$\partial_i G^0_{ij}(\boldsymbol{r}-\boldsymbol{r}';\omega) = 0, \tag{3.22}$$

with the condition that both $\boldsymbol{G}^0$ and $\boldsymbol{P}^0$ decay to zero[13] at infinity. The tensor $\boldsymbol{G}^0$ is often called the *unsteady Oseen tensor*. The corresponding term this generates in a multipole expansion is referred to as the *unsteady Stokeslet*.[14]

[12] Or so we have made them appear by allowing for complex wavenumbers.

[13] Of course, the pressure could in general decay to a constant, but we will choose this constant to be zero.

[14] We have assumed here that the singularity is used to model the flow external to a boundary inside which it resides. For internal flows, there is an alternate set of singularity solutions, beginning with the *Stokeson* [see e.g. Kim & Karrila, 2013]. We shall not concern ourselves with internal flows in this work.

The above equations may be solved in the same manner outlined in Section 3.3. The result for $\boldsymbol{G}^0$ is given by [Mazur & Bedeaux, 1974; Felderhof, 2012; Kim & Karrila, 2013]

$$\boldsymbol{G}^0(\boldsymbol{q};\omega) = -\frac{1}{\eta}\Big(G(\boldsymbol{q};\omega)\mathbb{1} + \alpha^{-2}\boldsymbol{\nabla}\boldsymbol{\nabla}\left[G(\boldsymbol{q};0) - G(\boldsymbol{q};\omega)\right]\Big), \tag{3.23}$$

where $G(\boldsymbol{q};\omega) = -\dfrac{\mathrm{e}^{-\alpha|\boldsymbol{q}|}}{4\pi|\boldsymbol{q}|}$ is the fundamental solution of the Helmholtz equation (with complex α), and $G(\boldsymbol{q};0)$ is that of the Laplace equation.

The second difference from electrostatics is that anti-symmetric moments appear in the multipole expansion. The next singularity that may be considered would have the nature $\delta_{ij}\partial_k\delta(\boldsymbol{r}-\boldsymbol{r}')$, whereby the corresponding solutions are $\partial_k G^0_{ij}$ and $\partial_k P^0_j$. We may split the rank-3 tensor $\partial_k G^0_{ij}$ into symmetric and anti-symmetric parts (G_{ij} is already symmetric) along indices k and j. The trace part, $\partial_k G^0_{kj}$, is zero by virtue of the incompressibility condition $\boldsymbol{\nabla}\cdot\boldsymbol{v} = 0$. Of the remaining, the anti-symmetric component may be written as $\boldsymbol{\nabla}\times\boldsymbol{G}^0$, which corresponds to the solution due to a point torque. The corresponding term in the multipole expansion is called the *unsteady rotlet* or *unsteady couplet*. The symmetric component corresponds to the solution due to a infinitesimally separated pair of forces that produces a point stress. The corresponding term is called the *unsteady stresslet*. Thus, a similar multipole expansion may be written in terms of these singularity solutions.

3.6 Unsteady Stokes flow around an Oscillating Sphere

We briefly review here the well-known problem of a sphere oscillating in an unbounded fluid. The problem was first solved by Stokes [1851]. However, we shall follow the presentation of Landau & Lifshitz [1987, §24, Prob. 5] as it is more convenient for our purposes[15]. A more expansive discussion of this problem may be found in the appendix A.

Using the ansatz $\boldsymbol{v}_\omega(\boldsymbol{r}) = \boldsymbol{\nabla}\times\boldsymbol{\nabla}\times(f(r)\boldsymbol{u}_\omega)$ for the velocity field $\boldsymbol{v}_\omega(\boldsymbol{r})$ generated by the sphere oscillating with velocity $\boldsymbol{u}_\omega$, the unsteady incompressible Stokes

[15]However, we shall use notation that is consistent with the rest of this work. This involves the changes $R\to a$, $a\to A$, $b\to B$, $-\mathrm{i}kR\to\delta$ from the notation used in Landau-Lifshitz to our notation.

equations (3.10) reduce to

$$\Delta^2 f = \alpha^2 \Delta f, \tag{3.24}$$

whose solution subject to the no-slip boundary conditions $\boldsymbol{v}_\omega|_{\partial S} = \boldsymbol{u}_\omega$ on the surface of the sphere and decay condition at infinity is $f(r)$ such that,

$$\frac{f'(r)}{r} = \frac{1}{r^3}\left[A\mathrm{e}^{-\alpha r}\left(r + \frac{1}{\alpha}\right) + B\right], \tag{3.25}$$

with the constants,

$$\begin{aligned} A &= \frac{3a^2}{2\delta}\mathrm{e}^{\delta}, \\ B &= -\frac{3a^3}{2\delta^2}\left(1 + \delta + \frac{\delta^2}{3}\right), \end{aligned} \tag{3.26}$$

where $\delta := \alpha a = \sqrt{-\mathrm{i}\omega\tau_f}$, $\Re[\delta] > 0$. Here, the origin of the spherical coordinate system (r, θ, φ) is at the center of the sphere, and the polar axis is along $\boldsymbol{u}_\omega$. It must be noted that the combination $f'(r)/r$ is dimensionless.

From the above, the components of the velocity in the same coordinate system may be calculated as,

$$\begin{aligned} \hat{\boldsymbol{e}}_r \cdot \boldsymbol{v}_\omega &= -2u_\omega \frac{f'(r)}{r}\cos\theta, \\ \hat{\boldsymbol{e}}_\theta \cdot \boldsymbol{v}_\omega &= u_\omega \sin\theta \left[-\frac{A\alpha}{r}\mathrm{e}^{-\alpha r} - \frac{f'(r)}{r}\right]. \end{aligned} \tag{3.27}$$

It must be noted that the problem possesses axial symmetry, by which $\hat{\boldsymbol{e}}_\varphi \cdot \boldsymbol{v}_\omega = 0$ and there is no φ dependence for most quantities.

The drag force on the sphere may be calculated using (3.13). The resulting drag force on the sphere, as mentioned earlier, is given by $\boldsymbol{F}_\omega^{\mathrm{drag}} = -\gamma_0(\omega)\boldsymbol{u}_\omega$ where

$$\gamma_0(\omega) = \gamma_s(1 + \delta + \delta^2/9), \tag{3.28}$$

and $\gamma_s := 6\pi\eta a$ is the well-known steady Stokes drag coefficient (for a sphere translating with constant velocity).

3.7 Faxén's Law, and its generalizations

In the drag calculation of Section 3.6, we assumed that the fluid was otherwise quiescent, and the only flow in the fluid was produced by the sphere. However, a more

general problem would be to find the drag on a spherical particle in the presence of a background flow caused by some other agent in the fluid.

The formula for the drag on a stationary rigid sphere suspended in a pre-existing steady background flow $\boldsymbol{v}_0(\boldsymbol{r})$ was first derived by Faxén [1921]. The drag force is given by a very simple formula – for no-slip boundary conditions on the sphere, $\boldsymbol{F}^{\text{drag}} = \gamma_s \bar{\boldsymbol{v}}_0^S$, where $\bar{\boldsymbol{v}}_0^S$ is the average of the background flow field over the surface of the sphere. This result is often referred to as *Faxén's law*, or as *Faxén's theorem*.

Faxén's theorem has been generalized to obtain the drag force on a sphere with a no-slip boundary in incompressible [Mazur & Bedeaux, 1974] and compressible [Bedeaux & Mazur, 1974] unsteady Stokes flow. Albano *et al.* [1975] have generalized the incompressible version to the case of partial slip boundary conditions on the sphere, and generalization to the force density induced on the sphere has been effected by Felderhof [1976]. As it is the most relevant to this work, we shall review the incompressible case for translational oscillations of a no-slip sphere derived by Mazur & Bedeaux [1974].

Consider an arbitrary background fluid flow described by $\{\boldsymbol{v}_0(\boldsymbol{r};\omega),\ P_0(\boldsymbol{r};\omega)\}$ extant in $\mathbb{R}^3$, which solves the unsteady incompressible Stokes equations with a body force distribution $\boldsymbol{S}_0(\boldsymbol{r};\omega)$ consistent with the background flow, i.e.

$$\begin{aligned} \Delta \boldsymbol{v}_0 - \alpha^2 \boldsymbol{v}_0 &= \frac{\boldsymbol{\nabla} P_0 - \boldsymbol{S}_0}{\eta}, \\ \boldsymbol{\nabla} \cdot \boldsymbol{v}_0 &= 0. \end{aligned} \tag{3.29}$$

Suppose that we now place a no-slip sphere of radius a, which executes small translational oscillations with velocity $\boldsymbol{u}_\omega$ in the fluid under the influence of some external force. The fluid flow is altered by the boundary conditions imposed by the sphere. Since the system is linear, we could think of this as being due to an additional flow $\{\boldsymbol{v}'(\boldsymbol{r};\omega),\ P'(\boldsymbol{r};\omega)\}$. Once again due to linearity, we expect that this flow depends linearly on both the boundary condition $\boldsymbol{u}_\omega$ and the background flow $\boldsymbol{v}_0$, P_0.

This relationship is expressed readily if we convert the boundary condition into a source, as is often done in electrodynamics and fluid mechanics. Introducing an induced force[16] density $\boldsymbol{S}_{\text{ind}}(\boldsymbol{r};\omega)$ that has support only in the region occupied by the

[16]The notion of induced forces, as described by Mazur & Bedeaux [1974], is analogous to the notion of bound charges in electrostatics.

sphere (which we shall assume in this section to be $|\boldsymbol{r}| \leq a$), we obtain the equations

$$\begin{aligned} \Delta \boldsymbol{v}' - \alpha^2 \boldsymbol{v}' &= \frac{\boldsymbol{\nabla} P' - \boldsymbol{S}_{\rm ind}}{\eta}, \\ \boldsymbol{\nabla} \cdot \boldsymbol{v}' &= 0. \end{aligned} \tag{3.30}$$

In the above, we assume that there is no longer a boundary, but fluid filling the region $|\boldsymbol{r}| \leq a$. A key requirement is that $\boldsymbol{S}_{\rm ind}$ be chosen so the momentum flux through the boundary in this problem matches that through the sphere oscillating with velocity $\boldsymbol{u}_\omega$. We shall additionally require that the total flow $\boldsymbol{v} = \boldsymbol{v}_0 + \boldsymbol{v}'$ be equal to $\boldsymbol{u}_\omega$ in the entire $|\boldsymbol{r}| \leq a$ region.

We may write the formal solution of (3.30) as[17]

$$\boldsymbol{v}(\boldsymbol{r};\omega) = \boldsymbol{v}_0(\boldsymbol{r};\omega) + \int_{|\boldsymbol{r}'|\leq a} \mathrm{d}^3 r' \; \boldsymbol{G}^0(\boldsymbol{r}-\boldsymbol{r}';\omega) \cdot \boldsymbol{S}_{\rm ind}(\boldsymbol{r}';\omega) \tag{3.31}$$

To find $\boldsymbol{S}_{\rm ind}$, it appears that one would need to solve the above integral equation, where the left hand side is known to be $\boldsymbol{u}_\omega$ inside the spherical region. However, it turns out its explicit value is not required for our purposes – to compute the drag force $\boldsymbol{F}_\omega^{\rm drag}$ on the sphere, it suffices to compute the integrated value of $\boldsymbol{S}_{\rm ind}$ over the volume of the sphere, for

$$\begin{aligned} \boldsymbol{F}_\omega^{\rm drag} &= \oint_{|\boldsymbol{r}|=a} \mathrm{d}^2 r \; \boldsymbol{\sigma} \cdot \hat{\boldsymbol{n}} = \int_{|\boldsymbol{r}|\leq a} \mathrm{d}^3 r \; \boldsymbol{\nabla} \cdot \boldsymbol{\sigma} \\ &= -\left[\mathrm{i}\omega m_f \boldsymbol{u}_\omega + \int_{|\boldsymbol{r}|\leq a} \mathrm{d}^3 r \; \boldsymbol{S}_{\rm ind}(\boldsymbol{r};\omega) \right] \end{aligned} \tag{3.32}$$

as required for the induced force to mimic the presence of the sphere, with $m_f = \frac{4}{3}\pi a^3 \rho_f$ being the mass of fluid displaced by the sphere. The last step was effected by writing

$$\boldsymbol{\nabla} \cdot \boldsymbol{\sigma} = -\boldsymbol{\nabla} P + \eta \Delta \boldsymbol{v} = \eta \alpha^2 \boldsymbol{v} - \boldsymbol{S}_{\rm ind} - \boldsymbol{S}_0, \tag{3.33}$$

and noting that $\boldsymbol{S}_0$ may be set without loss of generality to 0 in the region $r \leq a$ (by lumping whatever value it had into $\boldsymbol{S}_{\rm ind}$), as well as that $\boldsymbol{v}$ has the constant value $\boldsymbol{u}_\omega$ in the region $r \leq a$ whereby the integral of $\boldsymbol{v}$ over that region is simply $\boldsymbol{u}_\omega$ times the volume of the sphere.

[17] Equation (3.31) can be seen to be identical to equation (3.15) of Mazur & Bedeaux [1974] upon employing (3.23).

By various manipulations, it can be shown that averages of the equation (3.31) suffice to determine $\int_{|\boldsymbol{r}|\leq a} \mathrm{d}^3 r\ \boldsymbol{S}_{\mathrm{ind}}$, whereby setting $\boldsymbol{v}(\boldsymbol{r};\omega) = \boldsymbol{u}_\omega$ for $|\boldsymbol{r}| \leq a$ and averaging (3.31) over the surface and the volume of the sphere, the desired result for the drag force is obtained to be

$$\boldsymbol{F}_\omega^{\mathrm{drag}} = -\gamma_0(\omega)\boldsymbol{u}_\omega + \gamma_s \left[(1+\alpha a)\bar{\boldsymbol{v}}_0^S(\omega) + \frac{1}{3}\alpha^2 a^2 \bar{\boldsymbol{v}}_0^V(\omega)\right], \tag{3.34}$$

where

$$\gamma_0(\omega) := \gamma_s \left(1 + \alpha a + \frac{1}{9}\alpha^2 a^2\right) \tag{3.35}$$

is the unsteady Stokes-Boussinesq drag coefficient for a sphere, and $\bar{\boldsymbol{v}}_0^S$ and $\bar{\boldsymbol{v}}_0^V$ denote the averages of $\boldsymbol{v}_0$ over the surface and volume of the sphere respectively. The above result is the generalization of Faxén's theorem by Mazur & Bedeaux [1974].

3.8 Boundary integral equations for the unsteady Stokes equations

3.8.1 The reciprocal identity and boundary integral equations for electrostatics

In the spirit of starting with something familiar, we shall begin with the reciprocal identity in electrostatics and its usefulness in obtaining an integral representation for the electrostatic potential. The reciprocal identity in electrostatics, also known as *Green's second identity*,

$$\int_D (\phi\Delta\psi - \psi\Delta\phi)\ \mathrm{d}^3x' = \oint_{\partial D} \left[\phi\frac{\partial\psi}{\partial n'} - \psi\frac{\partial\phi}{\partial n'}\right]\ \mathrm{d}^2x', \tag{3.36}$$

may be derived by considering

$$\boldsymbol{\nabla}\cdot(\phi\boldsymbol{\nabla}\psi) = \phi\Delta\psi + \boldsymbol{\nabla}\phi\cdot\boldsymbol{\nabla}\psi,$$

integrating both sides, using the divergence theorem to convert the volume integral on the left hand side into a surface integral, and then subtracting the similar identity obtained by interchanging ϕ and ψ. The details may be found for example in Jackson [1999, §1.8].

In order to obtain an integral equation for the electrostatic potential ϕ that satisfies the Poisson equation,

$$-\Delta\phi(\boldsymbol{x}) = \rho(\boldsymbol{x}), \tag{3.37}$$

we choose $\psi(\boldsymbol{x}'|\boldsymbol{x})$ to be the fundamental solution of the differential operator under consideration, which is the Laplacian Δ. Then, we have $\psi(\boldsymbol{x}'|\boldsymbol{x}) = \dfrac{-1}{4\pi|\boldsymbol{x}-\boldsymbol{x}'|}$ and $\Delta\psi = \delta(\boldsymbol{x}-\boldsymbol{x}')$, where $\boldsymbol{x} \in D$ is interpreted as the source point and $\boldsymbol{x}'$ is interpreted as the field point. Upon integration over $\boldsymbol{x}'$, the $\phi\Delta\psi$ term simplifies to $\phi(\boldsymbol{x})$. Let D be a sufficiently nice domain.[18] Then we have, for any point $\boldsymbol{x} \in D$,

$$\begin{aligned}\phi(\boldsymbol{x}) = &\int_D \mathrm{d}^3x' \, \frac{\rho(\boldsymbol{x}')}{4\pi|\boldsymbol{x}-\boldsymbol{x}'|} \\ &+ \frac{1}{4\pi}\oint_{\partial D} \mathrm{d}^2x' \, \left[\frac{1}{|\boldsymbol{x}-\boldsymbol{x}'|}\frac{\partial\phi}{\partial n'} - \phi(\boldsymbol{x}')\frac{\partial}{\partial n'}\,\frac{1}{|\boldsymbol{x}-\boldsymbol{x}'|}\right].\end{aligned} \tag{3.38}$$

The two surface terms in the right hand side of the above equation may be interpreted as arising from a surface charge layer (with charge density $\sigma = \frac{\partial\phi}{\partial n'}$, the *single-layer potential*) and a surface dipole layer (with dipole moment density $D = -\phi$, the *double-layer potential*). The volume term corresponds to a volume charge density. This equation is not a solution to the boundary value problem, since arbitrary specification of both ϕ and $\frac{\partial\phi}{\partial n}$ on the boundary is an over-specification of the problem.

To solve the Dirichlet boundary value problem, we instead set $\psi(\boldsymbol{x}') = G_D(\boldsymbol{x}'|\boldsymbol{x})$, a Green's function that satisfies the homogeneous Dirichlet boundary conditions on ∂D . Then, $\Delta\psi(\boldsymbol{x}') = \delta(\boldsymbol{x}-\boldsymbol{x}')$, and $G_D(\boldsymbol{x}|\boldsymbol{x}') = 0 \; \forall \boldsymbol{x}' \in \partial D$.

This results in the undesired surface term vanishing, and we have for $\boldsymbol{x} \in D$

$$\phi(\boldsymbol{x}) = \int_D \mathrm{d}^3x' \, G_D(\boldsymbol{x}|\boldsymbol{x}')\rho(\boldsymbol{x}') - \oint_{\partial D} \mathrm{d}^2x' \, \frac{\partial G_D}{\partial n'}(\boldsymbol{x}|\boldsymbol{x}')\phi(\boldsymbol{x}'). \tag{3.39}$$

Neumann boundary conditions may be treated similarly, but is more involved. See Jackson [1999, §1.10] for more details.

Another method to solve a boundary value problem is to develop (3.38) for points $\boldsymbol{x} \in \partial D$, wherein the double-layer integral is singular and must be treated with care. This can then be interpreted as an integral equation for the unknown (in the case of the Dirichlet problem, it would be the value of $\partial\phi/\partial n'$ on ∂D). Once the solution to the integral equation is found, both surface terms are known.

[18] By D, we shall mean the open domain not including the boundary ∂D. The closed domain will be denoted by $\bar{D}$.

$$\phi(\boldsymbol{r}) = \int_D \rho(\boldsymbol{r}') \frac{1}{4\pi|\boldsymbol{r}-\boldsymbol{r}'|}\, \mathrm{d}^3\boldsymbol{r}' + \int_{\partial D} \sigma(\boldsymbol{r}') \frac{1}{4\pi|\boldsymbol{r}-\boldsymbol{r}'|}\, \mathrm{d}^2\boldsymbol{r}'$$

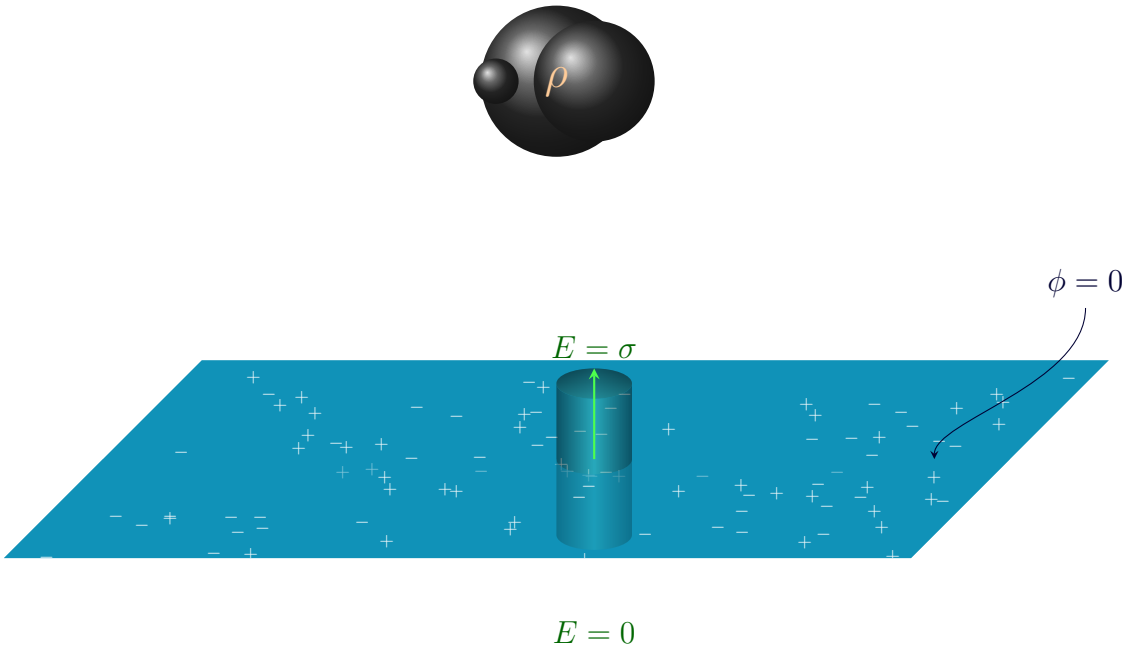

Figure 3.1: A cartoon visualizing the induced charge on the surface of a grounded conducting plane. The induced surface charge density σ contributes a single-layer term to the integral representation of the electrostatic potential. The normal derivative of the potential at the surface is permitted to be discontinuous, and the jump is proportional to the induced surface charge density. One way to determine the distribution σ would be to evaluate the integral representation for the potential on the plane, impose the boundary condition, and solve the integral equation for σ.

When using the above method, it may be helpful to eliminate one of the potentials by assuming some sort of extension for $\phi(\boldsymbol{x})$ outside the domain D. For example, to eliminate the double-layer, we choose to extend ϕ in a continuous manner outside the domain. Writing (3.36) for the outside of D, which we will denote by D^c, but while keeping the singularity source for ψ still at $\boldsymbol{x} \in D$. Then, the right hand side vanishes, since the region of integration D^c doesn't include the singularity and we assume that ρ has no support in D^c. The latter is a choice that determines how ϕ extends outside our domain, which is anyway immaterial to our purposes. The resulting equation reads

$$\frac{1}{4\pi} \oint_{\partial D} \mathrm{d}^2 x' \, \left[\frac{1}{|\boldsymbol{x} - \boldsymbol{x}'|} \left(\frac{\partial \phi}{\partial n'} \right)_{\text{outside}} - \phi(\boldsymbol{x}') \frac{\partial}{\partial n'} \frac{1}{|\boldsymbol{x} - \boldsymbol{x}'|} \right] = 0, \tag{3.40}$$

where we have allowed the normal derivative of the potential (the normal component of electric field) to jump across the boundary. This is the price we pay for keeping the potential continuous. It is then easy to see that

$$\begin{aligned} \phi(\boldsymbol{x}) = & \int_D \mathrm{d}^3 x' \, \frac{\rho(\boldsymbol{x}')}{4\pi |\boldsymbol{x} - \boldsymbol{x}'|} \\ & + \frac{1}{4\pi} \oint_{\partial D} \mathrm{d}^2 x' \, \frac{1}{|\boldsymbol{x} - \boldsymbol{x}'|} \left[\left(\frac{\partial \phi}{\partial n'} \right)_{\text{inside}} - \left(\frac{\partial \phi}{\partial n'} \right)_{\text{outside}} \right], \end{aligned} \tag{3.41}$$

which is the familiar idea that the jump in the normal component of the electric field at a conducting plane (for example) may be thought of as arising from an induced surface charge density proportional to the size of the jump,

$$\sigma_{\text{ind}} = \left[\left(\frac{\partial \phi}{\partial n'} \right)_{\text{inside}} - \left(\frac{\partial \phi}{\partial n'} \right)_{\text{outside}} \right]. \tag{3.42}$$

If the boundary condition is given in terms of the potential, this surface charge density may be obtained by solving the integral equation (3.41) for σ_{ind}.

What we have demonstrated, is that the reciprocal identity leads to an integral representation for the solution in terms of single-layer and double-layer potentials. However, in boundary value problems, only one of the two potentials is specified. Either one must eliminate the unknown potential by the use of a proper Green's function, or solve the boundary integral equation for the unknown potential in terms of the known potential. The latter task may be simplified by eliminating one of the two potentials depending on the problem.

We shall now proceed to explore analogous ideas for the unsteady Stokes equations.

3.8.2 The Lorentz reciprocal identity for the unsteady Stokes equations

Consider the unsteady Stokes equations,

$$\begin{aligned} \boldsymbol{\nabla}\cdot\boldsymbol{\sigma} &= \boldsymbol{b} + \mathrm{i}\omega\rho_f\boldsymbol{v}, \\ \boldsymbol{\nabla}\cdot\boldsymbol{v} &= 0, \end{aligned} \tag{3.43}$$

where $\boldsymbol{b}(\boldsymbol{x})$ is a body force density that the fluid is subject to, and $\boldsymbol{\sigma}$ with components $\sigma_{ij} = -p\delta_{ij}+\eta(\partial_i v_j+\partial_j v_i)$ is the stress tensor for the incompressible Stokes equations, as mentioned earlier. We have dropped the subscripts ω since we will exclusively work in frequency domain in this section. We have written the unsteady Stokes equations in this specific form to draw a connection with the previous procedure for electrostatics.

Our aim is to develop an integral representation for $\boldsymbol{v}(\boldsymbol{x})$. To effect this, we recall that in the electrostatic case, we wanted to solve the equation $\boldsymbol{\nabla}\cdot\boldsymbol{\nabla}\phi = -\rho$, whereby we considered the total derivative $\boldsymbol{\nabla}\cdot(\phi\boldsymbol{\nabla}\psi)$ so that one of the terms in the expansion would have the form $\phi\boldsymbol{\nabla}\cdot\boldsymbol{\nabla}\psi$. Then, by letting ψ be the fundamental solution, we recovered a term of the form $\phi\,\delta(\boldsymbol{x}-\boldsymbol{x}')$ that would, when integrated, give us $\phi(x)$. In a similar spirit, consider two (possibly unrelated) velocity fields $\boldsymbol{v}$ and $\boldsymbol{v'}$ and their corresponding stress tensors $\boldsymbol{\sigma}$ and $\boldsymbol{\sigma'}$ that satisfy the Stokes equations (3.43). Now consider the identity,

$$\boldsymbol{\nabla}\cdot(\boldsymbol{v}\cdot\boldsymbol{\sigma'}) = \partial_j(v_i\sigma'_{ij}) = (\partial_j v_i)\sigma'_{ij} + v_i(\partial_j\sigma'_{ij}). \tag{3.44}$$

The latter term in the right hand side of the above equation, $\boldsymbol{v}\cdot(\boldsymbol{\nabla}\cdot\boldsymbol{\sigma'})$ looks like the term that we want. We now swap the primed and unprimed fields to obtain another similar identity,

$$\partial_j(v'_i\sigma_{ij}) = (\partial_j v'_i)\sigma_{ij} + v'_i(\partial_j\sigma_{ij}). \tag{3.45}$$

Now, as we did before, we subtract (3.45) from (3.44) to obtain

$$\begin{aligned} \partial_j(v_i\sigma'_{ij}) - \partial_j(v'_i\sigma_{ij}) = &\left[(\partial_j v_i)\sigma'_{ij} - (\partial_j v'_i)\sigma_{ij}\right] \\ &+ \left[v_i(\partial_j\sigma'_{ij}) - v'_i(\partial_j\sigma_{ij})\right]. \end{aligned}$$

Considering the first bracket on the right hand side, and substituting the expression for the stress tensor in terms of the pressure and velocity fields, we obtain

$$\left[(\partial_j v_i)\sigma'_{ij} - (\partial_j v'_i)\sigma_{ij}\right] = \eta\left[(\partial_j v_i)(\partial_j v'_i + \partial_i v'_j) - (\partial_j v'_i)(\partial_j v_i + \partial_i v_j)\right] = 0$$

wherein the terms containing pressure vanish because of the continuity equations $\boldsymbol{\nabla \cdot v} = 0$, $\boldsymbol{\nabla \cdot v'} = 0$ and the remaining terms cancel.

Thus, we are left with

$$\partial_j(v_i\sigma'_{ij}) - \partial_j(v'_i\sigma_{ij}) = \left[v_i(\partial_j\sigma'_{ij}) - v'_i(\partial_j\sigma_{ij})\right], \tag{3.46}$$

which we may now integrate as before to obtain,

$$\oint_{\partial D} \mathrm{d}^2x \ \left[v_i\sigma'_{ij}n_j - v'_i\sigma_{ij}n_j\right] = \int_D \mathrm{d}^3x \ \left[v_i(\partial_j\sigma'_{ij}) - v'_i(\partial_j\sigma_{ij})\right], \tag{3.47}$$

where n_j represents the components of the outward unit vector $\hat{\boldsymbol{n}}$ normal to the surface ∂D. This is a form of the reciprocal identity for the unsteady Stokes equations, derived by Lorentz [1907, §2, Eq. (I')].

If both the flows $\boldsymbol{v}$ and $\boldsymbol{v'}$ have no singularities, the flows are steady ($\omega = 0$) and there are no body forces $\boldsymbol{b}$ and $\boldsymbol{b'}$, then we may set $\boldsymbol{\nabla \cdot \sigma} = 0$, $\boldsymbol{\nabla \cdot \sigma'} = 0$, to obtain

$$\oint_{\partial D} \mathrm{d}^2x \ \left[v_i\sigma'_{ij}n_j - v'_i\sigma_{ij}n_j\right] = 0, \tag{3.48}$$

which is another form of Lorentz's reciprocal identity [Pozrikidis, 1992, §1.4].

3.8.3 From the reciprocal identity to an integral representation for the unsteady Stokes equations

One way to obtain an integral representation for the unsteady Stokes equations analogous to equation (3.38) for electrostatics would be to use the reciprocal identity just as we did earlier.

For $(\boldsymbol{\sigma}, \boldsymbol{v})$, we choose the actual flow and for $(\boldsymbol{\sigma'} = \boldsymbol{T}^0_k, \boldsymbol{v'} = \boldsymbol{G}^0_k)$, we choose the fundamental solution produced by a singularity at $\boldsymbol{x}_0 \in D$. The fundamental solution satisfies

$$\begin{aligned} \boldsymbol{\nabla \cdot T}^0_k(\boldsymbol{x} - \boldsymbol{x}_0) &= \delta(\boldsymbol{x} - \boldsymbol{x}_0)\hat{\boldsymbol{e}}_k + \mathrm{i}\omega\rho_f\boldsymbol{G}^0_k, \\ \boldsymbol{\nabla \cdot G}^0_k(\boldsymbol{x} - \boldsymbol{x}_0) &= 0, \end{aligned} \tag{3.49}$$

and decays to zero at infinity. The Green's function $\boldsymbol{G}^0_k$ with components G^0_{ik} is the unsteady Oseen tensor (3.23), and represents the i^{th} component of the velocity field produced by a point force in the $\hat{\boldsymbol{e}}_k$ direction. The object $\boldsymbol{T}^0_k$ with components T^0_{ijk} is the corresponding stress tensor.

Henceforth, to avoid the confusion caused by the dangling k-index, we will work purely in index notation. The equations (3.49) may then be rewritten as

$$\begin{aligned} \partial_j T^0_{ijk}(\boldsymbol{x}-\boldsymbol{x}_0) &= \delta(\boldsymbol{x}-\boldsymbol{x}_0)\delta_{ik} + \mathrm{i}\omega\rho_f G^0_{ik}, \\ \partial_i G^0_{ik}(\boldsymbol{x}-\boldsymbol{x}_0) &= 0. \end{aligned} \tag{3.50}$$

We now proceed to adapt the reciprocal identity to produce an integral representation for the velocity field in a manner analogous to that done for electrostatics. Setting $v'_i = G^0_{ik}(\boldsymbol{x}-\boldsymbol{x}_0)$ and $\sigma'_{ij} = T^0_{ijk}(\boldsymbol{x}-\boldsymbol{x}_0)$ in (3.47) and using the equations (3.50), we obtain

$$\oint_{\partial D} \left[v_i T^0_{ijk} n_j - G^0_{ik}\sigma_{ij} n_j \right] \, \mathrm{d}^2x = \int_D \left[v_i \delta_{ik}\delta(\boldsymbol{x}-\boldsymbol{x}_0) - G^0_{ik} b_i \right] \, \mathrm{d}^3x, \tag{3.51}$$

where b_i is the body force contributing the actual flow $\boldsymbol{v}$. To obtain the above, we have used $\partial_j \sigma_{ij} = b_i + \mathrm{i}\omega\rho_f v_i$ and canceled the $v_i G^0_{ik}$ terms. Noting that $\sigma_{ij} n_j = f_i$ is the surface traction, we may write

$$\begin{aligned} v_k(\boldsymbol{x}_0) = &\int_D G^0_{ik}(\boldsymbol{x}-\boldsymbol{x}_0)\, b_i \, \mathrm{d}^3x \\ &+ \oint_{\partial D} \left[v_i \, T^0_{ijk}(\boldsymbol{x}-\boldsymbol{x}_0)\, n_j - f_i \, G^0_{ik}(\boldsymbol{x}-\boldsymbol{x}_0) \right] \, \mathrm{d}^2x, \end{aligned} \tag{3.52}$$

where $\boldsymbol{x}_0 \in D$. We have thus obtained an integral representation for the flow, where the second term on the right hand side represents a double-layer potential, and the third term represents a single-layer potential. It must be noted that if $\boldsymbol{x}_0$ lies on the boundary ∂D instead of being inside the domain, the term with T^0_{ijk} becomes a singular integral and appropriate care must be taken. See Pozrikidis [1992] for details.

3.8.4 Eliminating the double-layer potential

It is usually convenient to eliminate either the single-layer or double-layer potential to obtain a simpler expression. One way to do this is to use a Green's function tailored to the boundary, as done in the electrostatic case, which gives us a direct representation for the flow in terms of the boundary conditions. However, having such a Green's function in the unsteady Stokes context is already a luxury. If the Green's functions specific to the boundary are not known, it is still possible to eliminate one of the potentials as we did in the electrostatic case, at the cost of solving integral equations to determine the densities of forces / stresses [Pozrikidis, 1992, §2.3, Ch. 4].

In this work, we will choose to eliminate the double-layer potential and work with the single-layer potential. The up-side of this is that we do not need to deal with the complications of computing T^0_{ijk} and taking care with the singularities involved. The down-side would be that representation by a single-layer potential leads to a Fredholm integral equation of the first kind, which is generally harder to solve as one cannot use iterative procedures.

Following Pozrikidis [1992], we introduce a complementary flow $\tilde{\boldsymbol{v}}$ that has support outside the domain D (including on ∂D). On the boundary ∂D, $\tilde{\boldsymbol{v}}$ has the same value as the original flow $\boldsymbol{v}$. The value of $\tilde{\boldsymbol{v}}$ is not really of concern, whereby we may assume that there are no body forces contributing to this flow within D^c. Choosing $\sigma'_{ij} = T^0_{ijk}(\boldsymbol{x}-\boldsymbol{x}_0)$, $v'_i = G^0_{ik}(\boldsymbol{x}-\boldsymbol{x}_0)$ ($\boldsymbol{x}_0 \in D$) as before in (3.47), but choosing $v_i = \tilde{v}_i$ on ∂D, and the domain of integration to be the outside D^c of ∂D instead, we see that the the volume integrals on the right hand side of (3.47) vanish (the singularity source of the Green's function at $\boldsymbol{x}_0$ lies outside D^c) and we have

$$\oint_{\partial D} \left[\tilde{v}_i\, T^0_{ijk}(\boldsymbol{x}-\boldsymbol{x}_0)\, n_j - \tilde{f}_i\, G^0_{ik}(\boldsymbol{x}-\boldsymbol{x}_0)\right]\, \mathrm{d}^2x = 0. \tag{3.53}$$

But on ∂D, $\tilde{v}_i = v_i$, whereby we obtain

$$\oint_{\partial D} v_i\, T^0_{ijk}(\boldsymbol{x}-\boldsymbol{x}_0)\, n_j\, \mathrm{d}^2x = \oint_{\partial D} \tilde{f}_i\, G^0_{ik}(\boldsymbol{x}-\boldsymbol{x}_0)\, \mathrm{d}^2x, \tag{3.54}$$

which we substitute into (3.55) to obtain

$$v_k(\boldsymbol{x}_0) = \int_D G^0_{ik}(\boldsymbol{x}-\boldsymbol{x}_0)\, b_i\, \mathrm{d}^3x + \oint_{\partial D} q_i\, G^0_{ik}(\boldsymbol{x}-\boldsymbol{x}_0)\, \mathrm{d}^2x \qquad (\boldsymbol{x}_0 \in D), \tag{3.55}$$

where $\boldsymbol{q} := \tilde{\boldsymbol{f}} - \boldsymbol{f}$ is an unknown force distribution that must be determined by imposing boundary conditions. Intuitively, this shows that a boundary can be replaced by a sheet of forces that have the same effect as imposing the boundary conditions, analogous to the replacement of the electrostatic boundary conditions by a sheet of charges.

The validity of this procedure rests on the existence of the complementary flow $\tilde{\boldsymbol{u}}$. As shown by Pozrikidis [1992, §4.1, 4.2], the condition for existence of such a flow is that

$$\oint_{\partial D} \boldsymbol{v}(\boldsymbol{x}) \cdot \hat{\boldsymbol{n}}(\boldsymbol{x})\, \mathrm{d}^2x = 0, \tag{3.56}$$

i.e. that there is no flux of fluid through the boundary of the domain. This is trivially satisfied for closed boundaries ∂D which impose the no-penetration boundary condition[19] by virtue of incompressibility. However, care must be taken when applying the above to non-compact boundaries.

In this work, we will concern ourselves with a half-space domain $D = \mathbb{R}^2 \times \mathbb{R}^+$, where we do have a non-compact boundary given by a plane. So we must see if the integral constraint (3.56) holds for a non-compact boundary. To investigate, we assume that the flow can be thought of as being generated by a compact distribution of sources. We consider the flux through a closed hemispherical surface of radius R that completely encompasses the distribution. The net flux through this closed surface must be zero, and we may break it up into two parts – the flux through the hemispherical surface, and the flux through the disk of radius R that closes the surface. Looking at the asymptotics of the unsteady Oseen tensor (3.23), we see that for any finite $|\alpha| > 0$, the largest term as $q \to \infty$ decays like[20] $1/q^3$ – the other terms are suppressed by exponential decays. The result is therefore that the velocity field generated from a finite distribution drops like $1/R^3$, whereas the area of the hemispherical section grows only like R^2. Therefore, the net flux through the hemispherical section is zero, whereby we may conclude from incompressibility that the flux through the disk of radius R is also zero. As R tends to infinity, the disk becomes a plane, therefore showing that the integral constraint (3.56) is satisfied even for non-compact surfaces provided that the field $\boldsymbol{v}$ may be generated by a finite source distribution and the frequency of oscillation $\omega > 0$. It should be possible to analytically continue results to the $\omega = 0$ case. Thus, we may use a single-layer potential to represent flow in a half-space.

3.9 Added mass and the high-frequency limit

Any agency that attempts to accelerate a rigid body S in a fluid must also accelerate the fluid in front of the particle. Therefore, the effective inertia felt by the agency is larger than just the inertia of the particle. To calculate how much larger, we may find the drag coefficient using the machinery developed in Section 3.4 and then rewrite

[19] In this work, the no-penetration boundary condition will always hold. We do not treat porous boundaries.

[20] This term comes from the $\boldsymbol{\nabla}\boldsymbol{\nabla} G(\boldsymbol{q}; 0)$ term.

the drag coefficient thus obtained by extracting the term proportional to $\mathrm{i}\omega$ as

$$\gamma(\omega) = \zeta(\omega) - \mathrm{i}\omega m_a, \tag{3.57}$$

where m_a is a constant. Then the drag force $\boldsymbol{F}_\omega^{\mathrm{drag}} = -\zeta(\omega)\boldsymbol{u}_\omega + \mathrm{i}\omega m_a \boldsymbol{u}_\omega$ and the latter term may be added to the inertial term. m_a is generally called the *added mass* or *induced mass*. Thus the effective mass or *virtual mass* of the particle in the fluid is given by $m^* := m_p + m_a$. In the case of a sphere in unbounded fluid (3.35), it can be seen that the term $\gamma_s \alpha^2 a^2 = -\mathrm{i}\omega m_f/2$ where $m_f = \frac{4}{3}\pi a^3 \rho_f$ is the mass of the fluid displaced by the sphere, whereby the effective mass is $m^* = m_p + m_f/2$.

An alternate way to compute the added mass at low Reynolds numbers is using potential flow [Landau & Lifshitz, 1987, §12]. Going back to (3.5), if we assume $\mathrm{Re} \ll 1$ and $\tau \ll \tau_f$, i.e. extremely short time-scales of motion of the particle, we could conceive a dominant balance between the time-derivative term and the pressure term, dropping both the advective term and the viscosity term. This is technically incorrect because the term $\eta\Delta\boldsymbol{v}_\omega$ is the highest-order derivative in the equation, whereby this should be handled appropriately as a singular perturbation. The author does not know of a thorough boundary layer analysis of this regime. If we nevertheless simply drop the viscosity term, we are left with

$$\begin{aligned} -\mathrm{i}\omega\rho_f \boldsymbol{v}_\omega &= -\boldsymbol{\nabla} p_\omega, \\ \boldsymbol{\nabla}\cdot\boldsymbol{v}_\omega &= 0. \end{aligned} \tag{3.58}$$

As before, the latter equation results in a Laplace equation for pressure, $\Delta p_\omega = 0$, and the velocity is simply given by the gradient of a scalar potential,

$$\boldsymbol{v}_\omega = \boldsymbol{\nabla}\left(\frac{p}{\mathrm{i}\omega\rho_f}\right). \tag{3.59}$$

This is the regime of potential flow, which is significantly simpler to handle. It is expected (although the author has not been able to find a proof) that calculating the drag force

$$\boldsymbol{F}_\omega^{\mathrm{drag}} = \oint_{\partial S} \mathrm{d}^2 r \; p_\omega \, \hat{\boldsymbol{n}} \tag{3.60}$$

would reproduce the added mass, i.e. $\boldsymbol{F}_\omega^{\mathrm{drag}} = \mathrm{i}\omega m_a \boldsymbol{u}_\omega$ where m_a is the added mass. The added mass for a number of geometries has been calculated using potential flow and the results are well-known [Brennen, 1982].

Thus, we may postulate that at high frequencies, the drag force from the full unsteady Stokes calculations must tend to the added mass contribution from potential flow calculations. Although we have not proven this statement rigorously, it seems plausible and the author does not know of counterexamples.

Chapter Four: Theory of Brownian motion in bulk fluid

In this chapter, we will put together the theory of Brownian motion developed in Chapter 2 and the fluid dynamics developed in Chapter 3, particularly Section 3.6, to develop the theory for Brownian motion in an unbounded fluid medium. This theory is well-known and may be found, for example, in Zwanzig & Bixon [1970]; Clercx & Schram [1992]. We analyze various aspects of the theory here, mostly to make the work self-contained. Such analyses may also be found in the supplementary material of Franosch *et al.* [2011]; Kheifets *et al.* [2014].

4.1 Theory of Brownian motion of a sphere in bulk incompressible Newtonian fluid

We consider a spherical particle (density ρ_p, radius a, mass $m_p = 4\pi a^3\rho_f/3$) in thermal equilibrium at temperature T with an otherwise unbounded incompressible Newtonian fluid medium (density ρ_f, dynamic shear viscosity η, kinematic viscosity $\nu = \eta/\rho_f$). No-slip boundary conditions are assumed on the sphere, which is realistic for most solid particles that are not intentionally designed to be hydrophobic. The drag coefficient for this system was discussed in Section 3.6, and is given by equation (3.28),

$$\gamma_0(\omega) = \gamma_s(1 + \sqrt{-\mathrm{i}\omega\tau_f} - \mathrm{i}\omega\tau_f/9), \tag{4.1}$$

where as we had earlier, $\gamma_s = 6\pi\eta a$ is the steady Stokes drag coefficient, and $\tau_f = a^2\rho_f/\eta$ is the time-scale for vorticity diffusion over the size of the sphere. The branch of the square-root is chosen so that $\sqrt{-\mathrm{i}} = (1-\mathrm{i})/\sqrt{2}$.

Splitting the above into real and imaginary parts, we may write

$$\begin{aligned} \Re[\gamma_0] &= \gamma_s\left(1 + \sqrt{\frac{\omega\tau_f}{2}}\right), \\ \mathrm{i}\,\Im[\gamma_0] &= -\mathrm{i}\gamma_s\sqrt{\frac{\omega\tau_f}{2}} - \mathrm{i}\omega\frac{m_f}{2}, \end{aligned} \tag{4.2}$$

where $m_f := 4\pi\rho_f a^3/3$ is the mass of fluid displaced by the particle. The term $-\mathrm{i}\omega m_f/2$ represents an additional inertia of $m_f/2$; thus the particle in the fluid may be thought of as having an effective mass of $m^* := m_p + m_f/2$.

Through the machinery developed in Chapter 2, we have seen that once the drag coefficient is known, the statistical properties characterizing the Brownian motion may be determined. Given that the system is isotropic, the admittance may be reduced to the scalar

$$Y(\omega) = \frac{1}{-\mathrm{i}\omega m^* + \gamma_s\left(1 + \sqrt{-\mathrm{i}\omega\tau_f}\right)}. \tag{4.3}$$

If a harmonic trap is present, the trap may induce anisotropy. In this case, we will simplify our description by considering a single dimension, x, with trap strength K. The admittance for that coordinate is then given by

$$Y_K(\omega) = \frac{1}{-\mathrm{i}\omega m^* + \gamma_s\left(1 + \sqrt{-\mathrm{i}\omega\tau_f}\right) - K/(\mathrm{i}\omega)}. \tag{4.4}$$

The (two-sided[1]) power spectral density of the Langevin force is given by

$$S_F(\omega) = 2k_BT\left(1 + \sqrt{\frac{\omega\tau_f}{2}}\right). \tag{4.5}$$

The (two-sided) power spectral density of velocity fluctuations is given by

$$S_u(\omega) = 2k_BT\frac{1 + \sqrt{\omega\tau_f/2}}{\left|-\mathrm{i}\omega m^* + \gamma_s\left(1 + \sqrt{-\mathrm{i}\omega\tau_f}\right) - K/(\mathrm{i}\omega)\right|^2}, \tag{4.6}$$

and the (two-sided) power spectral density of position fluctuations is given by

$$S_x(\omega) = 2k_BT\frac{1 + \sqrt{\omega\tau_f/2}}{\omega^2\left|-\mathrm{i}\omega m^* + \gamma_s\left(1 + \sqrt{-\mathrm{i}\omega\tau_f}\right) - K/(\mathrm{i}\omega)\right|^2}. \tag{4.7}$$

The velocity auto-correlation function can be obtained by Fourier-transforming $S_u(\omega)$. The results have been given by Clercx & Schram [1992]. In the absence of a trap,

$$C_u(t) = \frac{k_BT}{m^*(B - A)}\left[B\,\mathrm{w}(\mathrm{i}B\sqrt{t}) - A\,\mathrm{w}(\mathrm{i}A\sqrt{t})\right], \tag{4.8}$$

[1]The one-sided PSD is given by twice the two-sided PSD, at all values except the DC value. When dealing with continuous frequency, as opposed to windowed signals, it is convenient to just define it to be exactly twice the two-sided PSD for all values of frequency. While the experimental measurements will frequently feature one-sided PSDs, we will stick to two-sided PSDs in most of the theory.

where

$$\begin{aligned} A &:= \frac{1}{2m^*}\left[z + \sqrt{z^2 - 4\gamma_s m^*}\right], \\ B &:= \frac{1}{2m^*}\left[z - \sqrt{z^2 - 4\gamma_s m^*}\right], \\ z &:= 6\pi a^2 \sqrt{\rho_f \eta}, \end{aligned} \tag{4.9}$$

and w is the Faddeeva function[2] $\mathrm{w}(q) := e^{-q^2}\mathrm{erfc}(-\mathrm{i}q)$ [DLMF, Eq. 7.2.3]. In the presence of a harmonic trap, there are more roots, and the expression is rather complicated. It may be found in Eqs. (2.11) to (2.14) of Clercx & Schram [1992].

The mean-squared displacement may also be calculated in closed-form, and has been given by Clercx & Schram [1992, Eqs. (1.11), (2.25)–(2.26)].

4.2 Analysis of the hydrodynamic VACF

Using the power series expansion of $\mathrm{w}(q)$ [DLMF, Eq. 7.6.3] in equation (4.8), we find that [Kheifets *et al.*, 2014, Suppl. Material]

$$C_u(t) \sim \frac{k_B T}{m^*}\left[1 - \sqrt{\frac{t}{\tau_v}}\right], \tag{4.10}$$

where

$$\tau_v := \frac{\pi}{4}\frac{\tau_p^2}{\tau_f}, \tag{4.11}$$

and here $\tau_p := m^*/\gamma_s$, i.e. using the effective mass.

Two observations are in order:

1. The value of $\langle u^2 \rangle$ is $k_B T/m^*$, and not $k_B T/m_p$ as may be expected from the equipartition theorem. This paradox is resolved by including the effects of compressibility [Zwanzig & Bixon, 1975], whereby the VACF shows a rapid decay from the actual value of $k_B T/m_p$ to the effective value of $k_B T/m^*$ over time-scales of the order of $\tau_c := a/c$. We shall refer to the result $\langle u^2 \rangle = k_B T/m^*$ as the "modified" equipartition theorem in this work, and the corresponding velocity $u(t)$ on these time-scales as the "hydrodynamic" instantaneous velocity of the particle.

[2]The Faddeeva function arises in the context of decay with a fractional derivative of half-integer order, which is possibly the case for this system [Saichev & Woyczynski, 2013, Ch. 6].

2. The VACF has an initial decay that is faster than that predicted by the EOU theory. Whereas in the EOU theory, we had an exponential decay $C_u^{\mathrm{EOU}}(t) \sim \langle u^2 \rangle (1 - t/\tau_p)$, the hydrodynamic VACF decays like $1 - \sqrt{t/\tau_v}$, and for small t, $\sqrt{t}$ is larger than t.

The long-time asymptotic of $C_u(t)$ is given by Clercx & Schram [1992] as

$$C_u(t) \sim k_B T \, \frac{z}{2\gamma_s^2 \sqrt{\pi}} \, \frac{1}{t\sqrt{t}} \qquad t \to \infty, \tag{4.12}$$

which is the famous $t^{-3/2}$ long-time tail of the hydrodynamic VACF. Thus, at long time-scales the hydrodynamic VACF retains more correlation than the exponential decay of the EOU theory.

These two aspects of the hydrodynamic VACF – the faster decay at short time-scales, and the slower decay at long time-scales – may be seen in figure 4.2, where it is compared against the VACF from the EOU theory.

Intuitively speaking, these effects may be explained as follows [Kheifets *et al.*, 2014]: At short time-scales, there is more drag than in the EOU theory, because of the additional $\gamma_s \sqrt{\omega\tau_f/2}$ term in the real part of $\gamma_0(\omega)$. Therefore, the VACF decorrelates faster at short time-scales. However, at long time-scales, there is more inertia than in the EOU theory, because if we interpret the $\mathrm{i}\gamma_s \sqrt{\omega\tau_f/2}$ as a frequency-dependent contribution to the added mass, we find that $\Im[\gamma_0] = -\mathrm{i}\omega m_{\mathrm{added}}(\omega) = -(\mathrm{i}\omega m_f/2)(1 + 9/\sqrt{2\omega\tau_f})$. Thus, at small frequencies, there is a significant added inertia. The extra inertia bolsters the memory of velocity and prevents the VACF from decaying.

These ideas are further illustrated by the comparison in figure 4.2. In the figure, the blue coloring is proportional to the magnitude of flow velocity. The green coloring is proportional to $\sigma_{r\theta}$, the component of the shear stress tensor primarily responsible for the drag. Sub-figure (a) shows pure potential flow around a sphere, which contributes an added mass of $m_f/2$. Compare this with sub-figure (c), which shows the solution to the unsteady Stokes equations (Section 3.6) for $\omega = 0.7/\tau_f$ (long time-scales). The larger amount of fluid being entrained by the particle is indicative of a higher effective inertia. Sub-figure (b) shows the steady Stokes flow around a sphere, which produces a drag force of $\gamma_s u$ on the sphere. Compare this with sub-figure (d), which shows the solution to the unsteady Stokes equations (Section 3.6) for $\omega = 25/\tau_f$

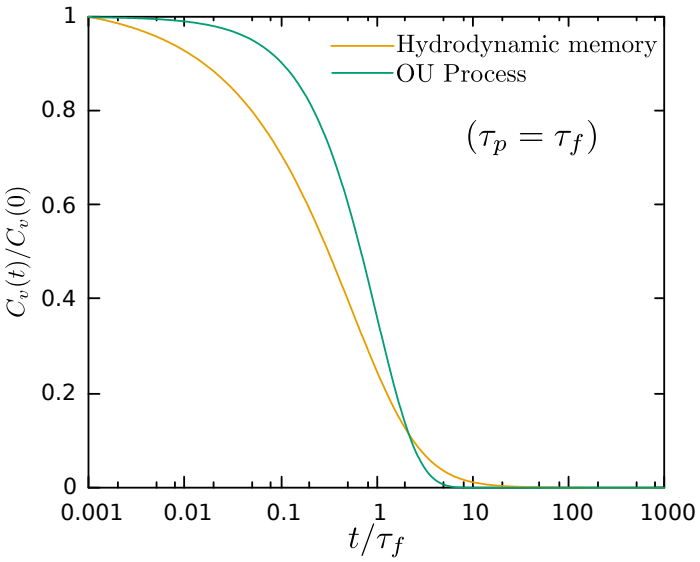

Figure 4.1: Semi-logarithmic plots of the velocity auto-correlation functions predicted by the Einstein-Ornstein-Uhlenbeck (EOU) theory, and by the hydrodynamic theory of Zwanzig & Bixon [1970]. The hydrodynamic VACF was obtained by numerical computation of the Fourier transform of the position PSD using the GNU Scientific Library's `qawo` routine. Non-dimensionalized time is measured in units of $\tau_p = \tau_f$. The VACF has been normalized to its initial value of $\langle u^2 \rangle$. The hydrodynamic VACF shows a faster initial decay compared to the EOU theory, followed by a slower decay at long time-scales.

(short time-scales). The larger amount of shear stress in the fluid close to the sphere is indicative of a larger drag force.

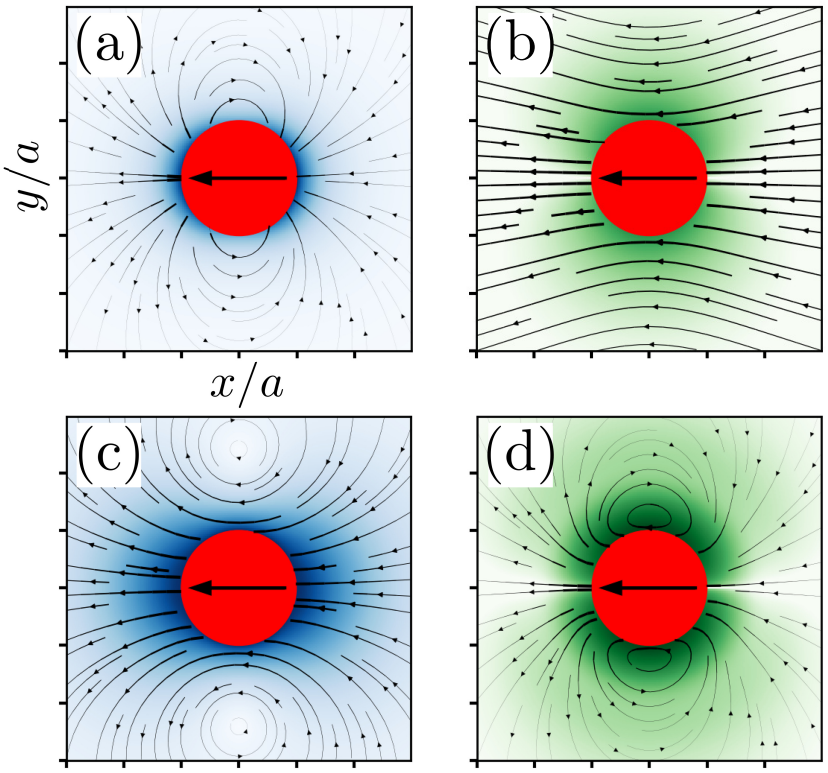

Figure 4.2: An illustration of the hydrodynamic effects on Brownian motion in a dense liquid. The x-y plane represents a section of the full 3D problem through the origin, where the center of the spherical particle is located. The red circle represents the section of a rigid, no-slip sphere performing small translational oscillations in sub-figures (a), (c) and (d), and moving with a constant velocity in sub-figure (b). The plots (a), (c), (d) represent a snapshot in time when the sphere has just passed the equilibrium point and is moving along the negative x-direction. The black lines with arrows show the streamlines of the velocity field around the particle, with the thickness indicating the magnitude of the velocity field. In sub-figures (a) and (c), the strength of blue color represents the magnitude of the flow velocity normalized to the velocity of the particle. In sub-figures (b) and (d), the strength of the green color represents the magnitude of the shear stress tensor component $\sigma_{r\theta}$. Sub-figure (a) shows the results from pure potential flow. Sub-figure (b) shows the results from the unsteady Stokes equations (Section 3.6) for $\omega = 0.7/\tau_f$. Sub-figure (c) shows the results from steady Stokes flow. Sub-figure (d) shows the results from the unsteady Stokes equations (Section 3.6) for $\omega = 25/\tau_f$. The plots suggest an explanation for the rapid decorrelation of the velocity at short time-scales, but the slower decorrelation at long time-scales, as compared with the EOU theory. At short time-scales, the shear stress is much higher than that in steady Stokes flow, leading to rapid decorrelation. At long time-scales, there is more fluid entrained by the sphere than in potential flow, leading to slow decorrelation.

Chapter Five: Experimental Setup to study Brownian Motion

In this chapter, we describe the general experimental setup used in the Raizen Lab to study Brownian motion of micron-sized particles in liquids at short time-scales. The experimental setup described here is common to the following published work: Kheifets *et al.* [2014]; Mo *et al.* [2015*a*,*b*].

This experimental setup is described in detail in Ph.D. dissertations by Mo [2015] and Kheifets [2014]. The author will briefly review the various aspects of the experimental setup in general, while emphasizing and detailing those parts to which he contributed the most. These include the construction and maintenance of the flow cell (Section 5.2), the LabVIEW software for control of the experiment and data acquisition, and the binary file format for data storage (Section 5.4), the software for the alignment system for the cut-mirror (Section 5.7), and the system for measurement of detector response (Section 5.8).

5.1 Optical Tweezers

Optical tweezers form one of the de facto tools to control and manipulate objects of microscopic or nanoscopic sizes. The trapping of particles by laser beams was first demonstrated by Ashkin [1970]. Ashkin showed that a TEM_{00} laser beam with a few milliwatts of power was able to produce a stable trapping force on dielectric microspheres in water when focused down to a reasonably tight spot. Since then, optical tweezers have become an indispensable tool in physics and biology. For a survey of applications, see e.g. Berg-Sørensen & Flyvbjerg [2004].

A laser beam of intensity I exerts a radiation pressure of the order of I/c, where c denotes the speed of light, and the exact factor depends on the reflectivity of the surface. For a 1 mW laser beam completely incident on a particle (i.e. the waist of the laser beam is of the order of the size of the particle), we expect a force of the order of 10^{-11} N. While this force appears to be extremely small, if we consider the weight of a micron-sized particle made of glass ($\rho_p \approx 2.0$ g/cm^3), we find it to be of

the order of 10^{-13} N. Thus, the force exerted by optical tweezers can be almost 100 $\sim 10^4$ times the weight. The key requirement of concentrating the beam over the size of the particle may be achieved using coherent light from a laser.

A focused laser beam, hitting a partially reflecting and partially transmitting dielectric particle that has a higher refractive index than its surrounding medium, exerts two types of forces – the reflection causes momentum of photons to be transferred to the particle, pushing it in the direction of propagation of the laser beam by exerting the *scattering force*; and the non-uniform intensity profile of a focused Gaussian laser beam produces a force that tends to pull the particle to the center of the beam, a force referred to as the *gradient force*.

5.1.1 Mechanism of optical tweezers in the regime of ray optics

In the approximate regime of ray optics, which describes optical tweezers well when the particle size is much larger than the wavelength of the laser used, the gradient force may be understood by studying figure 5.1.

The equilibrium position of the particle is along the axis of the beam, but ahead of the beam focus along the direction of propagation. This is because of the scattering force pushing the particle forward along the beam direction. This scattering force is balanced by an axial gradient force, which can be understood as follows: if the particle moves forward along the beam direction from the equilibrium position, the beam is re-focused by the particle more tightly, whereby the beam has a larger net momentum along the forward axial direction. By momentum conservation, the particle feels a kick in the opposite direction. The amount of focusing increases with the forward excursion of the particle, and therefore, the restoring force on the particle increases in strength with displacement. Similarly, if the particle moves against the beam direction, the transmitted beam becomes more defocused, and the net axial momentum of the beam is decreased. Therefore, the particle feels a restoring force in the beam direction.

If the particle moves away from equilibrium in a lateral direction, the beam is refracted in the same direction. Thus, the beam gains a net momentum in the direction of displacement of the particle. By momentum conservation, the particle must suffer a net momentum in the direction in the opposite direction of displacement.

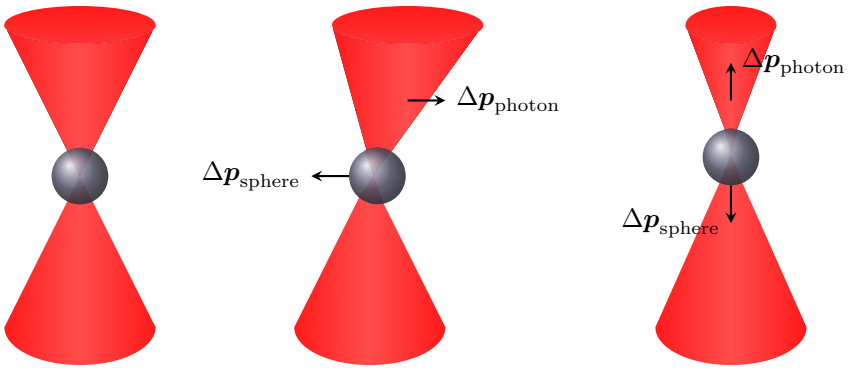

(a) Equilibrium (b) Lateral restoring force (c) Axial restoring force

Figure 5.1: Mechanism of optical tweezers explained in the regime of ray optics. The spherical particle is of higher refractive index than the surrounding medium. The laser is shown propagating upwards from below. (a) In the equilibrium position, the particle sits slightly ahead of the laser focus, where the scattering and axial restoring forces balance. (b) If the particle is laterally displaced, the laser beam is refracted in the direction of the displacement. Momentum conservation demands that the particle feel a force in the direction opposite to the displacement, which pushes it back towards the axis of the beam. (c) If the particle is displaced along the axis, the beam becomes more tightly / loosely focused depending on the displacement. In the figure, an upward displacement is shown, which causes the transmitted beam to become more focused. This indicates a larger beam momentum in the forward direction, resulting in a force on the particle in the downward direction, which pushes it back towards the equilibrium position.

The deviation of the beam, and therefore the restoring force on the particle, increases with the displacement of the particle.

Thus, the focused laser beam produces a restoring force on the particle in all three spatial directions, that is, at least over a small regime, a monotonic function of the displacement of the particle. For small displacements, we may assume that this force is linear and therefore model the gradient force as a harmonic restoring force.

5.1.2 Theory of optical tweezers in the Rayleigh regime

Where the Rayleigh approximation can be made (i.e. particle size a much smaller than wavelength of light λ), closed-form expressions may be obtained for the scattering and gradient forces on a particle.

The magnitude of scattering force is given by [Harada & Asakura, 1996; Ashkin

et al., 1986]

$$F_{\text{scat}}(\boldsymbol{r}) = \frac{128\pi^5 n_f^5}{3\mathfrak{c}\lambda_0^4} a^6 \left[\frac{\mu^2 - 1}{\mu^2 + 2}\right]^2 I(\boldsymbol{r}), \tag{5.1}$$

and its direction is along the propagation of the laser beam. The gradient force is given by [Harada & Asakura, 1996; Ashkin *et al.*, 1986]

$$F_{\text{grad}}(\boldsymbol{r}) = \frac{2\pi n_f a^3}{\mathfrak{c}} \left[\frac{\mu^2 - 1}{\mu^2 + 2}\right] \boldsymbol{\nabla} I(\boldsymbol{r}). \tag{5.2}$$

In the above expressions, λ_0 denotes the wavelength of the light in vacuum, n_f is the refractive index of the fluid (medium), $\mathfrak{c}$ is the speed of light in vacuum, and $\mu := n_p/n_f$ is the ratio of the refractive index of the particle n_p to that of the medium n_f. $I(\boldsymbol{r})$ is the intensity distribution of the laser beam. It is clear from the expressions why the gradient force is called as such.

For a free-space TEM_{00} Gaussian beam, the intensity profile $I(\boldsymbol{r})$ is given by [Paschotta]

$$I(x,\, y,\, z) = \frac{2P}{\pi w^2(z)} \mathrm{e}^{-2(x^2+y^2)/w^2(z)}, \tag{5.3}$$

where $w(z)$, the waist of the laser beam at distance z from the focus, is given by

$$w(z) = w_0 \sqrt{1 + (z/z_R)^2}, \tag{5.4}$$

where the Rayleigh length $z_R := \pi w_0^2/\lambda$, λ being the wavelength of the fluid in the medium, i.e. λ_0/n_f. The waist at the focus w_0 is determined by the focusing optics and the initial size of the beam.

5.1.3 The Lorentz-Mie regime

In the cases of experiments described in this work, the particle sizes ($1.5 \sim 4$ μm) are sufficiently close to the wavelength of light (1.0 μm in vacuum), whereby neither of the above approximations work. In that case, the forces must be calculated from the sophisticated Lorentz-Mie theory. Computational toolboxes are available to predict the forces on particles in this regime. See Mo [2015] for details.

Nevertheless, the expressions from the Rayleigh regime may be used to get a rough intuitive sense of the dependence of optical trapping on various parameters.

5.1.4 Considerations for optical trapping

For a stable optical trap, firstly, the refractive index of the particle must be larger than that of the medium. Another key condition is that the gradient force must be capable of balancing the scattering force in the beam-propagation direction. High numerical aperture produces a stronger gradient force without affecting the scattering force significantly. If this is insufficient, counter-propagating beams may be used so as to cancel the scattering force and enhance the gradient force.

5.1.4.1 Numerical Aperture

The laser beam is typically focused using microscope objectives, since a very tight spot is needed. An important parameter of the focusing optics combined with the medium in which the light is being focused is the Numerical Aperture (NA), defined through $\text{NA} := n_f \sin\theta$ where n_f is the medium in which the light is being focused, and θ is the half-angle of the cone of converging light formed. The maximum possible NA of the lens is obtained when the full aperture is filled.

The trap is stronger if the NA is higher, since a high NA produces a small waist for the laser beam at the focus, resulting in sharper gradients of intensity.

5.1.4.2 Choice of wavelength

The laser wavelength must be chosen so as to prevent heating of the fluid medium or the particles, and also be available easily. The 1064 nm infrared light from an Nd:YAG laser is a suitable choice, although it produces a very small amount of heating in water. If even this heating is a problem, heavy water can be substituted instead. 532 nm from a frequency-doubled Nd:YAG laser is a second possible choice.

5.1.4.3 Counter-propagating beams

In some cases, especially for large particles or particles with high refractive index (relative to the medium), the scattering force becomes stronger than the gradient force in the axial direction. Typically, the axial direction possesses the slowest variation of intensity and therefore the weakest gradient force. In such cases, the particle may still be trapped by introducing another laser beam traveling in the opposite direction, so that the scattering force is diminished and the gradient force is bolstered. The

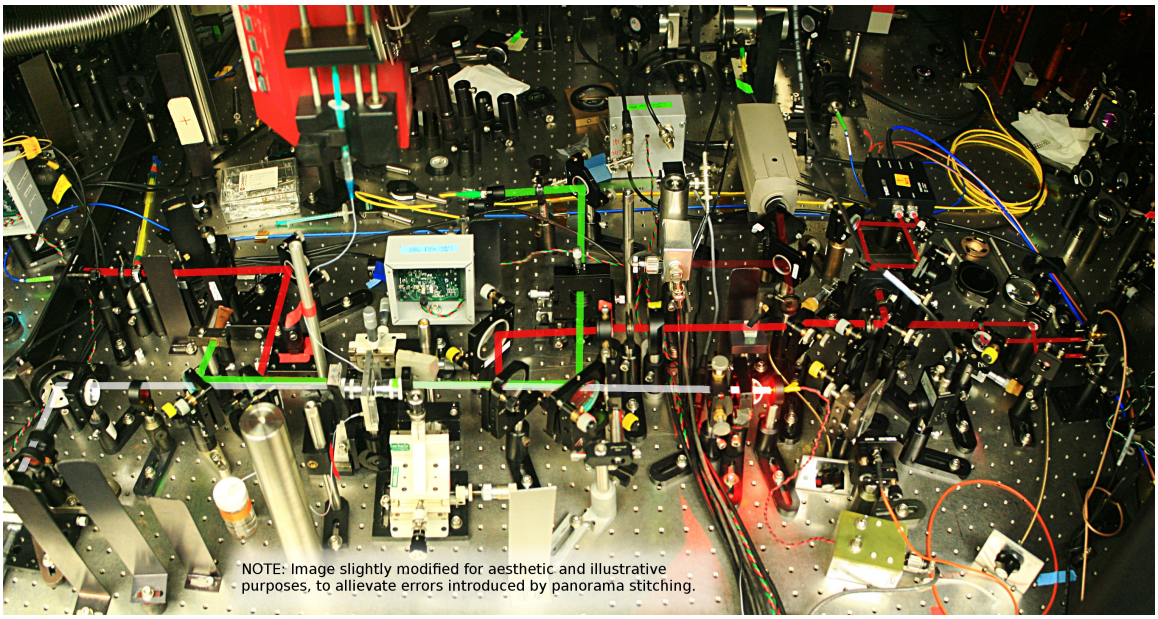

Figure 5.2: Picture of the optical setup used for the measurement of Brownian motion in liquids in the Raizen Lab at the University of Texas at Austin. The paths of a 1064nm laser beam, a 532nm laser beam, and visible light illumination are depicted in red, green and white respectively.

path of the counter-propagating beam will need to be different, and hence it must be separated from the main beam in either wavelength or polarization, so that the optics can direct them differently. Some care must be taken to align the axes and foci of the two beams so that they overlap – if not, there would be multiple stable trapping positions, but this does not pose a significant problem since the local potential is still approximately harmonic.

If back-focal-plane detection is to be done, generally, one of the trapping locations will provide better signal than the others. The power of the laser beams can be slowly altered to shuffle the particle between the traps till it is in the location that is desired.

5.1.5 The setup used in our experiments

The optical tweezers setup used in the Raizen lab to measure Brownian motion primarily used a 1064 nm Nd:YAG laser system (Innolight, Mephisto) with a maximum power output of 1.2 W. The laser was coupled into a single-mode optical fiber, and after passing through some beam-resizing optics, introduced into a water-immersion

microscope objective (LOMO, OM-25) (henceforth referred to as OBJ1) with an NA of 1.23, focal length of 2.5mm and working distance of 140 μm. The objectives focus the light into the flow cell chamber filled with liquid (usually water or acetone), where the particle is trapped. The transmitted laser beam is collected by an identical microscope objective (LOMO, OM-25) (henceforth referred to as OBJ2), re-collimated, and then used as the detection beam (see Section 5.3).

When trapping particles with higher refractive index (especially particles made of Barium Titanate glass), a counter-propagating 532nm laser beam (Coherent, Verdi V-10) was used. This laser was coupled into a single-mode optical fiber, and after passing through some beam-resizing optics, introduced into OBJ2, where it was focused down into the flow cell chamber. The transmitted 532nm light was collected by OBJ1 and the majority of it was sent to a beam dump, a small amount optionally sent to the imaging camera for alignment purposes.

These beam paths are shown, along with the remainder of the optical setup, in the schematic of figure 5.3. The red, green and blue lines indicate the paths taken by 1064nm, 532nm lasers, and visible light illumination respectively. The following abbreviations are used – DM: Dichroic Mirror, CCD: Charge-Coupled Device, HWP: Half-Wave Plate, OBJ: Objective, PBS: Polarizing Beam Splitter, PD: Photo-Diode, CM: Cut Mirror, BS: Beam Splitter, LED: Light-Emitting Diode.

5.2 Flow cell

The primary constraint on the experimental chamber comes from the working distance of the objectives. Our objectives had a working distance of about 140 μm (in practice, it was slightly different because of the use of an infrared laser as opposed to visible light), meaning that the chamber was constrained to be less than about 280 μm thick. Producing a chamber this thin has its obvious difficulties. In addition, one must be able to flow in liquid and micro-spheres into the chamber.

The methods of building optical tweezers for biophysics have been developed in detail and outlined by the Bustamante group and are available on a website called TweezersLAB [Steve Smith *et al.*]. We closely followed their procedures for the construction of our experimental chambers, which we also refer to as "flow cells" in this work, but with some differences. We primarily focus on the differences here. The

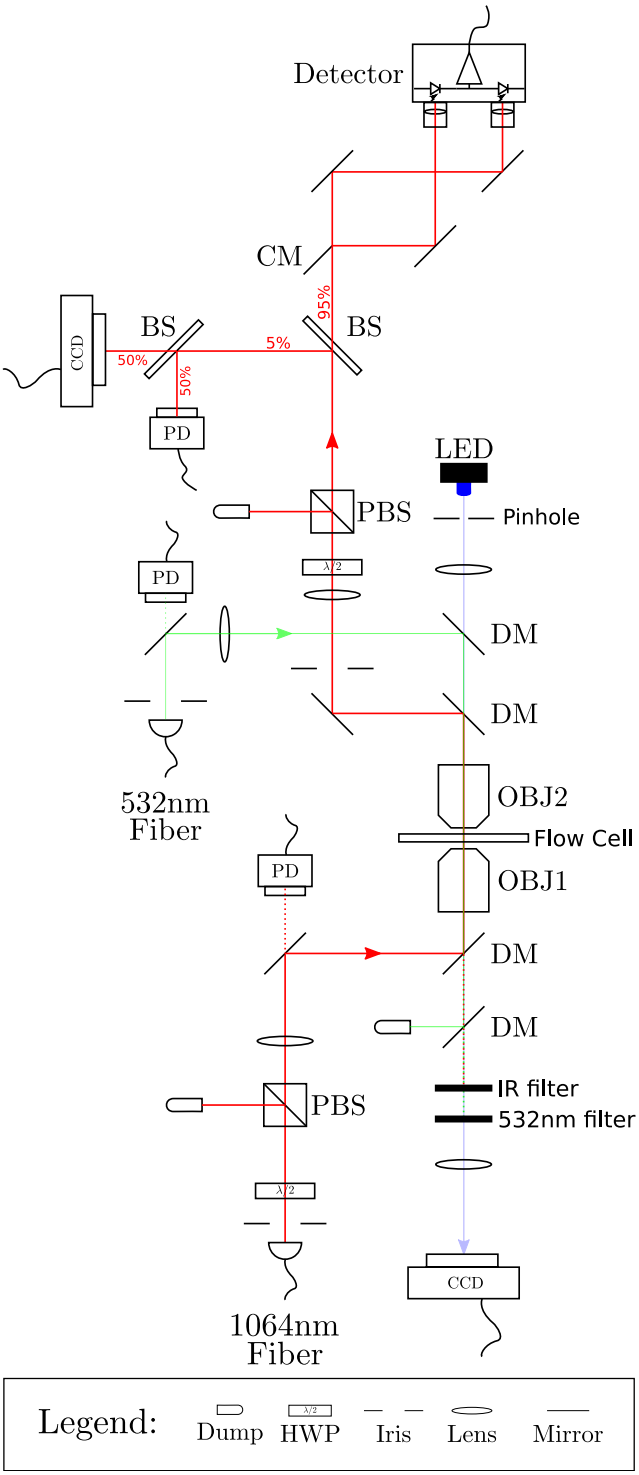

Figure 5.3: Schematic of optical setup used. See §5.1.5 for details.

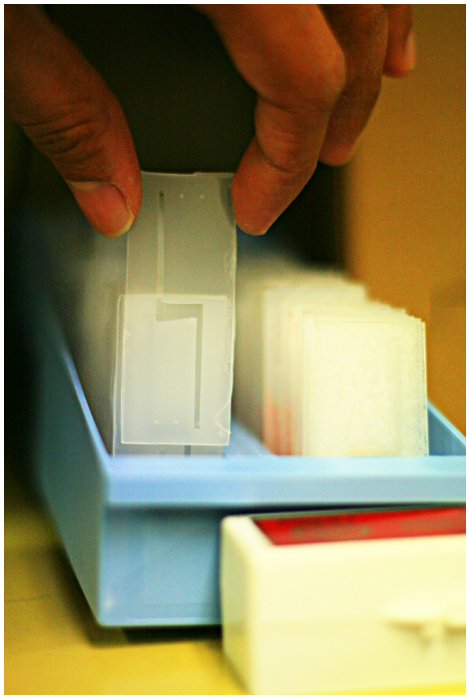

Figure 5.4: A finished flow cell used for trapping Barium Titanate glass particles in liquids. The Z-shape of the channel is required to trap the dense Barium Titanate glass spheres (§6.3).

remaining details are largely identical to the description on TweezersLAB, under the headers "Fluidics Set" and "Micro-chamber". Specifically, our flow cell is made of #0 cover-slips, does not have a micro-pipette, and has a single channel with a single inlet and a single outlet. Commercially available syringe pumps were used to drive the syringe, instead of a pinch valve. The holes in the #0 cover-slips were drilled using a CNC mill as opposed to being laser etched, and a single layer of nescofilm hand-cut on a template was used. The details are described in the subsequent paragraphs.

The flow cells are primarily constructed by sandwiching a film of sealing plastic in between thin, flat pieces of glass. Channels are cut in the sealing plastic to provide a way to introduce the particles and liquid and perform the experiment. Holes drilled in one of the glass pieces allows for introducing liquid and particles into the chamber. Figure 5.4 shows a finished flow cell.

For the glass, we used cover glass slips with a thickness of $80 \sim 130$ μm (Ted Pella, Gold Seal #0) and a size of 24×60 mm. Typically, #1 cover-glasses are used, which are easier to work with because they have a higher thickness. However, the objectives

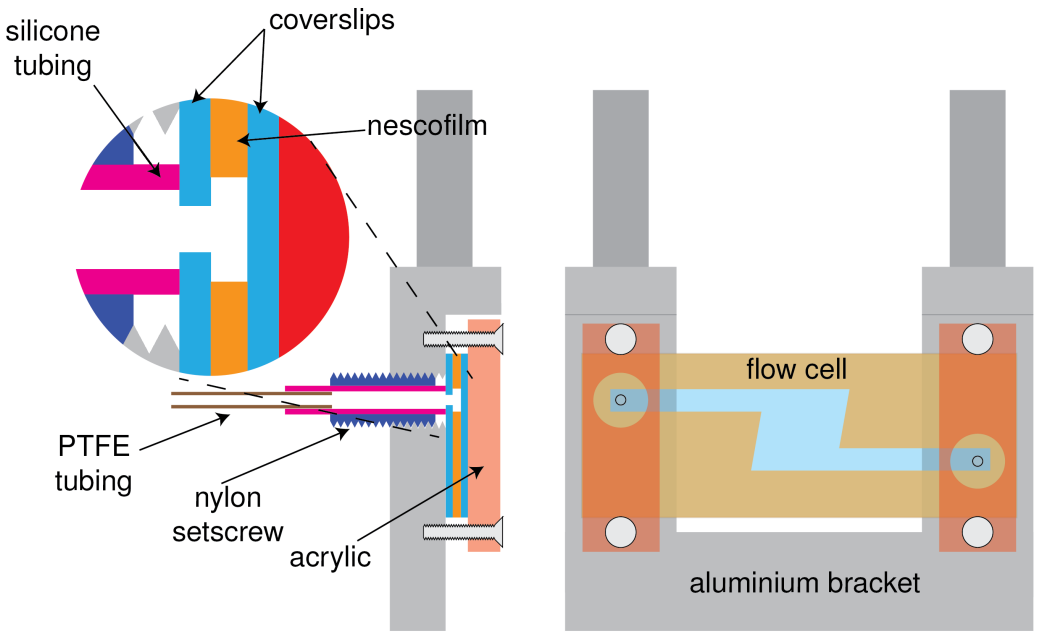

Figure 5.5: Schematic showing the flow cell and the mounting setup. The setup is largely based on TweezersLAB [Steve Smith *et al.*]. The acrylic pieces that hold down the flow cell are transparent in order to check the seal made by the silicone (or rubber) tubing on the glass. The "Z"-shape of the chamber cut out in the flow cell is designed to trap the dense Barium Titanate glass micro-spheres (§6.3). Figure courtesy of Dr. Simon Kheifets.

we used have a much shorter working distance, and therefore using #0 cover-glasses was necessary.

Two of the heat-sealing plastic films suitable for the purpose of making the chamber are Parafilm M (Bemis) which has a mean thickness of about 125 μm, and Nescofilm[1] (Bando Chemical Ind. Ltd.) which has a mean thickness of about 80 μm. Both films are resistant to water. Parafilm has poor resistance to acetone, but generally produces a stronger seal. Nescofilm has reasonable resistance to acetone, but the seal is generally weaker. Nescofilm was however generally preferred since it produced a thinner cell.

[1]Nescofilm seems to be unavailable from distributors in the United States as of this writing.

5.2.1 Drilling the cover-slips

#0 cover-slips are very thin, and this makes drilling holes in them for the plumbing extremely challenging. It was observed that attempting to hand-drill them would often cause it to shatter in spokes around the point of drill contact, and these were sufficient to cause leakage.

A novel method was found by the machinists in our department machine shop. A jig was constructed to hold stacks of cover-slips that were held flat and together by wax, and a diamond burr bit was run through them using a CNC mill. The drilled cover-slips were stuck together in stacks, which were separated by ultrasonication in a solution of distilled water and Micro-90 Cleaning Solution (Cole-Parmer). The cover-slips were then carefully pulled apart and placed in a clean slide file.

5.2.2 Making the flow cells

When a new flow cell is to be constructed, drilled and plain cover-slips are cleaned by ultrasonication in a solution of HPLC-grade water and Micro-90 (Cole-Parmer), and then rinsed several times with HPLC-grade water. They are further cleaned using acetone and lens-cleaning tissue just before use. A sharp, clean razor blade is used to cut the sealing film (Nescofilm / Parafilm) on a clean template slide into shape to make the channels for fluid flow. The sealing film cut out is carefully placed over a clean drilled cover-slip with the channels aligned up with the holes. A clean cover-slip without holes is placed on top. The sandwich is placed between clean optical tissue and gently pressed with a slide to help form a temporary seal. The temporary seal is made permanent by baking on a hot plate. Nescofilm generally requires a longer duration of heat than Parafilm. After cool down, the excess Nescofilm is carefully trimmed off using a razor blade. The flow cell thus created is still extremely fragile and must be handled with care.

The finished flow cell is placed in the flow cell holder, clamped down gently using acrylic clamps, and the plumbing connections are made. When using acetone, cut-outs of a glass slide were used to protect the acrylic from any acetone that may have leaked.

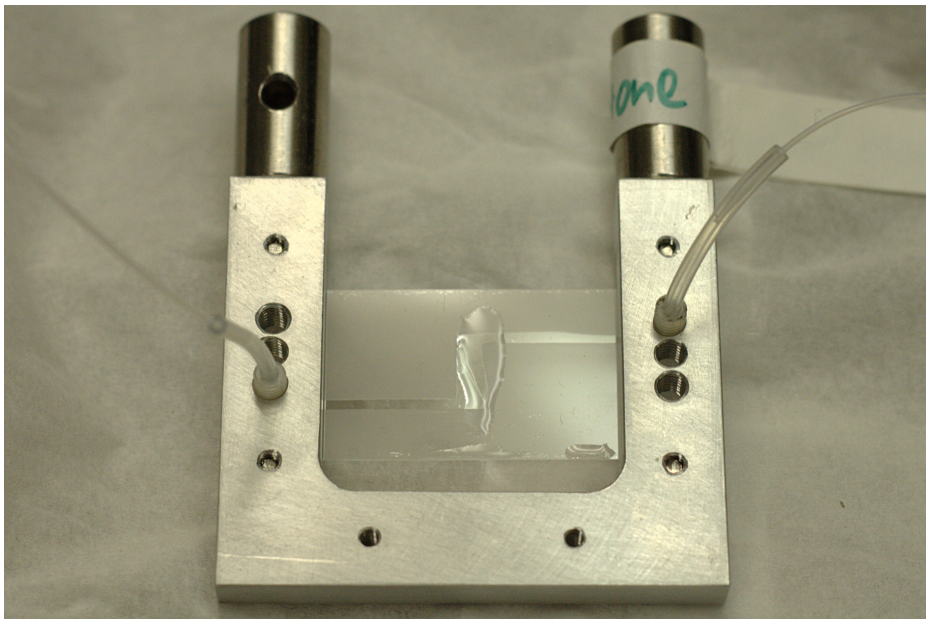

Figure 5.6: A flow cell mounted in a flow cell mount, with plumbing connections. The liquid on the center of the cell is synthetic microscope immersion oil with the same refractive index as water.

5.2.3 Flow system

We followed TweezersLAB very closely for the flow system connections, except that we had only one inlet and one outlet. A syringe pump was used to pump the liquid (with our without particles) into the chamber at a uniform rate. This prevented accidental breakage of the flow cell by application of excess pressure. While using acetone, the Cole Parmer C-Flex silicone tubing, which is not acetone resistant, was replaced by EPDM rubber tubing (McMaster Carr, 9776T14). The nylon set screws were drilled with a correspondingly smaller drill bit on the lathe.

A mounted flow cell with the plumbing connections is shown in 5.6.

5.3 Detection system

Typically with optical tweezers, the trapping beam that has passed through the particle under study is re-collimated and used as a detection beam. It is well-known that very small changes in the position of the particle (smaller than nanometers) may be measured by *back-focal-plane detection*, where the beam is incident on a quadrant

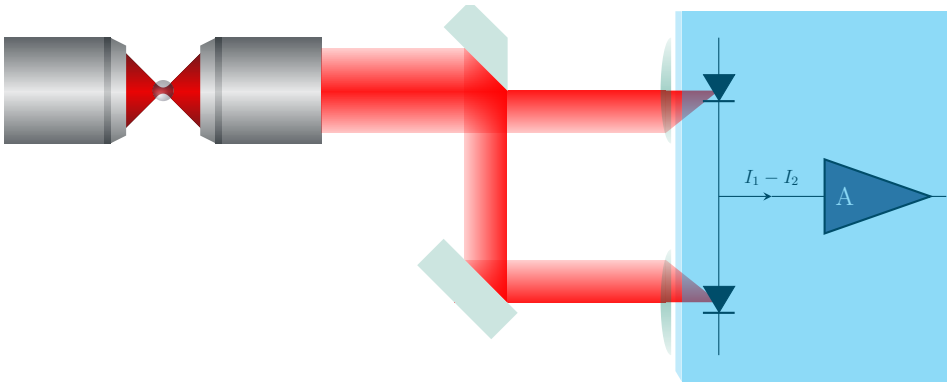

Figure 5.7: Simplified schematic of split-beam detection system used to measure the position of the Brownian particle by tracking the transmitted laser beam. The transmitted beam is incident on a D-shaped mirror, where 50% is reflected and 50% transmitted. The two halves of the beam are focused on two photo-diodes and the difference of the current is amplified by a trans-impedance amplifier.

photo-diode, and the difference in intensities between the left quadrants and the right quadrants is used as a measure of the horizontal deflection of the beam and therefore of the particle.

The problem with detection using quadrant photo-diodes is that they have large surface area and therefore high capacitance. This implies that they will not provide a sufficiently large bandwidth for the detection of short time-scale motion of the particle. A novel detection scheme using a optic fiber bundle[2] has been proposed and used successfully by Chavez *et al.* [2008]. A simpler alternative, first used by Li *et al.* [2010] and subsequently used in our setup, involves a D-shaped cut mirror (Thorlabs, BBD05-E03) that is aligned so as to split the detection beam in half, such that the intensity that is reflected and the intensity that is transmitted are equal at the equilibrium position of the particle. The cut mirror is shown in figure 5.8. The reflected and the transmitted beams are incident on a balanced detector, consisting of two identical photo-diodes which are wired to a trans-impedance amplifier in a differential configuration. Any displacement of the particle produces imbalances the reflected and transmitted power, and this change is detected by the balanced detector. The amplified differential signal is digitized by a data acquisition card and recorded in digital form on a computer.

A schematic illustrating the split-beam detection system is shown in figure 5.7. For details pertaining to alignment of the mirror, see Section 5.7.

[2]Not to be confused with the similar term in differential geometry!

Figure 5.8: A D-shaped cut mirror (Thorlabs, BBD05-E03) is used to split the beam into equal halves at the equilibrium position of the particle. The mirror is mounted on a translation stage as it needs to be frequently aligned (§5.7).

As we shall describe in Section 5.5, the Signal to Noise Ratio (SNR) of detection at high frequencies is proportional to the square root of the detected power. As a result, the balanced detector must be able to handle a high power. Commercial balanced detectors such as Thorlabs models PDB-120C and PDB-110C have a very low rating of $\sim$ 5 mW per photo-diode. These were used in contexts where the noise floor was not of prime concern (such as low-frequencies, where the signal is many orders of magnitude larger than the noise with 10 mW detected power). To provide better SNR, especially for short-time measurements, a balanced detector was designed and built in-house (figure 5.9) by Kheifets [2014]. The detector was built using InGaAs photo-diodes with thermal dissipation capability of 100 mW (Excelitas, C30641). The differential current from the two photo-diodes was amplified using an op-amp (Texas Instruments, OPA 847) in a trans-impedance configuration with high-pass and low-pass filters with 3 dB points at about 600 Hz and about 60 MHz. The low-pass filtration, achieved by a small feedback capacitance, is necessary to stabilize

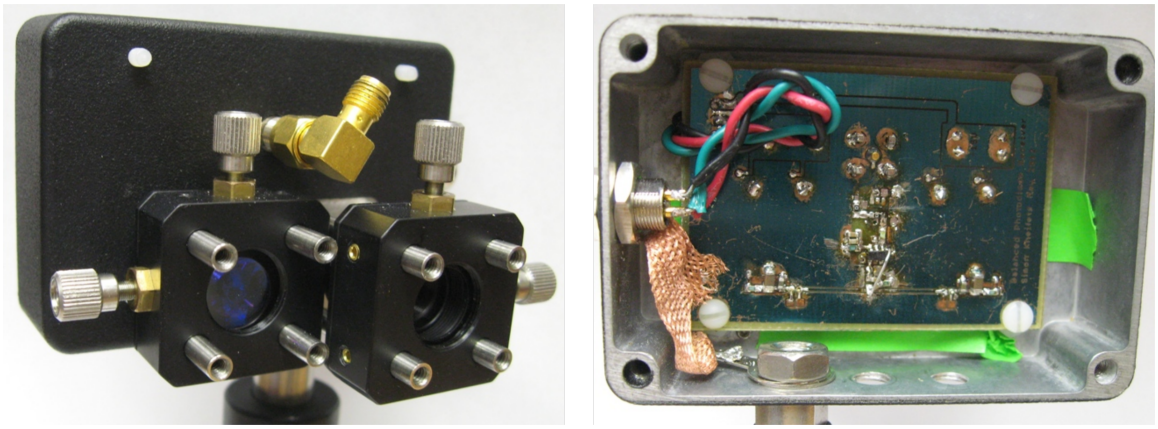

Figure 5.9: Picture of a high-bandwidth balanced detector, capable of accepting 100 mW of laser power per photo-diode, built in-house by Kheifets [2014]. InGaAs photo-diodes are wired in series and the differential current is AC-coupled into a trans-impedance amplifier. Picture courtesy of Dr. Simon Kheifets.

the amplifier with a capacitive load at the input. The op-amp OPA 847 is designed for a high gain-bandwidth product at the cost of other features, whereby the high-pass filter is necessary to prevent saturation of the op-amp from the strong signal at low-frequencies. The detector's response was measured as described in Section 5.8 and accounted for in data analysis. A DC-coupled detector, Thorlabs PDB-110C, was also setup in parallel to "fill in" the low-frequency data (not shown in figure 5.3, but seen in figure 5.2). The output of the detectors was fed into two channels of a high-quality data acquisition card, which we shall discuss in Section 5.4.

5.4 Data acquisition system and Experiment control

5.4.1 Acquisition of Brownian motion data

The primary requirements on a digitizer (analog to digital converter) to measure short time-scale aspects of Brownian motion are high channel bandwidth, high sample-rate, and low quantization noise. The channel bandwidth and sample rate of the digitizer must not be a limiting factor in the ability to measure short time-scale fluctuations. The bandwidth must be larger than the usable bandwidth of the detection system

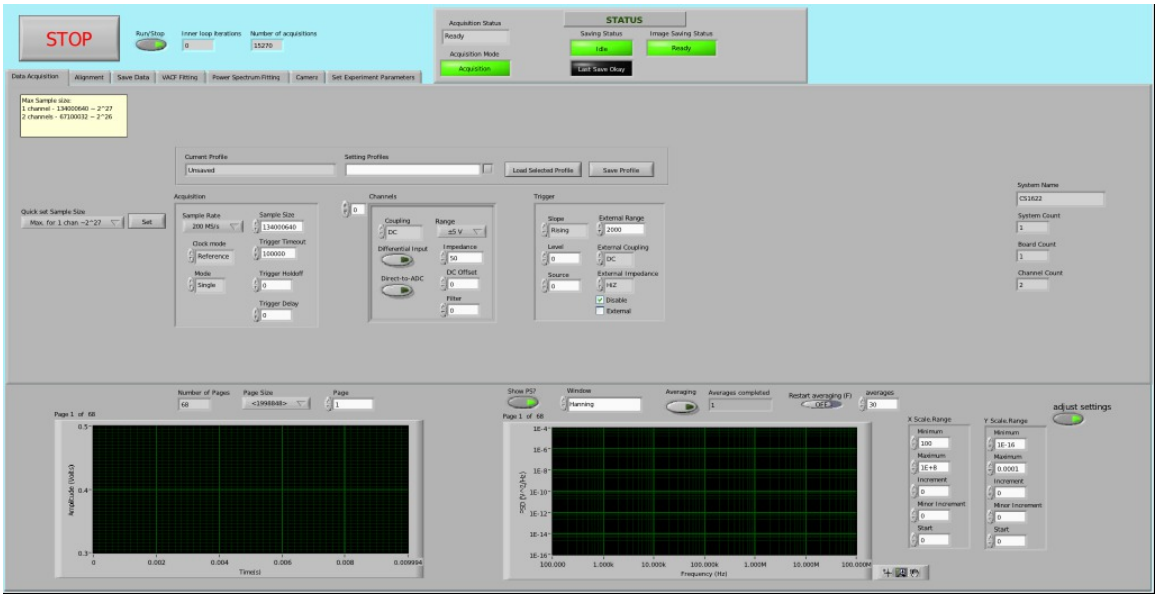

Figure 5.10: Main LabVIEW interface for data acquisition, alignment of cut mirror, and remote control of experimental parameters. The wave-form and power spectrum of a small segment of each acquisition is visualized at the bottom of the interface, and forms a very helpful tool to detect anomalies.

(see §5.5 and Chapter 6) including the bandwidth of the balanced detector, and the sample rate must be larger than twice this bandwidth (by the Nyquist-Shannon criterion), preferably even higher to prevent noise from being aliased back into the pass-band. The quantization noise must not limit measurement (see § 5.5).

These requirements were met by the digitizer used in our setup (GaGe, Razor 1622 Express CompuScope), which has a 16-bit quantizer, a 200 MSa/s sample rate, a channel bandwidth of 125 MHz, and an on-board memory for 128 MSa (64 MSa in 2-channel operation).

A full dump of data from our digitizer would amount to about 0.25 GB of data (128 MSa $\times$ 2 bytes per sample), and even more if the data is written as floating-point scaled voltage values. Given the large size of the data, a binary data file format was designed specifically for the experimental data, so as to facilitate fast writing and reading without the overhead of conversion into ASCII strings. The binary file format also contains metadata about the experiment, the nature of the acquisition (bead present vs. absent), the values of various experimental parameters, the readouts from various sensors (such as photo-diodes measuring the laser power)

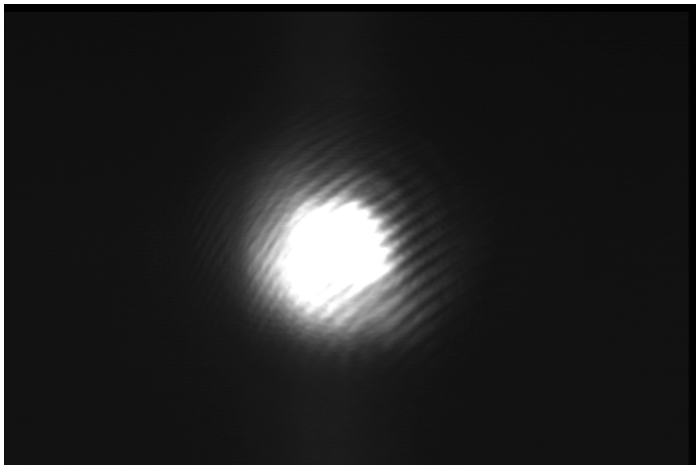

Figure 5.11: Example detection beam profile image recorded by the CCD camera monitoring the beam, digitized through the USB video capture card and saved by the LabVIEW program.

and the configuration of the digitizer. The binary file format also contains checks to identify data corruption.

The digitizer provided a LabVIEW VI interface, which was integrated in a larger LabVIEW application to allow configuration of the acquisition, and transfer of the data from digitizer memory to binary file. Given the large number of samples to be transferred, the transfer was done by copying the memory one 'page' at a time.

Speeding up of the data acquisition, transfer, and writing to disk was important, as it was sometimes difficult to trap a particle without contamination for a long time. This process was profiled using LabVIEW's profiling features and optimized to bring down the time taken. Speeds of writing to the disk were improved by using a solid-state drive.

5.4.2 Experiment control and acquisition of other experimental parameters

To isolate any problems, the control of parts of the apparatus, as well as the acquisition of experimental parameters and optical images of the chamber was done by a different computer (referred to as the auxiliary computer). The main computer that ran the acquisition software communicated changes and read values from the auxiliary computer over the network. LabVIEW's Network Shared Variable was used to

achieve this communication. A spin-lock was implemented to make the asynchronous operations that are typical of LabVIEW synchronous.

Experimental parameters such as laser intensities were controlled from constant voltage signals generated from an analog output board (National Instruments, PXI-6713), controlled by LabVIEW. The power of the main trapping and detection laser was controlled using a half-wave plate mounted on a rotary mount (Newport, Pico-motor) followed by a Polarizing Beam Splitter (PBS) cube. This laser was left in open-loop as the laser itself was sufficiently stable, and any closed-loop system would increase the noise floor (see §5.5). The power of the counter-propagating laser beam (whenever applicable) was maintained by a closed-loop PID system with the beam power monitored by a photo-diode, and feedback applied through an acousto-optic deflector.

Auxiliary measurements from various sensors, such as estimated power at the balanced detector and estimated powers of the lasers at fiber outputs were acquired using a data acquisition card (National Instruments, PCI-6133) and read in through LabVIEW software.

A USB CCD camera (Mightex Systems) was used to record an optical image of the chamber (see §5.6). An analog-output video camera was used to monitor the detection laser beam profile, and the signal was then digitized using a USB video capture card (EasyCap). Both of these images were acquired by the auxiliary computer, and transferred asynchronously to the main computer with a delay of the order of seconds. The images were time-stamped for clarity. The asynchronous capture of chamber and beam profile images ensured that the main acquisition process was not slowed down by waiting for images.

5.5 Sources of noise

There are several sources of noise that hinder the measurement of Brownian motion of the particle:

1. **Mechanical noise**: This originates from the mechanical vibrations of the building[3] and the ground on which the experiment is being performed. It could

[3]We found that a 240 Hz power-line harmonic hum was audible upon putting ones ears to any wall in the building, presumably from pump machinery. Our musical training proved useful in

couple to the measurement through the vibration of optics, or the vibration of the particle itself. To mitigate this, the optical table on which the experiment is setup is floated over a blanket of air.

2. **Power line harmonics**: The power-line noise at 60 Hz and its harmonics can couple easily into electronics, despite filtering. To suppress this noise, the power lines in the balanced detector had bypass capacitors placed at all recommended locations.

3. **Acoustic noise**: It was observed that the sound, even from the experimenters talking, was picked up by the experimental setup. Our hypothesis is that this sound coupled to the measurement through changes in the refractive index of the air through which the laser beams were traveling (akin to synthetic Schlieren imaging of fluids). It was mitigated by attempting to keep a quiet environment while acquiring data, and keeping the laser curtains closed.

4. **Electronic noise in the balanced detector and digitizer**: The electronic noise of the detector and digitizer was sufficiently low so as to be unimportant. The detector was designed with low-noise as a goal.

5. **Quantization noise**: This arises from the round-off error in converting the analog signal to digital. The high resolution (16-bits) of the digitizer made this irrelevant.

6. **Laser intensity noise (classical)**: Classical noise in the laser may arise from the internal electronics of the laser. Most lasers feature a closed-loop system to suppress this noise. However, any such system converts some of the shot noise from the part of the beam used for sensing (which is relatively higher corresponding to the low detected power) into classical noise which it feeds back into the laser system. Thus, while such a closed-loop system might suppress any noise peaks, it will raise the noise-floor, at least over the bandwidth of the detector. This has been observed with the "noise eater" that came on the Innolight Mephisto laser, and is theoretically impossible to beat unless the sensed power is high enough. To mitigate classical laser noise, we upgraded

determining the frequency of the hum!

from a noisy laser to a laser that was sufficiently free from classical noise even when any closed-loop noise suppressors were turned off.

7. **Laser pointing noise**: Laser pointing noise can cause the beam to move around mimicking a signal. Fiber coupling reduces the pointing noise by converting it into intensity noise. If the laser intensity were maintained in closed-loop, this could be servo-ed out, but for the reasons mentioned earlier, this may not be a good idea. This is probably one of the smaller contributors to low-frequency noise in our system.

8. **Laser shot noise**: This is the most important kind of noise in the system, and was the limiting factor in our measurement. Shot noise is inherent quantum noise present in the laser beam, and grows proportional to the square root of the power of the laser beam. Therefore, relative to the signal, which is proportional to the power of the beam, we have SNR $\sim \sqrt{\text{Power}}$. Almost all the other types of noise mentioned above (except possibly for classical intensity noise in the laser) are dominant only at low frequencies. At high-frequencies, shot noise is usually the limiting factor as it is white noise.

The measured power spectrum of noise in our system is depicted (along with signal from two micro-sphere-in-liquid systems) in figure 5.12. The red triangles represent the noise.

Looking at the position power spectrum of Brownian motion, it is easy to see that it is roughly flat at low frequencies, and decays like $1/\omega^4$ in the EOU theory and like $1/\omega^{3.5}$ in the hydrodynamic theory. So the low-frequency components are strong, whereas the high-frequency components are weak. With appropriate measures to suppress low-frequency noise, the SNR at low and intermediate frequencies can be improved. However, eventually, either the detection system bandwidth or the laser shot noise floor will determine the SNR at short time-scales. In our system, the detection bandwidth was not the limiting factor – shot noise was.

5.6 Imaging system

In order to trap particles and study their motion, being able to see the particle and the chamber is extremely important. To this effect, optical imaging needs to be set

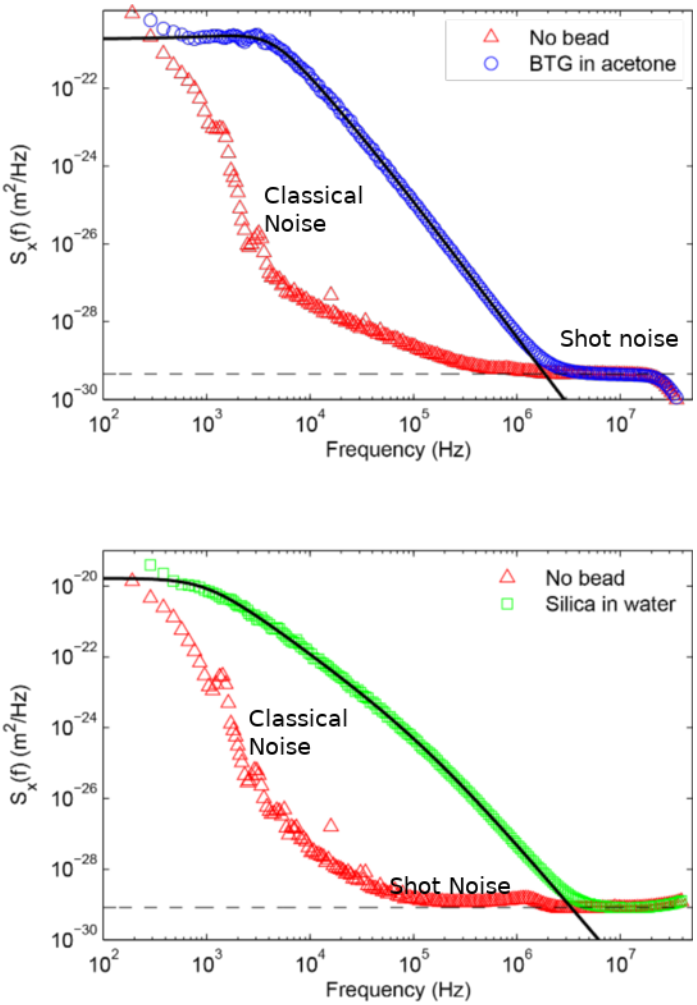

Figure 5.12: Measured power spectral density of Brownian motion of particles, and of noise in the detection system. The noise measurements, represented by red triangles, were obtained by the same system but without a particle present in the optical trap. Classical sources of noise are dominant at low frequencies, whereas shot noise dominates the high frequencies. The weak peak seen in the noise in the lower plot at about 1 MHz corresponds to noise from the Nd:YAG laser pump. The blue circles and green circles represent the PSD of position of a BTG micro-sphere in acetone, and of a silica micro-sphere in water respectively. Figure from Kheifets *et al.* [2014, Supplementary Material], annotated to show the types of noise.

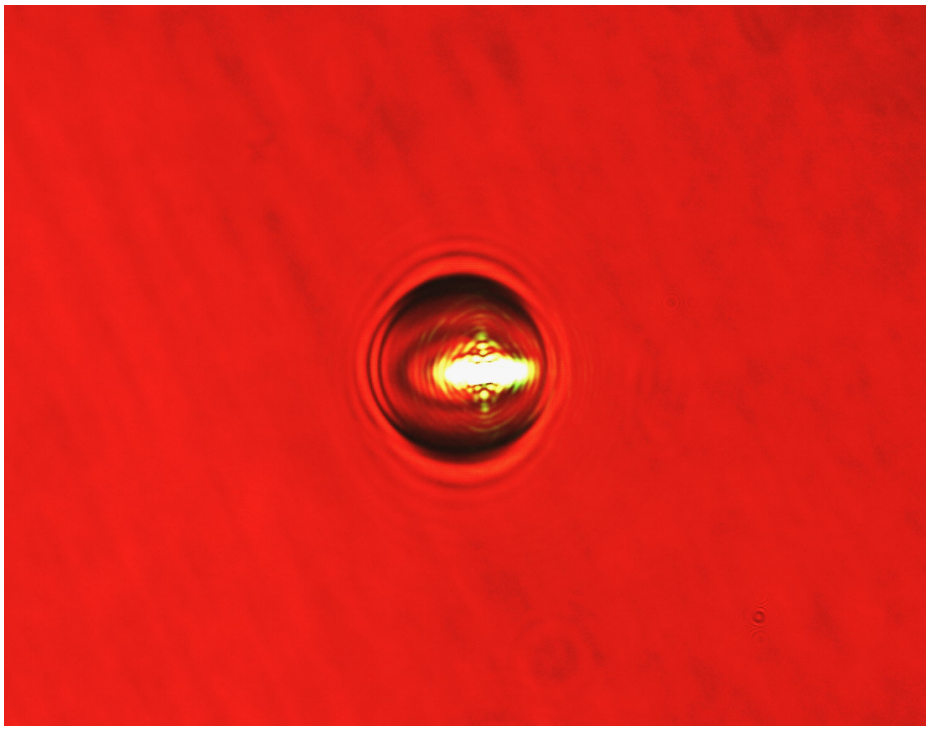

Figure 5.13: Image of a Barium Titanate glass micro-sphere trapped in the experimental chamber. The red color of the image is a result of using red illumination. The green light is leakage of the 532nm counter-propagating beam through the dichroic mirror reaching the camera in the absence of a strong 532nm filter.

up in the tweezers system. It is possible to use the same objectives to set up Köhler illumination, where the rays from a light source are collimated by a condenser lens to uniformly illuminate the object under study, while simultaneously avoiding the structure of the light source (i.e. filament of an incandescent lamp, or patterning of an LED) from being imaged on the camera. The idea is that the illumination beam be collimated at the conjugate focal planes of the object under study.

In our setup, light from a red LED source of adjustable brightness was focused by a lens roughly at the back-focal plane of OBJ2. Red light was chosen because the LED was easily available, and because the dichroic mirrors designed to reflect the 532nm laser would transmit it. OBJ2 played the role of the condenser lens. The image of the chamber, formed through OBJ1, was focused using an appropriate lens on a CCD camera (Mightex Systems). Figure 5.13 shows an image of a trapped micro-sphere in the chamber.

5.7 Methods of alignment

The D-shaped mirror is mounted on a translation stage so as to be able to adjust it to balance the mean power incident on the two photo-diodes in the balanced detector. If the detector is DC-coupled, one could simply null the difference between the mean read-out of the two photo-diodes. However, with the AC-coupled detector, one cannot do this.

To align the D-shaped mirror in the case of an AC-coupled detector, we introduce a common-mode signal at a sufficiently high-frequency into the laser and minimize the strength of the signal. When the balanced detector is balanced, it should be sensitive only to the differential-mode. This method of alignment can be performed even when a particle is present in the trap. The common-mode signal should preferably be a pure sinusoid so that the amplitude at that frequency can be selectively read out to determine the strength of the signal.

We introduced a sinusoidal signal of about $1 \sim 2$ MHz frequency into the laser using an electro-optic modulator. The electro-optic modulator was directly connected to a function generator without an amplifier, as the electronic noise of the amplifier was observed to couple into the laser beam. The frequency was chosen so that it lay in a region where the signal due to Brownian motion itself was sufficiently small, and the modulator's response was sufficiently strong (the modulator had a bandwidth of the order of a few hundred kilohertz). This way, the signal would tower over the Brownian motion of the particle allowing the alignment to be done when a particle was in the trap. The function generator that produced the output was automatically gated from the LabVIEW program to turn the signal on/off whenever the alignment tab in the software was opened/closed, in order to prevent accidentally acquiring data with the signal turned on. The measured signal from the digitizer was then processed to extract the strength of the specific frequency component. The operator of the experiment could then move the cut mirror to minimize this signal and easily balance the detector. The signal was never completely eliminated because vibrational noise could move the optics involved and let some of the common-mode noise through. However the signal could be suppressed by many orders of magnitude when properly balanced.

5.8 Measurement of detector response

The detection system's response significantly colors the measurement. Assuming that the detection system is Linear and Time-Invariant (LTI),[4] we may characterize it by its response $h(t)$ to a unit impulse, or more conveniently by the Fourier transform $H(\omega)$ of $h(t)$. $H(\omega)$, called the *transfer function* in engineering terminology, characterizes the complex (amplitude and phase) response of the system to a pure sinusoid of a given frequency[5] ω.

If the transfer function of an LTI system is known, then the Fourier transform of its input, which we will denote by $X(\omega)$, and the Fourier transform of its output $Y(\omega)$ are related by

$$Y(\omega) = X(\omega)H(\omega). \tag{5.5}$$

We may treat $Y(\omega)$ as the output of the detection system with transfer function $H(\omega)$, when it is tasked with measuring the actual signal $X(\omega)$. Therefore, we may recover an estimate of the actual signal incident on the detection system by simply dividing the measured signal in frequency domain by the transfer function.

The transfer function of a system (or more generally, the s-parameters of a two-port network) may be measured effectively using a network analyzer. However, network analyzers are expensive, and the input to our detection system came in the form of light. Therefore, we deemed it best to build our own system for measurement of the photo-detectors' transfer functions.

We used a fast transmitter (Avago Technologies, HFBR-1119TZ) designed for fiber optic communications, with a rise / fall time of $\sim$ 2.2 ns (leading to a bandwidth of $>$ 150 MHz) to produce a rapidly flashing infrared light. The transmitter is an integrated package with a driver designed to accept a differential digital logic signal, so that we may be assured that the intensity of the flashes is uniform over frequencies $<$ 150 MHz owing to the digital nature. The transmitter was driven ultimately from the output of a function generator, which was scanned over frequencies. The function generator we used at low frequencies had a floating ground, whereby we did not need special means to convert its single-ended output to differential. For

[4]By time-invariant, we mean that the response of the pattern of response of the detection system is unchanged under translations in time. The detector's response to a sudden impulse may however involve a rise time and a decay time.

[5]More comprehensive discussions of LTI systems may be found in standard references such as Oppenheim *et al.* [1983].

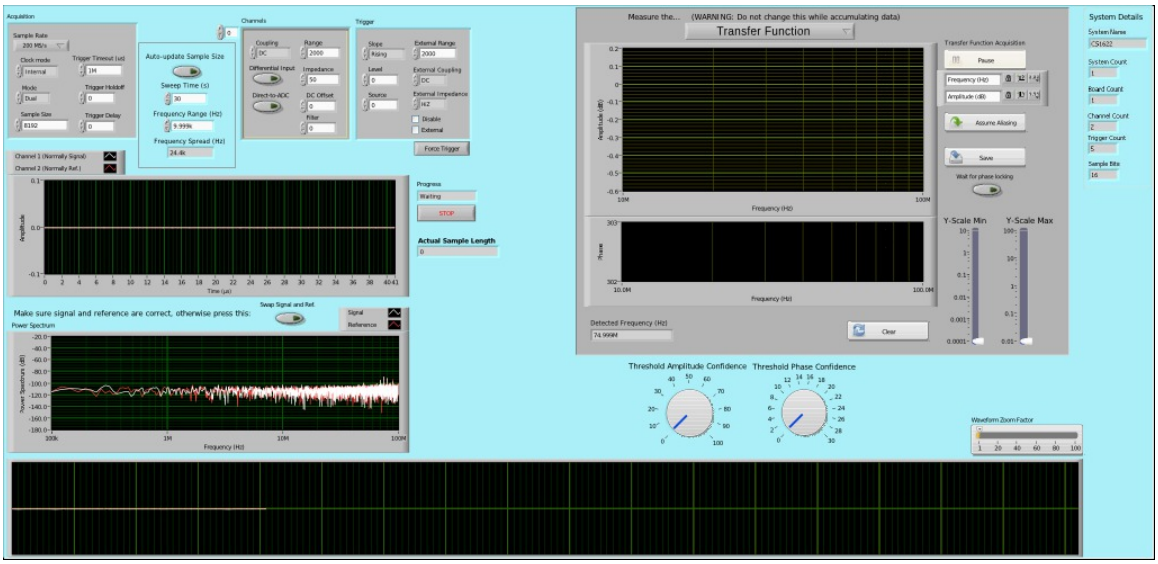

Figure 5.14: LabVIEW interface for measuring the transfer function of an electrical system. The stimulus is applied from a function generator, and the response is digitized through the data-acquisition card and processed in LabVIEW. A fast fiber-optic transmitter can be used to convert the stimulus into light for measurement of transfer functions of photo-detectors.

the high-frequency case, a 1:2 balun was used to convert the single-ended output to differential input for the transmitter (figure 5.15). The output of the transmitter was fiber-coupled using a communications patch cable and pointed in the general direction of the photo-detector whose response we wished to measure.

The output of the photo-detector was fed into the digitizer and analyzed in LabVIEW (figure 5.14). The flashing of the LED being on/off, the response of the detector is closer to a band-passed square wave with many harmonics. The LabVIEW program identified the peak signal, and locked-in on it to measure amplitude and phase. The frequencies chosen to step through were sufficiently incommensurate with the sample rate so as to prevent any aliased harmonics from overlapping with the fundamental and affecting the measurement. Only points that passed certain confidence thresholds were recorded. The data was saved into a text file and analyzed in MATLAB. Measuring the phase response correctly requires proper triggering of the digitizer, and accounting correctly for cable delays. However, because we only need to calculate power spectra of Brownian motion, the magnitude response suffices. We ignored measurement of the phase response. A pole-zero model is fit to the

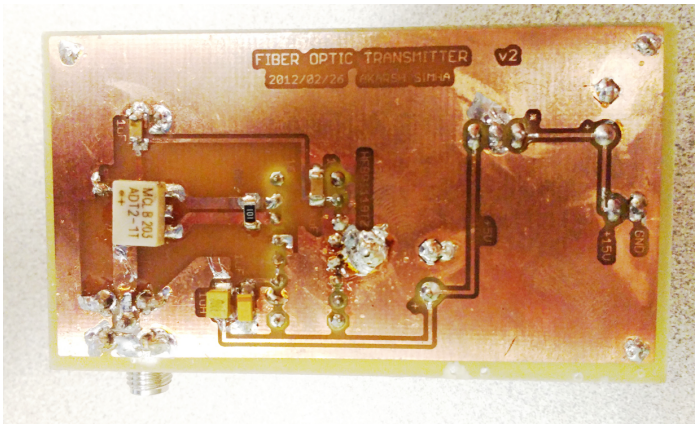

Figure 5.15: A picture of the home-built circuit used to drive the fiber-optic transmitter, in order to measure the transfer functions of photo-detectors.

transfer function magnitude data to produce an analytic interpolation. The analytic interpolation is used in data analysis.

The transfer function of the digitizer channel itself could be measured using the same program by applying the function generator's output to the digitizer directly. When the photo-detector's response alone is desired, the transfer function of the digitizer may be divided out from the measurement. However, this is not necessary in practice, since we typically want to know the entire detection + digitization system's response.

5.9 Methods of data analysis

The voltage samples read by the digitizer are assumed to be proportional to the displacement of the particle, by a proportionality constant C with the units of V/m. We shall denote the raw digital signal, after appropriate scaling to convert into a voltage, as $V[t]$. The brackets, as opposed to parentheses, reminds us that the time is discrete from the sampling, as is standard notation. Then we may write $x[t] = CV[t]$. We may differentiate the signal $V[t]$ using a discrete differentiation operator so as to get a signal proportional to the velocity.

However, high-frequency noise becomes significantly amplified upon differentiation. One way to look at this is to see that a stochastic process with a flat spectrum becomes develops a spectrum that grows like $|-\mathrm{i}\omega|^2 = \omega^2$ upon differentiation.

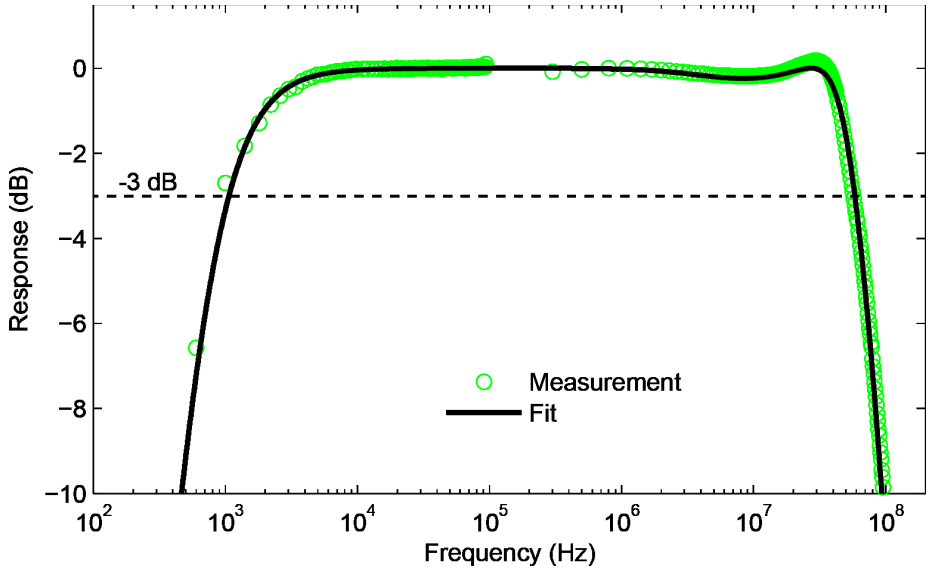

Figure 5.16: Plot of the transfer function of the detection system, consisting of the high power balanced detector built in-house as well as the data acquisition system. The measurements are indicated by green circles and the solid black line is a fit to a ratio of polynomials. Figure from Kheifets *et al.* [2014, Supplementary Material].

Therefore, heavy binning is necessary. The samples may be either binned by convolution with a sinc function (which results in a brick-wall filter in frequency domain), or a rectangular window (which results in a sinc filter in frequency domain). The difference may be combined with the sinc in frequency domain by multiplication by $-\mathrm{i}\omega$. (In fact, the forward difference operator translates in frequency domain to multiplication by a sinc multiplied by $-\mathrm{i}\omega$.)

The power spectra of position $x[t]$ and velocity $v[t]$ may be calculated up to the calibration constant by taking the absolute square of their Fast Fourier Transform (FFT) and dividing by the appropriate numerical factor. It is at this stage that division by the squared magnitude of the transfer function is incorporated. A window function such as Hamming or Hann window may be used before performing the FFT. This may be written explicitly as

$$\begin{aligned} X[k] &:= \mathrm{fft}(\, x[t]\, w[t]\,), \\ \mathrm{PSD}[k] &= \frac{\Delta t}{N}\, |\, X[k]\,|^2\,, \end{aligned} \tag{5.6}$$

where $w[t]$ is a L^2-normalized window function, fft( ) denotes the FFT operation, Δt is the time-step between subsequent samples, and N is the number of samples. The

above calculates the two-sided PSD. To calculate the one-sided version, we simply multiply all components but for the DC component by 2.

Similar measurements of the background noise in the system are made in the absence of a bead, with just the laser passing through an empty chamber and hitting the detector. The transmitted power in the presence and absence of the bead can be different, so the power is adjusted so that the shot-noise floor in the data acquisition matches that in the noise acquisition. The noise acquired in this manner is analyzed similarly to the signal, and subtracted from the corresponding measurements of spectra and correlation functions. This procedure is valid under the assumption that the noise is not correlated to the particle's motion, and is stationary. Of course, this is not entirely true in practice, but the procedure nevertheless removes a significant amount of noise.

The VACF may be computed (up to the calibration constant) by FFT of the velocity power spectral density. The Position Auto-correlation Function (PACF) is computed by FFT of the position PSD, and the MSD (up to calibration constant) is obtained from the PACF. In computing the PACF, data points at frequencies much lower than the trap frequency $F_k = 1/(2\pi\tau_k)$, $\tau_k := \gamma/K$ are discarded, as they are plagued by the low-frequency noise in the system, and the PSD is assumed to be flat in this region.

Least-squares fitting of the MSD or the VACF is then used to determine various fit parameters, including the calibration constant C, the radius of the particle a, and the trap stiffness K. Additional fit parameters exist in other variants of the experiment.

Once the calibration constant is known, all the remaining measurements can be correctly re-scaled to physical units of the motion of the particle.

We may also calculate the PSD of the Langevin force by using the admittance. Since we have $u(\omega) = Y_K(\omega)F_{\text{th}}(\omega)$, we deduce for the position $x(\omega) = (-\mathrm{i}\omega)^{-1}u(\omega)$ a power spectral density given by

$$S_x(\omega) = \omega^{-2}\left|Y_K(\omega)\right|^2 S_F(\omega), \tag{5.7}$$

whereby we may numerically compute the PSD of the Langevin force from the position PSD using $\omega^2\left|Y_K(\omega)\right|^{-2} S_x(\omega)$. This computation does not make any reference to the fluctuation-dissipation theorem. It is valid so long as the theoretical expression for the admittance is correct, and the ideas of linear response theory are valid. In our experiments, the agreement of the experimental PSD computed in this man-

ner with the expression $2k_BT\,\Re[\gamma]$ may be therefore treated as a verification of the fluctuation-dissipation theorem subject to the assumption that the hydrodynamic theory is correct. This is also an indication that the laser heating in the system is negligible.

Chapter Six: Experimental investigations on short time-scale Brownian motion in bulk fluid

In this chapter, we primarily describe two experiments measuring short time-scale aspects of Brownian motion in liquids. The work described here has been published in Kheifets *et al.* [2014] and Mo *et al.* [2015*a*]. The author contributed to the instrumentation of both experiments as outlined in Chapter 5, and contributed to the conduct of the experiments. Specifically, the author acquired the final experimental measurements for Kheifets *et al.* [2014], did an independent check of the data analysis, and contributed to making the plots that went into the paper. The author assisted the data acquisition and analysis for Mo *et al.* [2015*a*].

6.1 Previous experiments

The ballistic regime of Brownian motion was probed by Blum *et al.* [2006] in a rarefied gas. Subsequently, the instantaneous velocity of a Brownian particle was measured in air by Li *et al.* [2010]. They were able to trap silica micro-spheres in air at two different pressures, and record the trajectory with sufficient resolution so as to make a histogram of velocities and show that the statistics followed Boltzmann statistics with the RMS velocity given by the equipartition theorem.

In liquids, the first observation of the ballistic regime was reported by Huang *et al.* [2011], based on the detector design of Chavez *et al.* [2008]. They observed the transition of the mean-squared displacement from slope 2 (ballistic) to slope 1 (diffusive) on a log-log plot, and also verified the hydrodynamic theory of Clercx & Schram [1992]. Franosch *et al.* [2011] observed the long time-scale aspects of Brownian motion in liquids, notably a resonance in the position power spectrum arising from the colored nature of the thermal force, and verified the hydrodynamic theory at these time-scales.

6.2 Considerations for the measurement of instantaneous velocity in liquids

Measuring the true instantaneous velocity of a Brownian particle in a liquid is still elusive, for the time-scale τ_c associated with the effects of compressibility is generally of the order of a few nanoseconds. Therefore, to measure the true instantaneous velocity, a time resolution of shorter than $\tau_c/10$ is required. It is already a formidable challenge to measure the hydrodynamic instantaneous velocity (defined in §4.2), and this forms the primary subject of the work of Kheifets *et al.* [2014].

To measure the hydrodynamic instantaneous velocity, one must measure the velocity before it significantly decorrelates. This is much more challenging than observing the ballistic regime in the MSD or VACF, since the MSD and VACF are averaged measurements – obtaining sufficient statistics will bring error bars due to noise down, since shot-noise, which is the dominant noise limiting the measurement, is uncorrelated and averages out to zero. As we have seen in Chapter 4, the velocity decorrelates on a time-scale of the order of τ_v, defined in (4.11). Not only is it necessary to have a bandwidth larger than $1/\tau_v$, but also necessary to have a good signal-to-noise ratio at this bandwidth, a consideration that is not required for VACF or MSD measurements.

If we integrate the velocity power spectrum of Brownian motion (in an incompressible fluid), we obtain the (hydrodynamic) RMS velocity,

$$\langle v^2 \rangle = \int_{-\infty}^{\infty} S_v(\omega) \, \frac{\mathrm{d}\omega}{2\pi}. \tag{6.1}$$

Basically, the integral of the power spectral density is the zero-time value of the VACF. However, suppose we had a hypothetical brick-wall low-pass filter with frequency cut-off Ω, so that we measured only

$$\langle v_\Omega^2 \rangle := \int_{-\Omega}^{\Omega} S_v(\omega) \, \frac{\mathrm{d}\omega}{2\pi}, \tag{6.2}$$

we would expect to find a velocity distribution that had a smaller RMS value than $k_B T/m^*$, simply because we are not measuring all the power in the velocity spectrum.

However, the noise in the system adds to the signal, and given that the experiment is shot-noise limited, the power in the noise in the position measurement is constant over frequency. When we differentiate the measured signal (which is proportional to the position) to get the velocity, the noise in the velocity measurement

now has a power spectrum that grows like $\sim \omega^2$. When we ask what amount of power in the noise is admitted into our measurement of velocity with bandwidth Ω, we must integrate this spectrum, and therefore obtain a result that grows like $\sim \omega^3$. This cumulative noise spectrum that grows extremely rapidly as ω^3 limits the signal-dominated bandwidth of the system, as long as the actual bandwidth of the detection system is larger than this bandwidth.

Figure 6.1 shows the integral of the velocity PSD (6.1), normalized by $k_B T/m^*$, as a function of bandwidth Ω in units of $1/\tau_p$ for various values of τ_f/τ_p. A representative cumulative spectrum of noise in the velocity measurement $(\Omega\tau_p/100)^3$ is also plotted. The figure illustrates how the rapidly growing noise spectrum determines the noise-free bandwidth. For silica particles in a rare fluid like air, $\tau_f \ll \tau_p$, and the normalized cumulative VPSD hits 1 at a lower value of Ω, so that the same shot-noise level would affect the measurement in air less than in water, where $\tau_f \sim \tau_p$.

If we had a larger detection bandwidth beyond the point where shot-noise becomes dominant, the noise would contribute an increasing amount to the measurement. One must therefore dial down the bandwidth Ω (which can be done digitally using binning) to reduce the noise contribution, but this comes at the loss of some of the signal power. Therefore one needs some sort of criterion to set the amount of binning, with a reasonable signal-to-noise trade-off. In our experiments, we chose the binning number that would give us a SNR of 14 dB. This corresponds to 4% of the net power in the measurement coming from noise. Thus, conceptually speaking, the bandwidth we impose by low-pass filtering lies slightly to the left of the point where the cumulative shot-noise curve meets the cumulative velocity power spectrum in figure 6.1.

Therefore, for successful measurement of the (hydrodynamic) instantaneous velocity,

1. the bandwidth of the detection system must be sufficiently larger than $1/\tau_v$,
2. the shot-noise must be low-enough so that the shot-noise limited bandwidth must be larger than $1/\tau_v$.

Therefore, there are two general ways to improve the ability to measure (hydrodynamic) instantaneous velocity:

1. Choose a particle/fluid combination that slows down the dynamics so that $\tau_v \propto \tau_p \rho_p/\rho_f \propto (\rho_p^2 a^2)/(\rho_f \eta)$ is smaller,

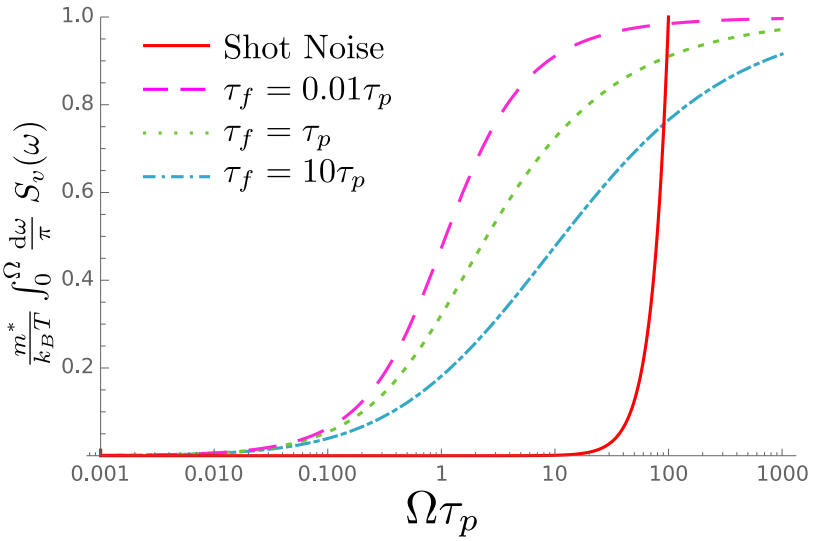

Figure 6.1: Semi-logarithmic plots showing the integral of the velocity PSD (6.1), normalized by k_BT/m^*, for various values of τ_f/τ_p. The horizontal axis is the bandwidth Ω non-dimensionalized by $1/\tau_p$. A representative cumulative spectrum of noise in the velocity measurement $(\Omega\tau_p/100)^3$ is also plotted.

2. Improve the signal to noise ratio.

To address the first consideration, we used Barium Titanate Glass (BTG) particles suspended in acetone. The higher density of BTG ($\rho_p \approx 4.1$ g/cm^3), the lower density of acetone ($\rho_f \approx 0.79$ g/cm^3), and the lower viscosity of acetone[1] ($\eta \approx 3 \times 10^{-4}$ Pa·s) helped slow down the decorrelation of the VACF. The higher refractive index of BTG ($n_p \approx 1.9$) also addressed the second criterion, by increasing the optical gain of the detection system. Another factor was the increased detection power of $> 100mW$. As described in §5.3, the SNR grows like the square-root of detected power. These improvements enabled the measurement of instantaneous velocity.

6.3 Experimental challenges

The experimental challenges posed by detection of high power were already discussed in Chapter 5. A detector was built in-house [Kheifets, 2014] using photo-diodes capable of handling a much higher power.

[1]While hexane has an even lower density and viscosity than acetone, it was not used because the experimenters valued their lives more than the improvement that it would provide over acetone.

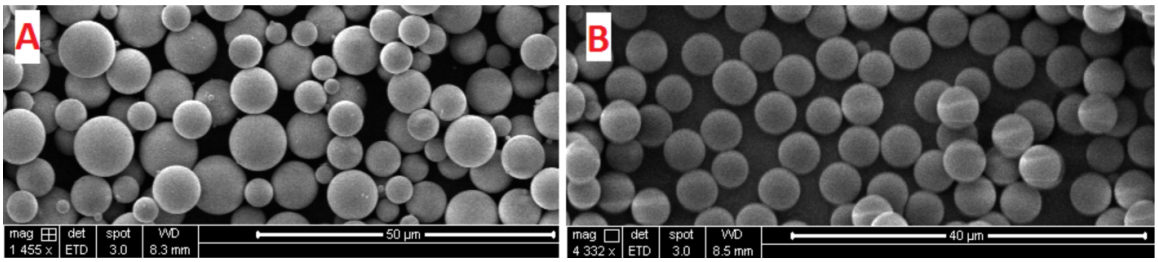

Figure 6.2: Scanning electron micrograph of (A) widely-dispersed (0.1 – 10 μm) Barium Titanate Glass micro-spheres, (B) mono-disperse ($2a \approx 3\mu$m) silica micro-spheres. The particles were sputtered with about 10nm Au/Pd in 60/40 ratio for imaging. Both samples of particles show high-sphericity. Figure from Mo *et al.* [2015*a*], courtesy of Dr. Jianyong Mo.

The use of acetone required us to make sure that all components of the fluidics system were acetone-resistant. This required us to make changes to the tubing and use Nescofilm, as described in Chapter 5.

The use of BTG particles posed another set of experimental challenges. Notably, the available sample of BTG particles (Mo-Sci Specialty Products, GL-0176) had a wide spread in size, unlike the more traditionally used silica particles (eg: SS05N/5411, Bangs Laboratories). A scanning electron micrograph of the samples is shown in figure 6.2.

The large dispersion of sizes, especially with very small particles (0.1μm) made the control of purity of the trap extremely difficult, as a small stray particle could easily get into the trap given enough time. The stray particles could, however be detected even by visually looking at the tail of the position power spectral density in the LabVIEW program, as the time-scale of their dynamics is much shorter. Therefore, the signal from the tiny particles dominates the spectrum at high frequencies despite the lower scattering volume. This made it possible to tell when the trap was pure.

Another complication of using BTG particles was that counter-propagating dual-beam tweezers were required owing to the high refractive index. The ratio of the two beams' powers was adjusted by trial-and-error until a strong trap was achieved.

The third complication associated with BTG particles was that their terminal velocity in the fluid under gravity was substantially high that they would roll close to the bottom of the channel and fall with a fairly high speed in the vertical part of the channel. For this purpose, the channel in our flow cells were cut in a Z-shape

(figure 5.5), creating a "cliff" and allowing the laser beam to be positioned below the cliff without blockage by the sealing film. Upon introduction into the flow chamber, the particles would fall vertically down from the cliff and the trap positioned below the cliff would catch a particle, which then had to be moved quickly away from the vertical line of falling of the BTG particles to prevent another particle from knocking the trapped particle out.

Additionally, for the work presented in Mo *et al.* [2015*a*], the BTG particles needed to be trapped for extended durations of time in order to amass sufficient statistics. For this, the sample of BTG particles was further purified using velocity sedimentation [Cheng *et al.*, 2010], and the chamber was gently flushed with pure HPLC-grade acetone after the particle was trapped. This enabled retention of the particle without contamination for a few minutes.

6.4 Hydrodynamic instantaneous velocity, and short-time statistics of Brownian motion

We shall present a selection of the experimental results from Kheifets *et al.* [2014] in this section. The experiment achieved a shot-noise floor below 3 fm/$\sqrt{\text{Hz}}$ with a band-width of more than 50 MHz. Brownian dynamics in two systems were reported – a 2.9 μm silica particle in water, and a 3.7 μm BTG particle in acetone. In the BTG / acetone system, particle dynamics was resolved to time-scales as short as $\tau_f/300$.

Figure 6.3 shows the results for the MSD and the VACF of the two systems. The blue circles and green squares represent the experimental data for the BTG / acetone and silica / water systems respectively. In sub-figure (A), the red dashed-lines represent the ballistic regime of the MSD. The MSD saturates to a value given by k_BT/K owing to the existence of the optical trap. In sub-figure (B), the red dashed-lines represent the short-time behavior of the VACF (4.10). The blue and green solid lines represent the EOU theory. The zero-crossings are a consequence of the optical trap.

Figure 6.4 shows statistical properties of the Langevin force inferred from the experimental data. The blue circles, green squares, and solid black lines have the same meaning as before. Sub-figure (A) shows the colored component of the Langevin force (theoretically expected to be $\sqrt{\omega\tau_f/2}$). The power law of $\omega^{1/2}$ is evident from the

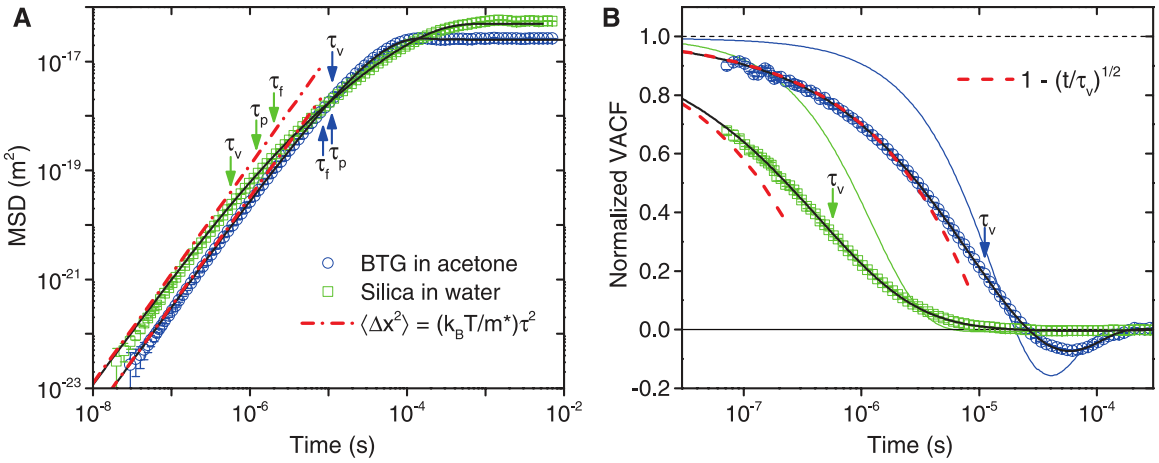

Figure 6.3: Experimental and theoretical results for the MSD and VACF of two particle-fluid systems. (A) Logarithmic plots of the MSD, and (B) semi-logarithmic plots of the VACF normalized by k_BT/m^*. The blue circles correspond to the system of the 3.7μm diameter BTG particle in acetone ($\tau_p = 11.0\mu$s, $\tau_f = 8.5\mu$s, $\tau_v = 11.2\mu$s). The green squares correspond to the system of the 2.9μm diameter silica particle in water ($\tau_p = 1.2\mu$s, $\tau_f = 2.01\mu$s, $\tau_v = 0.57\mu$s). The solid black lines correspond to the hydrodynamic theory, Chapter 4. In sub-figure (A), the red dashed lines indicate ballistic motion, whereas in sub-figure (B), they correspond to the small t expansion of the VACF, $1 - \sqrt{t/\tau_v}$. In sub-figure (B), the green and blue solid lines correspond to the EOU theory, which neglects hydrodynamic interactions. The zero-crossings of the VACF, as well as the saturation of the MSD, are a result of the optical trap. Figure from Kheifets *et al.* [2014].

slope 1/2 on the logarithmic plot. Sub-figure (B) shows the auto-correlation function of the Langevin force, which shows that the force is anti-correlated. The inset is a log-log plot, which shows the power-law dependence of the auto-correlation function. The paradox of instantaneous anti-correlation seems to be an artifact of incompressibility. Sub-figure (C) shows the cross-correlation between velocity and the Langevin force. This cross-correlation is asymmetric in time. The observation that the past velocity is correlated with the future force is not a violation of causality [Balakrishnan, 1979]. The experimental data in this figure was calculated by inverting the mechanical susceptibility on the position, and therefore does not assume the fluctuation-dissipation theorem. The fact that the data in this figure agrees with the theory can be interpreted as a verification of the fluctuation-dissipation theorem subject to the validity of the hydrodynamic theory.

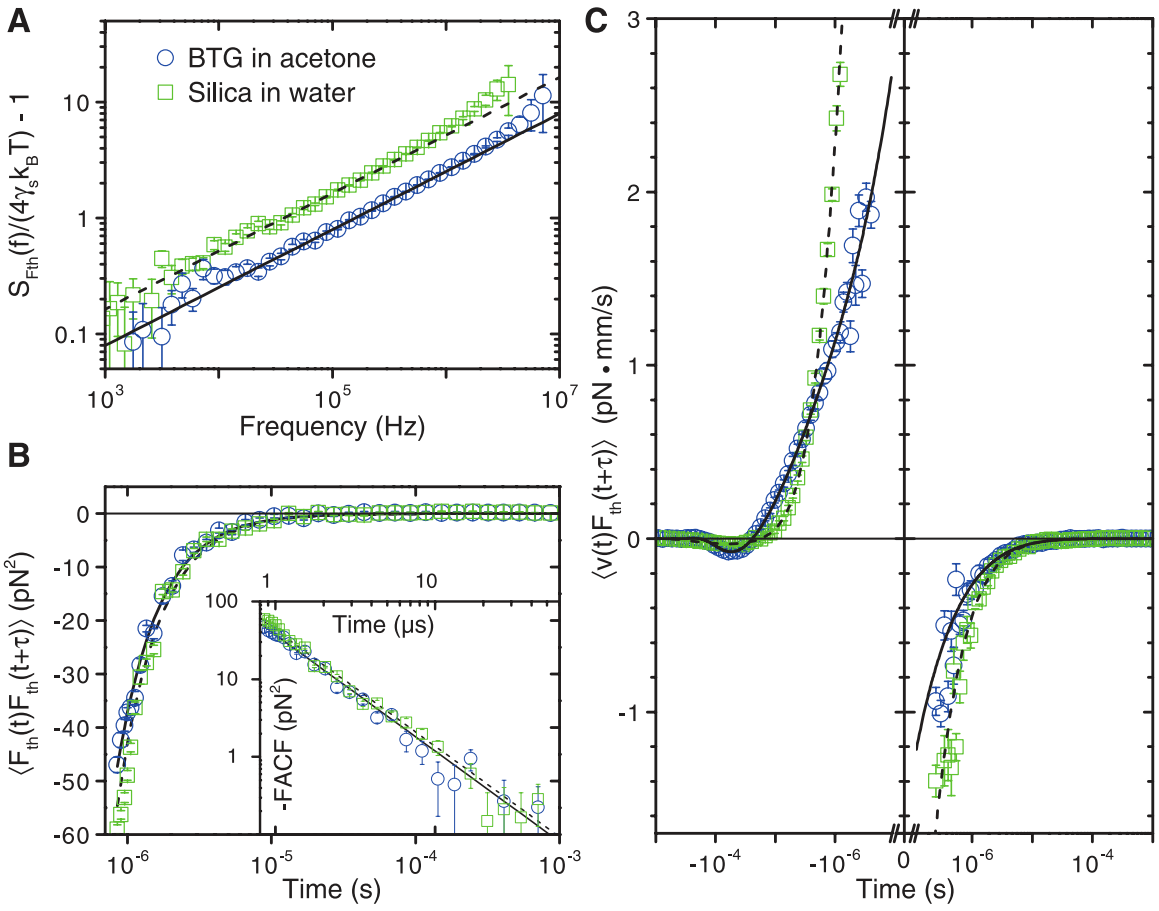

Figure 6.4: Statistical properties of the thermal force inferred from experimental data. Sub-figure (A) shows a log-log plot of the colored component of the thermal force. Sub-figure (B) shows a semi-logarithmic plot of the auto-correlation function of the thermal force, the negative values indicating an anti-correlation. The inset shows the absolute value of the same on a log-log scale to evince its power-law dependence. Sub-figure (C) shows a semi-logarithmic plot of the velocity-force cross-correlation function. Figure from Kheifets *et al.* [2014].

6.5 Testing the Maxwell-Boltzmann distribution

While Kheifets *et al.* [2014] does report a verification of Boltzmann statistics $e^{-m^*v^2/k_BT}$ of (hydrodynamic) instantaneous velocities, the counts, especially in the tails, are very low. There was a need to perform an experiment amassing much more statistics to better verify the Maxwell-Boltzmann distribution. We reported the results of a follow-up experiment achieving this [Mo *et al.*, 2015*a*], which is the subject of this section.

The most challenging part of this experiment, as described, was retaining the particle in the chamber without contamination for the long durations required to acquire the particle trajectories. The small particles in the BTG sample were partially eliminated by velocity sedimentation as stated earlier. However, efforts were made to speed-up the acquisition process in LabVIEW. In addition to profiling the LabVIEW program and improving the processing time, the primary data storage was upgraded to a solid-state drive for faster write throughput. The data acquisition was done in a team with one operator at the experiment monitoring the data acquisition process, and another at a computer analyzing a sampling of the data-sets in real time. This allowed us to monitor contamination or other problems very quickly, avoiding continued acquisition of bad data.

The digitizer we used, as mentioned earlier, has a 2^{27}-sample memory. At the maximum sample rate of 200 MSa/s, this translates to about 0.7s of time per acquisition of a trajectory. We studied three systems – silica in water, silica in acetone and BTG in acetone – acquiring 677, 143, and 43 such trajectories respectively! After appropriate binning (bin sizes of 25, 85, and 40 respectively), this gave us 3.6 billion, 200 million and 144 million velocity data points for the three systems respectively. The bin size was chosen to have the same SNR $\approx$ 14 dB for all three systems. The resulting histogram of velocities from this data is shown in 6.5. In the silica / water and silica / acetone systems, the full hydrodynamic instantaneous velocity could not be measured, owing to which the measured histogram has a lower variance than the k_BT/m^* expected from the modified equipartition theorem. A Gaussian fit with the measured lower variance is plotted to show the Gaussianity of the distribution. In the BTG / acetone system, the hydrodynamic instantaneous velocity is fully measured resulting in agreement with Boltzmann statistics well into the tails. The agreement is seen over a large dynamic range of 5 orders of magnitude in count-rate and 5 standard

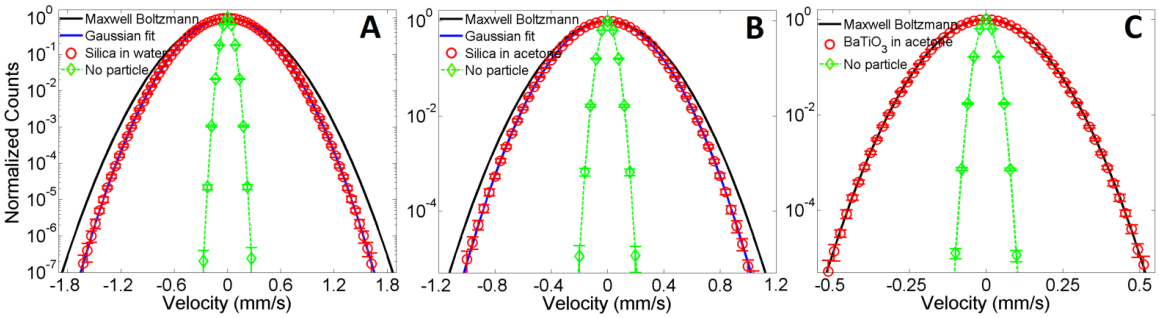

Figure 6.5: Normalized velocity distributions of Brownian particles along one-dimension. Sub-figure (A) shows the results for the system of silica particles in water, (B) for the system of silica particles in acetone, and (C) for the system of BTG particles in acetone. The histograms are calculated using 3.6 billion, 200 million, and 144 million velocity data points respectively. The red circles represent the experimental measurements with trapped particles, and the green diamonds represent the noise acquisitions, i.e. without any particle present, but with power adjusted to match the shot-noise level. Black lines represent the theoretical predictions from Maxwell-Boltzmann statistics $e^{-m^*v^2/k_BT}$ for the distribution of hydrodynamic instantaneous velocities. Blue lines (overlapping with the black line in sub-figure C) are Gaussian fits of the measured histograms. From the Gaussian fits, it was determined that 78%. 83% and 100% of the total kinetic energy of the particle was measured in the three systems respectively. Figure from Mo *et al.* [2015*a*].

deviations in velocity. In all three systems, the noise contributes about 4% to the variance.

Chapter Seven: Unsteady Stokes Flows near Boundaries: The Point-Particle Approximation

So far, we have described theories of, and experiments probing Brownian motion in liquids, sufficiently far away from any boundaries so that the fluid medium may be treated as infinite. However, Brownian motion near boundaries has significant practical relevance. We mentioned in the Introduction (Chapter 1) that the presence of boundaries makes problems of unsteady Stokes flow harder to solve. We therefore turn to investigate approximation methods to solve problems of unsteady Stokes flow.

In this chapter, we will study in particular the application of a Point-Particle Approximation (PPA) to such problems, in general terms. The intention is to eventually specialize to the geometry of a spherical particle near a plane wall (Chapter 8).

The material of this chapter is largely lifted from a draft of an article [Simha *et al.*, 2017] that the author of this dissertation has co-authored with Dr. Jianyong Mo and Prof. Philip J. Morrison.[1]

7.1 Introduction

In Chapter 3, we described the regime of unsteady Stokes flow and outlined the general procedure for obtaining unsteady drag coefficients. We also pointed out that these problems may not be analytically tractable in closed-form without approximation, despite the linearity, particularly in situations with reduced symmetry. To take a specific example, while the problem of a sphere translating near a plane wall may be solved by means of separable eigenfunction expansions in the case of steady Stokes flow [O'Neill, 1964], this is not true with unsteady Stokes flow: the choice of

[1] A. Simha, J. Mo, and P. J. Morrison, "Unsteady Stokes flow near boundaries: the point-particle approximation and the method of reflections." Submitted for review to the *Journal of Fluid Mechanics* in July 2017. A. Simha, with the help of J. Mo, discovered the problem with Felderhof's calculation. Discussions between A. Simha and P. J. Morrison led to the modification required to fix the asymptotic behavior in the stimulating environment of the "GFD trailer" next to Walsh Cottage, Woods Hole, MA. A. Simha also implemented the details of the perturbative analysis in the boundary integral equation formalism, based on the ideas and guidance of P. J. Morrison. Much of the text of this work was authored and typeset by A. Simha, with many helpful suggestions from P. J. Morrison and J. Mo.

coordinates that is apt for the symmetry of the problem is the bi-spherical coordinate system, and the Helmholtz equation obtained by considering harmonic oscillations is not separable in this coordinate system, although the Laplace equation is [Morse & Feshbach, 1953].

However, such problems of complicated geometries have been long studied in the context of steady Stokes flow, where several approximation techniques are well-developed. Lorentz [1896] studied the effect of a plane boundary on the motion of a particle and developed a formula for the flow reflected from a plane wall, which they later [Lorentz, 1907] employed to calculate the first order correction to the drag on a spherical particle due to the presence of the wall. In the same paper, Lorentz also introduced the notion of a point force solution (also known as the stokeslet) for steady Stokes flow, showing that the flow produced by a point force of strength $\boldsymbol{F}_s = 6\pi\eta a\boldsymbol{v}$, where η is the dynamic viscosity of the fluid, is equivalent to the flow produced by a small sphere moving with velocity $\boldsymbol{v}$ at the same location.

These two themes of Lorentz's work have led to approximate methods to determine the effects of boundaries on the slow motion of particles in viscous fluids. Firstly, the method of reflections, which is described in detail in e.g. Happel & Brenner [1965], has been used extensively for this purpose. Secondly, although Lorentz did not use it as such, the notion of a point force solution leads to another approximation to calculate the drag on a particle in a complicated geometry – the particles under consideration may be approximated by modeling them by a combination of singularities, i.e. by a multipole expansion. This is particularly useful when the particles under consideration are sufficiently distant from the confining walls so that they may be well approximated by just a point force. [see e.g. Kim & Karrila, 2013]. Another approximation method, that of matched asymptotic expansions [O'Neill & Stewartson, 1967], has also been used successfully to describe steady Stokes flows in complicated geometries.

The key subject of this chapter and the next is to address the issue of extending two of these methods – the point-particle approximation, and the method of reflections – to unsteady Stokes flows. In particular, Felderhof [2005, 2006*a*, 2009*b*, 2012] has applied a point-particle approximation to determine the dynamics of a sufficiently small spherical particle performing small oscillations in a number of confined geometries[2]. In essence, their method involves approximating the spherical particle by a

[2]Although Felderhof's work includes generalizations to compressible fluids, we shall restrict

point force for purposes of calculating the correction to the flow induced by the confining boundary. This results in a significant simplification of the original problem to what is, in essence, a Green's function problem. However, it appears that the effective mass inferred from Felderhof's result for the RMS velocity of a sphere near a plane wall does not agree with the effective mass obtained from potential flow calculations [Lamb, 1932; Milne-Thomson, 1968]. The results also lead to a drag coefficient that depends on the density of the particle, which is inconsistent with the fact that one may calculate the drag coefficient without any reference to the particle's density (§3.4).

Moreover, it is not obvious that the point-particle approximation generalizes to the case of unsteady Stokes flow. This is because it neglects the size of the particle with respect to two length-scales, viz. the distance of the particle to the boundaries and the skin-depth of vorticity. As we have seen in Chapter 3, the skin-depth of vorticity $\sim |\alpha|^{-1}$ is a frequency-dependent quantity and because Brownian motion contains velocity fluctuations of all frequencies, no assumptions can be made about the size of $|\alpha|$. Loosely speaking, the conditions for the validity that we may naïvely expect here are analogous to the conditions for the Rayleigh approximation to hold in scattering theory – not only does the field point have to be in the far field, but the wavelength of the scattered radiation also needs to be much larger than the particle size.

The first issue is related to determining the strength of the point force that reproduces the flow field of the sphere in the far field. In the case of steady Stokes flow, as we stated earlier, this is simply equal to $6\pi\eta\boldsymbol{v}_s$, where $\boldsymbol{v}_s$ is the velocity with which the sphere translates [Lorentz, 1907, §7]. In the unsteady case, Felderhof uses the external force $\boldsymbol{F}_\omega^{\text{ext}}$ acting on the sphere as the point-force acting on the fluid. However, this produces a result that does not agree in the far field, and as we stated earlier, results in a spurious dependence of the drag coefficient on the density of the particle. In this paper, we show that the point force that reproduces the flow from a sphere in the far field is the induced force $\boldsymbol{F}_\omega^{\text{ind}}$ described by Mazur & Bedeaux [1974]. Making this change in Felderhof's theory results in correct values for the effective mass, and removes the spurious dependence of the drag coefficient on particle density.

As for the second issue of the existence of two length scales, we develop a formu-

ourselves to incompressible fluids in this analysis

lation of the problem in terms of boundary integral equations. We then introduce a perturbative parameter given by the ratio of the particle size to the distance to the walls, and develop an ordering of integral equations in increasing powers of the parameter. We show that a series of systematic approximations results in a geometric series which can be summed to obtain the point-particle approximation. In doing so, we note important differences between the unsteady Stokes problem and the Rayleigh scattering problem that arise from the structure of the Oseen tensor. We thereby discover the non-trivial reasons why the approximation works in practice, as has been seen through its agreement with experiments [Jeney *et al.*, 2008; Mo *et al.*, 2015*b*].

7.2 The point-particle approximation

Throughout this chapter, we consider the problem of determining the drag force $\boldsymbol{F}_{\omega}^{\mathrm{drag}}$ on a small rigid body S of generic shape performing small translational oscillations[3] in an arbitrary direction at arbitrary[4] frequency ω in an incompressible fluid of dynamic viscosity η and density ρ_f. The fluid is bounded by various additional stationary surfaces (walls) W_i (which could have arbitrary shapes). The intention at a later stage will be to specialize S to a sphere, and then consider a single plane wall W.

7.2.1 An overview of the point-particle framework of Felderhof

In this subsection, we shall review Felderhof's framework for computing particle dynamics using the point-particle approximation in general terms. Felderhof has applied the point-particle approximation to a number of situations [see e.g. Felderhof, 2005, 2006*a*, 2009*b*, 2012], especially in the context of the hydrodynamic theory of Brownian motion. In this approximation, the body S is replaced by a point force. This is in the spirit of a multipole expansion (Kim & Karrila [see e.g. 2013], Chapter 3),

[3] As stated before in Chapter 3, it is assumed for simplicity that the boundary of the particle itself does not change position, but the velocity boundary condition on that boundary changes. This results in a linear problem, and one would expect it to be good so long as the amplitude of oscillations is small and gets smaller as the frequency grows [see e.g. Zwanzig & Bixon, 1970; Mazur & Bedeaux, 1974]

[4] It is assumed however that the frequency is not high enough that the compressibility of the fluid becomes important

the idea being that in the far-field, the stokeslet part of the expansion dominates. Thus, for purposes of calculating the effects of the walls W_i, it suffices to truncate the multipole expansion at the stokeslet level. Linearity allows us to superpose the effects of the wall and the effects local to the body, a step that will later be effected using a generalized Faxén theorem.

We begin by computing the vector-valued Green's function[5] for the pressure field $\boldsymbol{P}$ (with components P_j) and tensor-valued Green's function for the velocity field $\boldsymbol{G}$ (with components G_{ij}), arising from a general point force of unit strength at a generic location $\boldsymbol{r}'$. The Green's functions satisfy the equations

$$\begin{aligned} \Delta G_{ij}(\boldsymbol{r}|\boldsymbol{r}';\omega) - \alpha^2 G_{ij}(\boldsymbol{r}|\boldsymbol{r}';\omega) - \frac{1}{\eta}\partial_i P_j(\boldsymbol{r}|\boldsymbol{r}';\omega) &= \delta_{ij}\delta(\boldsymbol{r}-\boldsymbol{r}'), \qquad (7.1) \\ \partial_i G_{ij}(\boldsymbol{r}|\boldsymbol{r}';\omega) &= 0, \qquad (7.2) \end{aligned}$$

and also obey the required boundary conditions on the walls W_i. As discussed before, they may be computed in principle by using the incompressibility condition in the first equation to get the Poisson equation for the pressure P_j,

$$-\frac{1}{\eta}\Delta P_j(\boldsymbol{r}|\boldsymbol{r}';\omega) = \partial_j \delta(\boldsymbol{r}-\boldsymbol{r}'), \qquad (7.3)$$

and then substituting the solution of the above as a source into equation (7.1). The resulting Helmholtz equations with complex wavenumber are then solved to determine G_{ij}. In practice, the equations are generally solved using eigenfunction expansions and then applying boundary conditions to determine the coefficients [Jones, 2004; Felderhof, 2005].

The effect of the boundary conditions on the surface of the body ∂S could in general be modeled by a force distribution (see Section 3.7), which could then be integrated against the above Green's function to obtain the velocity field. However, this is a non-trivial task in the complicated geometries of interest. In the point-particle approximation, the effect of the body S is instead modeled by a single point force $\boldsymbol{F}_\omega^{\text{ind}}$ at the location of the body[6] $\boldsymbol{r}_0$, which reproduces the flow from the actual

[5]While this is similar to the problem we addressed in §3.5, it is important to note that we are now talking about the Green's function that satisfies boundary conditions on the walls, and not the fundamental solution that satisfies decay conditions at infinity. As a reminder, the free-space Green's function (fundamental solution / unsteady Oseen tensor) will be denoted by $\boldsymbol{G}^0$ in this work.

[6]The problem of choosing this location is akin to finding a good choice for the origin in any multipole expansion

body at sufficiently large distances from the body. The change in the flow caused by the presence of the walls, may then be written as

$$\boldsymbol{v}_W(\boldsymbol{r}|\boldsymbol{r}_0;\omega) = \left[\boldsymbol{G}(\boldsymbol{r}|\boldsymbol{r}_0;\omega) - \boldsymbol{G}^0(\boldsymbol{r}-\boldsymbol{r}_0;\omega)\right]\cdot\boldsymbol{F}^{\text{ind}}_\omega, \tag{7.4}$$

where $\boldsymbol{G}^0$ is the free-space velocity Green's function (3.23). As described earlier (§3.5), one may obtain $\boldsymbol{G}^0$ by the same method described to compute G_{ij} except with the boundary condition being that the flow decay at infinity.

We are yet to specify what $\boldsymbol{F}^{\text{ind}}_\omega$ must be to reproduce the flow generated by the body sufficiently far from it, and we shall do so in Section 7.2.2. Once the effect of the wall $\boldsymbol{v}_W$ is known, a generalized Faxén theorem (Section 3.7) may be used to compute the drag coefficient.

When using the generalized Faxén theorem in the point-particle approximation, it suffices to evaluate $\boldsymbol{v}_W$ at the location of the particle. This suggests that it is useful to define the quantity [Felderhof, 2005],

$$\boldsymbol{R}(\boldsymbol{r}_0;\omega) := \lim_{\boldsymbol{r}\to\boldsymbol{r}_0}\left[\boldsymbol{G}(\boldsymbol{r}|\boldsymbol{r}_0;\omega) - \boldsymbol{G}^0(\boldsymbol{r}-\boldsymbol{r}_0;\omega)\right], \tag{7.5}$$

which Felderhof aptly calls the *reaction field tensor*.

7.2.2 The appropriate choice of the point force $\boldsymbol{F}^{\text{ind}}_\omega$

We now wish to address the following question: what must the point force $\boldsymbol{F}^{\text{ind}}_\omega$ of Section 7.2.1 be, to capture the effects on the fluid due to the presence of the body S? Felderhof [2005, eq. (2.8)] uses the external force $\boldsymbol{F}^{\text{ext}}_\omega$ that acts on the body by means of some external agent to keep it oscillating with velocity $\boldsymbol{u}_\omega$. However, as some of the momentum delivered by the force $\boldsymbol{F}^{\text{ext}}_\omega$ goes into accelerating the body S, it is unlikely that this is equal to the force applied on the fluid. It seems reasonable that the force must reproduce the momentum transport through the boundary ∂S of the small body, when the body's volume is replaced by fluid. This is the notion of induced force of Mazur & Bedeaux [1974], which as we described in Section 3.7, can be used to replace boundary conditions by sources.

Also in Section 3.7, we had stated in equation (3.32) an expression for the total induced force that replaces a spherical boundary oscillating at $\boldsymbol{u}_\omega$. Based on that, we propose that the value of the point force must be given by the same net force concentrated at a point,

$$\boldsymbol{F}^{\text{ind}}_\omega = -\boldsymbol{F}^{\text{drag}}_\omega - \mathrm{i}\omega m_f \boldsymbol{u}_\omega, \tag{7.6}$$

possibly also for bodies of generic shape. In this equation, we note that no reference has been made to the properties of the body or the external force acting on it. These aspects, however, do affect the velocity $\boldsymbol{u}_\omega$ through the equation of motion of the body,

$$\boldsymbol{F}_\omega^{\text{ext}} = -\boldsymbol{F}_\omega^{\text{drag}} - \mathrm{i}\omega m_p \boldsymbol{u}_\omega, \tag{7.7}$$

which leads to the alternate expression for the net induced force $\boldsymbol{F}_\omega^{\text{ind}}$,

$$\boldsymbol{F}_\omega^{\text{ind}} = \boldsymbol{F}_\omega^{\text{ext}} + \mathrm{i}\omega(m_p - m_f)\boldsymbol{u}_\omega. \tag{7.8}$$

as used by Felderhof [2005]. We would recover Felderhof's proposal of using $\boldsymbol{F}_\omega^{\text{ext}}$ as the force that represents the body if the body had the same density as the fluid.

To establish our proposal for $\boldsymbol{F}_\omega^{\text{ind}}$, we observe that we may write the velocity field $\boldsymbol{v}$ produced by the oscillating body at an arbitrary point $\boldsymbol{r}$ using the Green's function of equation (7.1) as

$$\boldsymbol{v}(\boldsymbol{r};\omega) = \int_S \mathrm{d}^3 r' \; \boldsymbol{G}(\boldsymbol{r}|\boldsymbol{r}';\omega) \cdot \boldsymbol{S}_{\text{ind}}(\boldsymbol{r}';\omega), \tag{7.9}$$

where we have replaced the body S by an appropriate induced force density. As is typical of multipole expansions, we may expand $\boldsymbol{G}$ in the source point in the far-field limit (i.e. $|\boldsymbol{r}| \gg 1/|\alpha|$, L where L denotes the size of the body) to obtain

$$\boldsymbol{v}(\boldsymbol{r};\omega) = \int_S \mathrm{d}^3 r' \; [\boldsymbol{G}(\boldsymbol{r}|\boldsymbol{r}_0;\omega) + (\boldsymbol{r} - \boldsymbol{r}_0) \cdot \boldsymbol{\nabla}\boldsymbol{G}(\boldsymbol{r}|\boldsymbol{r}_0;\omega) + \ldots] \cdot \boldsymbol{S}_{\text{ind}}(\boldsymbol{r}';\omega), \tag{7.10}$$

where $\boldsymbol{r}_0$ is some notion of the center of the body. Truncating the expansion to the first term gives the expression for the velocity due to a point force at $\boldsymbol{r}_0$, whose strength is indeed given by

$$\boldsymbol{F}_\omega^{\text{ind}} = \int_S \mathrm{d}^3 r' \; \boldsymbol{S}_{\text{ind}}(\boldsymbol{r}';\omega). \tag{7.11}$$

We shall further ratify our result for $\boldsymbol{F}_\omega^{\text{ind}}$ by checking it for the case of unbounded spherical bodies in the following manner: we shall take the far-field limit (i.e. $|\boldsymbol{r}| \gg 1/|\alpha|$, a) of the solution for the flow $\boldsymbol{v}_\omega^{\text{S}}(r,\theta)$ produced by a sphere of radius a at the origin oscillating with velocity $\boldsymbol{u}_\omega$ [see e.g. Landau & Lifshitz, 1987, §24], and compare it against the flow $\boldsymbol{v}_\omega^{\text{PF}}$ generated by a point force $\boldsymbol{F}_\omega$ at the origin [see e.g. Kim & Karrila, 2013, §6.2]. For conciseness, we shall compare only the radial component.

We have already discussed the solution of the unsteady Stokes equations for a spherical body oscillating in unbounded fluid in §3.6. In re-stating some of the same results here, we have adapted a notation that is more natural to the problem at hand.

Using spherical polar coordinates with the polar axis along $\boldsymbol{u}_\omega$, and introducing the notation $\varepsilon := a/r$, we find that the radial component of the velocity field for a sphere is given by

$$\hat{\boldsymbol{e}}_r \cdot \boldsymbol{v}_\omega^{\mathrm{S}}(r,\theta) = -u_\omega \frac{2f'(r)}{r}\cos\theta, \tag{7.12}$$

where [as given by Landau & Lifshitz, 1987, §24, Prob. 5]

$$\frac{f'(r)}{r} = \frac{3\varepsilon^3}{2\delta^2}\left[\mathrm{e}^{\delta(1-1/\varepsilon)}\left(1+\frac{\delta}{\varepsilon}\right) - \left(1+\delta+\frac{\delta^2}{3}\right)\right]. \tag{7.13}$$

On the other hand, for an unsteady stokeslet of strength $\boldsymbol{F}_\omega = F_\omega \hat{\boldsymbol{e}}_z$, where $\hat{\boldsymbol{e}}_z$ is the unit vector along the polar axis, we have

$$\hat{\boldsymbol{e}}_r \cdot \boldsymbol{v}_\omega^{\mathrm{PF}} = \frac{2\alpha\varepsilon^3}{\delta^3}\left[1-\left(1+\frac{\delta}{\varepsilon}\right)\mathrm{e}^{-\delta/\varepsilon}\right]\frac{F_\omega}{4\pi\eta}\cos\theta. \tag{7.14}$$

In the far-field limit ($\varepsilon \to 0^+$ with δ fixed and finite), we may drop the subdominant exponential terms of the form $\mathrm{e}^{-\delta/\varepsilon}$ and obtain

$$\begin{aligned}
\frac{f'(r)}{r} &\sim -\frac{3\varepsilon^3}{2\delta^2}\left(1+\delta+\frac{\delta^2}{3}\right), \\
\hat{\boldsymbol{e}}_r \cdot \boldsymbol{v}_\omega^{\mathrm{S}} &\sim u_\omega \cos\theta\, \frac{3\varepsilon^3}{\delta^2}\left(1+\delta+\frac{\delta^2}{3}\right), \\
\hat{\boldsymbol{e}}_r \cdot \boldsymbol{v}_\omega^{\mathrm{PF}} &\sim \frac{4\alpha\varepsilon^3}{\delta^3}\frac{F_\omega}{8\pi\eta}\cos\theta.
\end{aligned} \tag{7.15}$$

By setting the latter two expressions equal to each other, we find that,

$$\begin{aligned}
F_\omega &= \gamma_s u_\omega \left(1+\delta+\frac{\delta^2}{3}\right) \\
&= \gamma_s u_\omega \left(1+\delta+\frac{\delta^2}{9}\right) - \mathrm{i}\omega m_f u_\omega.
\end{aligned} \tag{7.16}$$

We now identify the first term to be $-F_\omega^{\mathrm{drag}} = \gamma_0(\omega)u_\omega$, whereby we find that $\boldsymbol{F}_\omega$ is indeed equal to the induced force $\boldsymbol{F}_\omega^{\mathrm{ind}}$. We are hence led to conclude that an unsteady stokeslet of strength $\boldsymbol{F}_\omega^{\mathrm{ind}}$ as defined by equation (7.6) reproduces the far-field behavior of a sphere, which would not be the case for Felderhof's choice of the external force $\boldsymbol{F}_\omega^{\mathrm{ext}}$. It is not unreasonable to expect from the physical and mathematical arguments presented earlier, that (7.6) also holds for bodies of generic shape.

7.2.3 From the reaction field tensor to the dynamics of a sphere

We will now follow Felderhof's approach, except with the modified point force $\boldsymbol{F}_\omega^{\text{ind}}$ given by (7.6), to arrive at expressions for the drag coefficient and other relevant quantities characterizing the dynamics of a *sphere* oscillating in a fluid, in terms of the reaction field tensor $\boldsymbol{R}$.

In the point-particle framework of Felderhof, the flow $\boldsymbol{v}_W$ calculated using (7.4) is considered to be the background flow $\boldsymbol{v}_0$ in Faxén's theorem (3.34). In addition, the surface and volume averages of $\boldsymbol{v}_0$ are approximated by evaluating $\boldsymbol{v}_W$ at the center of the sphere. Thus, using the definition (7.5) of the reaction field tensor, we may write in the point-particle limit,

$$\boldsymbol{F}_\omega^{\text{drag}} = -\gamma_0(\omega)\boldsymbol{u}_\omega + \gamma_s\left(1+\delta+\frac{\delta^2}{3}\right)\boldsymbol{R}\cdot\boldsymbol{F}_\omega^{\text{ind}}, \tag{7.17}$$

where as before, $\delta := \alpha a$, $\gamma_s := 6\pi\eta a$, and $\gamma_0(\omega) = \gamma_s(1+\delta+\delta^2/9)$. We must note that in the adaptation of the generalized Faxén theorem to Felderhof's framework, the net flow $\boldsymbol{v} = \boldsymbol{v}_W + \boldsymbol{v}'$ does not necessarily satisfy boundary conditions on the walls, and this is part of the approximation.

Using equations (7.17) and (7.6), we obtain

$$\boldsymbol{F}_\omega^{\text{ind}} = \gamma_s\left(1+\delta+\frac{\delta^2}{3}\right)\left[\boldsymbol{u}_\omega - \boldsymbol{R}\cdot\boldsymbol{F}_\omega^{\text{ind}}\right], \tag{7.18}$$

where we have used $-\mathrm{i}\omega m_f = (2/9)\gamma_s\delta^2$ to simplify the expression. The difference between this expression and that of Felderhof [2005, eq. 2.11] is the use of $\boldsymbol{F}_\omega^{\text{ind}}$ instead of $\boldsymbol{F}_\omega^{\text{ext}}$. We may use this to solve for $\boldsymbol{F}_\omega^{\text{ind}}$ as,

$$\boldsymbol{F}_\omega^{\text{ind}} = \tilde{\gamma}_0(\omega)\left[\mathbb{1}+\tilde{\gamma}_0(\omega)\boldsymbol{R}\right]^{-1}\cdot\boldsymbol{u}_\omega, \tag{7.19}$$

where we have defined for convenience,

$$\tilde{\gamma}_0(\omega) := \gamma_s\left(1+\delta+\frac{\delta^2}{3}\right) = \gamma_0(\omega) - \mathrm{i}\omega m_f \tag{7.20}$$

Thereafter, using the definition (3.14) and plugging (7.19) into (7.6), we obtain the drag coefficient tensor,

$$\boldsymbol{\gamma}(\omega) = \mathrm{i}\omega m_f\mathbb{1} + \tilde{\gamma}_0(\omega)\left[\mathbb{1}+\tilde{\gamma}_0(\omega)\boldsymbol{R}\right]^{-1}. \tag{7.21}$$

We observe that if we define $\tilde{\boldsymbol{\gamma}}(\boldsymbol{\omega}) := \boldsymbol{\gamma}(\omega) - \mathrm{i}\omega m_f \mathbb{1}$ as before (so that $\boldsymbol{F}_\omega^{\mathrm{ind}} = \tilde{\boldsymbol{\gamma}}(\omega) \cdot \boldsymbol{u}_\omega$), the correction of $\tilde{\gamma}_0$ to $\tilde{\boldsymbol{\gamma}}$ through $\boldsymbol{R}$ has the natural form of a Padé approximant.

Recall that the mechanical admittance tensor $\boldsymbol{Y}_\omega$, characterizing the linear response of the velocity $\boldsymbol{u}_\omega$ of the sphere to the external force $\boldsymbol{F}_\omega^{\mathrm{ext}}$ acting on it, is defined through

$$\boldsymbol{u}_\omega = \boldsymbol{Y}_\omega \cdot \boldsymbol{F}_\omega^{\mathrm{ext}},$$

and that it can be related to the drag coefficient through the equation of motion of the sphere (7.7), to obtain (2.26). We may now use (7.21) to write the admittance (without the effects of a harmonic trap) as

$$\begin{aligned} \boldsymbol{Y}_\omega &= \left[-\mathrm{i}\omega m_p \mathbb{1} + \boldsymbol{\gamma}(\omega)\right]^{-1} \\ &= \left[\tilde{\gamma}_0 \left(\mathbb{1} + \tilde{\gamma}_0 \boldsymbol{R}\right)^{-1} - \mathrm{i}\omega(m_p - m_f)\mathbb{1}\right]^{-1}. \end{aligned} \tag{7.22}$$

It is worth noting that we may use (7.21) in (2.36) instead whenever we wish to include the effects of a harmonic restoring force (see §2.5).

7.3 The validity of the point-particle approximation

7.3.1 Is the point-particle approximation valid?

Like we have stated earlier, there are two length scales in the problem in addition to the particle size – the scale of the dimensions of the confining geometry h, and the scale of the skin-depth of vorticity $1/|\alpha|$ (see §3.2). The point-particle approximation neglects the size of the particle a in comparison to both these length scales insofar as the computation of the effect of the wall is concerned, and when computing the surface and volume averages of the flow that enter the generalized Faxén theorem. It must be noted that no approximations[7] are made in the generalized Faxén theorem (3.34) itself when the body is a sphere. However, for sufficiently large frequency ω of oscillations, $1/|\alpha|$ can become comparable to a. This brings up the question of whether the point-particle approximation works at high frequencies.

[7] excepting for the previously stated assumption that the boundary conditions may be applied on the equilibrium boundary of the sphere [Mazur & Bedeaux, 1974]

However, the agreement with experiment [Mo *et al.*, 2015*b*] at frequencies $\omega \sim \eta/(\rho_f a^2)$ is very good. We explain this intuitively as follows: at these frequencies, the vorticity shed by the boundaries has a very small skin-depth $1/|\alpha| \ll h$ and hence the vorticity from the wall is suppressed exponentially, and the reflected flow field is well approximated by potential flow. Since the potential satisfies Laplace's equation, the multipole expansion and therefore the point-particle approximation works well. At low frequencies $\omega \ll \eta/(\rho_f a^2)$, $1/|\alpha|$ is indeed large compared to a and the approximation works as expected.

In order to harden the above argument, we shall set up a general formalism (Section 7.3.2) for analyzing the problem in terms of boundary integral equations, and then systematically delineate the approximations made in order to recover Felderhof's framework in Section 7.3.3. The question then boils down to the validity of a far-field expansion of the unsteady Oseen tensor over a wide-range of frequencies, which we provide an argument for in Section 7.3.4. In Section 7.3.5 we shall extend the perturbative calculation to higher orders and recover the Padé-like form for the drag coefficient (7.21).

7.3.2 General formalism of boundary integral equations

In this sub-section, we will cast our problem in the general formalism of boundary integral equations [see e.g. Pozrikidis, 1992], which we discussed in §3.8. In this and the following sub-sections, we shall drop explicit reference to ω, the frequency, for notational simplicity. As before, the linearity and time-translation invariance ensure that the individual frequency components may be treated separately. The walls will also be assumed to be larger in size than the distance from the particle to any of them. We shall also assume no-slip boundary conditions on all interfaces for the purposes of this discussion.

The problem at hand may be restated as follows: Find the drag force

$$\boldsymbol{F}_{\text{drag}} = -\left[\mathrm{i}\omega m_f \boldsymbol{u} + \int_S \mathrm{d}^3 r'_S \; \boldsymbol{S}_S(\boldsymbol{r}'_S)\right] \tag{7.23}$$

exerted on the surface of the particle S oscillating with velocity $\boldsymbol{u}$, by the velocity field

$$\boldsymbol{v}(\boldsymbol{r}) = \int_S \mathrm{d}^3 r'_S \; \boldsymbol{G}^0(\boldsymbol{r} - \boldsymbol{r}'_S) \cdot \boldsymbol{S}_S(\boldsymbol{r}'_S) + \int_W \mathrm{d}^2 r'_W \; \boldsymbol{G}^0(\boldsymbol{r} - \boldsymbol{r}'_W) \cdot \boldsymbol{S}_W(\boldsymbol{r}'_W) \tag{7.24}$$

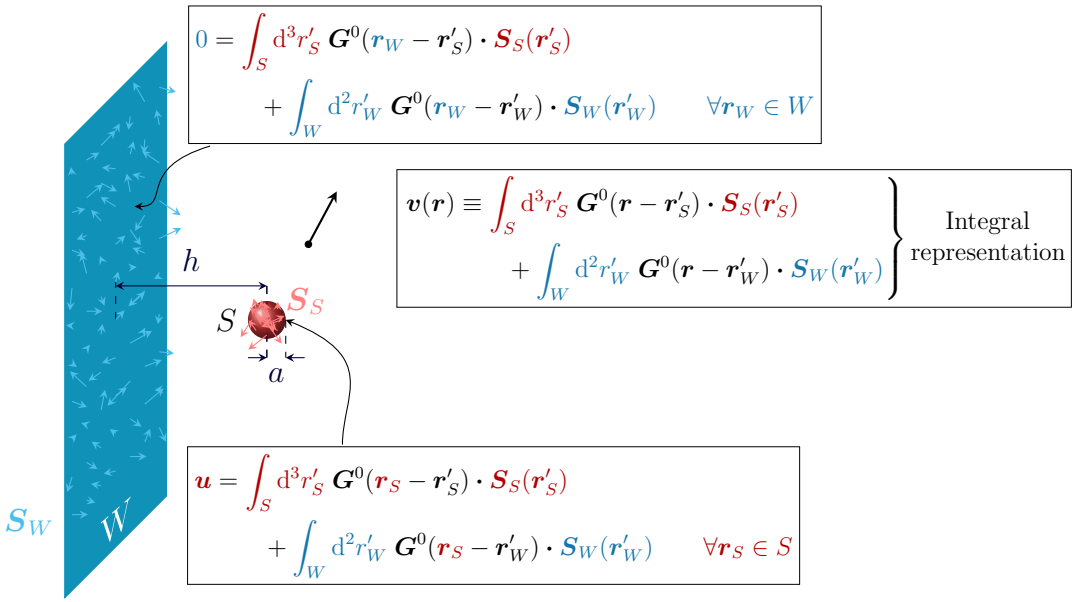

Figure 7.1: A cartoon visualization of the induced force distribution S_W on the wall(s) and S_S on the sphere, along with the boundary integral equations to be solved to determine them. The specific example shown here assumes no-slip boundary conditions on the wall. The integral representation of the velocity field in terms of these distributions is also shown.

which is assumed to be generated from two induced force distributions[8] – a volume force density $\boldsymbol{S}_S$ supported in the volume (inclusive of the surface) of the body S, and a surface force density[9] $\boldsymbol{S}_W$ supported on the surfaces of the walls $W = \bigcup_i W_i$ – which are to be determined from the no-slip boundary conditions. Thus $\boldsymbol{S}_S$ and $\boldsymbol{S}_W$ satisfy the Fredholm integral equations of the first kind,

$$\boldsymbol{u} = \int_S \mathrm{d}^3 r'_S\, \boldsymbol{G}^0(\boldsymbol{r}_S - \boldsymbol{r}'_S) \cdot \boldsymbol{S}_S(\boldsymbol{r}'_S) + \int_W \mathrm{d}^2 r'_W\, \boldsymbol{G}^0(\boldsymbol{r}_S - \boldsymbol{r}'_W) \cdot \boldsymbol{S}_W(\boldsymbol{r}'_W) \qquad \forall \boldsymbol{r}_S \in S, \tag{7.25}$$

[8]We assume that the surfaces involved satisfy the requirements outlined by Pozrikidis [1992, §4.1, 4.2] for representation of the flow by a single-layer potential, i.e. the surfaces are Lyapunov surfaces. While the integral condition $\int_D \boldsymbol{v}(\boldsymbol{r}') \cdot \hat{\boldsymbol{n}}(\boldsymbol{r}')\, \mathrm{d}^2 r' = 0$ is satisfied for compact D by virtue of non-penetration, we have shown (§3.8.4) that we would expect it to hold for each non-zero frequency component of the unsteady Stokes flow for an infinite wall too. In particular, one may explicitly solve for the Green's function satisfying no-slip conditions on a plane wall by means of a single-layer potential in the place of the wall. This explicit calculation is presented in appendix B.

[9]While it would be possible to use a volume force density instead here as well, it does not make a difference for our purposes.

$$0 = \int_S \mathrm{d}^3 r'_S \, \boldsymbol{G}^0(\boldsymbol{r}_W - \boldsymbol{r}'_S) \cdot \boldsymbol{S}_S(\boldsymbol{r}'_S) + \int_W \mathrm{d}^2 r'_W \, \boldsymbol{G}^0(\boldsymbol{r}_W - \boldsymbol{r}'_W) \cdot \boldsymbol{S}_W(\boldsymbol{r}'_W) \qquad \forall \boldsymbol{r}_W \in W. \tag{7.26}$$

We remark that if the Green's function $\boldsymbol{G}$ that satisfies the boundary conditions on the walls were known, it would be possible to rewrite the problem purely in terms of S_S as

$$\begin{aligned} \boldsymbol{v}(\boldsymbol{r}) &= \int_S \mathrm{d}^3 r'_S \, \boldsymbol{G}(\boldsymbol{r}|\boldsymbol{r}'_S) \cdot \boldsymbol{S}_S(\boldsymbol{r}'_S), \\ \boldsymbol{u} &= \int_S \mathrm{d}^3 r'_S \, \boldsymbol{G}(\boldsymbol{r}_S|\boldsymbol{r}'_S) \cdot \boldsymbol{S}_S(\boldsymbol{r}'_S) \qquad \forall \boldsymbol{r}_S \in S. \end{aligned} \tag{7.27}$$

We shall now proceed to introduce a formal perturbative expansion in a parameter λ, which represents the ratio of the body size ($\sim a$) to the distance to the walls ($\sim h$). We begin by introducing expansions for the force distributions,

$$\begin{aligned} \boldsymbol{S}_S &= \boldsymbol{S}_S^{(0)} + \lambda \boldsymbol{S}_S^{(1)} + \lambda^2 \boldsymbol{S}_S^{(2)} + \dots, \\ \boldsymbol{S}_W &= \boldsymbol{S}_W^{(0)} + \lambda \boldsymbol{S}_W^{(1)} + \lambda^2 \boldsymbol{S}_W^{(2)} + \dots. \end{aligned} \tag{7.28}$$

These expansions induce expansions for the other quantities in the problem,

$$\begin{aligned} \boldsymbol{v} &= \boldsymbol{v}^{(0)} + \lambda \boldsymbol{v}^{(1)} + \lambda^2 \boldsymbol{v}^{(2)} + \dots, \\ \boldsymbol{F}_{\mathrm{drag}} &= \boldsymbol{F}_{\mathrm{drag}}^{(0)} + \lambda \boldsymbol{F}_{\mathrm{drag}}^{(1)} + \lambda^2 \boldsymbol{F}_{\mathrm{drag}}^{(2)} + \dots. \end{aligned} \tag{7.29}$$

In analogy with examples from electrostatics, we expect that the effect of the induced force $\boldsymbol{S}_W$ on the walls is diminished in the region occupied by the body. We shall further investigate this assumption, restated formally in (7.34), at the end of this section. To emphasize this, we rewrite (7.25) as

$$\boldsymbol{u} = \int_S \mathrm{d}^3 r'_S \, \boldsymbol{G}^0(\boldsymbol{r}_S - \boldsymbol{r}'_S) \cdot \boldsymbol{S}_S(\boldsymbol{r}'_S) + \lambda \int_W \mathrm{d}^2 r'_W \, \frac{\boldsymbol{G}^0(\boldsymbol{r}_S - \boldsymbol{r}'_W) \cdot \boldsymbol{S}_W(\boldsymbol{r}'_W)}{\lambda} \qquad \forall \boldsymbol{r}_S \in S. \tag{7.30}$$

We would like a scheme where the velocity field from any $O(\lambda^k)$ truncation of the problem is faithful both near the walls and the body. The above convention makes this manifest.

We may now plug in the expansions and rewrite the problem {(7.24), (7.26), (7.30)} order-by-order as

$$\boldsymbol{v}^{(n)}(\boldsymbol{r}) = \int_S \mathrm{d}^3 r'_S \, \boldsymbol{G}^0(\boldsymbol{r} - \boldsymbol{r}'_S) \cdot \boldsymbol{S}_S^{(n)}(\boldsymbol{r}'_S) + \int_W \mathrm{d}^2 r'_W \, \boldsymbol{G}^0(\boldsymbol{r} - \boldsymbol{r}'_W) \cdot \boldsymbol{S}_W^{(n)}(\boldsymbol{r}'_W), \tag{7.31}$$

with the boundary condition on the body S

$$\begin{aligned}
\boldsymbol{u} &= \int_S \mathrm{d}^3 r'_S \; \boldsymbol{G}^0(\boldsymbol{r}_S - \boldsymbol{r}'_S) \cdot \boldsymbol{S}_S^{(0)}(\boldsymbol{r}'_S) \qquad \forall \boldsymbol{r}_S \in S, \\
0 &= \int_S \mathrm{d}^3 r'_S \; \boldsymbol{G}^0(\boldsymbol{r}_S - \boldsymbol{r}'_S) \cdot \boldsymbol{S}_S^{(n+1)}(\boldsymbol{r}'_S) \\
&\qquad + \frac{1}{\lambda} \int_W \mathrm{d}^2 r'_W \; \boldsymbol{G}^0(\boldsymbol{r}_S - \boldsymbol{r}'_W) \cdot \boldsymbol{S}_W^{(n)}(\boldsymbol{r}'_W) \qquad \forall n \geq 0, \; \forall \boldsymbol{r}_S \in S,
\end{aligned} \tag{7.32}$$

and the boundary condition on the walls

$$\begin{aligned}
0 &= \int_S \mathrm{d}^3 r'_S \; \boldsymbol{G}^0(\boldsymbol{r}_W - \boldsymbol{r}'_S) \cdot \boldsymbol{S}_S^{(n)}(\boldsymbol{r}'_S) \\
&\qquad + \int_W \mathrm{d}^2 r'_W \; \boldsymbol{G}^0(\boldsymbol{r}_W - \boldsymbol{r}'_W) \cdot \boldsymbol{S}_W^{(n)}(\boldsymbol{r}'_W) \qquad \forall n \geq 0, \; \forall \boldsymbol{r}_W \in W.
\end{aligned} \tag{7.33}$$

We shall now proceed to investigate the assumption that

$$\frac{1}{u} \int_W \mathrm{d}^2 r'_W \; \boldsymbol{G}^0(\boldsymbol{r}_S - \boldsymbol{r}'_W) \cdot \left[\lambda^k \boldsymbol{S}_W^{(k)}(\boldsymbol{r}'_W) \right] \in O(\lambda^{k+1}). \tag{7.34}$$

First, we note that $\boldsymbol{S}_W^{(k)}$ is obtained by solving (7.33) with the knowledge of $\boldsymbol{S}_S^{(k)}$. In the spirit of multipole expansions, since the free-space Green's function $\boldsymbol{G}^0(\boldsymbol{r}_W - \boldsymbol{r}'_S)$ in the first integral of (7.33) is evaluated at a far separation, we may expand it in the vicinity of the location of the body $\boldsymbol{r}_0$,

$$\begin{aligned}
\boldsymbol{G}^0(\boldsymbol{r}_W - \boldsymbol{r}'_S) &= \boldsymbol{G}^0(\boldsymbol{r}_W - \boldsymbol{r}_0) + (\boldsymbol{r}'_S - \boldsymbol{r}_0) \cdot \boldsymbol{\nabla} \boldsymbol{G}^0(\boldsymbol{r}_W - \boldsymbol{r}_0) + \ldots \\
&= \boldsymbol{G}^0(\boldsymbol{r}_W - \boldsymbol{r}_0) + o(\lambda), \qquad \boldsymbol{r}'_S \in S.
\end{aligned} \tag{7.35}$$

The issue of the validity of such an expansion is subtle and will be addressed in detail in Section 7.3.4. Using this expansion in (7.33), we have

$$\int_W \mathrm{d}^2 r'_W \; \boldsymbol{G}^0(\boldsymbol{r}_W - \boldsymbol{r}'_W) \cdot \boldsymbol{S}_W^{(k)}(\boldsymbol{r}'_W) = -\boldsymbol{G}^0(\boldsymbol{r}_W - \boldsymbol{r}_0) \cdot \int_S \mathrm{d}^3 r'_S \; \boldsymbol{S}_S^{(k)}(\boldsymbol{r}'_S) + o(\lambda). \tag{7.36}$$

We now state a useful result: if $\tilde{\boldsymbol{S}}_W$ satisfies the integral equation

$$\int_W \mathrm{d}^2 r'_W \; \boldsymbol{G}^0(\boldsymbol{r}_W - \boldsymbol{r}'_W) \cdot \tilde{\boldsymbol{S}}_W(\boldsymbol{r}'_W) = -\boldsymbol{G}^0(\boldsymbol{r}_W - \boldsymbol{r}_0) \cdot \tilde{\boldsymbol{F}} \quad \forall \boldsymbol{r}_W \in W \tag{7.37}$$

for arbitrary point $\boldsymbol{r}_0$ and force $\tilde{\boldsymbol{F}}$, then for general $\boldsymbol{r}$ in the domain,

$$\int_W \mathrm{d}^2 r'_W \boldsymbol{G}^0(\boldsymbol{r} - \boldsymbol{r}'_W) \cdot \tilde{\boldsymbol{S}}_W(\boldsymbol{r}'_W) = \left[\boldsymbol{G}(\boldsymbol{r}|\boldsymbol{r}_0) - \boldsymbol{G}^0(\boldsymbol{r} - \boldsymbol{r}_0) \right] \cdot \tilde{\boldsymbol{F}}, \tag{7.38}$$

where $\boldsymbol{G}(\boldsymbol{r}|\boldsymbol{r}_0)$ is the Green's function that satisfies no-slip boundary conditions on the walls. This is easily seen if we set up the problem for the no-slip Green's function for the walls by imposing the boundary condition through a surface force distribution $\tilde{\boldsymbol{S}}_W$ on the walls.

If we choose for $\tilde{\boldsymbol{F}}$ the force

$$\int_S \mathrm{d}^3 r'_S \; \boldsymbol{S}_S^{(k)}(\boldsymbol{r}'_S), \tag{7.39}$$

we find by comparing (7.36) and (7.37) that we may write

$$\begin{aligned} &\int_W \mathrm{d}^2 r'_W \; \boldsymbol{G}^0(\boldsymbol{r} - \boldsymbol{r}'_W) \cdot \boldsymbol{S}_W^{(k)}(\boldsymbol{r}'_W) \\ &\qquad = \big[\boldsymbol{G}(\boldsymbol{r}|\boldsymbol{r}_0) - \boldsymbol{G}^0(\boldsymbol{r} - \boldsymbol{r}_0)\big] \cdot \int_S \mathrm{d}^3 r'_S \; \boldsymbol{S}_S^{(k)}(\boldsymbol{r}'_S) + o(\lambda) \end{aligned} \tag{7.40}$$

for any point $\boldsymbol{r}$ in the domain.

Finally, we observe that we may approximate the expression in question as

$$\begin{aligned} &\frac{\lambda^k}{u} \int_W \mathrm{d}^2 r'_W \; \boldsymbol{G}^0(\boldsymbol{r}_S - \boldsymbol{r}'_W) \cdot \boldsymbol{S}_W^{(k)}(\boldsymbol{r}'_W) \\ &\qquad = \frac{\lambda^k}{u} \int_W \mathrm{d}^2 r'_W \; \boldsymbol{G}^0(\boldsymbol{r}_0 - \boldsymbol{r}'_W) \cdot \boldsymbol{S}_W^{(k)}(\boldsymbol{r}'_W) + o(\lambda^{k+1}) \\ &\qquad = \frac{\lambda^k}{u} \lim_{\boldsymbol{r}_S \to \boldsymbol{r}_0} \big[\boldsymbol{G}(\boldsymbol{r}_S|\boldsymbol{r}_0) - \boldsymbol{G}^0(\boldsymbol{r}_S - \boldsymbol{r}_0)\big] \cdot \int_S \mathrm{d}^3 r'_S \; \boldsymbol{S}_S^{(k)}(\boldsymbol{r}'_S) + o(\lambda^{k+1}) \\ &\qquad = \frac{\lambda^k}{u} \boldsymbol{R}(\boldsymbol{r}_0) \cdot \int_S \mathrm{d}^3 r'_S \; \boldsymbol{S}_S^{(k)}(\boldsymbol{r}'_S) + o(\lambda^{k+1}). \end{aligned} \tag{7.41}$$

Thus, if

$$\frac{1}{u} \boldsymbol{R}(\boldsymbol{r}_0) \cdot \int_S \mathrm{d}^3 r'_S \; \boldsymbol{S}_S^{(k)}(\boldsymbol{r}'_S) \in O(\lambda), \tag{7.42}$$

then the assumption (7.34) holds. Intuitively, one may expect the above condition to hold on the grounds that the reaction field tensor is the reflected flow evaluated at the location of the particle, and this reflected flow must be suppressed at least as $1/h$, h being the distance to the wall, whereas one would expect the remaining terms to produce a factor of a.

7.3.3 Formalization of the point-particle approximation

In this sub-section and the next, we seek to formalize the point-particle framework by explicitly performing all the approximations involved in a systematic manner, using

the formalism developed in the previous sub-section. We shall eventually specialize S to be a sphere while still keeping W arbitrary.

To solve the problem at order $n = 0$, we begin by noting that the solution to the first of (7.32) is the induced force on the body oscillating with velocity $\boldsymbol{u}$ in unbounded fluid, whereby

$$\boldsymbol{v}^S(\boldsymbol{r}) \equiv \int_S \mathrm{d}^3 r'_S \; \boldsymbol{G}^0(\boldsymbol{r} - \boldsymbol{r}'_S) \cdot \boldsymbol{S}_S^{(0)}(\boldsymbol{r}'_S) \tag{7.43}$$

where we have used $\boldsymbol{v}^S(\boldsymbol{r})$ to denote the velocity field generated by the body S oscillating in unbounded fluid. We must now find $\boldsymbol{S}_W^{(0)}$ using (7.33), which is not analytically tractable without approximation. Therefore, we make the same approximations that lead to (7.36). As we will see shortly, to compute the drag force to first order, we do not need to know $\boldsymbol{S}_W^{(0)}$, but only need to be able to compute the effect of this distribution in the vicinity of the body. Proceeding as we did in Section 7.3.2, we may therefore write (7.40) for $k = 0$ as

$$\int_W \mathrm{d}^2 r'_W \; \boldsymbol{G}^0(\boldsymbol{r} - \boldsymbol{r}'_W) \cdot \boldsymbol{S}_W^{(0)}(\boldsymbol{r}'_W) = \left[\boldsymbol{G}(\boldsymbol{r}|\boldsymbol{r}_0) - \boldsymbol{G}^0(\boldsymbol{r} - \boldsymbol{r}_0)\right] \cdot \boldsymbol{F}^{(0)} + o(\lambda), \tag{7.44}$$

where we have defined

$$\boldsymbol{F}^{(k)} := \int_S \mathrm{d}^3 r'_S \; \boldsymbol{S}_S^{(k)}(\boldsymbol{r}'_S). \tag{7.45}$$

We may now write (7.32) for $n = 1$ as

$$\begin{aligned} 0 = \int_S \mathrm{d}^3 r'_S \; \boldsymbol{G}^0(\boldsymbol{r}_S - \boldsymbol{r}'_S) \cdot \boldsymbol{S}_S^{(1)}(\boldsymbol{r}'_S) \\ + \frac{1}{\lambda}\left[\boldsymbol{G}(\boldsymbol{r}_S|\boldsymbol{r}_0) - \boldsymbol{G}^0(\boldsymbol{r}_S - \boldsymbol{r}_0)\right] \cdot \boldsymbol{F}^{(0)} \quad \forall \boldsymbol{r}_S \in S. \end{aligned} \tag{7.46}$$

Our aim is to determine the correction to the drag $\boldsymbol{F}^{(1)}_{\text{drag}}$ resulting from the field $\boldsymbol{v}^{(1)}$. To determine the drag force, we only need the velocity in the near field of the body, whereby in (7.31) at any order n, we may discard the contribution from $\boldsymbol{S}_W^{(n)}$, as the unsteady Oseen tensor multiplying it contributes an extra $O(\lambda)$ when compared to the contribution from the first term when the point of evaluation $\boldsymbol{r}$ is close to the body. As a result, we obtain

$$\boldsymbol{v}^{(n)}(\boldsymbol{r}_S) = \int_S \mathrm{d}^3 r'_S \; \boldsymbol{G}^0(\boldsymbol{r}_S - \boldsymbol{r}'_S) \cdot \boldsymbol{S}_S^{(n)}(\boldsymbol{r}'_S) + O(\lambda) \qquad \forall \boldsymbol{r}_S \in S. \tag{7.47}$$

Thus, we observe that at order 0, we may use $\boldsymbol{v}^S$ of (7.43) to compute $\boldsymbol{F}^{(0)}_{\text{drag}}$, which is simply equal to the drag force on the body oscillating in unbounded fluid; and at order 1, knowledge of $\boldsymbol{S}^{(1)}_W$ is not required for the computation of $\boldsymbol{F}^{(1)}_{\text{drag}}$.

We now specialize to S being a sphere of radius a and proceed to determine $\boldsymbol{F}^{(1)}_{\text{drag}}$ for this case. If we set $\boldsymbol{v}_0(\boldsymbol{r}) := \left[\boldsymbol{G}(\boldsymbol{r}|\boldsymbol{r}_0) - \boldsymbol{G}^0(\boldsymbol{r}-\boldsymbol{r}_0)\right]\cdot\boldsymbol{F}^{(0)}$ and $\boldsymbol{v}(|\boldsymbol{r}|\leq a) = 0$ in equation (3.31), we see that (7.46) is identical to (3.31). Therefore, $\boldsymbol{F}^{(1)}_{\text{drag}}$ is given by the generalized Faxén theorem of equation (3.34), whereby we may write

$$\lambda\boldsymbol{F}^{(1)}_{\text{drag}} = \gamma_s\left[(1+\alpha a)\left\langle \boldsymbol{v}^{(1)}_W\right\rangle_S + \frac{1}{3}\alpha^2a^2\left\langle \boldsymbol{v}^{(1)}_W\right\rangle_V\right] \tag{7.48}$$

with

$$\lambda\boldsymbol{v}^{(1)}_W := \left[\boldsymbol{G}(\boldsymbol{r}|\boldsymbol{r}_0) - \boldsymbol{G}^0(\boldsymbol{r}-\boldsymbol{r}_0)\right]\cdot\boldsymbol{F}^{(0)}, \tag{7.49}$$

and $\langle\,\rangle_S$ and $\langle\,\rangle_V$ denoting surface and volume averages over the sphere respectively. We wish to note that the analysis shows that the reaction field tensor is already $O(\lambda)$, which may be verified with Felderhof's expressions for the case of a flat wall. So the total drag force may be written by adding $\boldsymbol{F}^{(0)}_{\text{drag}} = -\gamma_0(\omega)\boldsymbol{u}$ and $\lambda\boldsymbol{F}^{(1)}_{\text{drag}}$ recovering (3.34) for the drag up to first order, with $\boldsymbol{v}_0 = \lambda\boldsymbol{v}^{(1)}_W$.

We now make the approximation of truncating the infinite series to first order, excluding $o(\lambda)$ terms. As a side effect, we observe that

$$\lambda\boldsymbol{v}^{(1)}_W = \left[\boldsymbol{G}(\boldsymbol{r}|\boldsymbol{r}_0) - \boldsymbol{G}^0(\boldsymbol{r}-\boldsymbol{r}_0)\right]\cdot\left(\boldsymbol{F}^{(0)} + \lambda\boldsymbol{F}^{(1)}\right) + o(\lambda). \tag{7.50}$$

Identifying the parentheses in the above equation with the total induced force to first order,

$$\boldsymbol{F}^{\text{ind}}_{\omega} = \boldsymbol{F}^{(0)} + \lambda\boldsymbol{F}^{(1)} \tag{7.51}$$

we have shown that $\lambda\boldsymbol{v}^{(1)}_W$ is identical with $\boldsymbol{v}_W$ of equation (7.4) to lowest order.

We shall now investigate the possibility of replacing the surface and volume averages of $\lambda\boldsymbol{v}^{(1)}_W$ by evaluation of (7.49) at $\boldsymbol{r}\to\boldsymbol{r}_0$. Applying the expansion of (7.35) to (7.44) evaluated for $\boldsymbol{r}\in S$ (as done in (7.41)), we see that $\lambda\boldsymbol{v}^{(1)}_W$ may indeed be assumed to have $o(\lambda)$ variation over the region occupied by the sphere. This justifies replacing the averages in (7.48) with $\lambda\boldsymbol{v}^{(1)}_W$ evaluated as $\boldsymbol{r}\to\boldsymbol{r}_0$, subject to the validity of the expansion of (7.35).

Finally, we remark that it can be verified by plotting the explicit formulas given by Felderhof [2005] (also see erratum Felderhof [2006*b*]) over a wide range of frequencies, that the components of the reaction field tensor for the no-slip sphere-plane-wall

configuration, non-dimensionalized by multiplication with γ_s, do not significantly exceed $1(a/h)$ (see §9.3). Thus, the reaction field tensor for this particular case satisfies (7.42) and therefore validates the assumption of (7.34) by the arguments made in Section 7.3.2.

7.3.4 Far-field expansion of the unsteady Oseen tensor

In this section, we will address the validity of an expansion of the unsteady[10] Oseen tensor, of the kind described in (7.35).

It is natural to our original problem to non-dimensionalize the Oseen tensor by $\gamma_s = 6\pi\eta a$, given that our notion of forces is best normalized by $\gamma_s u$ – this results in $\boldsymbol{F}^{(0)}_{\text{drag}}$ being $O(1)$ in our book-keeping. However, the Oseen tensor $\boldsymbol{G}^0(\boldsymbol{q})$ is naturally a function of $\alpha\boldsymbol{q}$, whereby for this analysis, it will be convenient to normalize it by $1/\alpha$ and write

$$\begin{aligned} 4\pi\bar{\boldsymbol{G}}^0(\alpha\boldsymbol{q}) := 4\pi\eta\boldsymbol{G}^0(\boldsymbol{q})/\alpha = \hat{\boldsymbol{e}}_q\hat{\boldsymbol{e}}_q\frac{2}{(\alpha q)^3}\left[1-(1+\alpha q)\mathrm{e}^{-\alpha q}\right] \\ + (\mathbb{1}-\hat{\boldsymbol{e}}_q\hat{\boldsymbol{e}}_q)\,\frac{1}{(\alpha q)^3}\left[(1+\alpha q+\alpha^2 q^2)\mathrm{e}^{-\alpha q}-1\right], \end{aligned} \tag{7.52}$$

where $\hat{\boldsymbol{e}}_q$ denotes the unit vector along $\boldsymbol{q}$. In expansions of the form of (7.35), we write $\boldsymbol{q} = \boldsymbol{q}_L + \boldsymbol{q}_S$ where $\boldsymbol{q}_L$ denotes a large displacement of $O(h)$ and $\boldsymbol{q}_S$ denotes a small displacement of $O(a)$. Typically, $\boldsymbol{q}_L$ is $\boldsymbol{r}_0 - \boldsymbol{r}'_W$ where $\boldsymbol{r}'_W$ is some point on the wall and $\boldsymbol{q}_S$ is $\boldsymbol{r}_S - \boldsymbol{r}_0$ where $\boldsymbol{r}_S$ is some point in the body S. We write

$$\bar{\boldsymbol{G}}^0(\alpha\boldsymbol{q}) = \bar{\boldsymbol{G}}^0(\alpha\boldsymbol{q}_L) + \alpha\boldsymbol{q}_S\cdot\boldsymbol{\nabla}_{\alpha\boldsymbol{q}_S}\bar{\boldsymbol{G}}^0(\alpha\boldsymbol{q}_L) + o(\alpha\boldsymbol{q}_S), \tag{7.53}$$

where $\boldsymbol{\nabla}_{\alpha\boldsymbol{q}_S}$ denotes a gradient with respect to the quantity $\alpha\boldsymbol{q}_S$. Such an expansion may be expected to be valid whenever the function is sufficiently slowly varying for small changes in $\boldsymbol{q}_S$ (i.e. changes over the scale of the size of the body). However, for sufficiently high wavenumbers α, it appears that oscillating terms of the nature $\mathrm{e}^{\mathrm{i}\,\Im(\alpha)\,\boldsymbol{q}_S}$ would vary very rapidly – whereby care must be taken to analyze such an expansion. Specifically, for the Helmholtz Green's function $-\mathrm{e}^{\mathrm{i}kq}/(4\pi\mathrm{i}kq)$, such an expansion is strictly valid only if $|\boldsymbol{q}_S| \ll 1/k$ and $|\boldsymbol{q}_S| \ll |\boldsymbol{q}_L|$, as is often noted

[10] In this work, we will frequently drop the adjective unsteady to simplify our language. Since our work primarily concerns unsteady flow, this should not cause confusion. We will explicitly specify so when we refer to the steady Oseen tensor.

when considering multipole expansions for electromagnetic radiation [see e.g. Jackson, 1999, §9.1]. However, in the Oseen tensor, the complex wavenumber $\alpha = ik$ has a positive real part which causes significant suppression of the exponentials at large values of α, in comparison to the terms originating from the fundamental solution of the Laplace equation $G(\boldsymbol{q};0)$. Essentially, for large α, the contribution from $G(\boldsymbol{q};\omega)$ becomes subdominant, which results in the expansion once again being valid for large α. However, it must be noted that the expansion may not work if the subdominant behavior is of primary interest, as could be the case.

We may verify the above intuitive remarks about the expansion by considering the ratio of the first order term in the Taylor expansion to the zeroth order term. To get an order of magnitude estimate, we will treat the longitudinal and transverse components of $\bar{\boldsymbol{G}}^0$ separately, and specifically set $q_L = h$ and $q_S = a$. Then, the desired ratios have the form

$$\frac{a}{h}\frac{\mathrm{e}^{-\mathfrak{v}}(3+3\mathfrak{v}+\mathfrak{v}^2)-3}{\mathrm{e}^{-\mathfrak{v}}(1+\mathfrak{v})-1}, \tag{7.54}$$

and

$$\frac{a}{h}\frac{\mathrm{e}^{-\mathfrak{v}}(3+3\mathfrak{v}+2\mathfrak{v}^2+\mathfrak{v}^3)-3}{\mathrm{e}^{-\mathfrak{v}}(1+\mathfrak{v}+\mathfrak{v}^2)-1}, \tag{7.55}$$

respectively, where we have used the shorthand[11] $\mathfrak{v} := \alpha h$. While a/h is assumed to be small from the geometry of the problem, no assumptions can be made about α. So we must check that the parts of the ratios that contain only $\mathfrak{v}$ remain $\lesssim 1$. Noting that $\mathfrak{v}$ has the form $\frac{1-\mathrm{i}}{\sqrt{2}}|\mathfrak{v}|$ and plotting these parts against a large range of values of $|\mathfrak{v}|$ (or alternately, by analysis), we find that the real and imaginary parts of the above ratios are bounded and do not significantly exceed 1 throughout the range. This indicates that the approximation can be expected to work well for all values of α so long as a/h is small.

Intuitively speaking, this seems to suggest that at high frequencies, the primary contribution to the correction of the drag on the particle due to the presence of walls comes from the pressure, rather than from vorticity diffusion. The skin-depth of the vorticity is then too small for the effects of vorticity diffusion from the wall to be significant at the location of the particle and vice versa. The effects of vorticity

[11] The same quantity we denote by $\mathfrak{v}$ in this work has been denoted by v in Felderhof's articles, and by ν in Simha *et al.* [2017]. We wish to avoid any ambiguity with ν being used for kinematic viscosity and v being used for fluid velocities.

local to the particle and the wall themselves are however, important, and they are accounted for correctly in the framework.

Thus, we have shown that Felderhof's point-particle framework, with our modified point force $\boldsymbol{F}_\omega^{\text{ind}}$, may be expected to work well at all frequencies[12] so long as $a/h \ll 1$.

7.3.5 Computing the perturbative expansion to all orders

Before we begin, we shall rewrite the result of the generalized Faxén theorem (Section 3.7) in a form that is readily usable in this section. In equation (3.31), we set $\boldsymbol{v} = 0$ within the region of the sphere, and we correspondingly set $\boldsymbol{u}_\omega = 0$ in (3.34) and use (3.32) to obtain the following result: If the force distribution $\tilde{\boldsymbol{S}}$ on a sphere of radius a obeys the integral equation

$$\int_{|\boldsymbol{r}'_S|\leq a} \boldsymbol{G}^0(\boldsymbol{r}_S - \boldsymbol{r}'_S) \cdot \tilde{\boldsymbol{S}}(\boldsymbol{r}'_S)\, \mathrm{d}^3 r'_S = -\boldsymbol{v}_0(\boldsymbol{r}_S), \qquad \forall |\boldsymbol{r}_S| \leq a, \tag{7.56}$$

for some vector field $\boldsymbol{v}_0(\boldsymbol{r}_S)$ having support in the region of the sphere, then we may write the net induced force in the region of the sphere as

$$\int_{|\boldsymbol{r}'_S|\leq a} \tilde{\boldsymbol{S}}(\boldsymbol{r}'_S)\, \mathrm{d}^3 r'_S = -\gamma_s \left[(1+\alpha a)\bar{\boldsymbol{v}}_0^S(\omega) + \frac{1}{3}\alpha^2 a^2 \bar{\boldsymbol{v}}_0^V(\omega) \right]. \tag{7.57}$$

We now consider the extension of the calculation performed in Section 7.3.3 to higher orders for the case where S is a sphere of radius a. By using the result (7.41) in the boundary condition on the body (7.32), we may write

$$\begin{aligned} 0 = \int_S \mathrm{d}^3 r'_S\, \boldsymbol{G}^0(\boldsymbol{r}_S - \boldsymbol{r}'_S) \cdot \boldsymbol{S}_S^{(n+1)}(\boldsymbol{r}'_S) \\ + \frac{1}{\lambda}\boldsymbol{R}(\boldsymbol{r}_0) \cdot \int_S \mathrm{d}^3 r'_S\, \boldsymbol{S}_S^{(n)}(\boldsymbol{r}'_S) \qquad \forall n \geq 0,\ \forall \boldsymbol{r}_S \in S. \end{aligned} \tag{7.58}$$

We note that the second term is independent of $\boldsymbol{r}_S$ to the lowest order.

By comparing the above equation with equation (7.56), we see that (7.57) gives us

$$\int_S \mathrm{d}^3 r'_S\, \boldsymbol{S}_S^{(n+1)}(\boldsymbol{r}'_S) = \left[\frac{-\tilde{\gamma}_0 \boldsymbol{R}(\boldsymbol{r}_0)}{\lambda} \right]^{n+1} \cdot \int_S \mathrm{d}^3 r'_S\, \boldsymbol{S}_S^{(0)}(\boldsymbol{r}'_S), \tag{7.59}$$

[12] It must still be the case however, as stated earlier, that the frequencies be small enough that the fluid may be considered to be incompressible. For micron-sized particles in water, the regime where compressibility matters is usually of the order of GHz.

which yields a geometric series. This indicates that we may write the net induced force on the sphere as

$$\begin{aligned}\boldsymbol{F}_{\omega}^{\mathrm{ind}} = \int_S \mathrm{d}^3 r'_S \; \boldsymbol{S}_S(\boldsymbol{r}'_S) &= \sum_{k=0}^{\infty} \int_S \mathrm{d}^3 r'_S \; \lambda^k \boldsymbol{S}_S^{(k)}(\boldsymbol{r}'_S) \\ &= \left(\sum_{k=0}^{\infty} \left[-\tilde{\gamma}_0 \boldsymbol{R}(\boldsymbol{r}_0) \right]^k \right) \cdot \int_S \mathrm{d}^3 r'_S \; \boldsymbol{S}_S^{(0)}(\boldsymbol{r}'_S) \\ &= \left[\mathbb{1} + \tilde{\gamma}_0 \boldsymbol{R}(\boldsymbol{r}_0) \right]^{-1} \cdot \int_S \mathrm{d}^3 r'_S \; \boldsymbol{S}_S^{(0)}(\boldsymbol{r}'_S),\end{aligned} \tag{7.60}$$

provided the geometric series converges.

By comparing the first of (7.32) with (7.56), we find from (7.57) that

$$\int_S \mathrm{d}^3 r'_S \; \boldsymbol{S}_S^{(0)}(\boldsymbol{r}'_S) = \tilde{\gamma}_0 \boldsymbol{u}.$$

Thereafter, using (3.32) we find that the drag force to all orders in a/h is given by

$$\boldsymbol{F}_{\omega}^{\mathrm{drag}} = -\mathrm{i}\omega m_f - \tilde{\gamma}_0 \left[\mathbb{1} + \tilde{\gamma}_0 \boldsymbol{R}(\boldsymbol{r}_0) \right]^{-1} \cdot \boldsymbol{u}, \tag{7.61}$$

whereby we recover the result (7.21). Thus, it appears that in the region of convergence of the geometric series, the results of the point-particle framework are correct to all orders of perturbation theory.

However, this does not mean that it is exact irrespective of how large a/h is, since the perturbative process does not necessarily capture the corrections that lie beyond all orders faithfully, which become significant as $a/h \to 1$. In fact, in the next section, we will compare the first order results from the point-particle approximation against the method of reflections for the simpler case of full-slip boundary conditions on the wall, and discover that the subdominant terms do differ.

Chapter Eight: The Point-Particle Approximation and Method of Reflections – a comparative study

In this chapter, we will present a calculation of the unsteady drag coefficient of a no-slip sphere near a full-slip plane wall using the method of reflections, and also present results for the drag coefficient of a no-slip sphere near a full-slip plane wall obtained using the unmodified [Felderhof, 2012] and modified (Chapter 7) point-particle approximation. We shall compare the results from the three methods, viz. the method of reflections, the unmodified PPA (also referred to as Felderhof's PPA in this work), and our modified PPA, both by asymptotic analysis and by numerical evaluation.

The purpose of these comparisons is to investigate the claims of Chapter 7 in a simple, specific case-study, where the alternative calculation using the method of reflections may be performed without any approximations that involve assumptions on the skin-depth of vorticity. The key results of this comparative study are (i) the modification to the point-particle approximation results in a drag coefficient that asymptotes to the added mass obtained through potential flow calculations, (ii) the point-particle approximation does not faithfully capture all non-perturbative (as $\epsilon \to 0^+$) terms, but where these non-perturbative terms are important, the assumptions of the point-particle approximation are indeed valid, whereby it works in practice.

The material of this chapter is largely lifted from a draft of an article [Simha *et al.*, 2017] that the author of this dissertation has co-authored with Dr. Jianyong Mo and Prof. Philip J. Morrison.[1]

[1] A. Simha, J. Mo, and P. J. Morrison, "Unsteady Stokes flow near boundaries: the point-particle approximation and the method of reflections." Submitted for review to the *Journal of Fluid Mechanics* in July 2017. This method of reflections problem was envisioned by P. J. Morrison and A. Simha. A. Simha, J. Mo and Wolfram Mathematica were responsible for performing and cross-checking the calculations presented here. A. Simha made the graphics and plots that appear here. Much of the text of this work was authored and typeset by A. Simha, with many helpful suggestions from P. J. Morrison and J. Mo.

8.1 Method of Reflections – a no-slip sphere near a full-slip plane wall

The method of reflections has been heavily used as an approximation method in the context of steady Stokes flow [see e.g. Happel & Brenner, 1965; Kim & Karrila, 2013]. A proof of the convergence of the iterative process for steady Stokes flows under certain restrictions exists [Luke, 1989], although this has not been extended to unsteady Stokes flows (to the best of our knowledge).[2] The method of reflections has been used in the context of unsteady Stokes flows for the case of two spheres with no-slip boundary conditions by Ardekani & Rangel [2006], but their procedure involves evaluation of the reflected field at the center of the sphere at each iteration. Although the procedure converges and produces consistent results, for our comparative study, we would prefer to investigate a procedure that would avoid any further approximation beyond truncation of the iterative process, so that we can be confident that the approximation works at all frequencies of oscillation. We remark however, that the analysis of Ardekani & Rangel [2006] seems to be similar in content to that of Section 7.3.5, whereby we may expect their result to differ only in corrections that lie beyond all orders.

Here, we shall consider the same geometry of a small sphere performing small oscillations near a flat wall, but with the simpler case of free-slip boundary conditions on the wall. As before, we shall assume no-slip boundary conditions on the sphere. We shall truncate the iterative procedure after one reflection from the wall, but without further approximation, yielding results that are expected to be correct to lowest order in a/h for arbitrary frequency of oscillation ω. The choice of full-slip boundary conditions on the wall,[3] as opposed to the more common no-slip / partial-slip boundary conditions, makes the problem particularly simple as we may employ the method of images, and place an image sphere behind the wall in order to satisfy boundary conditions on the wall. This simplicity enables exact evaluation of the surface and volume average integrals that enter the generalized Faxén theorem (Section 3.7) in closed form.

[2] A formalism of the sort developed in 7.3.2 could serve as a starting point for a proof.

[3] Full-slip boundary conditions are physically realizable at gas-liquid interfaces [Wang *et al.*, 2009], and can be approximately realized at some solid-liquid interfaces by means of nano-fabricated structures [Choi & Kim, 2006]

We shall break up the problem into two sub-problems: one with the sphere oscillating perpendicular to the wall, and the other with the sphere oscillating parallel to the wall along any particular direction. In each case, we shall compute the drag force along the direction of oscillation.

In anisotropic geometries, in addition to the drag, the sphere may also experience a force in the directions normal to its motion, which would correspond to off-diagonal terms in $\boldsymbol{\gamma}(\omega)$. We show that within the approximations used in this work, these forces are zero. In the steady case, such effects have been shown to exist when the advective term of the Navier-Stokes equations is retained in the Oseen approximation [see e.g. Faxén, 1921; Shinohara & Hashimoto, 1979]

We shall use the results for the flow around a sphere oscillating in an unbounded fluid, discussed in §3.6, in the calculations that follow.

8.1.1 Image system for a full-slip plane wall: Perpendicular oscillations

Let the fluid fill the half-space $\mathbb{R}^+ \times \mathbb{R}^2$ indexed by cylindrical coordinates $\rho > 0,\ z > -h,\ 0 \leq \varphi < 2\pi$ $(h > 0)$. Let the sphere S of radius a lie at the point $\rho = 0,\ z = 0$. The plane wall W is located at the plane $z = -h$. For convenience, we introduce additional coordinate systems: a spherical coordinate system $(r,\, \theta,\, \varphi)$ with origin at $z = 0$ and polar axis along the positive z-axis; and a spherical coordinate system $(r',\, \theta',\, \varphi)$ with origin at $z = -2h$ and polar axis along the positive z-axis. Let the sphere oscillate with velocity $\boldsymbol{u}_\omega = +1\hat{\boldsymbol{e}}_z$, where $\hat{\boldsymbol{e}}_z$ is the unit vector along the positive z-direction. The situation is visualized in figure 8.1.1.

The velocity field (3.27) of the sphere does not satisfy the full-slip boundary conditions on the wall W,

$$\hat{\boldsymbol{e}}_z \cdot \boldsymbol{v}_\omega|_W = 0,$$
$$\hat{\boldsymbol{e}}_z \cdot \boldsymbol{\nabla} \boldsymbol{v}_{\omega,\perp}|_W = \boldsymbol{0},$$

where $\boldsymbol{v}_{\omega,\perp} = \boldsymbol{v}_\omega - (\hat{\boldsymbol{e}}_z \cdot \boldsymbol{v}_\omega)\hat{\boldsymbol{e}}_z$, although it satisfies the no-slip boundary conditions on the sphere S. Thus, we introduce an additional field[4] $\boldsymbol{v}_\omega^{(1)}$ such that $\boldsymbol{v}_\omega + \boldsymbol{v}_\omega^{(1)}$ satisfies full-slip boundary conditions at wall W. The field $\boldsymbol{v}_\omega^{(1)}$ could be regarded as the flow reflected from the wall. We could consider $\boldsymbol{v}_\omega^{(1)}$ to be produced by an *image*

[4]While there are indeed pressure fields associated with each of these velocity fields, it turns out that they are not directly relevant to our calculations.

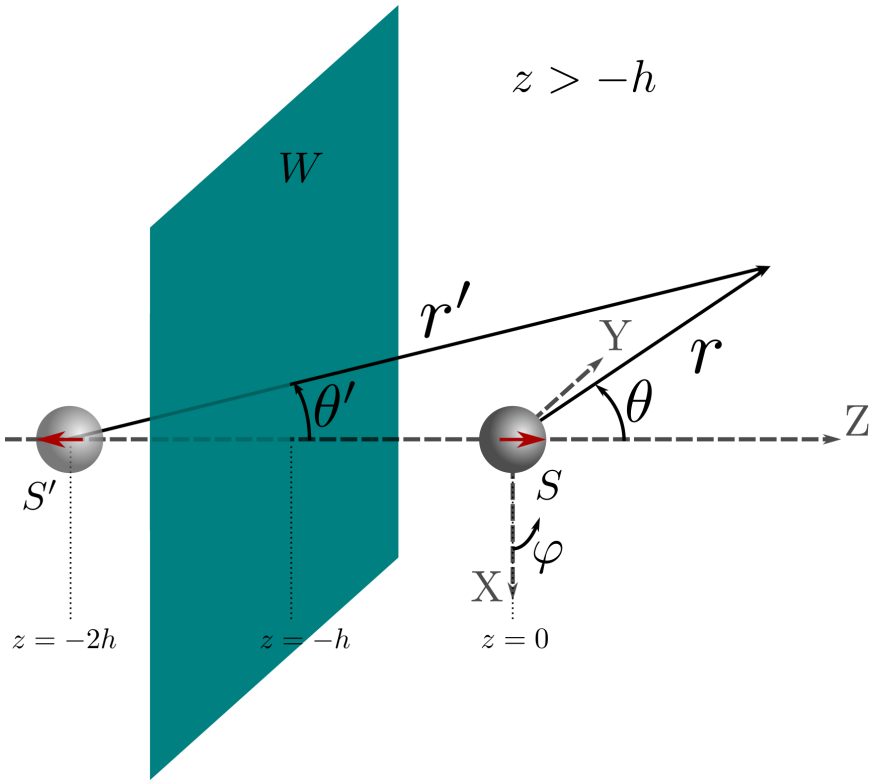

Figure 8.1: Image system for oscillations perpendicular to the wall, and coordinate systems adapted to the geometry.

sphere S' centered at $z = -2h$ and having velocity $\boldsymbol{u'}_\omega = -1\hat{\boldsymbol{e}}_z$. By symmetry, the boundary conditions at W are then satisfied. However, the combined field $\boldsymbol{v}_\omega + \boldsymbol{v}_\omega^{(1)}$ will not satisfy the no-slip boundary conditions on ∂S. Instead of computing the next reflected field $\boldsymbol{v}_\omega^{(2)}$ that corrects for the boundary conditions on the sphere, we shall simply employ $\boldsymbol{v}_\omega^{(1)}$ as the background field in the generalized Faxén theorem (3.34) to calculate the drag coefficient. The iterative procedure of reflections shall be truncated at this point. Thus, it suffices to calculate the image field $\boldsymbol{v}_\omega^{(1)}$. The image field is simply given by using (3.27) with the replacements $u_\omega \to -1$, $\theta \to \theta'$, $r \to r'$. However, in order to employ the generalized Faxén theorem, we would need to average this field over ∂S and S. To do so, the following co-ordinate conversion formulas are

handy,

$$\begin{aligned} \rho &= r' \sin\theta' = r \sin\theta, \\ z &= r\cos\theta = r'\cos\theta' - 2h, \\ r'^2 &= 4h^2 + r^2 + 4rh\cos\theta, \\ r^2 &= \rho^2 + z^2, \\ r'^2 &= \rho^2 + (2h+z)^2. \end{aligned} \tag{8.1}$$

It is also convenient to introduce the non-dimensionalized variables, $\xi := r'/(2h)$, $\delta = \alpha a$, $\epsilon = a/h$. Then we may write the dimensionless function $F_0(\xi) := f'(r')/r'$, i.e. the function of equation (3.25) evaluated instead at r', as

$$F_0(\xi) = \frac{1}{\xi^3}\left[p\,\mathrm{e}^{-2\delta\xi/\epsilon}\left(1 + \frac{2\delta\xi}{\epsilon}\right) - q\right], \tag{8.2}$$

where the constants $p := 3\epsilon^3\mathrm{e}^{\delta}/(16\delta^2)$ and $q := 3\epsilon^3(1+\delta+\delta^2/3)/(16\delta^2)$.

8.1.2 Drag coefficient for perpendicular oscillations

With these preparations, we are ready to calculate the drag force on the sphere for oscillations perpendicular to the wall. To do so, we need to compute the averages of the first reflected field $\boldsymbol{v}_\omega^{(1)} = -\boldsymbol{\nabla}\times\boldsymbol{\nabla}\left[f(r')\hat{\boldsymbol{e}}_z\right]$ on ∂S and S. For this purpose, it is convenient to leave $\boldsymbol{v}_\omega^{(1)}$ in this form rather than expand it out as in equation (3.27). By symmetry, we observe that the only non-vanishing contribution comes from the z-component

$$V := \hat{\boldsymbol{e}}_z \cdot \boldsymbol{v}_\omega^{(1)} = -\hat{\boldsymbol{e}}_z \cdot \boldsymbol{\nabla}\left(\hat{\boldsymbol{e}}_z \cdot \boldsymbol{\nabla} f(r')\right) + \Delta f(r'). \tag{8.3}$$

We begin by computing the average over the surface of a sphere of radius $r = a\zeta$ centered about $z = 0$, given by,

$$\bar{V}^S(\zeta) = \frac{1}{4\pi}\int_0^\pi 2\pi\sin\theta\,\mathrm{d}\theta\; V, \tag{8.4}$$

where we have already performed the trivial $\mathrm{d}\varphi$ integral.

Writing $\boldsymbol{\nabla}$ in the cylindrical coordinate system[5] as

$$\boldsymbol{\nabla} = \hat{\boldsymbol{e}}_z\left(\frac{\partial}{\partial z}\right)_\rho + \hat{\boldsymbol{e}}_\rho\left(\frac{\partial}{\partial\rho}\right)_z,$$

[5]We will frequently ignore the φ derivatives in these expressions as they are zero due to axial symmetry.

we find from (8.1) that $(\partial r'/\partial z)_\rho = (z+2h)/r'$, and use this in the expression for V to obtain,

$$\begin{aligned} V &= -\hat{\boldsymbol{e}}_z \cdot \boldsymbol{\nabla}\left[\frac{z+2h}{r'} f'(r')\right] + f''(r') + 2\frac{f'(r')}{r'} \\ &= -\frac{(z+2h)^2}{r'}\,\frac{\mathrm{d}}{\mathrm{d}r'}\left[\frac{f'(r')}{r'}\right] + f''(r') + \frac{f'(r')}{r'} \\ &= -\frac{(z+2h)^2}{r'}\,\frac{\mathrm{d}}{\mathrm{d}r'}\left[\frac{f'(r')}{r'}\right] + \frac{1}{r'}\,\frac{\mathrm{d}}{\mathrm{d}r'}[r' f'(r')]\,. \end{aligned} \tag{8.5}$$

We now observe from (8.1) that since we are integrating on a surface of constant r, $\frac{1}{2}\sin\theta\,\mathrm{d}\theta = -(2r)^{-1}\,\mathrm{d}z = -(\epsilon\zeta)^{-1}\xi\,\mathrm{d}\xi$, whereby the integral may be rewritten in terms of the non-dimensionalized variables as,

$$\begin{aligned} \bar{V}^S(\zeta) &= \frac{1}{\epsilon\zeta}\int_{1-\frac{1}{2}\epsilon\zeta}^{1+\frac{1}{2}\epsilon\zeta} \xi\,\mathrm{d}\xi\; V \\ &= \frac{1}{\epsilon\zeta}\int_{1-\frac{1}{2}\epsilon\zeta}^{1+\frac{1}{2}\epsilon\zeta} \mathrm{d}\xi\,\left\{-\frac{1}{4}\left(\xi^2 - \frac{\epsilon^2\zeta^2}{4} + 1\right)^2\,\frac{\mathrm{d}}{\mathrm{d}\xi}[F_0(\xi)] + \,\frac{\mathrm{d}}{\mathrm{d}\xi}\left[\xi^2 F_0(\xi)\right]\right\}. \end{aligned} \tag{8.6}$$

The advantage of this form is that the integral may be conveniently evaluated using integration by parts, and with the definitions,

$$\begin{aligned} F_1(\xi) &:= \int \xi F_0(\xi)\,\mathrm{d}\xi = -\frac{1}{\xi}\left[p\,\mathrm{e}^{-2\delta\xi/\epsilon} - q\right], \\ F_2(\xi) &:= \int \xi F_1(\xi)\,\mathrm{d}\xi = \left[p\frac{\epsilon}{2\delta}\mathrm{e}^{-2\delta\xi/\epsilon} + q\xi\right], \end{aligned} \tag{8.7}$$

we have,

$$\begin{aligned} \bar{V}^S(\zeta) &= -\frac{2}{\epsilon\zeta}\left[F_2(\xi) - \xi F_1(\xi)\right]_{1-\frac{1}{2}\epsilon\zeta}^{1+\frac{1}{2}\epsilon\zeta} \\ &= \frac{2}{\epsilon\zeta}\left[2p\,\mathrm{e}^{-2\delta/\epsilon}\sinh(\delta\zeta)\left(1+\frac{\epsilon}{2\delta}\right) - q\epsilon\zeta\right]. \end{aligned} \tag{8.8}$$

The average $\bar{V}^S$ on the surface of the sphere ∂S is just obtained by evaluating the above at $\zeta = 1$.

We define the volume average of V,

$$\begin{aligned} \bar{V}^V &:= \frac{1}{\frac{4}{3}\pi a^3}\int_0^a 4\pi r^2\,\mathrm{d}r\;\bar{V}^S(r/a) \\ &= \int_0^1 3\zeta^2\,\mathrm{d}\zeta\;\bar{V}^S(\zeta), \end{aligned} \tag{8.9}$$

which may be evaluated to obtain,

$$\bar{V}^V = \frac{12p}{\epsilon\delta^2}\left(1+\frac{\epsilon}{2\delta}\right)\mathrm{e}^{-2\delta/\epsilon}\left(\delta\cosh\delta-\sinh\delta\right)-2q. \tag{8.10}$$

We now rewrite the generalized Faxén theorem (3.34) as,

$$\frac{\gamma_\perp^R}{\gamma_s} = \frac{\gamma_0}{\gamma_s} - \left[(1+\delta)\bar{V}^S + \frac{\delta^2}{3}\bar{V}^V\right], \tag{8.11}$$

where we have introduced the superscript R to distinguish the results from the method of reflections from the other methods considered in this work. We then use the above to obtain the drag coefficient $\gamma_\perp^R$ as,

$$\frac{\gamma_\perp^R}{\gamma_s} = \left(1+\delta+\frac{\delta^2}{9}\right) + \frac{3\epsilon}{8\delta^2}\left[\epsilon^2\left(1+\delta+\frac{\delta^2}{3}\right)^2 - \mathrm{e}^{2\delta(1-1/\epsilon)}(2\epsilon\delta+\epsilon^2)\right]. \tag{8.12}$$

8.1.3 Image system for a full-slip plane wall: Parallel oscillations

As before, we consider the fluid to fill the half-space $\mathbb{R}^+ \times \mathbb{R}^2$. We will instead prefer to use a Cartesian coordinate system $(x,\, y,\, z)$ where the half-space occupied by the fluid corresponds to $z > -h$ $(h > 0)$. Let the sphere S of radius a lie at the origin of the Cartesian coordinate system. The plane wall W is located at $z = -h$. For convenience, as before, we introduce additional coordinate systems: a spherical coordinate system $(r,\, \theta,\, \varphi)$ with origin at $z = 0$ and polar axis along the positive z-axis; a spherical coordinate system $(r',\, \theta',\, \varphi)$ with origin at $z = -2h$ and polar axis along the positive z-axis; and another spherical coordinate system $(R,\, \Theta,\, \Phi)$ with origin at $z = -2h$ and polar axis along the positive x-axis. Let the sphere oscillate with velocity $\boldsymbol{u}_\omega = +1\hat{\boldsymbol{e}}_x$, where $\hat{\boldsymbol{e}}_x$ is the unit vector along the x-direction. The situation is visualized in figure 8.1.3.

As before, we introduce an image sphere S' centered at $z = -2h$, but to satisfy the boundary conditions on $z = -h$, the image sphere must have the same velocity as the actual sphere, i.e. $\boldsymbol{u'}_\omega = +1\hat{\boldsymbol{e}}_x$. We list the relevant coordinate conversion formulas involving the $(x,\, y,\, z)$ and the $(R,\, \Theta,\, \Phi)$ systems below:

$$\begin{aligned} R &= r' \\ x &= r'\sin\theta'\sin\varphi. \end{aligned} \tag{8.13}$$

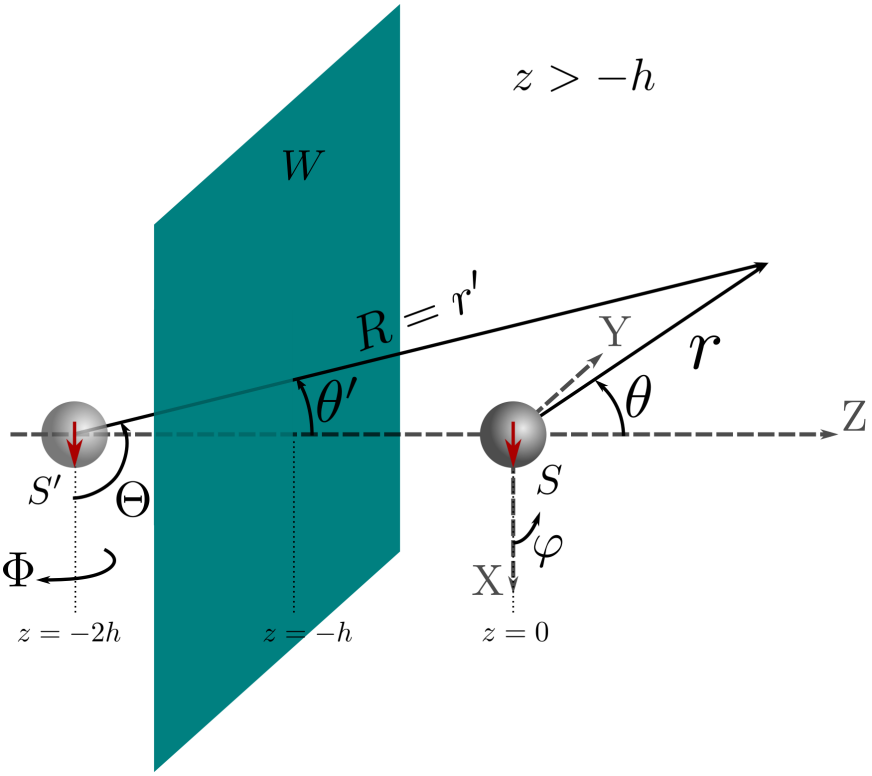

Figure 8.2: Image system for oscillations parallel to the wall, and coordinate systems adapted to the geometry.

8.1.4 Drag coefficient for parallel oscillations

We now proceed to calculate the drag force on the sphere for oscillations parallel to the wall. The first reflected field is now given by,

$$\boldsymbol{v}_\omega^{(1)} = +\boldsymbol{\nabla} \times \boldsymbol{\nabla} \left[f(R) \hat{\boldsymbol{e}}_x \right]. \tag{8.14}$$

The relevant component is the x-component,

$$V := \hat{\boldsymbol{e}}_x \cdot \boldsymbol{v}_\omega^{(1)} = +\hat{\boldsymbol{e}}_x \cdot \boldsymbol{\nabla} \left(\hat{\boldsymbol{e}}_x \cdot \boldsymbol{\nabla} f(R) \right) - \Delta f(R). \tag{8.15}$$

While there is no immediate reason to preclude the drag force from having a z-component, we will later show that there is none in the first-reflection approximation that we compute here.

The average over the surface of a sphere of radius $r = a\zeta$ centered about $z = 0$ is given by,

$$\bar{V}^S(\zeta) = \frac{1}{4\pi} \int_{\theta=0}^{\pi} \int_{\varphi=0}^{2\pi} \sin\theta \, \mathrm{d}\theta \, \mathrm{d}\varphi \, V, \tag{8.16}$$

as we do not have azimuthal symmetry in this case.

Writing $\boldsymbol{\nabla}$ in the Cartesian coordinate system as

$$\boldsymbol{\nabla} = \hat{\boldsymbol{e}}_x \left(\frac{\partial}{\partial x}\right)_{y,\,z} + \hat{\boldsymbol{e}}_x \left(\frac{\partial}{\partial y}\right)_{x,\,z} + \hat{\boldsymbol{e}}_z \left(\frac{\partial}{\partial z}\right)_{x,\,y},$$

we find from the coordinate conversion formulas (8.1) that $(\partial r'/\partial x)_{y,z} = x/r'$, and use this in the expression for V to obtain,

$$\begin{aligned} V &= \hat{\boldsymbol{e}}_x \cdot \boldsymbol{\nabla}\left[\frac{x}{r'} f'(r')\right] - f''(r') - \frac{2f'(r')}{r'} \\ &= \frac{x^2}{r'}\,\frac{\mathrm{d}}{\mathrm{d}r'}\left[\frac{f'(r')}{r'}\right] - f''(r') - \frac{f'(r')}{r'} \\ &= \frac{x^2}{r'}\,\frac{\mathrm{d}}{\mathrm{d}r'}\left[\frac{f'(r')}{r'}\right] - \frac{1}{r'}\,\frac{\mathrm{d}}{\mathrm{d}r'}[r' f'(r')]\,. \end{aligned} \tag{8.17}$$

We now write $x = r\sin\theta\cos\varphi$ in the expression for V and observe that $\int_0^{2\pi} \mathrm{d}\varphi\ \cos^2\varphi = \pi$, whereby we may reduce (8.16) to,

$$\bar{V}^S(\zeta) = \frac{r^2}{4}\int_0^{\pi} \mathrm{d}\theta\ \sin^3\theta\ \frac{1}{r'}\,\frac{\mathrm{d}}{\mathrm{d}r'}\left[\frac{f'(r')}{r'}\right] - \frac{1}{\epsilon\zeta}\int_{1-\epsilon\zeta/2}^{1+\epsilon\zeta/2} \mathrm{d}\xi\ \ \frac{\mathrm{d}}{\mathrm{d}\xi}\left[\xi^2 F_0(\xi)\right], \tag{8.18}$$

where we have treated the second term in equation (8.17) as we did in the case of perpendicular oscillations. For the first integral in the above equation, we note that since r is constant, we may write $r^2\sin^3\theta\,\mathrm{d}\theta = (r\sin\theta\,\mathrm{d}\theta)r(1-\cos^2\theta) = -\mathrm{d}z\,(r^2 - z^2)/r$ and substitute for z in terms of r' to obtain,

$$\begin{aligned} \frac{r^2}{4}\int_0^{\pi} \mathrm{d}\theta\ \sin^3\theta\ \frac{1}{r'}\,\frac{\mathrm{d}}{\mathrm{d}r'}\left[\frac{f'(r')}{r'}\right] &= \frac{1}{4r}\int_{1-\epsilon\zeta/2}^{1+\epsilon\zeta/2} \frac{\mathrm{d}r'}{2h}\, r'^2\,\frac{\mathrm{d}}{\mathrm{d}r'}\left[\frac{f'(r')}{r'}\right] \\ &\quad + \frac{1}{2}\left[-\frac{1}{2r}\int_{-r}^{r}\frac{\mathrm{d}z}{r'}(2h+z)^2\,\frac{\mathrm{d}}{\mathrm{d}r'}\left[\frac{f'(r')}{r'}\right]\right]. \end{aligned} \tag{8.19}$$

The second integral in the above expression was previously evaluated for the perpendicular case, so we may simply use the result. In non-dimensionalized variables, the first integral has the form

$$\frac{1}{2\epsilon\zeta}\int_{1-\epsilon\zeta/2}^{1+\epsilon\zeta/2} \mathrm{d}\xi\,\xi^2\,\frac{\mathrm{d}}{\mathrm{d}\xi}F_0(\xi), \tag{8.20}$$

which may be easily integrated by parts and expressed in terms of $F_1(\xi)$. Thus, we have

$$\bar{V}^S(\zeta) = \frac{1}{\epsilon\zeta}\left[(\xi-1)F_1(\xi) - F_2(\xi) - \xi^2 F_0(\xi)\right]_{1-\epsilon\zeta/2}^{1+\epsilon\zeta/2}, \tag{8.21}$$

which simplifies to,

$$\bar{V}^S(\zeta) = 2p\,\mathrm{e}^{-2\delta/\epsilon}\frac{\sinh(\delta\zeta)}{\epsilon\zeta}\left(1+\frac{2\delta}{\epsilon}+\frac{\epsilon}{2\delta}\right) - q. \tag{8.22}$$

The average $\bar{V}^S$ on the surface of the sphere ∂S is just obtained by evaluating the above at $\zeta = 1$.

As before, the volume average of V may be obtained

$$\bar{V}^V = \frac{6p}{\epsilon\delta^2}\left(1+\frac{2\delta}{\epsilon}+\frac{\epsilon}{2\delta}\right)\mathrm{e}^{-2\delta/\epsilon}\left[\delta\cosh\delta - \sinh\delta\right] - q. \tag{8.23}$$

We now adapt the generalized Faxén theorem (3.34) as we did in equation (8.11) to obtain the drag coefficient $\gamma_\parallel^R$ as,

$$\frac{\gamma_\parallel^R}{\gamma_s} = \left(1+\delta+\frac{\delta^2}{9}\right) + \frac{3\epsilon}{16\delta^2}\left[\epsilon^2\left(1+\delta+\frac{\delta^2}{3}\right)^2 - \mathrm{e}^{2\delta(1-1/\epsilon)}(4\delta^2+2\epsilon\delta+\epsilon^2)\right]. \tag{8.24}$$

We will now show that there is no force along the z-direction to first order. The z-component of the first reflected field due to parallel oscillations of the sphere is given by,

$$\begin{aligned} v^{(1)}_{xz,\,\omega} &= \hat{\boldsymbol{e}}_z \cdot \boldsymbol{\nabla}\left(\hat{\boldsymbol{e}}_x \cdot \boldsymbol{\nabla} f(r')\right) - \hat{\boldsymbol{e}}_x \cdot \hat{\boldsymbol{e}}_z \Delta f(r') \\ &= \hat{\boldsymbol{e}}_z \cdot \boldsymbol{\nabla}\left(\frac{x}{r'} f'(r')\right) - 0 \\ &= \frac{(z+2h)x}{r'}\,\frac{\mathrm{d}}{\mathrm{d}r'}\left[\frac{f'(r')}{r'}\right].w \end{aligned} \tag{8.25}$$

Substituting $x = r\sin\theta\cos\varphi$ as before, we see that the surface average $\bar{V}^S$ contains the integral $\int_0^{2\pi}\mathrm{d}\varphi\,\cos\varphi = 0$. Thus, the surface average vanishes on any spherical surface centered about $z = 0$, and consequently, the volume integral over the sphere S also vanishes.

The results from equations (8.12) and (8.24) are plotted in figure 8.3 as a function of the non-dimensionalized frequency $\omega\tau_f = \mathrm{i}\delta^2$, where $\tau_f := a^2\rho_f/\eta$ is the time-scale over which vorticity diffuses over the size of the sphere [Franosch *et al.*, 2011].

8.2 Comparison of the point-particle approximation and the method of reflections

In this section, we compare results for the drag coefficient for a sphere near a full-slip plane wall obtained by the two methods considered earlier, viz. the point-particle

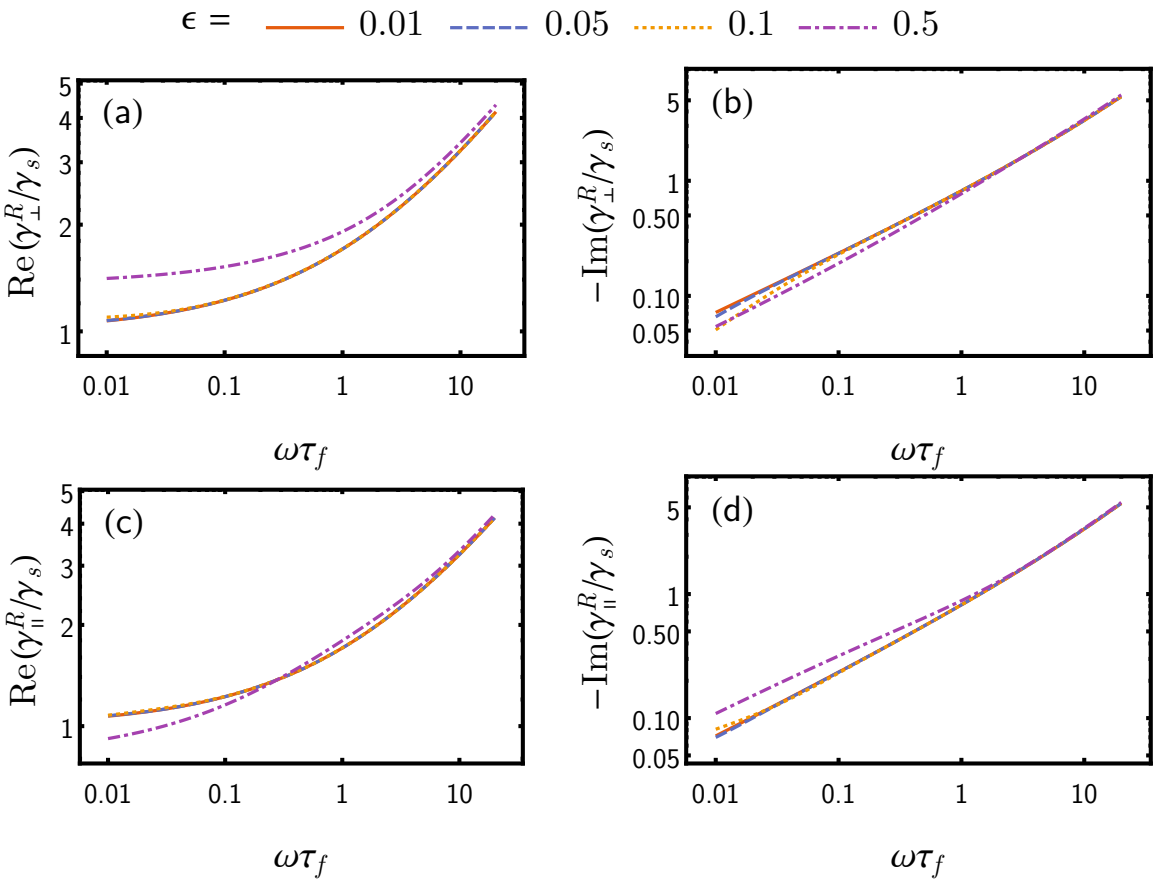

Figure 8.3: Logarithmic plots of the normalized drag coefficient for a no-slip sphere (radius a) in a viscous fluid near a full-slip plane wall (distance h), for various values of $\epsilon = a/h$, obtained using the method of reflections (§8.1) in the perpendicular direction (8.12) (a) real part and (b) negative imaginary part, and in the parallel direction (8.24) (c) real part and (d) negative imaginary part. The drag coefficient is normalized to the steady free-space Stokes drag coefficient γ_s. The horizontal axis is the non-dimensionalized frequency of oscillation of the sphere $\omega\tau_f$, where $\tau_f = a^2\rho_f/\eta$ is the timescale for vorticity diffusion over the size of the sphere.

approximation (§7.2) and the method of reflections (§8.1). Where relevant, we will also compare our modified point-particle approximation with the point-particle approximation as used by Felderhof [2012].

While we may directly use the expressions for the reaction field tensor from Felderhof [2012] in equation (7.21) to compute the drag coefficients in the parallel and perpendicular directions, it is however useful for purposes of comparison to first put the expression for the drag coefficient in a form similar to those obtained using the method of reflections in equations (8.12) and (8.24). To effect this, we first assume that $\gamma_s \boldsymbol{R}$ is small (which we would expect to be true on physical grounds in the regime of validity of the point-particle approximation), whereby we may expand (7.21) to first order in $\gamma_s \boldsymbol{R}$ to obtain[6],

$$\begin{aligned}\boldsymbol{\gamma} &= \gamma_0(\omega)\left[\mathbb{1} - (1+\delta+\delta^2/3)\gamma_s\boldsymbol{R}\right] - \frac{2}{9}\gamma_s\delta^2(1+\delta+\delta^2/3)\gamma_s\boldsymbol{R} + o[\gamma_s\boldsymbol{R}] \\ &= \gamma_0(\omega)\mathbb{1} - \gamma_s(1+\delta+\delta^2/3)^2(\gamma_s\boldsymbol{R}) + o[\gamma_s\boldsymbol{R}].\end{aligned} \tag{8.26}$$

Plugging in the expressions from Felderhof [2012, eq. (3.5) and (3.16)],

$$\begin{aligned}\gamma_s R_{zz} &= \frac{3\epsilon}{2}\left\{-\frac{1}{4\mathfrak{v}^2}\left[1-(1+2\mathfrak{v})\mathrm{e}^{-2\mathfrak{v}}\right]\right\}, \\ \gamma_s R_{xx} &= \frac{3\epsilon}{2}\left\{-\frac{1}{8\mathfrak{v}^2}\left[1-(1+2\mathfrak{v}+4\mathfrak{v}^2)\mathrm{e}^{-2\mathfrak{v}}\right]\right\},\end{aligned} \tag{8.27}$$

for the components $R_{zz} := \hat{\boldsymbol{e}}_z \cdot \boldsymbol{R} \cdot \hat{\boldsymbol{e}}_z$ and $R_{xx} := \hat{\boldsymbol{e}}_x \cdot \boldsymbol{R} \cdot \hat{\boldsymbol{e}}_x$ of $\boldsymbol{R}$, where $\mathfrak{v} := \alpha h = \delta/\epsilon$, into the above expression, we obtain the expressions

$$\begin{aligned}\frac{\gamma_\perp^P}{\gamma_s} &\approx \left(1+\delta+\frac{\delta^2}{9}\right) + \frac{3\epsilon}{8\delta^2}\left(1+\delta+\frac{\delta^2}{3}\right)^2\left[\epsilon^2 - \mathrm{e}^{-2\delta/\epsilon}\left(2\epsilon\delta+\epsilon^2\right)\right] \\ \frac{\gamma_\parallel^P}{\gamma_s} &\approx \left(1+\delta+\frac{\delta^2}{9}\right) + \frac{3\epsilon}{16\delta^2}\left(1+\delta+\frac{\delta^2}{3}\right)^2\left[\epsilon^2 - \mathrm{e}^{-2\delta/\epsilon}\left(4\delta^2+2\epsilon\delta+\epsilon^2\right)\right].\end{aligned} \tag{8.28}$$

We now compare these against equations (8.12) and (8.24) to find that the expressions from the two methods indeed differ, but in the factor in front of the subdominant (as $\epsilon \to 0^+$, δ fixed) exponential term $\mathrm{e}^{-2\delta/\epsilon}$. We shall show in the following subsections that in the regimes where the exponential terms actually matter, the two

[6]We remark that this form is likely inferior for numerical computations, since the original expression was in the form of a Padé approximant, which has been observed in many cases to perform better (see Section 8.2.2).

results agree to first order in ϵ. Thus, unless the physics under investigation expressly relies on the subdominant terms, the results from the two methods agree to first order.

8.2.1 Asymptotic comparison

Since there are two length scales, there are four asymptotic regimes that we may consider, depending on how α compares with a and h. Of particular interest here are two regimes – the regime of low frequencies where $\alpha h \sim 1$, and that of high frequencies where $\alpha a \gg 1$. The former regime is of interest owing to our discussion about the subdominant exponential terms (sections 7.3.5 and 8.2). The latter regime is of interest owing to the discrepancy in effective mass mentioned in the Introduction. It can be easily verified that the results from the method of reflections as well as the modified point-particle approximation agree in the regime of intermediate frequencies $\alpha a \sim 1$.

8.2.1.1 Steady drag coefficient

We now take the $\omega \to 0$ limit of the drag coefficients computed through either method, and check that they agree with results from previous calculations in the regime of steady Stokes flow. This also corresponds to the regime where $\alpha^{-1} \gg h \gg a$, i.e. the skin-depth of the vorticity is larger than the other length scales in the problem.

In the point-particle calculation, this is achieved by taking the $\omega \to 0$ limit of (7.21) and using the zero-frequency asymptotics of R_{xx} and R_{zz} as given by Felderhof [2012, equations (4.7) and (3.5)]. We obtain,

$$\frac{\boldsymbol{\gamma}^P}{\gamma_s} \sim (\mathbb{1} + \gamma_s \boldsymbol{R})^{-1} \qquad (\omega \to 0), \tag{8.29}$$

whereby,

$$\begin{aligned} \frac{\gamma_\perp^P}{\gamma_s} &\sim \frac{1}{1 - \frac{3}{4}\frac{a}{h}} = 1 + \frac{3}{4}\left(\frac{a}{h}\right) + o(a/h), \\ \frac{\gamma_\parallel^P}{\gamma_s} &\sim \frac{1}{1 + \frac{3}{8}\frac{a}{h}} = 1 - \frac{3}{8}\left(\frac{a}{h}\right) + o(a/h). \end{aligned} \qquad (\omega \to 0) \tag{8.30}$$

In the results from the method of reflections, this is achieved by taking $\delta \to 0$ with ϵ fixed in equations (8.12) and (8.24). We thus obtain,

$$\begin{aligned} \frac{\gamma_\perp^R}{\gamma_s} &\sim 1 + \frac{5}{8}\epsilon^3 - \frac{3\epsilon^3}{8}\left(-\frac{2}{\epsilon^2} + 2\right) = 1 + \frac{3}{4}\epsilon + o(\epsilon), \\ \frac{\gamma_\parallel^R}{\gamma_s} &\sim 1 - \frac{3}{8}\epsilon - \frac{1}{16}\epsilon^3 = 1 - \frac{3}{8}\epsilon + o(\epsilon). \end{aligned} \qquad (\omega \to 0) \tag{8.31}$$

Thus, the two methods agree with results obtained through image systems for steady Stokes flows [Frydel & Rice, 2006]. The steady-state drag coefficient for motion parallel to a full-slip flat wall is indeed smaller than the bulk drag coefficient, which has been verified by experiment [Wang *et al.*, 2009].

8.2.1.2 Low frequencies

We now consider non-zero, but low frequencies, where $\mathfrak{v} := \alpha h \sim 1$ but $\delta = \alpha a \ll 1$, i.e. the skin-depth of vorticity is comparable to the sphere-wall separation, and is much larger than the size of the sphere.

In the point-particle calculation, no approximation can be made in the expressions for the reaction field tensor [Felderhof, 2012, equations (3.5) and (3.16)] in this regime. However, we substitute $\delta = \epsilon\mathfrak{v}$ in (7.21) and keep terms to first order in ϵ while noting that $\gamma_s \boldsymbol{R}$ is first order in ϵ to obtain,

$$\boldsymbol{\gamma} \sim \gamma_s \left[\mathbb{1}(1 + \epsilon\mathfrak{v}) - \gamma_s \boldsymbol{R}\right], \tag{8.32}$$

which, upon substitution for the components of $\boldsymbol{R}$ yields

$$\begin{aligned} \frac{\gamma_\perp^P}{\gamma_s} &\sim 1 + \epsilon\mathfrak{v} + \frac{3\epsilon}{8\mathfrak{v}^2}\left[1 - (1 + 2\mathfrak{v})\,\mathrm{e}^{-2\mathfrak{v}}\right] + o(\epsilon), \\ \frac{\gamma_\parallel^P}{\gamma_s} &\sim 1 + \epsilon\mathfrak{v} + \frac{3\epsilon}{16\mathfrak{v}^2}\left[1 - \left(1 + 2\mathfrak{v} + 4\mathfrak{v}^2\right)\mathrm{e}^{-2\mathfrak{v}}\right] + o(\epsilon). \end{aligned} \tag{8.33}$$

For the results from the method of reflections, we once again substitute $\delta = \epsilon\mathfrak{v}$ in equations (8.12) and (8.24) and keep terms to first order in ϵ, and obtain the same results as above for $\gamma_\perp^R$ and $\gamma_\parallel^R$.

Thus, even where the subdominant exponential terms are important, the two results agree to lowest order in ϵ.

We may also take the $\alpha \to 0$ limit in the above and as expected, we recover expressions that agree with results obtained through image systems for steady Stokes flows [Frydel & Rice, 2006].

8.2.1.3 Intermediate frequencies

We now consider the range of frequencies where $\mathfrak{v} = \alpha h \gg 1$, but $\delta = \alpha a \sim 1$, i.e. the skin-depth of vorticity is much smaller than the sphere-wall distance, but is comparable to the size of the sphere.

In the point-particle calculation, we substitute $\mathfrak{v} = \delta/\epsilon$ in the asymptotic forms as $\mathfrak{v} \to +\infty$ of the expressions for the reaction field tensor [Felderhof, 2012, equations (3.5) and (3.16)] to obtain,

$$\begin{aligned} \gamma_s R_{zz} &\sim -\frac{3\epsilon^3}{8\delta^2}, \\ \gamma_s R_{xx} &\sim -\frac{3\epsilon^3}{16\delta^2}. \end{aligned} \qquad (\mathfrak{v} \to +\infty, \delta \sim 1) \tag{8.34}$$

Given that the components of $\boldsymbol{R}$ are of order ϵ^3, we may use (8.26) to obtain

$$\begin{aligned} \frac{\gamma_\perp^P}{\gamma_s} &\sim \left(1 + \delta + \frac{\delta^2}{9}\right) + \frac{3\epsilon^3}{8\delta^2}\left(1 + \delta + \frac{\delta^2}{3}\right)^2 + o(\epsilon^3), \\ \frac{\gamma_\parallel^P}{\gamma_s} &\sim \left(1 + \delta + \frac{\delta^2}{9}\right) + \frac{3\epsilon^3}{16\delta^2}\left(1 + \delta + \frac{\delta^2}{3}\right)^2 + o(\epsilon^3). \end{aligned} \qquad (\delta/\epsilon \to +\infty) \tag{8.35}$$

For the results from the method of reflections, we simply drop the terms containing subdominant exponential factors of the form $\mathrm{e}^{-\delta/\epsilon}$ in equations (8.12) and (8.24), and it is seen by inspection that we obtain the same results as above for $\gamma_\perp^R$ and $\gamma_\parallel^R$.

8.2.1.4 High frequencies

We finally consider the range of frequencies $\omega \gg \eta/(\rho_f a^2)$, where $1/|\alpha| \ll a \ll h$. In this regime, we expect that the viscous contributions to the drag coefficient are negligible compared to the inertial contributions, i.e. the added mass term. For instance, in the case of a spherical particle in an unbounded fluid medium, the drag coefficient in this regime $\gamma_0(\omega) \sim \gamma_s \delta^2/9 = -\mathrm{i}\omega m_f/2$, which is the added mass contribution from the fluid.

The added mass of a particle executing small oscillations in a fluid is usually obtained by means of potential flow [see e.g. Landau & Lifshitz, 1987; Brennen, 1982]. In particular, the added mass of a spherical particle near a plane wall is a well-studied problem [Lamb, 1932; Milne-Thomson, 1968; Yang, 2010], and the expressions for the

effective masses in this case,

$$\begin{aligned} m_\perp^* &= m_p + \frac{m_f}{2}\left[1 + \frac{3}{8}\left(\frac{a}{h}\right)^3\right], \\ m_\parallel^* &= m_p + \frac{m_f}{2}\left[1 + \frac{3}{16}\left(\frac{a}{h}\right)^3\right], \end{aligned} \tag{8.36}$$

are well-known. It must be noted that owing to the absence of $\Delta \boldsymbol{v}_\omega$, the differential equation is of lower order, whereby fewer boundary conditions are needed for the potential flow calculation, and thus the added mass obtained from potential flow does not distinguish between full-slip and no-slip boundary conditions.

It has been pointed out [Mo *et al.*, 2015*b*] that Felderhof's expressions do not agree with these results. As pointed out by Zwanzig & Bixon [1975], the velocity autocorrelation function for a Brownian particle in an incompressible fluid asymptotes to $k_B T/m^*$ as $t \to 0$, where m^* is the effective mass of the particle in the fluid.[7] This has been verified in unbounded fluid by experiments [Kheifets *et al.*, 2014; Mo *et al.*, 2015*a*]. However, the results from Felderhof [2005, eq. (4.5)] (see also erratum Felderhof [2006*b*]) suggest values for the added masses as $(m_f/2)(1 + a^3/(8h^3) + o(a^3/h^3))$ and $(m_f/2)(1 + a^3/(16h^3) + o(a^3/h^3))$. As we will presently demonstrate, this discrepancy is resolved by our modification of the point-particle framework described in sections 7.2.2 and 7.2.3.

In our modified point-particle framework, we take the asymptotics of the components of the reaction field tensor as $\mathfrak{v} \to \infty$ to obtain

$$\begin{aligned} \gamma_s R_{zz} &\sim -\frac{3\epsilon}{8\mathfrak{v}^2}, \\ \gamma_s R_{xx} &\sim -\frac{3\epsilon}{16\mathfrak{v}^2}. \end{aligned} \qquad (\mathfrak{v} \to +\infty) \tag{8.37}$$

We then replace $\delta = \epsilon\mathfrak{v}$ in (7.21), substitute the above asymptotic forms for the components of $\boldsymbol{R}$, and expand to lowest order in ϵ to obtain,

$$\begin{aligned} \frac{\gamma_\perp^P}{\gamma_s} &\sim \frac{1}{9}\epsilon^2\mathfrak{v}^2\left(1 + \frac{3}{8}\epsilon^3\right) + o(\epsilon^5), \\ \frac{\gamma_\parallel^P}{\gamma_s} &\sim \frac{1}{9}\epsilon^2\mathfrak{v}^2\left(1 + \frac{3}{16}\epsilon^3\right) + o(\epsilon^5). \end{aligned} \qquad (\mathfrak{v} \to +\infty) \tag{8.38}$$

[7] The apparent contradiction with the energy equipartition theorem, which reports a $k_B T/m$ asymptote, is resolved by including the effects of compressibility.

Thereafter, identifying $\epsilon^2\mathfrak{v}^2/9 = -\mathrm{i}\omega m_f/2$, we obtain added masses consistent with the effective masses given in (8.36).

For the results from the method of reflections, we take the asymptotic as $\delta \to \infty$ with fixed ϵ in equations (8.12) and (8.24). The subdominant exponential terms drop and we are left with

$$\begin{aligned} \frac{\gamma_\perp^R}{\gamma_s} &\sim \frac{1}{9}\delta^2\left(1 + \frac{3}{8}\epsilon^3\right), \\ \frac{\gamma_\parallel^R}{\gamma_s} &\sim \frac{1}{9}\delta^2\left(1 + \frac{3}{16}\epsilon^3\right), \end{aligned} \qquad (\delta \to +\infty) \tag{8.39}$$

which are once again consistent with the results from the modified point-particle approximation and with calculations from potential flow [Lamb, 1932; Milne-Thomson, 1968; Brennen, 1982].

8.2.2 Numerical comparison

In this section, we present numerical comparisons of predictions for the drag coefficients from three methods – the point-particle approximation proposed by Felderhof [2012], the modified point-particle approximation presented in this work (§7.2), and the method of reflections (§8.1).

Generally speaking, for purposes of numerical evaluation, it is likely that keeping the expression for $\boldsymbol{\gamma}(\omega)$ in the form of a Padé approximant as in equation (7.21) gives better results. In the context of the method of reflections for the steady Stokes equations, Happel & Brenner [1965, chap. 7] suggest the use of a geometric series extrapolation to account for higher order reflections in the absence of any further information, which essentially amounts to turning the result from the method of reflections into a Padé approximant. We also noted this when we computed the perturbative result to all orders in Section 7.3.5. Several experiments have employed the Padé form of the steady drag [Schäffer *et al.*, 2007; Mo *et al.*, 2015*b*, Fig. 2] with good results.

However, in order to appropriately compare and highlight the differences between the theories, it is necessary that we compare results expressed in similar forms. In the plots that follow, when comparing the method of reflections against the modified point-particle approximation (figure 8.4 and figure 8.5), we use the form of (8.28) for the point-particle approximation. When comparing the modified point-particle

approximation against that of Felderhof [2012] (figures 8.6 and 8.7), we shall use the original forms from equations (8.40) and (7.21).

We obtain the drag coefficients from Felderhof's point-particle framework by setting the expression for the admittance from Felderhof [2012, equation (2.9)] equal to (7.22):

$$\boldsymbol{\gamma}^F(\omega) = \mathrm{i}\omega m_p \mathbb{1} + (-\mathrm{i}\omega m_p + \gamma_0)\left[\mathbb{1} + \left(1 + \delta + \frac{\delta^2}{3}\right)\gamma_s \boldsymbol{R}\right]^{-1}. \tag{8.40}$$

We observe that unlike with the other results, the drag coefficient depends on the mass of the particle m_p, which does not cancel out even if we expand to first order in $\gamma_s \boldsymbol{R}$. The drag coefficients from the modified point-particle framework are calculated from (7.21) using the expressions for the reaction field tensor from Felderhof [2012, equations (3.5) and (3.16)], which we have reproduced in equation (8.27).

Figure 8.4 compares the real and imaginary parts of drag coefficients for a no-slip sphere near a full-slip wall obtained from the method of reflections, and from the modified point-particle approximation for the case of $\epsilon = a/h = 0.5$. The free-space drag coefficient $\gamma_0(\omega)$ has been subtracted in order to clearly show the difference between the methods. The inset in sub-figure (c) shows a log-log plot of $\Re(\gamma_\parallel/\gamma_s)$, i.e. without subtraction of the free-space drag coefficient, exemplifying the excellent agreement between the two methods even for the large value of ϵ. The relative discrepancy between these two methods, calculated as $|\gamma^R - \gamma^P|/|\gamma^P|$ and expressed as a percentage, is plotted in figure 8.5 for different values of ϵ. As expected, the discrepancy becomes larger as the value of the small parameter ϵ increases, i.e. as the particle is moved closer to the wall, but is still quite small even for $\epsilon = 0.5$ when the particle's center is one diameter away from the wall.

Figure 8.6 compares the real and imaginary parts of drag coefficients for a no-slip sphere near a full-slip wall obtained from Felderhof's point-particle approximation, and from the modified point-particle framework, for the case of $\epsilon = 0.5$ and $\rho_p = 19\rho_f$. If the liquid is water, this density corresponds roughly to that of gold particles. As before, the free-space drag coefficient $\gamma_0(\omega)$ has been subtracted in order to clearly highlight the disagreement between the methods at high frequencies. The inset in sub-figure (c) shows a log-log plot of $\Re(\gamma_\parallel/\gamma_s)$, i.e. without subtraction of the free-space drag coefficient, showing that there is still visible disagreement between the two methods for large ρ_p/ρ_f. The relative error between these two approximations,

calculated as $|\gamma^F - \gamma^P|/|\gamma^P|$ and expressed as a percentage, is plotted in figure 8.7 for different values[8] of ρ_p. The error is zero when $\rho_p = \rho_f$, and the errors become larger as ρ_p deviates from ρ_f.

Figure 8.8 shows the high-frequency behavior of the imaginary components of the drag coefficients from Felderhof's version, and from the modified version of the point-particle approximation on a log-log scale. A line corresponding to the added mass contribution predicted from potential flow [Milne-Thomson, 1968] is shown. The plots show the agreement of the modified point-particle approximation with the potential flow results at high frequencies.

[8]If the liquid is water, the values 2, 4 and 19 for ρ_p/ρ_f roughly correspond to particles made of silica glass, Barium Titanate glass, and gold respectively. These are common choices in optical tweezers experiments.

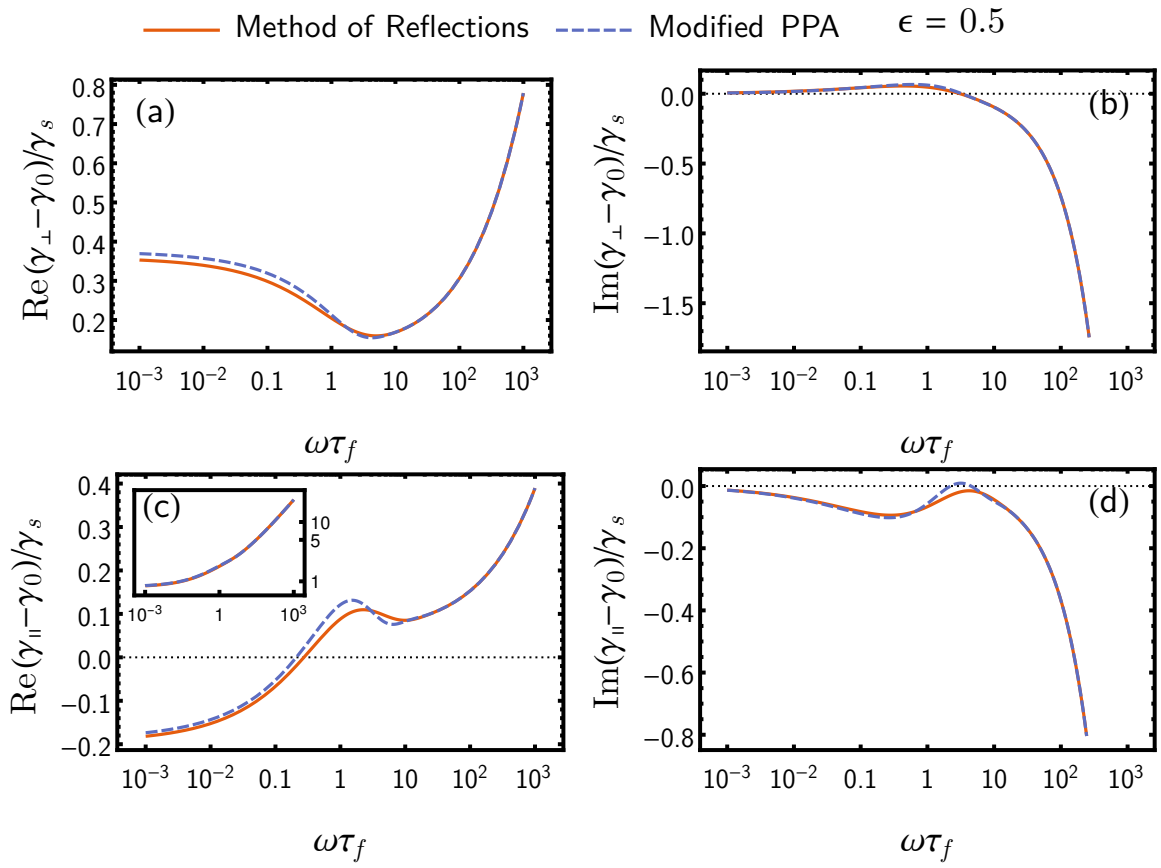

Figure 8.4: Semi-logarithmic plots comparing the results for the drag coefficient of a no-slip sphere near a full-slip plane wall ($\epsilon = 0.5$) from the method of reflections (§8.1) and the modified point-particle approximation ("Modified PPA") (§7.2) in the perpendicular direction (a) real part and (b) imaginary part, and in the parallel direction (c) real part and (d) imaginary part. In each case, the free-space drag coefficient $\gamma_0(\omega)$ has been subtracted in order to clearly highlight the small differences, and the coefficients have been normalized by γ_s. The inset in (c) shows a log-log plot of the real parts of the normalized drag coefficients in the parallel direction without subtraction of γ_0.

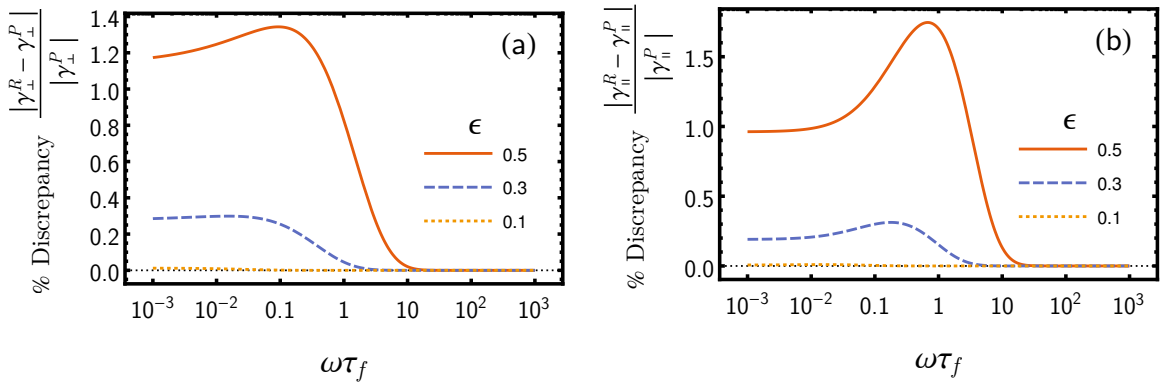

Figure 8.5: Semi-logarithmic plots of the percentage discrepancy between the drag coefficients obtained through the two approximation methods plotted in figure 8.4, calculated using $100\% \left|\gamma^R - \gamma^P\right| / \left|\gamma^P\right|$ for various values of ϵ (a) in the perpendicular direction, (b) in the parallel direction to the wall. As expected, the discrepancy becomes very small at small ϵ, i.e. when the particle is further from the wall.

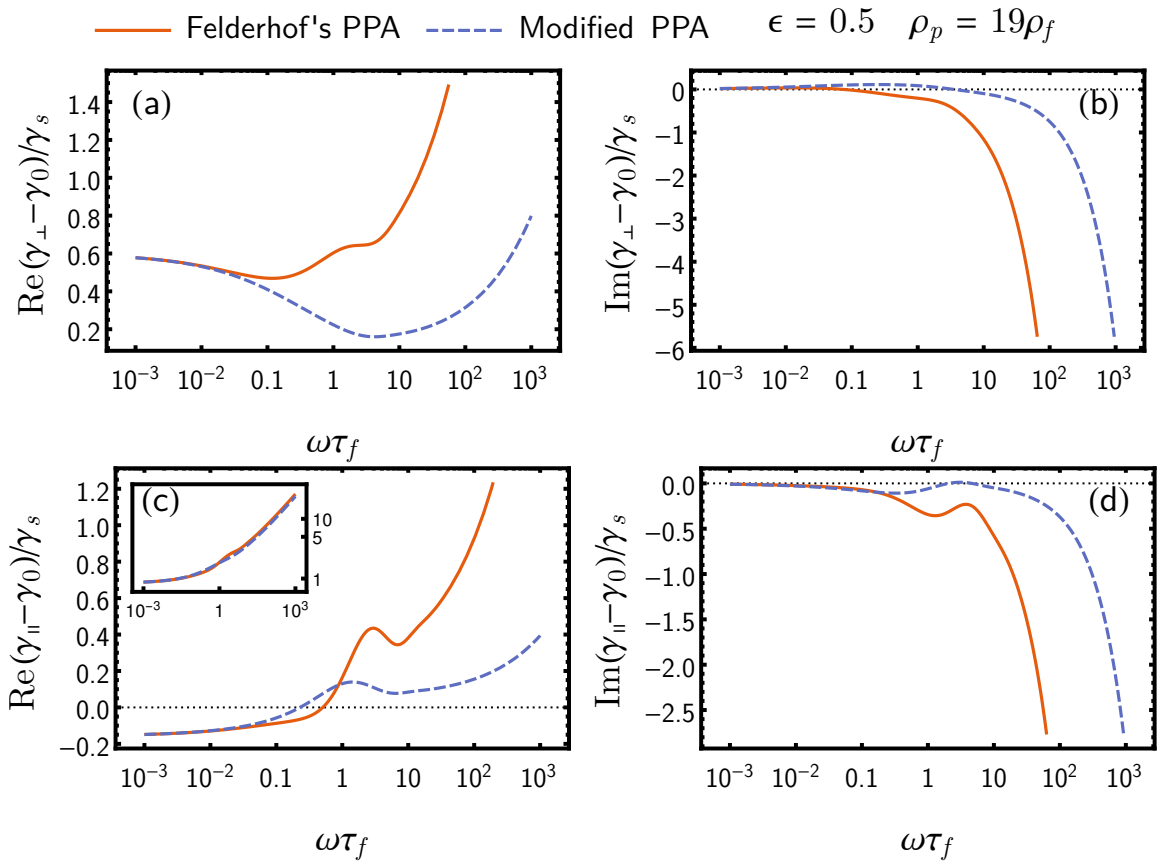

Figure 8.6: Semi-logarithmic plots comparing the results for the drag coefficient of a no-slip sphere near a full-slip plane wall ($\epsilon = 0.5$) from the point-particle approximation of Felderhof [2012] ("Felderhof's PPA") and the modified version of the point-particle approximation described in §7.2 ("Modified PPA") in the perpendicular direction (a) real part and (b) imaginary part, and in the parallel direction (c) real part and (d) imaginary part. In each case, the free-space drag coefficient $\gamma_0(\omega)$ has been subtracted in order to clearly highlight the differences, and the coefficients have been normalized by γ_s. Since the drag coefficient (8.40) from Felderhof's PPA depends on the density of the particle ρ_p, we set $\rho_p = 19\rho_f$ (which is approximately the case for gold particles in water) to highlight the differences. The inset in (c) shows a log-log plot of the real parts of the normalized drag coefficients in the parallel direction without subtraction of γ_0.

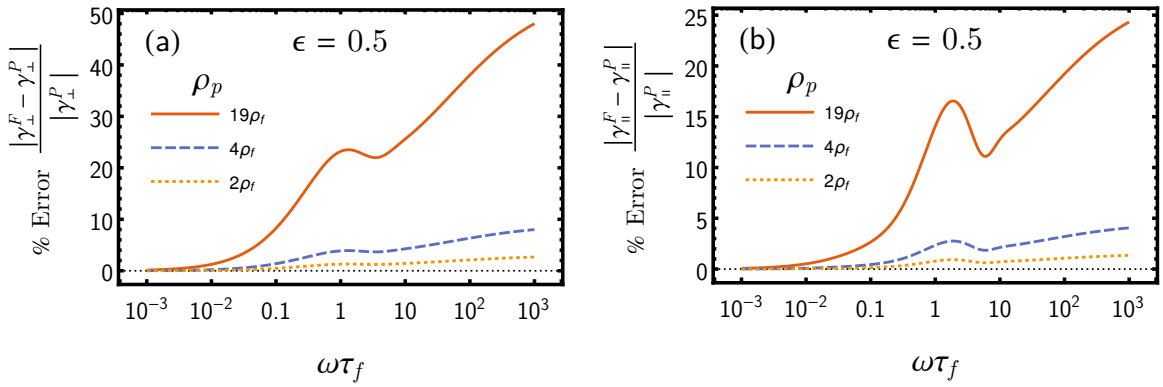

Figure 8.7: Semi-logarithmic plots of the percentage error between the drag coefficients for a no-slip sphere near a full-slip plane wall obtained from Felderhof's PPA and the Modified PPA and calculated as $100\% \left|\gamma^F - \gamma^P\right| / \left|\gamma^P\right|$, for various values of particle density ρ_p ($\epsilon = 0.5$) (a) in the perpendicular direction, (b) in the parallel direction to the wall.

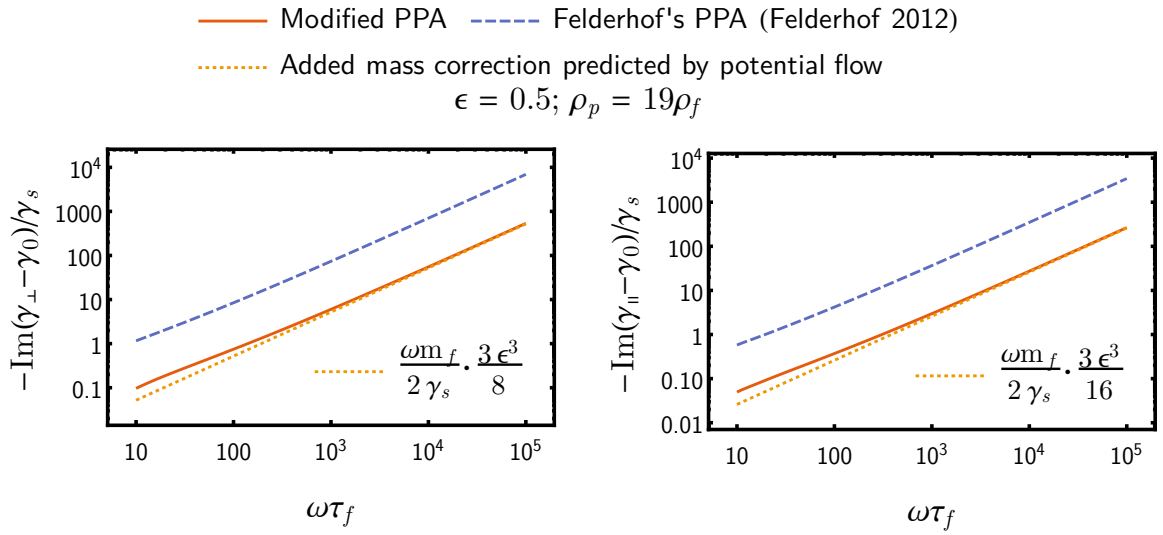

Figure 8.8: Logarithmic plots of $-\Im(\gamma - \gamma_0)/\gamma_s$ for a no-slip sphere near a full-slip plane wall obtained from the modified (solid orange) and from Felderhof's original (dashed blue line) point-particle approximation against non-dimensionalized frequency $\omega\tau_f$. The region of slope 1 of these lines represents the regime where the term corresponding to the increase in added mass due to the boundary is dominant. The dotted orange line plots the added mass correction from potential flow calculations. Values $\epsilon = 0.5$ and $\rho_p = 19\rho_f$ are chosen to highlight the difference. It is observed that the modified point-particle approximation reproduces the results from potential flow at high frequencies.

Chapter Nine: Theory of Brownian motion near a boundary

In this chapter, we shall adapt the results of Felderhof [2005, 2012] and the material of chapters 7 and 8 to provide expressions useful to compute statistics of the Brownian motion of a no-slip sphere near a plane wall, with either no-slip or full-slip conditions[1] on the wall. Some of these results were used in the analysis of experimental work [Mo *et al.*, 2015*b*] and appear in that work, as well as in Simha *et al.* [2017].

We also discuss results for the hindered diffusion coefficient near a flat [Happel & Brenner, 1965] as well as a cylindrical [Alam *et al.*, 1980] boundary owing to its relevance to Chapter 10.

9.1 General remarks

First, we make some general remarks that are common to the analysis that follows.

It must be noted that, to the approximations we have worked with in chapters 7 and 8, the tensor of drag coefficients $\boldsymbol{\gamma}(\omega)$ for a spherical particle near a flat wall is diagonal. If we assume that the tensor of trap stiffness coefficients $\boldsymbol{K}$ is also diagonal in the same coordinate system, our analysis becomes simplified, as all the other tensors involved (the admittance, the power spectral densities, the correlation functions etc. in Chapter 2) become diagonal. This allows us to break the analysis into the analysis of motion perpendicular to the wall, and of motion parallel to the wall.

Experimentally speaking, the assumption of $\boldsymbol{K}$ being diagonal in the same basis as $\boldsymbol{\gamma}(\omega)$ requires that the natural coordinate axes of the laser beam(s) creating the optical trap, the axes of the wall, and the axes of the measurement be square with one-another. In other words, it is sufficient for the laser(s) creating the trap to have an axi-symmetric profile (so it could be TEM_{00}, the donut mode, etc.) with the axis of propagation either parallel or perpendicular to the wall, and the axis of measurement

[1] Whereas Felderhof [2012] has obtained results for the case of partial slip, the spatial Fourier transform along the dimensions tangential to the plane needs to be inverted numerically, which complicates the analysis.

to be either parallel or perpendicular to the wall. Given that this was largely the case (up to misalignment) in the experiment [Mo *et al.*, 2015*b*] discussed in this work, we shall proceed to analyze the parallel and perpendicular components separately. Of course, there is no significant complication if the tensors are not simultaneously diagonalizable – all the computations can be done, only with the extra overhead of having to work with 3×3 matrices.

As we discussed in Chapter 3, vorticity in the fluid takes a time of $\sim L^2/\nu$ to diffuse over a region of size L, where ν is the kinematic viscosity of the fluid. In the problem of Brownian motion of a spherical particle (radius a) near a boundary, distance between the particle's center and the boundary being h, there are two choices for the length-scale L. This allows us to construct two time-scales, $\tau_f := a^2/\nu$ as before, and an additional time-scale,

$$\tau_w := h^2/\nu. \tag{9.1}$$

Since vorticity shed by the oscillating sphere takes order of τ_w to reach the walls, the effects of the boundary become significant only on time-scales $\gtrsim \tau_w$. Since the pressure transmission (in an incompressible fluid) is instantaneous, there is an effect of the boundary on time-scales shorter than τ_w – but it is expected to be of the order of $(a/h)^3$, since fundamental solution for the pressure $\boldsymbol{P}^0(\boldsymbol{r})$ decays like $1/r^2$ [Kim & Karrila, 2013, §6.2], whereby its contribution to the velocity of the reflected flow, which is used in Faxén's theorem to calculate the drag, drops like $\sim 1/h^3$. While this argument is a heuristic, this can be generally observed in the nature of the drag coefficient – the lowest order terms without exponentials are generally speaking of the order of ϵ^3, and the corrections to the added mass are indeed of order ϵ^3. Therefore, the more significant effects take order of τ_w to set in, and this can be seen in both the theoretical predictions and experimental measurements of statistical properties of Brownian motion.

In the spirit of being experiment-friendly, in this chapter, we will try to keep the expressions in dimensionful, physical quantities.

9.2 Brownian motion near a full-slip flat wall

In the modified PPA, we may compute the components of $\boldsymbol{\gamma}(\omega)$ using (7.21),

$$\gamma_{\perp,\parallel}(\omega) = \mathrm{i}\omega m_f + \gamma_s \frac{1 + \sqrt{-\mathrm{i}\omega\tau_f} - \mathrm{i}\omega\tau_f/3}{1 + \left[1 + \sqrt{-\mathrm{i}\omega\tau_f} - \mathrm{i}\omega\tau_f/3\right](\gamma_s R_{\perp,\parallel})}, \tag{9.2}$$

and subsequently compute the admittances using (2.36),

$$Y^K_{\perp,\parallel}(\omega) = \frac{1+\left(1+\sqrt{-\mathrm{i}\omega\tau_f}-\mathrm{i}\omega\tau_f/3\right)(\gamma_s R_{\perp,\parallel})}{\left[\mathrm{i}\omega(m_f-m_p)-\frac{K_{\perp,\parallel}}{\mathrm{i}\omega}\right]\left[1+\left(1+\sqrt{-\mathrm{i}\omega\tau_f}-\mathrm{i}\omega\tau_f/3\right)(\gamma_s R_{\perp,\parallel})\right]+\left[\gamma_0(\omega)-\mathrm{i}\omega m_f\right]}, \tag{9.3}$$

where $\gamma_0(\omega) = \gamma_s(1 + \sqrt{-\mathrm{i}\omega\tau_f} - \mathrm{i}\omega\tau_f/9)$ and $\gamma_s = 6\pi\eta a$. As a reminder, the branch of the square roots in all these expressions is to be taken so that $\sqrt{-\mathrm{i}} = (1-\mathrm{i})/\sqrt{2}$.

We already noted the expressions provided by Felderhof [2012] for the reaction field tensors near a full-slip wall,

$$\begin{aligned}
\gamma_s R_\perp &= \frac{3a}{2h}\left\{-\frac{1}{4\mathfrak{v}^2}\left[1-(1+2\mathfrak{v})\mathrm{e}^{-2\mathfrak{v}}\right]\right\},\\
\gamma_s R_\parallel &= \frac{3a}{2h}\left\{-\frac{1}{8\mathfrak{v}^2}\left[1-(1+2\mathfrak{v}+4\mathfrak{v}^2)\mathrm{e}^{-2\mathfrak{v}}\right]\right\},
\end{aligned} \tag{8.27}$$

where[2] $\mathfrak{v} = \sqrt{-\mathrm{i}\omega\tau_w}$, which may be plugged into the above equations to compute various statistical properties of Brownian motion.

The various quantities such as PSD, VACF etc. are best calculated numerically using (2.29) and the methods described in that context. However, we wish to highlight the behavior of the thermal force at low frequencies. The (two-sided) thermal force PSD may be computed as $S_F(\omega) = 2k_BT\,\Re[\gamma_{\perp,\parallel}]$ and expanded (Wolfram Mathematica was used to do the expansion). The results are given by [Mo *et al.*, 2015*b*]

$$\begin{aligned}
S^{\mathrm{slip}}_{F,\parallel}(\omega) &\sim 2k_BT\gamma_s\left[\frac{1}{1+\frac{3a}{8h}} + \frac{64\sqrt{2}h^2}{(3a+8h)^2}(\omega\tau_f)^{\frac{1}{2}}\right],\\
S^{\mathrm{slip}}_{F,\perp}(\omega) &\sim 2k_BT\gamma_s\left[\frac{1}{1-\frac{3a}{4h}} + \frac{8\sqrt{2}\,(6h^4-5a^2h^2)}{15a^2\,(4h-3a)^2}(\omega\tau_f)^{\frac{3}{2}}\right],
\end{aligned} \tag{9.4}$$

as $\omega \to 0$ (i.e. $\omega \ll 1/\tau_f,\ 1/\tau_w$). The thermal force in the perpendicular direction therefore becomes less colored at low frequencies in the presence of a boundary, as is seen by the absence of the $\sqrt{\omega\tau_f}$ term.

[2] As a reminder, the branch of the square root should be chosen so that $\sqrt{-\mathrm{i}\omega\tau_f}$ and $\sqrt{-\mathrm{i}\omega\tau_w}$ have positive real part.

We may also adapt the results from the method of reflections to the computation of admittance. The point-particle approximation, using expression (7.21), has been experimentally seen [Mo *et al.*, 2015*b*] to perform surprisingly well for large values of $\epsilon \approx 0.5$, i.e. when the particle is one diameter away from the wall. Motivated by this, and by the discussion of §7.3.5, we cast the expressions from the method of reflections in the (Padé-like) form suggested by equation (7.21). This is akin to using a geometric series for higher-order reflections in the absence of any other information [Happel & Brenner, 1965]. We therefore write,

$$\gamma^R_{\perp,\parallel}(\omega) = \mathrm{i}\omega m_f + \gamma_s \frac{1 + \sqrt{-\mathrm{i}\omega\tau_f} - \mathrm{i}\omega\tau_f/3}{1 + \left[1 + \sqrt{-\mathrm{i}\omega\tau_f} - \mathrm{i}\omega\tau_f/3\right](\gamma_s \chi_{\perp,\parallel})}, \tag{9.5}$$

where the correction terms for the full-slip wall are given by,

$$\begin{aligned} \chi_\perp &= \frac{3a}{2h}\left\{-\frac{1}{4\mathfrak{v}^2}\left[1 - (1+2\mathfrak{v})\mathrm{e}^{-2\mathfrak{v}}\frac{\mathrm{e}^{2\delta}}{(1+\delta+\delta^2/3)^2}\right]\right\}, \\ \chi_\parallel &= \frac{3a}{2h}\left\{-\frac{1}{8\mathfrak{v}^2}\left[1 - (1+2\mathfrak{v}+4\mathfrak{v}^2)\mathrm{e}^{-2\mathfrak{v}}\frac{\mathrm{e}^{2\delta}}{(1+\delta+\delta^2/3)^2}\right]\right\}, \end{aligned} \tag{9.6}$$

where $\mathfrak{v} = \sqrt{-\mathrm{i}\omega\tau_w}$ and $\delta = \sqrt{-\mathrm{i}\omega\tau_f}$.

The numerically calculated statistical properties of Brownian motion (at temperature $T = 295$ K) for a representative system of a harmonically confined (stiffness $K = 100$ pN/μm) silica sphere (density $\rho_p = 2.0$ g/cm^3, diameter $2a = 3\mu$m) at a distance of $h = 3\mu$m ($\epsilon = 0.5$) from a full-slip flat wall in water (density $\rho_f = 1.0$ g/cm^3, viscosity $\eta = 10^{-3}$ Pa·s) using the above two results, as well as using the unmodified results of Felderhof [2012], are presented in figures 9.1 (perpendicular direction) and 9.2 (parallel direction). Also shown for comparison, are the predictions using the free-space drag coefficient $\gamma_0(\omega)$ (Chapter 4). In both figures, sub-figure (a) shows the MSD, (b) shows the (one-sided) PSD of velocity, (c) shows the VACF, and (d) shows the (one-sided) PSD of the thermal force.

As one can see, in this system, the difference between the unmodified PPA of Felderhof [2012] and our modified PPA is not easily discernible without very high-precision experiments. However, our modifications would be of significance when ρ_p is substantially different from ρ_f, as is the case for systems of metallic particles in liquids. Systems of gold and other nano-particles in liquids are extremely common in experiments, not only in those involving optical tweezers [see e.g. Svoboda & Block,

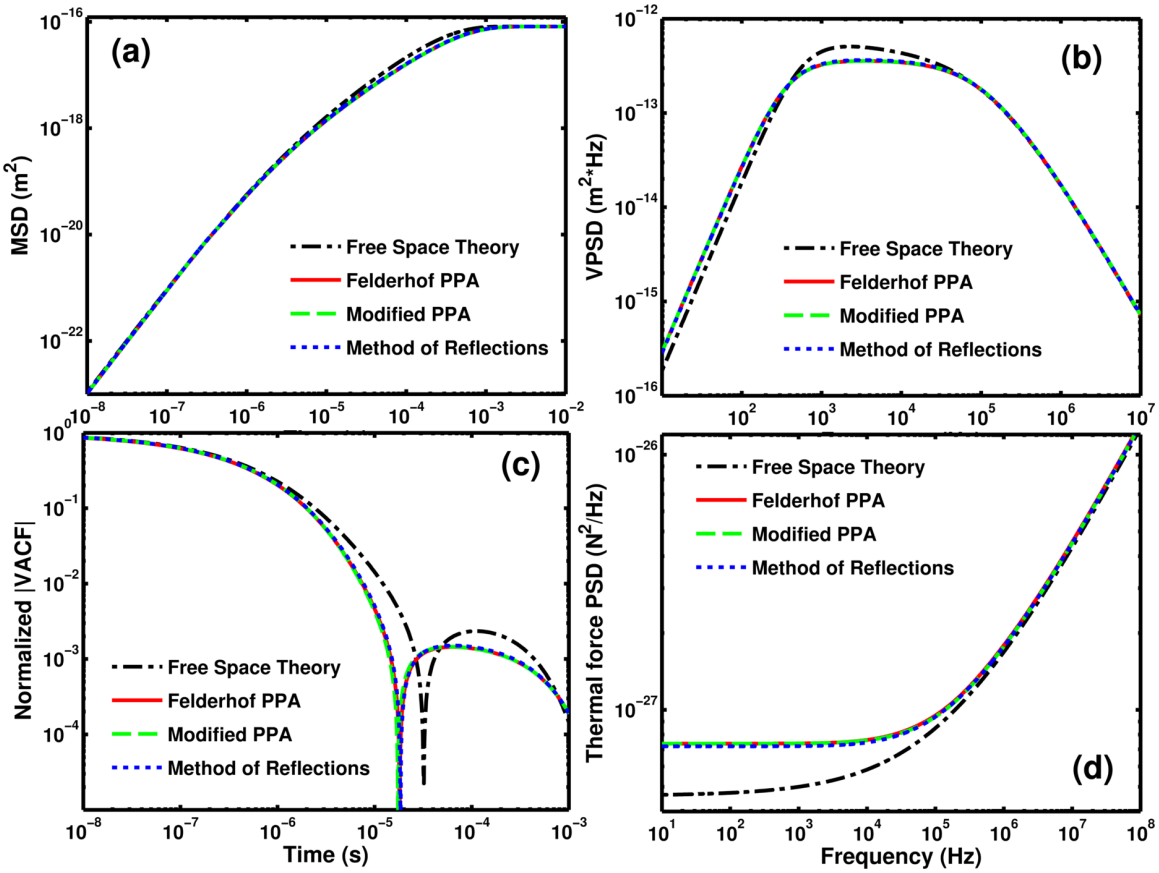

Figure 9.1: Theoretical predictions from various methods, for the statistical properties of the Brownian motion of a no-slip, spherical silica particle (density $\rho_p = 2.0$ g/cm^3, diameter $2a = 3\mu$m) in the *perpendicular* direction to a full-slip plane wall (sphere-wall distance $h = 3\mu$m) in water (density $\rho_f = 1.0$ g/cm^3, viscosity $\eta = 10^{-3}$ Pa·s) at a temperature of 295 K. The particle is assumed to be confined by a harmonic trap (stiffness $K = 100$ pN/μm). The long-dashed green line shows the prediction from our modified point-particle framework (9.2), (8.27) and (9.3). The solid red line shows the prediction from the point-particle approximation as used by Felderhof [2012], without modification. The short-dashed blue line shows the prediction of the method of reflections (9.6) and (9.5). The black line with varying dash length shows the predictions for a similar particle in an unbounded fluid medium (Chapter 4). Sub-figure (a) shows a log-log plot of the MSD, (b) shows the one-sided PSD of velocity $2S_v^{\perp}$, (c) shows the absolute value of the VACF $C_v^{\perp}$, normalized by $k_BT/m_{\perp}^*$, and (d) shows the one-sided spectral density of the thermal force $2S_F^{\perp}$. The cusps in sub-figure (c) correspond to zero-crossings that are a result of the harmonic confinement. Despite the large value of $\epsilon = 0.5$, the method of reflections and point-particle approximation agree very well. The difference between the modified and unmodified point-particle approximation is not discernible in the plots due to the small density difference ($\rho_p/\rho_f = 2$). Figure from Simha *et al.* [2017], courtesy of Dr. Jianyong Mo.

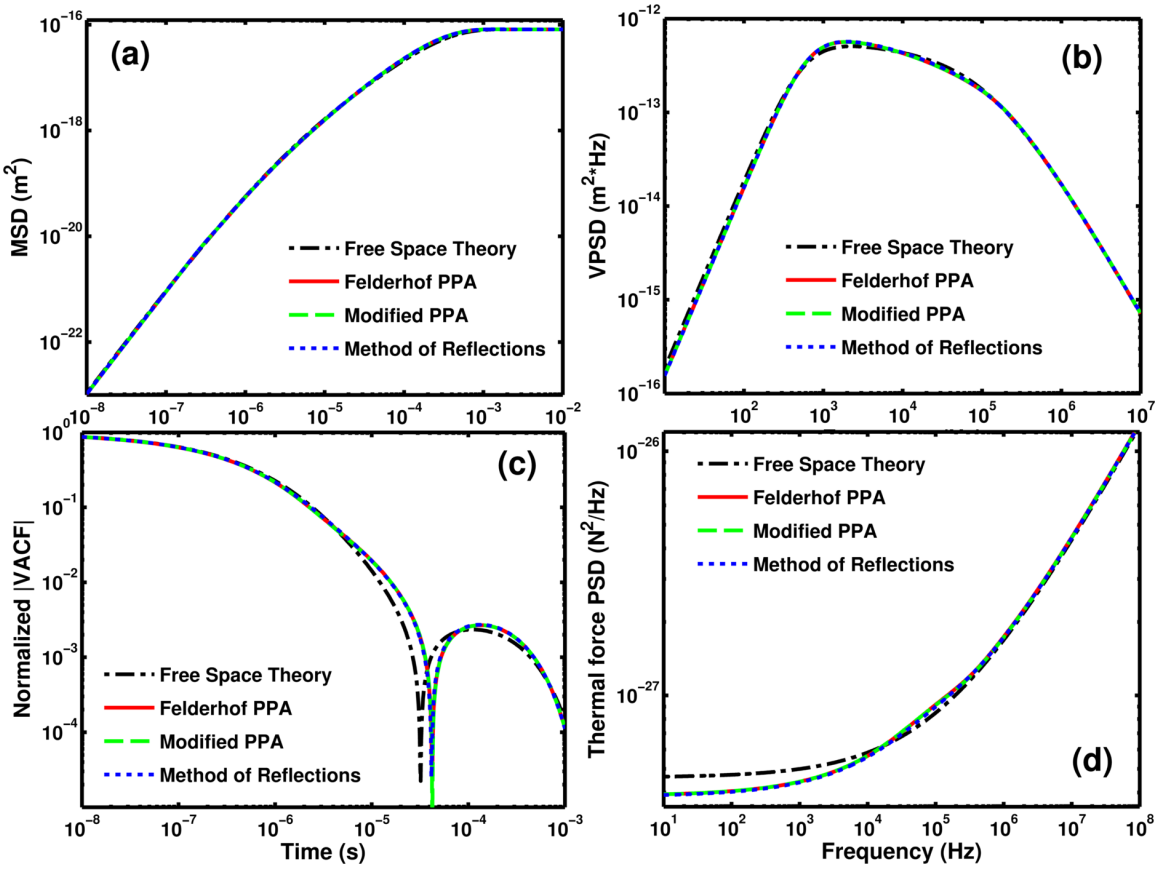

Figure 9.2: Theoretical predictions from various methods, for the statistical properties of the Brownian motion of a no-slip, spherical silica particle (density $\rho_p = 2.0$ g/cm^3, diameter $2a = 3\mu$m) in the *parallel* direction to a full-slip plane wall (sphere-wall distance $h = 3\mu$m) in water (density $\rho_f = 1.0$ g/cm^3, viscosity $\eta = 10^{-3}$ Pa·s) at a temperature of 295 K. The particle is assumed to be confined by a harmonic trap (stiffness $K = 100$ pN/μm). The long-dashed green line shows the prediction from our modified point-particle framework (9.2), (8.27) and (9.3). The solid red line shows the prediction from the point-particle approximation as used by Felderhof [2012], without modification. The short-dashed blue line shows the prediction of the method of reflections (9.6) and (9.5). The black line with varying dash length shows the predictions for a similar particle in an unbounded fluid medium (Chapter 4). Sub-figure (a) shows a log-log plot of the MSD, (b) shows the one-sided PSD of velocity $2S_v^{\parallel}$, (c) shows the absolute value of the VACF $C_v^{\parallel}$, normalized by $k_BT/m_{\parallel}^*$, and (d) shows the one-sided spectral density of the thermal force $2S_F^{\parallel}$. The cusps in sub-figure (c) correspond to zero-crossings that are a result of the harmonic confinement. Despite the large value of $\epsilon = 0.5$, the method of reflections and point-particle approximation agree very well. The difference between the modified and unmodified point-particle approximation is not discernible in the plots due to the small density difference ($\rho_p/\rho_f = 2$). Figure from Simha *et al.* [2017], courtesy of Dr. Jianyong Mo.

1994; Hajizadeh & Reihani, 2010], but also given the wide array of applications of gold nano-particles [Sardar *et al.*, 2009], and we believe that our modifications to the PPA would be relevant to such systems. To illustrate the differences due to our modifications, figure 9.3 (a) and (b) show predictions for the VACF from the three methods, viz. the modified PPA, the unmodified PPA and the method of reflections, in the perpendicular and parallel directions respectively, for a system of a gold particle ($\rho_p \approx 19.3 \times 10^3$ kg/m^3) in acetone ($\rho_f \approx 790$ kg/m^3) with the same geometry and temperature, harmonically confined in a trap of stiffness $K = 200$ pN/μm. The difference here is quite discernible, especially given that the VACF is an averaged measurement, whereby the experimental error from uncorrelated noise can be made smaller by accumulating more statistics. The PSD of thermal force in the same systems is shown in figure 9.4.

It must be noted that a traditional tweezers experiment to discern these differences may not be feasible, owing to the heating associated with absorption of the trapping laser by gold nano-particles [Seol *et al.*, 2006]. Novel methods of trapping and detection would need to be developed to study equilibrium Brownian motion of metallic particles. However, it is very plausible that the unsteady drag coefficients calculated here will find other applications in the context of metallic nano-particles, including possibly in the analysis of hot Brownian motion in scenarios where the fluid parameters are not significantly altered by heating.

9.3 Brownian motion near a no-slip flat wall

Felderhof [2005] (see also erratum Felderhof [2006*b*]) has calculated the parallel and perpendicular components of the reaction field tensor for a no-slip wall[3]. We re-write

[3]With much suffering, partially alleviated by significant consultation of EMOT, the author, along with Dr. Jianyong Mo, has independently verified these calculations by hand.

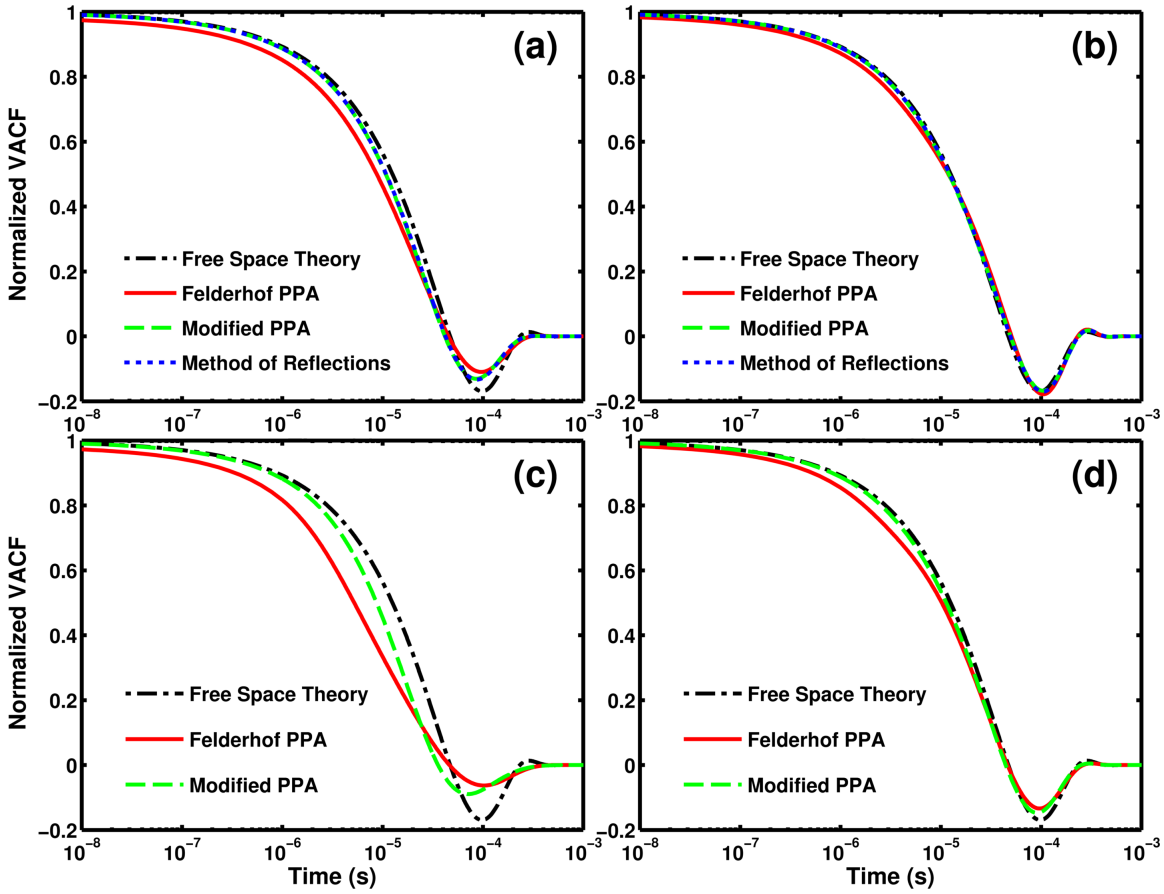

Figure 9.3: Predictions for the VACF of a spherical gold particle (diameter $2a = 3\mu$m, density $\rho_p \approx 19.3 \times 10^3$ kg/m^3) harmonically confined (stiffness $K = 200$ pN/μm) near a flat wall (sphere-wall distance $h = 3\mu$m) in acetone (density $\rho_f \approx 790$ kg/m^3, viscosity $\eta \approx 3 \times 10^{-4}$ Pa·s) at a temperature of 295 K, obtained from the three methods, viz. our modified point-particle framework (green line with long dashes), the point-particle approximation as used by Felderhof [2005, 2012], and in sub-figures (a) and (b), the method of reflections (blue line with short dashes). Sub-figures (a) and (b) show the perpendicular and parallel VACF for a full-slip wall, and (c) and (d) show the perpendicular and parallel VACF for a no-slip wall, respectively. The VACF is shown in absolute value and has been normalized by the velocity variance, using the added mass from potential flow calculations. The significant differences between the modified and unmodified PPA indicates that our modifications are indeed significant in this system ($\rho_p/\rho_f \approx 24.4$), which is experimentally quite common. Figure from Simha *et al.* [2017], courtesy of Dr. Jianyong Mo.

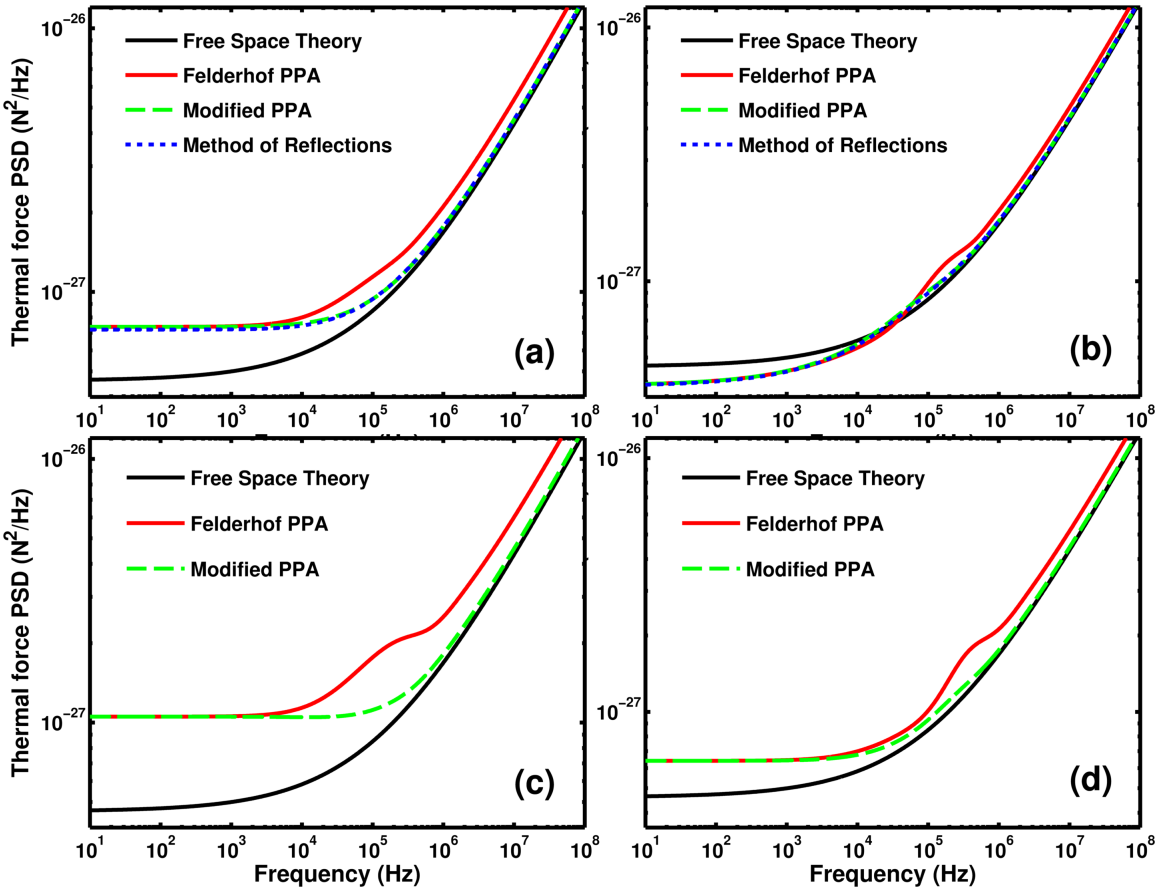

Figure 9.4: Predictions for the one-sided PSD of the thermal force acting on a spherical gold particle (diameter $2a = 3\mu$m, density $\rho_p \approx 19.3 \times 10^3$ kg/m^3) near a flat wall (sphere-wall distance $h = 3\mu$m) in acetone (density $\rho_f \approx 790$ kg/m^3, viscosity $\eta \approx 3 \times 10^{-4}$ Pa·s) at a temperature of 295 K, obtained from the three methods, viz. our modified point-particle framework (green line with long dashes), the point-particle approximation as used by Felderhof [2005, 2012], and in sub-figures (a) and (b), the method of reflections (blue line with short dashes). Sub-figures (a) and (b) show the perpendicular and parallel (one-sided) thermal force PSD for a full-slip wall, and (c) and (d) show the perpendicular and parallel thermal force PSD for a no-slip wall, respectively. The significant differences between the modified and unmodified PPA indicates that our modifications are indeed significant in this system ($\rho_p/\rho_f \approx 24.4$). Figure courtesy of Dr. Jianyong Mo.

their results in a manner convenient to our conventions as,

$$\begin{aligned}\gamma_s R_\perp = -\frac{1}{16\mathfrak{v}^4}\frac{a}{h}\Big\{ & 6(6+\mathfrak{v}^2+8\mathfrak{v}^3)+6(6+12\mathfrak{v}+9\mathfrak{v}^2+2\mathfrak{v}^3)\mathrm{e}^{-2\mathfrak{v}} \\ & -(144+144\mathfrak{v}+48\mathfrak{v}^2-6\mathfrak{v}^4+10\mathfrak{v}^5+\mathfrak{v}^6-\mathfrak{v}^7)\mathrm{e}^{-\mathfrak{v}} \\ & +\mathfrak{v}^6(12-\mathfrak{v}^2)\mathrm{E}_1(\mathfrak{v})+72\mathfrak{v}^2K_0(2\mathfrak{v})+36\mathfrak{v}(2+\mathfrak{v}^2)K_1(2\mathfrak{v}) \\ & +6\pi\mathfrak{v}\Big[2\mathfrak{v}(3-\mathfrak{v}^2)(Y_0(2\mathfrak{v})-\boldsymbol{H}_0(2\mathfrak{v})) \\ & \qquad -(6-5\mathfrak{v}^2)(Y_1(2\mathfrak{v})-\boldsymbol{H}_1(2\mathfrak{v}))\Big]\Big\},\end{aligned} \tag{9.7}$$

and

$$\begin{aligned}\gamma_s R_\parallel = -\frac{1}{32\mathfrak{v}^4}\frac{a}{h}\Big\{ & 36+27\mathfrak{v}+6\mathfrak{v}^2+6(6+12\mathfrak{v}+11\mathfrak{v}^2+6\mathfrak{v}^3+4\mathfrak{v}^4)\mathrm{e}^{-2\mathfrak{v}} \\ & -(144+144\mathfrak{v}+72\mathfrak{v}^2+24\mathfrak{v}^3 \\ & \qquad -6\mathfrak{v}^4+2\mathfrak{v}^5-\mathfrak{v}^6+\mathfrak{v}^7)\mathrm{e}^{-\mathfrak{v}} \\ & +\mathfrak{v}^8\mathrm{E}_1(\mathfrak{v})+12\mathfrak{v}^3(2\mathfrak{v}K_2(2\mathfrak{v})+3K_3(2\mathfrak{v})) \\ & +6\pi\mathfrak{v}^3\Big[2\mathfrak{v}(Y_2(2\mathfrak{v})-\boldsymbol{H}_{-2}(2\mathfrak{v})) \\ & \qquad -3(Y_3(2\mathfrak{v})+\boldsymbol{H}_{-3}(2\mathfrak{v}))\Big]\Big\}.\end{aligned} \tag{9.8}$$

In the above E_1 denotes the exponential integral, Y_n and K_n denote the Bessel and modified Bessel functions of the second kind of order n, and $\boldsymbol{H}_n$ denotes the Struve function of order n.

For the convenience of the reader, we provide Wolfram Mathematica code for the above:

```
E1[z_] := -ExpIntegralEi[-z] + I \[Pi]
Rzz[v_] := -1/(
  16 v^4) (6 (6 + v^2 + 8 v^3) +
    6 (6 + 12 v + 9 v^2 + 2 v^3) E^(-2 v) - (144 + 144 v + 48 v^2 -
       6 v^4 + 10 v^5 + v^6 - v^7) E^-v + v^6 (12 - v^2) E1[v] +
    72 v^2 BesselK[0, 2 v] + 36 v (2 + v^2) BesselK[1, 2 v] +
    6 \[Pi] v (2 v (3 - v^2) (BesselY[0, 2 v] -
          StruveH[0, 2 v]) - (6 - 5 v^2) (BesselY[1, 2 v] -
          StruveH[1, 2 v])))
Rxx[v_] := -1/(
  32 v^4) (36 + 27 v + 6 v^2 +
    6 (6 + 12 v + 11 v^2 + 6 v^3 + 4 v^4) E^(-2 v) - (144 + 144 v +
       72 v^2 + 24 v^3 - 6 v^4 + 2 v^5 - v^6 + v^7) E^-v +
    v^8 E1[v] + 12 v^3 (2 v BesselK[2, 2 v] + 3 BesselK[3, 2 v]) +
    6 \[Pi] v^3 (2 v BesselY[2, 2 v] - 3 BesselY[3, 2 v] -
       3 StruveH[-3, 2 v] - 2 v StruveH[-2, 2 v]))
```

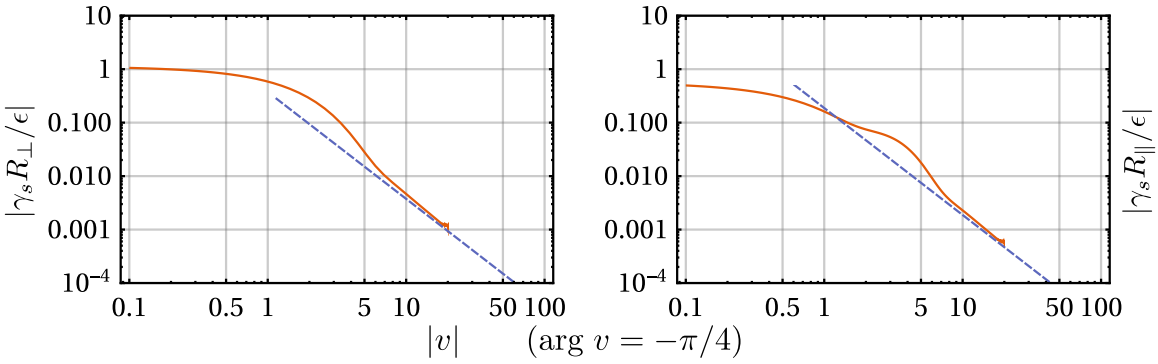

Figure 9.5: Log-log plots of the absolute values of components of the reaction field tensor given by Felderhof [2005] for a no-slip flat wall (9.7), (9.8), multiplied by γ_s and divided by $\epsilon = a/h$. The resulting quantity $|\gamma_s R_{\perp,\parallel}/\epsilon|$ is a function of $\mathfrak{v}$ alone, and since $\arg(\mathfrak{v}) = -\pi/4$, we can make a plot against $|\mathfrak{v}|$. The plot on the left shows the perpendicular component, whereas the plot on the right shows the parallel component. The orange solid curve corresponds to the evaluation of the full expressions 9.7 and 9.8, whereas the blue dashed line corresponds to the asymptotic expressions of (9.9). From the plots, it appears that both components are bounded by their DC absolute values of $9a/8h$ (which is only slightly larger than $1(a/h)$) and $9a/16h$

In numerical evaluation, it is possible that the accuracy of the Bessel and Struve functions for large $|\mathfrak{v}|$ is poor, which can result in spurious values for the reaction field tensor components. For example in Wolfram Mathematica 11.0, the numerics are no longer reliable for $|\mathfrak{v}| \gtrsim 20$, and the expression appears to diverge. However, at this point, the asymptotic expressions given by Felderhof [2005],

$$\begin{aligned} \gamma_s R_\perp &\sim -\frac{3}{8\mathfrak{v}^2}\frac{a}{h}, \\ \gamma_s R_\parallel &\sim -\frac{3}{16\mathfrak{v}^2}\frac{a}{h}, \end{aligned} \tag{9.9}$$

as $\mathfrak{v} \to \infty$ with argument $-\pi/4$ are already sufficiently accurate. This is seen in the log-log plots shown in figure 9.5, where the orange solid curve shows the absolute value of expressions of 9.7 and 9.8 divided by $\epsilon = a/h$, and the blue dashed line represents the corresponding asymptotic expressions.

As before, the various statistical properties of Brownian motion are best calculated numerically using (2.29) and the methods described in that context. The numerical predictions of the modified PPA for a no-slip wall are shown in Mo *et al.* [2017]. However, once again, we wish to comment on the nature of the thermal force. The

low-frequency expansions $\omega \ll \tau_f^{-1}$, τ_w^{-1} of the (two-sided) PSDs of the thermal force are given by [Mo *et al.*, 2015*b*]

$$\begin{aligned} S_{F,\parallel}(\omega) &\sim 2k_B T\gamma_s \left[\frac{1}{1-\frac{9a}{16h}} + \frac{128\sqrt{2}(3h^4 - a^2h^2)}{3a^2\left(16h-9a\right)^2}\left(\omega\tau_f\right)^{\frac{3}{2}}\right], \\ S_{F,\perp}(\omega) &\sim 2k_B T\gamma_s \left[\frac{1}{1-\frac{9a}{8h}} - \frac{32\sqrt{2}h^2}{3\left(9a-8h\right)^2}\left(\omega\tau_f\right)^{\frac{3}{2}}\right]. \end{aligned} \tag{9.10}$$

In this case, the lack of the $\sqrt{\omega\tau_f}$ term and the resulting enhanced flatness at low frequencies is observed in both parallel and perpendicular directions. This has also been verified by experiment [Mo *et al.*, 2015*b*] (Chapter 10).

A loose intuitive explanation is based on the analogy with hard and soft reflection. In the case of a no-slip wall, the boundary conditions for both parallel and perpendicular directions are "hard", i.e. the velocity goes to zero. However, in the case of a full-slip wall, the boundary conditions in the parallel directions are "soft", i.e. the normal derivatives of velocity go to zero. The hard reflection is expected to produce some sort of destructive interference to which, we may guess, the lack of the $\sqrt{\omega\tau_f}$ term could be attributed [Mo *et al.*, 2015*b*].

An analogous calculation using the method of reflections is rendered difficult by the lack of a simple image system.[4]

In figure 9.3, sub-figures (c) and (d) show the differences between the VACF of a 3μm-diameter gold particle near a no-slip flat wall in acetone as predicted by our modified point-particle framework, and by the point-particle approximation as used by Felderhof [2005]. The difference in the no-slip case in the perpendicular direction is very significant, and should be easily detected by measurements. However, as mentioned earlier, measurements of Brownian motion in such systems are rendered difficult due to the heating of the nano-particles by absorption of the trapping / detection laser beams, and novel trapping and detection techniques would need to be developed in order to make these measurements without heating.

[4]The image system for a point singularity near a no-slip wall is known in the context of steady Stokes flow, but is more complicated [Blake, 1971].

9.4 Diffusion near a no-slip flat wall

If the *steady* drag coefficient $\gamma(\omega = 0)$ obtained by solving the steady Stokes equations is known, the diffusion coefficient may be calculated using the Sutherland-Einstein relation $D = k_B T/\gamma(\omega = 0)$. To avoid any ambiguity, we shall use γ^{steady} to denote the steady drag coefficient.

Lorentz [1907] derived the first-order correction to the Stokes drag force on a sphere ($-6\pi\eta a\boldsymbol{u}$) due to the presence of a no-slip flat wall. Their results in our notation are

$$\begin{aligned} \gamma_{\perp}^{\text{steady}} &= \gamma_s \left(1 + \frac{9}{8}\frac{a}{h}\right), \\ \gamma_{\parallel}^{\text{steady}} &= \gamma_s \left(1 + \frac{9}{16}\frac{a}{h}\right). \end{aligned} \tag{9.11}$$

As a reminder, a denotes the radius of the spherical particle, h denotes the distance from its center to the wall, and $\gamma_s = 6\pi\eta a$ is the steady Stokes drag coefficient for a sphere.

Faxén [1921] derived more correction terms for the drag force in the direction parallel to the wall,[5] retaining the advection term to the Oseen approximation[6]. At very low Reynolds number, we may set σa and $\sigma\zeta$ in their formula to zero [Sharma *et al.*, 2010] and obtain (in our notation)

$$\gamma_{\parallel}^{\text{steady}} = \frac{\gamma_s}{1 - \frac{9}{8}\frac{a}{2h} + \left(\frac{a}{2h}\right)^3 - \frac{45}{16}\left(\frac{a}{2h}\right)^4 - 2\left(\frac{a}{2h}\right)^5}. \tag{9.12}$$

Note that the correction terms are in the denominator, in the fashion of a Padé approximant. It appears that these results were obtained through a boundary integral method.

Brenner [1961] provided a series for the drag coefficient in the perpendicular direction using eigenfunction expansions in bipolar coordinates. Their result, verified against many experiments [Liu *et al.*, 2014; Carbajal-Tinoco *et al.*, 2007; Ishii *et al.*,

[5] Faxén analyzes the problem in greater detail than we wish to explore here, including results for the transverse force and the rotational torque exerted on a sphere moving parallel to a plane wall.

[6] Faxén's thesis has been digitized by Google Inc. and is available at https://catalog.hathitrust.org/Record/010265690 as of July 2017.

2010], is

$$\gamma_{\perp}^{\text{steady}} = \gamma_s \Bigg[\frac{4}{3} \sinh\beta \sum_{n=1}^{\infty} \frac{n(n+1)}{(2n-1)(2n+3)} \times \left(\frac{2\sinh(2n+1)\beta + (2n+1)\sinh 2\beta}{4\sinh^2(n+1/2)\beta - (2n+1)^2 \sinh^2\beta} - 1 \right) \Bigg], \tag{9.13}$$

where[7] $\beta = \cosh^{-1}(h/a)$. The infinite sum can be truncated to about 80 terms and numerically evaluated.

9.5 Diffusion near a no-slip cylindrical wall

The steady drag on a spherical particle inside a cylindrical pipe may be obtained using the method of reflections, and is well-known [Happel & Brenner, 1965]. The steady drag coefficient for a spherical particle outside of a no-slip cylindrical wall has been obtained by Alam *et al.* [1980] (see also erratum, Alam *et al.* [1983]). The drag coefficients for motion in the axial, radial and tangential directions to the cylinder are provided. Initially, a literature search did not find this paper, so the author independently performed a calculation using the method of reflections, closely following Happel & Brenner [1965, Chap. 7] to obtain a result for the drag in the radial direction that agreed with Alam *et al.* [1980].

Owing to its relevance to Mo *et al.* [2015*b*], we present the result of Alam *et al.* [1980] for the radial drag coefficient,[8]

$$\gamma_{\text{radial}}^{\text{steady}} = \gamma_s \left(1 + \frac{a}{R} k_r \right), \tag{9.14}$$

where the radial drag correction k_r is given by

$$k_r = \frac{3}{2\pi} \Bigg\{ H - \frac{1}{4} \int_0^{\infty} \mathrm{d}\lambda \sum_{n=-\infty}^{\infty} \Big[(L_{n-1} + L_{n+1} - 2r_0 L_n) \times \left[L_{n-1} + L_{n+1} - r_0(L'_{n-1} + L'_{n+1}) + 2L'_n \right] / E_n \Big] \Bigg\}, \tag{9.15}$$

[7] We have used β instead of Brenner's notation α.

[8] The work of Alam *et al.* [1980] works in non-dimensionalized units where the radius of the cylinder is 1. We present them here again in fully dimensional units for the convenience of a user of the final expression.

with

$$
\begin{aligned}
H &= \int_0^\infty \mathrm{d}\lambda \sum_{n=-\infty}^{\infty} I_n(\lambda) \frac{K_n^2(\lambda r_0)}{K_n(\lambda)}, \\
L_n &= L_{-n} = \frac{K_n(\lambda r_0)}{K_n(\lambda)}, \\
L_n' &= \frac{\lambda K_n'(\lambda r_0)}{K_n(\lambda)}, \\
E_n &= 1 + \frac{\lambda K_n'(\lambda)}{K_n(\lambda)} - \frac{1}{2}\left(\frac{\lambda K_{n-1}'(\lambda)}{K_{n-1}(\lambda)} + \frac{\lambda K_{n+1}'(\lambda)}{K_{n+1}(\lambda)} \right), \\
r_0 &= (R+h)/R,
\end{aligned}
\tag{9.16}
$$

and R denotes the radius of the cylinder, and h is the radial distance from the center of the spherical particle to the outer edge of the cylinder (so that the distance to the axis would be $R+h$). As before γ_s is the steady Stokes drag coefficient $6\pi\eta a$ and a denotes the radius of the spherical particle.

The above (despite the infinite eigenfunction expansion) is a first order correction. We may write the correction in Padé form as

$$
\gamma_{\text{radial}}^{\text{steady}} = \frac{\gamma_s}{1 - \frac{a}{R} k_r}. \tag{9.17}
$$

As noted by Happel & Brenner [1965], this is equivalent to assuming a geometric series for higher order corrections, and this generally improves the accuracy of the result.

As before, the hindered diffusion coefficient may be calculated from the above drag coefficient as $D = k_B T / \gamma^{\text{steady}}$.

The numerical evaluation of the above result has some challenges owing to the poor accuracy of Bessel functions and large number cancelations. The expressions for L_n', $\frac{\lambda K_n'(\lambda)}{K_n(\lambda)}$ and the integrand of H are re-written as,

$$
\begin{aligned}
H &= \int_0^\infty \mathrm{d}\lambda \sum_{n=-\infty}^{\infty} \left[I_n(\lambda) K_n(\lambda) \right] L_n^2, \\
L_n' &= \left[-\frac{\lambda K_{n-1}(\lambda r_0)}{K_n(\lambda r_0)} - \frac{n}{r_0} \right] L_n \\
\frac{\lambda K_n'(\lambda)}{K_n(\lambda)} &= -\frac{\lambda K_{n-1}(\lambda r_0)}{K_n(\lambda r_0)} - n,
\end{aligned}
\tag{9.18}
$$

and the product $I_n(x)K_n(x)$ as well as the ratio $K_n(x)/K_{n-1}(x)$ are implemented separately.

To implement the product $I_n(x)K_n(x)$, we use a Taylor series expansion for small $x < 0.05n$, and an asymptotic series expansion for large $x > 50n$. When $x \sim n$, we attempt to call the built-in (in this case on MATLAB) functions and compute the product. If this fails, we use the integral representation using J_0 [DLMF, Eq. 10.32.16], where the upper bound may be truncated to a finite value owing to the quick decay of the integrand, and the integral may be evaluated using Gauss-Kronrod quadrature.

To implement the ratio $K_n(x)/K_{n-1}(x)$, we implement the ratio $I_n(x)/I_{n-1}(x)$ in the manner described by Gautschi & Slavik [1978] (recursion is used to compute the continued fraction, and the Perron algorithm is used to about 900 terms) and use the Wronskian $I_{n-1}(x)K_n(x) + I_n(x)K_{n-1}(x) = 1/x$ to turn the computation into that of $I_n(x)/I_{n-1}(x)$ and $I_n(x)K_n(x)$.

Chapter Ten: Experimental investigations on the hydrodynamic effects of boundaries on Brownian motion

In this chapter, we will describe an experiment studying short-time aspects of Brownian motion near a boundary, published by Mo *et al.* [2015*b*]. The author contributed to the design, implementation and conduct of the experiment, and wrote some of the sections of the manuscript.

10.1 Experimental methods

10.1.1 Experimental setup

The setup used for the experiments in bulk fluid (chapters 5, 6) required several modifications to allow the measurement of Brownian motion near a boundary.

Firstly, the flow-cell design had to be modified to include boundaries. We repurposed a single-mode optic fiber (Thorlabs, SM980G80) with a 80μm-diameter cladding to create cylindrical boundaries. The fiber's acrylate coating was stripped with a fiber stripping tool and the residue was cleaned with HPLC-grade acetone and

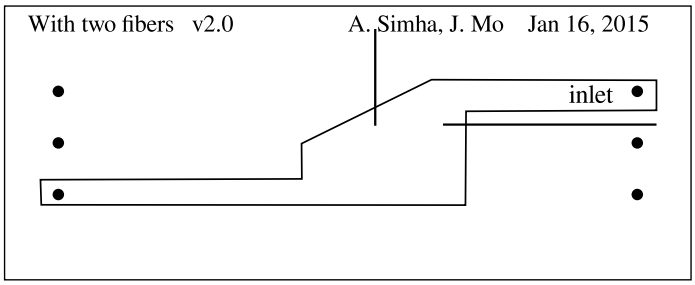

Figure 10.1: Template used to cut sealing film to create channels in the flow-cell for the experiment. The fibers with coating stripped were placed along the marked lines to create no-slip boundaries in the flow-cell. The different shape of the flow-cell with the slope on the top wall was designed so that there was enough sealing film around the vertical fiber to seal it well.

lens tissue, so that the cladding was exposed. The cladding of two fibers were then heat-sealed into the flow cell, one placed horizontally and the other placed vertically in the chamber. The alignment of the fibers was done by eye with the use of a printed template (shown in figure 10.1). The pressure during the melting of the sealing film is sufficient for the nescofilm or parafilm to flow around the fiber and make a tight seal – any attempts to cut a channel in the sealing film for the fiber leads to an incomplete seal and a leaky flow cell. After the flow-cell has been baked, care must be taken to cut any excess fiber protruding from the cell, as the stress may propagate and crack open the seal. Therefore, it is advisable to leave about $2 \sim 3$mm of fiber protruding and gently cut the excess beyond that point. The alignment of the fibers can be verified in the CCD image of the chamber. Figure 10.2 (A) and (B) shows the configuration of the fibers in the flow cell. Figures 10.3 (A) and (B) show trapped micro-spheres in the vicinity of the vertical and horizontal fibers respectively. Since the cut mirror we used (figure 5.8) cuts the beam vertically, the detector measures beam displacements in the horizontal direction, whereby the two cases measure Brownian motion in the perpendicular and parallel directions to the fibers respectively.

The 3-axis translation stage on which the flow-cell is mounted had two of its micrometers – in the directions lateral to the laser beam – replaced by micrometers with piezo-electric elements (Thorlabs, DRV517). The piezos were controlled with a driver (Thorlabs, BPC301) which provided a read-out of relative positions using a strain gauge mounted on the piezo. This allowed us to position the cylindrical fibers relative to the particle with a precision of $\sim$ 10nm in both lateral directions, giving us the ability to carefully control the sphere-wall separation. The piezo driver has closed-loop and an open-loop modes of operation. Given that it takes a long time for the piezo crystal to relax completely, the closed-loop mode varies the voltage applied to the piezo in order to keep the separation at the desired value. However, the feedback loop of the system was observed to introduce a noise at about a kHz frequency into the measurement. Therefore, it was kept in open loop, and we waited for the piezo crystal to relax naturally before acquiring data. As for the other axis (along the beam-propagation direction), it is adjusted so that the particle lies in the center of the chamber in that direction. This prevents the effects of the boundary formed by the cover-slip from being significant, since the separation $\sim 40\mu$m (half the thickness of the chamber) is much larger than the particle size. That 40μm is far enough for the chamber walls to be neglected in the context of a 3μm-diameter

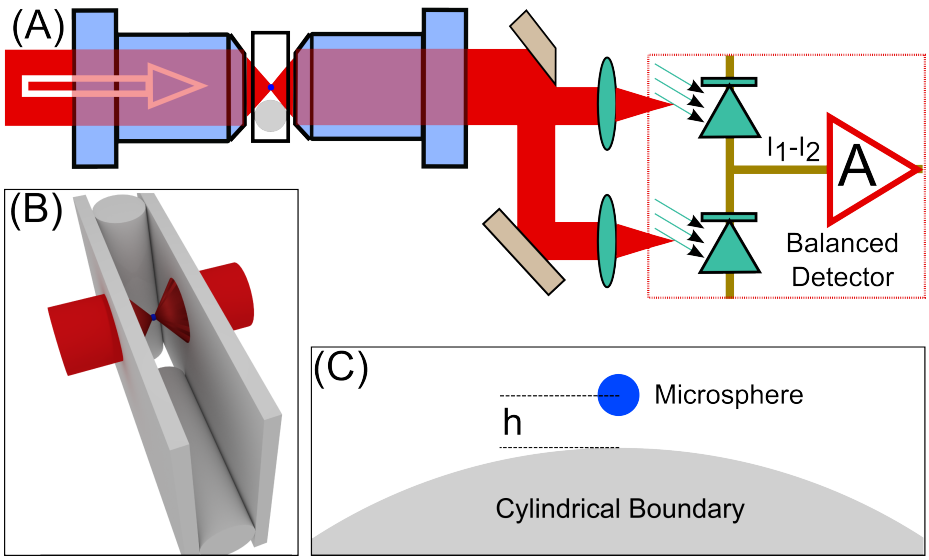

Figure 10.2: Experimental setup to study Brownian motion near a boundary. An approximate flat boundary is created by introducing two cylindrical glass fibers in the flow cell. Sub-figure (A) shows a simplified top-view schematic of the experimental setup, which is mostly similar to that used in the experiments in bulk liquid (chapters 5, 6). The primary difference lies in the inclusion of the cylindrical glass fibers into the chamber, as represented more clearly in sub-figure (B). Sub-figure (C) shows a representation of the relative sizes of the particle and cylindrical fiber to scale. The large diameter of the fiber compared to the size of the particle and the separation between the particle and wall h allows us to treat the wall as approximately flat. The distance h is defined as shown – measured from the center of the particle to the edge of the wall. Figure from Mo *et al.* [2015*b*], courtesy of Dr. Jianyong Mo.

sphere is verified post facto by the experiment.

The experiment used $\approx 3\mu$m-diameter silica spheres (Bangs Laboratories, SS05N) in HPLC-grade water. The diameter of the fiber was chosen to match the typical thickness of Nescofilm. The large diameter (80μm) of the fiber in comparison to the particles allows us to approximate the fiber by a flat no-slip wall, as is highlighted in figure 10.2 (C), at least for small sphere-wall separations.

10.1.2 Data analysis

The acquired data is analyzed in the same manner as described in §5.9. However, in addition to fitting the calibration factor, the trap stiffness, and the particle's diameter,

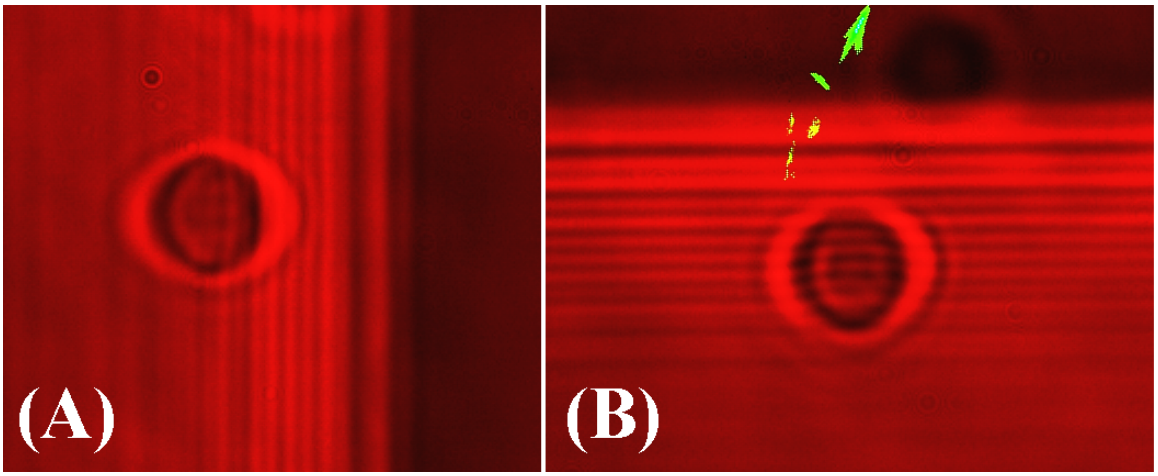

Figure 10.3: A silica micro-sphere is trapped in the vicinity of (A) vertically, and (B) horizontally, placed glass fibers. The many parallel lines seen are an artifact of diffraction. The green marks seen in figure (B) are dead pixels on the camera[1]. Figure courtesy of Dr. Jianyong Mo.

the distance to the wall h is also fit from the data. This is necessary because the piezo strain gauge can only tell us the relative distances between different positions of the particle, but not the absolute distance to the wall. It turns out that fitting the VACF gives the best results for the sphere-to-wall distance h, as may be verified by plotting the fit distance against the reading of the piezo strain gauge.

Another way to determine the absolute sphere-wall separation is by measuring the diffusion coefficient. Data is acquired with reduced trap strength while keeping the same particle in the trap, so that the MSD attains the diffusive regime before it saturates. The light is redirected to a DC-coupled detector, and the diffusion coefficient is determined from the long-time behavior of the MSD [Pralle *et al.*, 1998]. The behavior of the diffusion coefficient near a wall has been well-studied by previous experiments [Carbajal-Tinoco *et al.*, 2007; Ishii *et al.*, 2010; Liu *et al.*, 2014], bolstering confidence in this method. Specifically, the long-time behavior of the PACF is given by $\sim \langle x^2 \rangle \mathrm{e}^{-t/\tau_k}$ where $\tau_k = \gamma^{\mathrm{steady}}(h)/K$ where $\gamma^{\mathrm{steady}}(h)$ denotes the steady Stokes drag on a sphere in the presence of a no-slip wall as a function of the separation h. This expression may be obtained by approximating the drag coefficient in the GLE by $\gamma^{\mathrm{steady}}(h)$ for time-scales $t \ll \tau_f$, and solving the resulting Langevin equation with the

[1]These dead pixels may be obtained when necessary by inadvertently shooting a pico-second pulsed laser at the CCD camera.

harmonic trap in the usual manner. The diffusion coefficient may then be obtained using the Stokes-Einstein relation $D(h) = k_B T/\gamma^{\text{steady}}(h)$. Therefore, by fitting the MSD, or alternatively the PACF at long time-scales, one may extract $D(h)$, which can then be fit to either the theory for a flat wall [Brenner, 1961], or the theory for a cylindrical wall [Alam *et al.*, 1980] (discussed in Chapter 9).

10.2 Results

We shall now present a selection of results from Mo *et al.* [2015*b*].

Figure 10.4 (A) shows absolute measurements of sphere-wall separation obtained by fitting the VACF to the theoretical predictions. The horizontal axis represents the reading of the strain gauge on the piezo, after removing the fitted offset. The fact that the data (green-squares) follows the red $y = x$ line closely until about 7 μm shows that the VACF fit gives reliable results for small separations h. Sub-figure (B) shows the determination of sphere-wall separation by measuring the hindered diffusion coefficient. The data shows a trend towards the theory for a cylindrical wall, although more precise measurements are needed to discern between the two theories.

Figure 10.5 shows the experimental data and theoretical predictions for the MSD for Brownian motion perpendicular to the wall at four different sphere-wall separations: (A) $h = 30\mu$m, (B) $h = 6.1\mu$m, (C) $h = 4.9\mu$m, (D) $h = 3.1\mu$m. The insets zoom-in on the longer time-scales to help discern the difference between the theory with the boundary (red dashed line) and the bulk theory (solid black line). At about 30μm, the boundary is sufficiently far that the effects are negligible. This verifies our assumption of neglecting the effects from the boundary of the cover-slip. The boundary effects become more prominent as the particle is moved closer to the boundary, as is expected. Figure 10.6 shows the data and theory for the VACF, once again in the direction perpendicular to the wall. As before, the wall has hardly any effect at $h = 30\mu$m ($a/h \approx 1/20$). The VACF decays faster closer to the wall. Figure 10.7 and figure 10.8 show the velocity and thermal force power-spectral densities respectively, at the same four locations, in the perpendicular direction.

Figure 10.9 shows the experimental results along with theoretical predictions for statistical quantities characterizing Brownian motion in the parallel direction to the

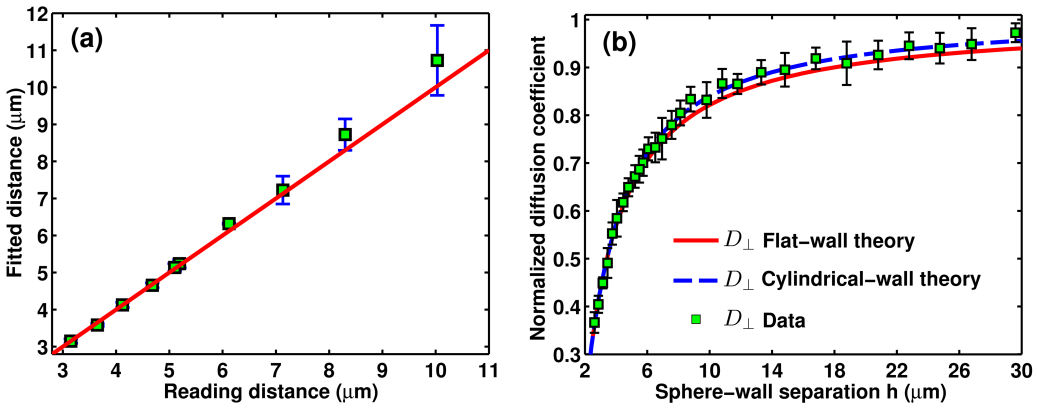

Figure 10.4: Absolute measurements of the distance between the 3μm-diameter spherical particle's center and the boundary (h), (a) obtained by fitting the VACF measured using an AC-coupled detector, (b) obtained by measuring the hindered diffusion coefficients using a DC-coupled detector. The green squares with error-bars indicate the data obtained by analysis of experimental measurements of Brownian motion in the perpendicular direction to the boundary. Sub-figure (a) plots the distance obtained by the fit against the relative distance read by the piezo strain gauge after subtracting the offset obtained by fitting. The red line is the $y = x$ line. It is observed that fitting the VACF gives reliable results when the separation is smaller than 7μm. Sub-figure (b) plots the hindered diffusion coefficients obtained by analysis of the PACF as described in the text. The red solid line represents the theoretical predictions for the diffusion coefficient near a flat wall [Brenner, 1961], whereas the blue dashed line represents those for a cylindrical wall [Alam *et al.*, 1980]. Figure from Mo *et al.* [2015*b*].

wall. Sub-figure (A) shows the MSD, (B) shows the velocity PSD, (C) shows the VACF, and (D) shows the PSD of the thermal force. The separation $h = 2.9\mu$m for all four sub-figures. The effects in the parallel direction are much weaker than the effects in the perpendicular direction for the same separation h.

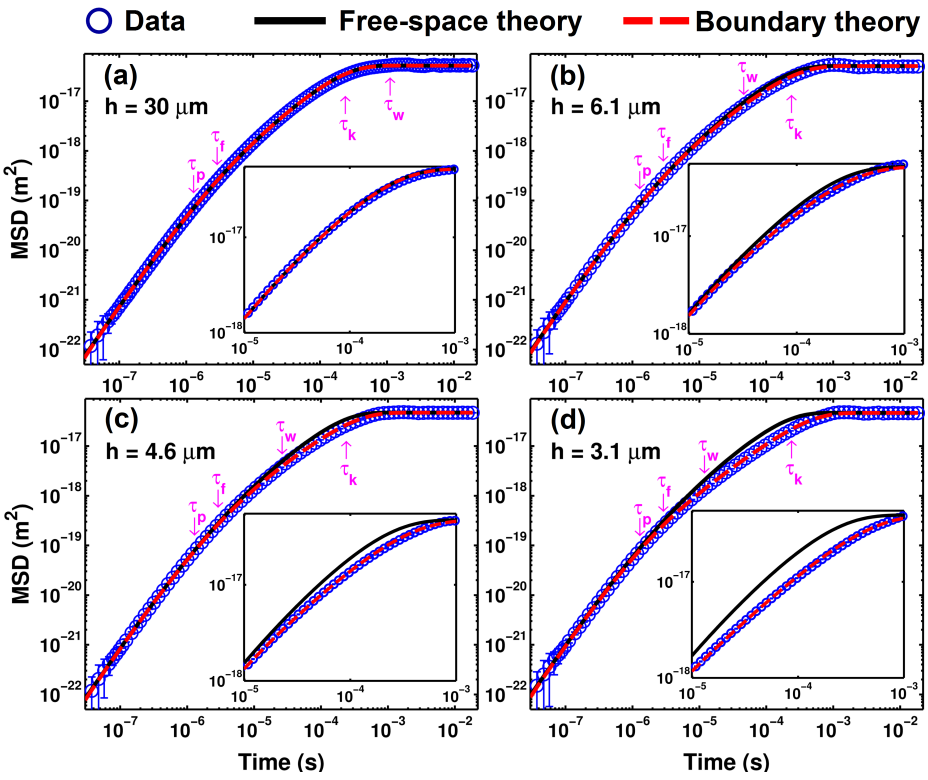

Figure 10.5: Log-log plots of the MSD of a Brownian particle ($2a = 3\mu$m) near a wall in the perpendicular direction. The sphere-wall separation in each case is (A) $h = 30\mu$m, (B) $h = 6.1\mu$m, (C) $h = 4.6\mu$m, (D) $h = 3.1\mu$m. The corresponding values of τ_w are 0.9 ms, 37 μs, 21 μs and 9.6 μs respectively. The blue circles represent the experimental data. The solid black line represents the predictions of the theory of Brownian motion in bulk fluid (Clercx & Schram [1992], Chapter 4), and the dashed red line represents the predictions of the theory of Brownian motion perpendicular to a flat wall (Chapter 8). The MSD becomes suppressed when the sphere is closer to the wall, and as expected, the effects of the wall are negligible at a sufficiently large distances ($a/h = 0.05$). The insets enlarge the region where there is significant difference between the bulk and boundary theories to show it clearly. Figure from Mo *et al.* [2015*b*].

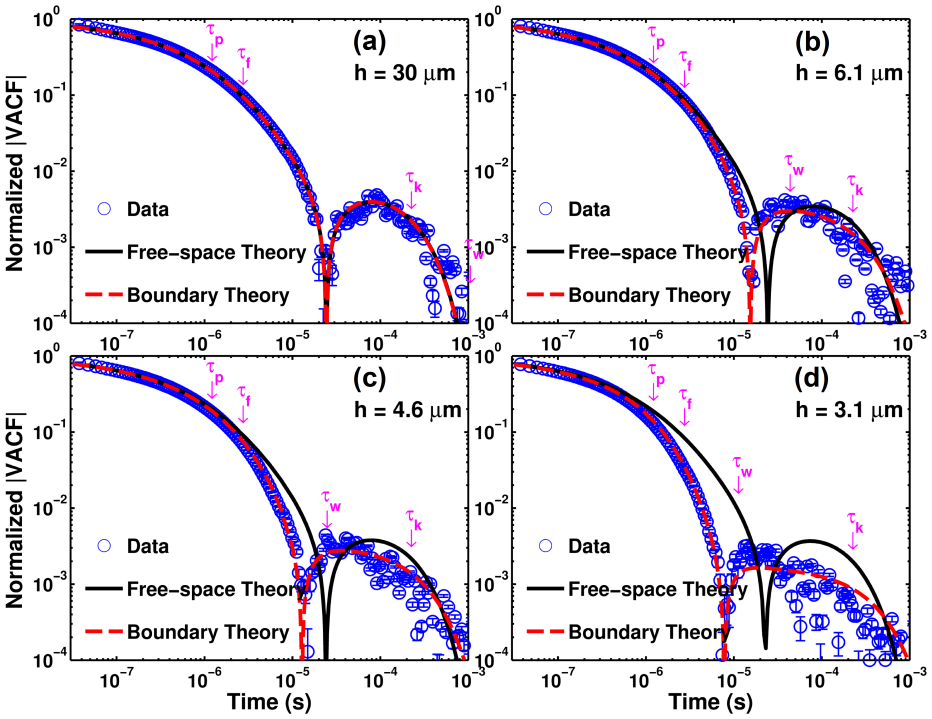

Figure 10.6: Log-log plots of the absolute value of the VACF of a Brownian particle ($2a = 3\mu$m) near a wall in the perpendicular direction, normalized by its zero-time value $k_BT/m^*_\perp$. The sphere-wall separation in each case is (A) $h = 30\mu$m, (B) $h = 6.1\mu$m, (C) $h = 4.6\mu$m, (D) $h = 3.1\mu$m. The corresponding values of τ_w are 0.9 ms, 37 μs, 21 μs and 9.6 μs respectively. The blue circles represent the experimental data. The solid black line represents the predictions of the theory of Brownian motion in bulk fluid (Clercx & Schram [1992], Chapter 4), and the dashed red line represents the predictions of the theory of Brownian motion perpendicular to a flat wall (Chapter 8). The velocity decorrelates faster when the sphere is closer to the wall, and as expected, the effects of the wall are negligible at a sufficiently large distances ($a/h = 0.05$). The cusps are a result of zero-crossings visualized on a log-log plot. These zero-crossings are a consequence of the optical trap. Figure from Mo *et al.* [2015*b*].

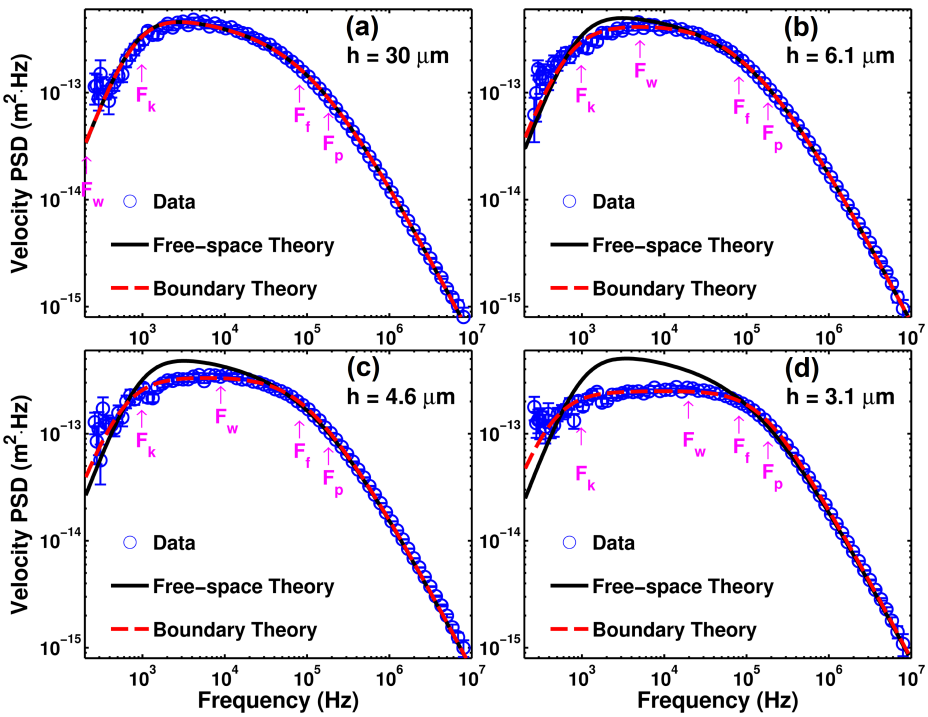

Figure 10.7: Log-log plots of the PSD of velocity of a Brownian particle ($2a = 3\mu$m) near a wall in the perpendicular direction. The sphere-wall separation in each case is (A) $h = 30\mu$m, (B) $h = 6.1\mu$m, (C) $h = 4.6\mu$m, (D) $h = 3.1\mu$m. The corresponding values of τ_w are 0.9 ms, 37 μs, 21 μs and 9.6 μs respectively. The blue circles represent the experimental data. The solid black line represents the predictions of the theory of Brownian motion in bulk fluid (Franosch *et al.* [2011], Chapter 4), and the dashed red line represents the predictions of the theory of Brownian motion perpendicular to a flat wall (Chapter 8). Figure from Mo *et al.* [2015*b*].

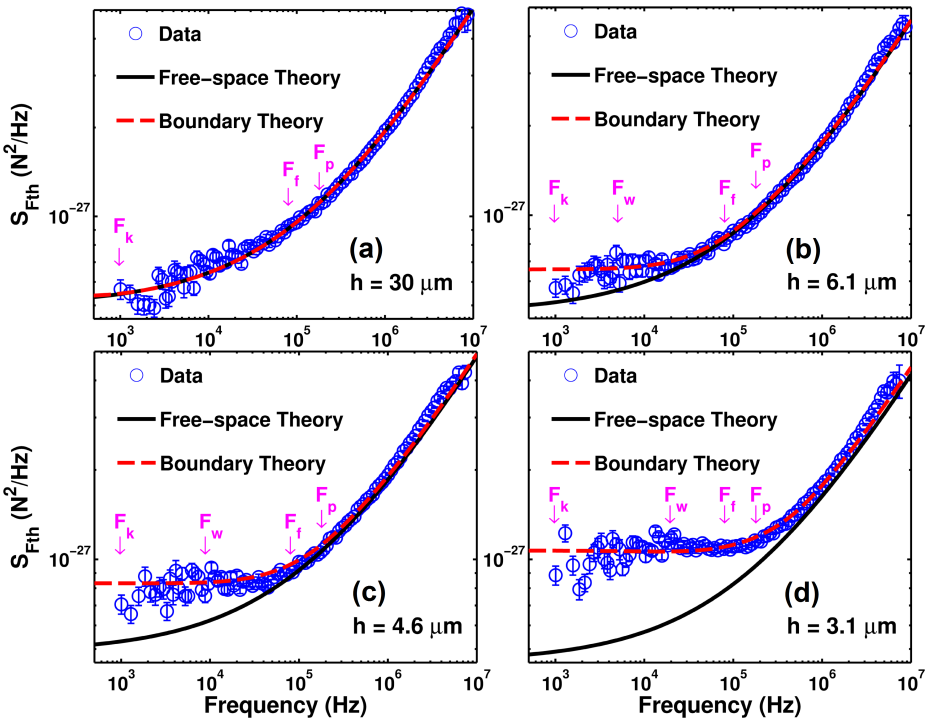

Figure 10.8: Log-log plots of the PSD of the Langevin force on a Brownian particle ($2a = 3\mu$m) near a wall in the perpendicular direction. The sphere-wall separation in each case is (A) $h = 30\mu$m, (B) $h = 6.1\mu$m, (C) $h = 4.6\mu$m, (D) $h = 3.1\mu$m. The corresponding values of τ_w are 0.9 ms, 37 μs, 21 μs and 9.6 μs respectively. The blue circles represent the experimental data. The solid black line represents the predictions of the theory of Brownian motion in bulk fluid (Franosch *et al.* [2011], Chapter 4), and the dashed red line represents the predictions of the theory of Brownian motion perpendicular to a flat wall (Chapter 8). The enhanced flatness of the force PSD at low frequencies is explained through the absence of the $\sqrt{\omega\tau_f}$ term (Chapter 8). Figure from Mo *et al.* [2015*b*].

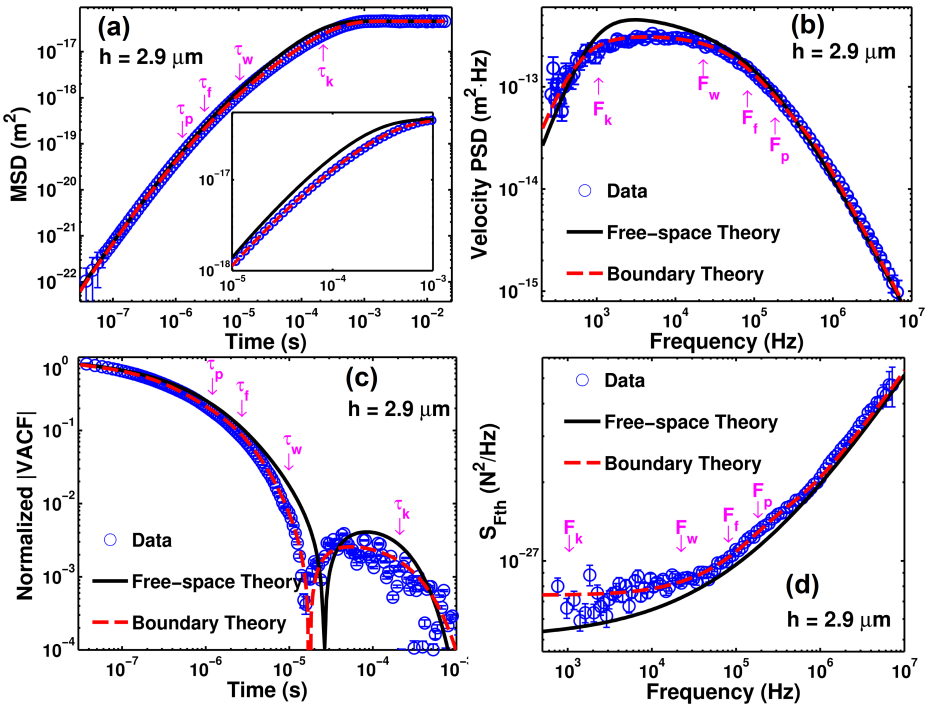

Figure 10.9: Statistical properties of Brownian motion of a sphere ($2a = 3\mu$m) in the direction parallel to a wall. The sphere-wall distance is $h = 2.9\mu$m. Sub-figure (A) shows the MSD, with the inset zooming in on the differences, (B) shows the velocity PSD, (C) shows the absolute value of the VACF, normalized by $k_BT/m^*_{\parallel}$, and (D) shows the PSD of the thermal force. The blue circles represent the experimental data. The solid black line represents the predictions of the theory of Brownian motion in bulk fluid (Clercx & Schram [1992]; Franosch *et al.* [2011], Chapter 4), and the dashed red line represents the predictions of the theory of Brownian motion parallel to a flat wall (Chapter 8). Figure from Mo *et al.* [2015*b*].

Appendix A: Detailed results for the problem of a no-slip sphere oscillating in bulk fluid

In this appendix, we expand on the problem of the drag force on a sphere oscillating in a viscous fluid, which was briefly outlined in Section 3.6. The problem was first solved by Stokes [1851] in the context of damping of pendulum bobs. As before, a modern derivation following Landau & Lifshitz [1987, §24, Prob. 5] will be presented here.

We shall assume that the fluid, which is otherwise quiescent, has a viscosity of η and is sufficiently incompressible on the timescales considered (see the discussion in 3.1) with constant density ρ_f. For convenience, we introduce the kinematic viscosity $\nu := \eta/\rho_f$. Let the sphere's velocity be described by $\boldsymbol{u}(t) = \boldsymbol{u}_\omega \Re\mathrm{e}^{-\mathrm{i}\omega t}$. Let us also suppose that the amplitude of oscillations of the sphere $A = u_\omega/\omega \ll a$, where a is the radius of the sphere. This condition, coupled with the low Reynolds number ($\mathrm{Re} = au_\omega/\nu \ll 1$), allows us to neglect the advection term in the incompressible Navier-Stokes equations, giving us the unsteady Stokes equations (3.6). We wish to solve (3.6) subject to the boundary conditions

$$\begin{aligned} \boldsymbol{v}(\boldsymbol{r},\, t) &\to 0 \text{ as} & \boldsymbol{r} &\to \infty, \\ \boldsymbol{v}(\boldsymbol{r},\, t) &= \boldsymbol{u}(t) \text{ when} & |\boldsymbol{r} - \boldsymbol{R}_t| &= a, \end{aligned} \tag{A.1}$$

where $\boldsymbol{R}(t)$ denotes the instantaneous position of the sphere. The latter boundary condition makes the problem a non-linear problem. In order to make the problem tractable, we evaluate the latter boundary condition at the equilibrium position $\boldsymbol{R}_0$ of the sphere. This assumption is equivalent to moving to the reference frame of the sphere and neglecting the inertial body force of amplitude $u_\omega\omega$ in comparison to other forces in the unsteady Stokes equations. Although it is prima face alarming that this force grows with ω, for any smooth velocity profile $\boldsymbol{u}(t)$, we expect the power spectral density to drop off at least as $1/\omega^2$, whereby this assumption is justified in most physical scenarios including the ones we shall apply it to.

For further simplicity, we shall choose to work in a coordinate system centered on the sphere, whereby $\boldsymbol{R}_0 = 0$. We now have a linear problem which also has time-

translation symmetry, whereby we may take a Fourier transform.[1] The transformed problem may be written as,

$$\begin{aligned} -\mathrm{i}\omega \boldsymbol{v}_\omega &= -\nabla p_\omega + \nu \Delta \boldsymbol{v}_\omega, \\ \nabla \cdot \boldsymbol{v}_\omega &= 0, \\ \boldsymbol{v}_\omega(\boldsymbol{r} \to \infty) &\to 0, \\ \boldsymbol{v}_\omega\big|_{|\boldsymbol{r}|=a} &= \boldsymbol{u}_\omega. \end{aligned} \tag{A.2}$$

We use Landau's ansatz $\boldsymbol{v}_\omega = \nabla \times \nabla \times [f(r)\boldsymbol{u}_\omega]$, which works specifically for a sphere. The explanation for why it works may be found in Landau & Lifshitz [1987, §20].

Firstly, in terms of this ansatz, using the double curl identity, we have

$$\boldsymbol{v}_\omega = \nabla\left[\nabla \cdot (f\boldsymbol{u}_\omega)\right] - \boldsymbol{u}\Delta f. \tag{A.3}$$

Taking the spherical polar components of the above and simplifying, we obtain

$$\begin{aligned} v_r &= -2u\cos\theta \frac{f'(r)}{r}, \\ v_\theta &= -u\sin\theta\left[f''(r) + \frac{f'(r)}{r}\right], \\ v_\phi &= 0. \end{aligned} \tag{A.4}$$

To find the function $f(r)$ itself, we first convert write down the vorticity diffusion equation

$$\nabla \times (-\mathrm{i}\omega \boldsymbol{v}_\omega - \nu\Delta \boldsymbol{v}_\omega) = 0, \tag{A.5}$$

and substitute the ansatz to obtain

$$\boldsymbol{u}_\omega \times \nabla(-\mathrm{i}\omega\Delta f - \nu\Delta^2 f) = 0. \tag{A.6}$$

The only way this can hold for all r, given that $\boldsymbol{u}_\omega$ is a fixed vector and the term in the parenthesis has a gradient that will be in the radial direction is if the gradient itself vanishes, i.e.

$$-\mathrm{i}\omega\Delta f - \nu\Delta^2 f = \text{constant}. \tag{A.7}$$

Given that the velocity field and its derivatives must vanish at infinity, the second derivative of f, which it depends on must also vanish at infinity. Thus, the asymptotic

[1] Our convention was specified in equation (2.5).

condition on the velocity field forces the constant to be 0. Thus, $f(r)$ satisfies the equation

$$\alpha^2 \Delta f - \Delta^2 f = 0, \tag{A.8}$$

where $\alpha := \sqrt{-\mathrm{i}\omega/\nu}$ with $\Re[\alpha] > 0$.

Before we solve this equation, we may determine an equation for the pressure in terms of f and its derivatives. To do so, we go back to the equation

$$\frac{\nabla p_\omega}{\rho} = \mathrm{i}\omega \boldsymbol{v}_\omega + \nu \Delta \boldsymbol{v}_\omega, \tag{A.9}$$

and substitute (A.3) into it to obtain,

$$\frac{\nabla p_\omega}{\rho} = \mathrm{i}\omega \nabla \left(\boldsymbol{u}_\omega \cdot \nabla f \right) - \nu \nabla \left(\boldsymbol{u}_\omega \cdot \nabla \Delta f \right). \tag{A.10}$$

In obtaining the above, we have used the fact that f satisfies (A.8). We can integrate the equation above, which amounts to removing the gradient on both sides, except for the presence of an integration constant p_0, which we shall set to zero without loss of generality as far as these calculations are concerned. We hence obtain

$$p = \left(\boldsymbol{u}_\omega \cdot \nabla \right) \left[\mathrm{i}\omega \rho f - \eta \Delta f \right], \tag{A.11}$$

which we may further simplify to

$$p = -\eta u \cos\theta \left[\alpha^2 f'(r) - \frac{\mathrm{d}}{\mathrm{d}r} \Delta f \right]. \tag{A.12}$$

We note that in all of the above, we do not need the actual function $f(r)$, but only its derivative $f'(r)$. We now solve the equation (A.8) for $f'(r)$. This is fairly straightforward since $f(r)$ depends only on a single variable r, so we have

$$\Delta f = \frac{1}{r^2} \frac{\mathrm{d}}{\mathrm{d}r} \left[r^2 f'(r) \right] = C \frac{\mathrm{e}^{-\alpha r}}{r}, \tag{A.13}$$

where we have only retained the solution that has the form of a decaying exponential (recall $\Re[\alpha] > 0$) as $r \to \infty$. We then find that $f'(r)$ is given by

$$f'(r) = \frac{1}{r^2} \left[A \left(r + \frac{1}{\alpha} \right) \mathrm{e}^{-\alpha r} + B \right], \tag{A.14}$$

where the constant A is related to the constant C through $A\alpha = -C$. The constants A and B must be determined using the boundary conditions $v_r(r = a, \theta) = u \cos\theta$

and $v_\theta(r=a,\theta) = -u\sin\theta$, whereby we find that $f'(a)/a = -1/2$ and $f''(a) = -1/2$. We thereafter find that

$$\begin{aligned} A &= \frac{3a}{2\alpha}\mathrm{e}^{\alpha a}, \qquad \text{and} \\ B &= -\frac{a^3}{2}\left[1 + \frac{3}{\alpha a} + \frac{3}{\alpha^2 a^2}\right]. \end{aligned} \tag{A.15}$$

We can thereby calculate the relevant components of the viscous stress tensor, viz.

$$\begin{aligned} \sigma_{r\theta} &= \eta\left[\frac{1}{r}\frac{\partial v_r}{\partial\theta} + \frac{\partial v_\theta}{\partial r} - \frac{v_\theta}{r}\right], \qquad \text{and} \\ \sigma_{rr} &= 2\eta\frac{\partial v_r}{\partial\theta}, \end{aligned} \tag{A.16}$$

which we can calculate to be

$$\begin{aligned} \sigma_{r\theta} &= u_\omega\eta\sin\theta f'''(r), \\ \sigma_{rr} &= -4u_\omega\eta\cos\theta\left[\frac{f''}{r} - \frac{f'}{r^2}\right], \end{aligned} \tag{A.17}$$

and evaluate them on the surface to obtain

$$\begin{aligned} \sigma_{r\theta}(r=a,\theta) &= \frac{3}{2a}(1+\alpha a)u_\omega\eta\sin\theta, \\ \sigma_{rr}(r=a,\theta) &= 0. \end{aligned} \tag{A.18}$$

To find the net drag force on the oscillating sphere due to the fluid, we integrate the normal component of the stress tensor over the surface of the sphere. Since we're interested in the drag, we only need to take the z-component (which we have chosen as the polar axis). Thus, we obtain,

$$\hat{\boldsymbol{e}}_z \cdot F = \oint_{r=a} \mathrm{d}\phi\,\mathrm{d}\theta\, a^2\sin\theta\ \left[-p(a,\theta)\cos\theta + \sigma_r r(a,\theta)\cos\theta - \sigma_{r\theta}(a,\theta)\sin\theta\right], \tag{A.19}$$

where the second term is zero, the integral over ϕ trivially evaluates to 2π, and we obtain

$$\boldsymbol{F}_{\text{drag}} = -6\pi\eta a\boldsymbol{u}_\omega\left[1 + \alpha a + \frac{\alpha^2 a^2}{9}\right], \tag{A.20}$$

where we once again recall that $\alpha = \sqrt{-\mathrm{i}\omega\rho/\eta}$ with $\Re[\alpha] > 0$. We may define the characteristic timescale $\tau_f := \rho a^2/\eta$, whereby the combination $\alpha a = \sqrt{-\mathrm{i}\omega\tau_f}$. The time-scale τ_f may be interpreted as the amount of time taken by vorticity to diffuse over a sphere's size in the fluid. This suggests that the effects of vorticity diffusion,

i.e. the deviations from steady Stokes drag, only come to prominence for $\omega \gtrsim 1/\tau_f$. Just to estimate, for a 1μm-sized particle in water, $\tau_f \sim 1\mu$s.

The author finds himself frequently fumbling for detailed results related to this classical problem and therefore wishes to re-summarize some of the key intermediate results below.

If we write $\boldsymbol{v}_\omega = \nabla \times \nabla \times [f(r)\boldsymbol{u}_\omega]$ for the fluid velocity field around a sphere at the origin oscillating with velocity $\boldsymbol{u}_\omega$, we find that

$$\begin{aligned} \frac{f'(r)}{r} &= \frac{a^3}{r^3}\left[\frac{3}{2\alpha^2 a^2}\left(1+\alpha a\right)\mathrm{e}^{\alpha(a-r)} - \frac{1}{2}\left(1+\frac{3}{\alpha a}+\frac{3}{\alpha^2 a^2}\right)\right], \\ \Delta f &= -\frac{3a}{2}\frac{\mathrm{e}^{\alpha(a-r)}}{r}, \end{aligned} \tag{A.21}$$

and the various derivatives of $f(r)$ have the values at $r = a$ given by

$$\begin{aligned} \frac{f'(a)}{a} &= -\frac{1}{2}, \\ \Delta f(a) &= -\frac{3}{2}, \\ f''(a) &= -\frac{1}{2}, \\ \frac{\mathrm{d}}{\mathrm{d}r}\Delta f(a) &= \frac{3}{2a}(1+\alpha a), \\ f'''(a) &= \frac{3}{2a}(1+\alpha a). \end{aligned} \tag{A.22}$$

As $r \to \infty$, all of these derivatives vanish.

The velocity and pressure field are given by

$$\begin{aligned} v_r &= -2u\cos\theta\frac{f'(r)}{r}, \\ v_\theta &= -u\sin\theta\left[\frac{f'}{r} - \Delta f\right], \\ v_\phi &= 0, \\ p &= -u\eta\cos\theta\left[\alpha^2 f' - \frac{\mathrm{d}}{\mathrm{d}r}\Delta f\right]. \end{aligned} \tag{A.23}$$

The viscous stress tensor's components are given by

$$\begin{aligned} \sigma_{rr} &= -4u\eta\cos\theta\left[\frac{f''}{r} - \frac{f'}{r^2}\right], \\ \sigma_{r\theta} &= u\eta\sin\theta f'''. \end{aligned} \tag{A.24}$$

Finally, for completeness, we recall that

$$\Delta f = f'' + \frac{2f'}{r}. \tag{A.25}$$

Appendix B: Application of boundary integral equations to find the Green's function for a no-slip wall

In this appendix, we study the problem of determining the Green's function of the unsteady Stokes equations that satisfies no-slip boundary conditions on a plane wall, using boundary integral equations. The purpose of this is to illustrate the use of boundary integral equations through an explicit calculation, and to provide an alternative method of calculation to that used by Jones [2004] and Felderhof [2005].

We shall first formulate a boundary integral equation that represents this Green's function in terms of an unknown source on the plane wall, and then solve the integral equation. We shall however, ignore the final step of inverting a Fourier transform to obtain the Green's function in regular space, being satisfied with results in k-space. It is not known to the author whether this final step can be effected in closed-form or not. It would also be interesting to investigate if an image system akin to that for the no-slip wall in the steady Stokes case [Blake, 1971] may be obtained for the present case.

B.1 The problem

The problem may be formulated as follows: solve

$$\begin{aligned} \frac{-\mathrm{i}\omega\rho}{\eta}\, G_{ij}(\boldsymbol{x}|\boldsymbol{x}_0) &= -\frac{1}{\eta}\partial_i p_j(\boldsymbol{x}|\boldsymbol{x}_0) + \Delta G_{ij}(\boldsymbol{x}|\boldsymbol{x}_0) + \delta_{ij}\delta(\boldsymbol{x}-\boldsymbol{x}_0), \\ \partial_i G_{ij}(\boldsymbol{x}|\boldsymbol{x}_0) &= 0, \end{aligned} \tag{B.1}$$

for $G_{ij}(\boldsymbol{x}|\boldsymbol{x}_0)$ subject to the boundary condition $G_{ij}(\boldsymbol{x}|\boldsymbol{x}_0) = 0 \quad \forall \boldsymbol{x} \in W$, where W represents the plane wall. Here, we have already Fourier-transformed the unsteady Stokes equations in time.

Suppose that we already know the free-space Green's function $G^0_{ij}(\boldsymbol{x}-\boldsymbol{x}_0)$, we may turn the boundary condition into an appropriately determined source S_{kj} on the

wall, and write,

$$G_{ij}(\boldsymbol{x}|\boldsymbol{x}_0) = G^0_{ij}(\boldsymbol{x}-\boldsymbol{x}_0) + \int_W \mathrm{d}^2x'\; G^0_{ik}(\boldsymbol{x}-\boldsymbol{x}')S_{kj}(\boldsymbol{x}'). \tag{B.2}$$

The source S_{kj} on the wall is to be determined by imposing the no-slip boundary condition,

$$G^0_{ij}(\boldsymbol{x}-\boldsymbol{x}_0) + \int_W \mathrm{d}^2x'\; G^0_{ik}(\boldsymbol{x}-\boldsymbol{x}')S_{kj}(\boldsymbol{x}') = 0 \qquad \forall \boldsymbol{x} \in W, \tag{B.3}$$

which is a Fredholm integral equation of the first kind.

We shall specifically choose Cartesian coordinates $(x,\, y,\, z)$ and let the wall be the plane $z = 0$. The half-space of interest shall be $z >= 0$. Owing to the translation symmetry, we may choose $\boldsymbol{x}_0$ to be the point $(0,\, 0,\, h)$ without loss of generality. Then, the boundary integral equation takes the form

$$G^0_{ij}(x,\, y,\, -h) + \int_{z=0} \mathrm{d}x'\,\mathrm{d}y'\; G^0_{ik}(x-x',\, y-y',\, 0)S_{kj}(x',\, y') = 0 \tag{B.4}$$

and the expression for the required half-space Green's function takes the form

$$\begin{aligned} G_{ij}(x,\, y,\, z) = {} & G^0_{ij}(x,\, y,\, z-h) \\ & + \int_{z=0} \mathrm{d}x'\,\mathrm{d}y'\; G^0_{ik}(x-x',\, y-y',\, z)S_{kj}(x',\, y') \end{aligned} \tag{B.5}$$

B.2 Free space Green's function

The free-space Green's function is a well-known result, sometimes referred to as the unsteady Oseen tensor. We shall re-derive it here to establish conventions. First, we shall assume for simplicity that $\boldsymbol{x}_0$ lies at the origin of the coordinate system. By Fourier transformation of the unsteady Stokes equation, we obtain

$$\begin{aligned} \alpha^2\; G^0_{ij}(\boldsymbol{k}) &= \mathrm{i}k_i\,\frac{p^0_j(\boldsymbol{k})}{\eta} - k^2\, G^0_{ij}(\boldsymbol{k}) + \delta_{ij}, \\ k_i\, G^0_{ij}(\boldsymbol{k}) &= 0. \end{aligned} \tag{B.6}$$

By multiplying the first of the above equations by k_i and using the second, we obtain

$$\mathrm{i}\,k^2\,\frac{p^0_j(\boldsymbol{k})}{\eta} + k_j = 0, \tag{B.7}$$

which has the solution

$$p_j^0(\boldsymbol{k}) = \mathrm{i}\eta \frac{k_j}{k^2}. \tag{B.8}$$

Plugging this solution for p_j^0 back into the first of (B.6), we obtain

$$(k^2 + \alpha^2)\, G_{ij}^0(\boldsymbol{k}) = -\frac{k_i k_j}{k^2} + \delta_{ij}. \tag{B.9}$$

Thus, the Oseen tensor (in k-space) is given by

$$G_{ij}^0(\boldsymbol{k}) = \frac{1}{k^2 + \alpha^2} \left(\delta_{ij} - \frac{k_i k_j}{k^2} \right). \tag{B.10}$$

Given the symmetry of our problem, it is natural to invert the Fourier transform along the $\hat{\boldsymbol{e}}_3 = \hat{\boldsymbol{z}}$ direction, but keep the other two axes Fourier transformed. Defining the inverse Fourier transform through

$$f(z) := \int_{-\infty}^{\infty} \frac{\mathrm{d}k_3}{2\pi}\, \mathrm{e}^{-\mathrm{i}k_3 z} \check{f}(k_3), \tag{B.11}$$

we may compute that $\check{G}_{ij}(k_1,\, k_2,\, z)$, the inverse Fourier transform of $G_{ij}^0(\boldsymbol{k})$ has components

$$\check{G} = \frac{1}{2\alpha^2} \begin{bmatrix} -\frac{k_1^2}{q} Q + \frac{k_1^2+\alpha^2}{s} S & -k1\, k_2 \left(\frac{Q}{q} - \frac{S}{s} \right) & \mathrm{i}k_1 \frac{z}{|z|} (Q - S) \\ -k1\, k_2 \left(\frac{Q}{q} - \frac{S}{s} \right) & -\frac{k_2^2}{q} Q + \frac{k_2^2+\alpha^2}{s} S & \mathrm{i}k_2 \frac{z}{|z|} (Q - S) \\ \mathrm{i}k_1 \frac{z}{|z|} (Q - S) & \mathrm{i}k_2 \frac{z}{|z|} (Q - S) & \frac{q}{s} (sQ - qS) \end{bmatrix}, \tag{B.12}$$

where $Q := \mathrm{e}^{-q|z|}$, $S := \mathrm{e}^{-s|z|}$, $q := \sqrt{k_1^2 + k_2^2}$, and $s := \sqrt{q^2 + \alpha^2}$ $\Re[s] > 0$.

B.3 Solving the integral equation

In the $(k_1,\, k_2,\, z)$-space, the integral equation takes a simple form

$$\check{G}_{ij}(\boldsymbol{q},\, -h) = -\check{G}_{ik}(\boldsymbol{q},\, 0) \check{S}_{kj}(\boldsymbol{q}), \tag{B.13}$$

where $\boldsymbol{q}$ has components k_1 and k_2. To solve for $\check{S}$, we need to invert the matrix $\check{G}(\boldsymbol{q},\, 0)$. This is done easily, and the result is

$$\check{G}^{-1}(\boldsymbol{q},\, 0) = \frac{2}{q} \begin{bmatrix} k_1^2 + sq & k_1 k_2 & 0 \\ k_1 k_2 & k_2^2 + sq & 0 \\ 0 & 0 & s(q+s) \end{bmatrix}. \tag{B.14}$$

Now, we can compute $\check{S} = -\check{G}^{-1}(\boldsymbol{q},\, 0)\, \check{G}(\boldsymbol{q},\, -h)$, and the result is

$$\check{S}(\boldsymbol{q}) = -\mathbb{1}\mathrm{e}^{-sh} + \frac{\mathrm{e}^{-qh} - \mathrm{e}^{-sh}}{q(s-q)} \begin{bmatrix} k_1^2 & k_1 k_2 & \mathrm{i}k_1 q \\ k_1 k_2 & k_2^2 & \mathrm{i}k_2 q \\ \mathrm{i}k_1 s & \mathrm{i}k_2 s & -qs \end{bmatrix}. \tag{B.15}$$

Next, we can compute the correction to the Green's function because of the wall for $z > 0$, given by $\check{C}(\boldsymbol{q},\, z|h) := \check{G}(\boldsymbol{q},\, z)\, \check{S}(\boldsymbol{q})$, and the result is

$$\check{C} = -\check{G}(\boldsymbol{q},\, z)\mathrm{e}^{-sh} - \frac{\mathrm{e}^{-qh} - \mathrm{e}^{-sh}}{2\alpha^2 q(s-q)} \left[(q+s)\mathrm{e}^{-qz} C_1 - 2\mathrm{e}^{-sz} C_2\right], \tag{B.16}$$

where the matrices C_1 and C_2 are given by

$$\begin{aligned} C_1 &:= \begin{bmatrix} k_1^2 & k_1 k_2 & \mathrm{i}k_1 q \\ k_1 k_2 & k_2^2 & \mathrm{i}k_2 q \\ \mathrm{i}k_1 q & \mathrm{i}k_2 q & q^2 \end{bmatrix}, \\ C_2 &:= \begin{bmatrix} sk_1^2 & sk_1 k_2 & \mathrm{i}k_1 qs \\ sk_1 k_2 & sk_2^2 & \mathrm{i}k_2 qs \\ \mathrm{i}k_1 q^2 & \mathrm{i}k_2 q^2 & q^3 \end{bmatrix}. \end{aligned} \tag{B.17}$$

Thereafter, the full Green's function for the half-space may be written as

$$\check{G}_{ij}^{\mathrm{wall}}(\boldsymbol{q},\, z|h) = \check{G}_{ij}(\boldsymbol{q},\, z-h) + \check{C}(\boldsymbol{q},\, z|h). \tag{B.18}$$

Bibliography

Alam, M. S., Ishii, K. & Hasimoto, H. 1980

Slow motion of a small sphere outside of a circular cylinder.

Journal of the Physical Society of Japan **49** (1), pp. 405–408.

[Cited on pages 134, 147, 154, and 155.]

Alam, M. S., Ishii, K. & Hasimoto, H. 1983

Errata: Slow motion of a small sphere outside of a circular cylinder.

Journal of the Physical Society of Japan **52** (10), pp. 3691–3691.

[Cited on page 147.]

Albano, A. M., Bedeaux, D. & Mazur, P. 1975

On the motion of a sphere with arbitrary slip in a viscous incompressible fluid.

Physica A: Statistical Mechanics and its Applications **80** (1), pp. 89–97.

[Cited on page 32.]

Alder, B. J. & Wainwright, T. E. 1970

Decay of the velocity autocorrelation function.

Physical review A **1** (1), p. 18.

[Cited on page 15.]

Ardekani, A. M. & Rangel, R. H. 2006

Unsteady motion of two solid spheres in Stokes flow.

Physics of Fluids **18** (10), p. 103306.

[Cited on page 112.]

Ashkin, A. 1970

Acceleration and trapping of particles by radiation pressure.

Phys. Rev. Lett. **24**, pp. 156–159.

[Cited on page 51.]

Ashkin, A., Dziedzic, J. M., Bjorkholm, J. E. & Chu, S. 1986

Observation of a single-beam gradient force optical trap for dielectric particles.

Opt. Lett. **11** (5), pp. 288–290.

[Cited on pages 53 and 54.]

Balakrishnan, V. 1979

Fluctuation-dissipation theorems from the generalised Langevin equation.
Pramana **12** (4), pp. 301–315.
[Cited on pages 18 and 86.]

Balakrishnan, V. 2008

Elements of nonequilibrium statistical mechanics.
Ane Books.
[Cited on pages 11 and 16.]

Basset, A. B. 1888

On the motion of a sphere in a viscous liquid.
Philosophical Transactions of the Royal Society of London. A **179**, pp. 43–63.
[Cited on pages 2 and 15.]

Bedeaux, D. & Mazur, P. 1974

A generalization of Faxén's theorem to nonsteady motion of a sphere through a compressible fluid in arbitrary flow.
Physica **78** (3), pp. 505–515.
[Cited on page 32.]

Berg-Sørensen, K. & Flyvbjerg, H. 2004

Power spectrum analysis for optical tweezers.
Review of Scientific Instruments **75** (3), pp. 594–612.
[Cited on pages 3 and 51.]

Bian, X., Kim, C. & Karniadakis, G. E. 2016

111 years of Brownian motion.
Soft Matter **12**, pp. 6331–6346.
[Cited on page 1.]

Blake, J. R. 1971

A note on the image system for a stokeslet in a no-slip boundary.
Mathematical Proceedings of the Cambridge Philosophical Society **70** (2), p. 303310.

[Cited on pages 145 and 167.]

Blum, J., Bruns, S., Rademacher, D., Voss, A., Willenberg, B. & Krause, M. 2006
Measurement of the translational and rotational Brownian motion of individual particles in a rarefied gas.
Phys. Rev. Lett. **97**, p. 230601.
[Cited on pages 4 and 80.]

Boussinesq, J. 1885
Sur la résistance qu'oppose un fluide indéfini au repos, sans pesanteur, au mouvement varié d'une sphère solide qu'il mouille sur toute sa surface, quand les vitesses restent bien continues et assez faibles pour que leurs carrés et produits soient négligeables.
CR Acad. Sci. Paris **100**, pp. 935–937.
[Cited on page 2.]

Brennen, C. E. 1982
A review of added mass and fluid inertial forces.
Tech. Rep. CR 82.010. Contract no. N62583-81-MR-554.
Naval Civil Engineering Laboratory.
[Cited on pages 43, 125, and 127.]

Brenner, H. 1961
The slow motion of a sphere through a viscous fluid towards a plane surface.
Chemical engineering science **16** (3-4), pp. 242–251.
[Cited on pages 146, 154, and 155.]

Brown, R. 1828
A brief account of microscopical observations made in the months of June, July and August 1827, on the particles contained in the pollen of plants; and on the general existence of active molecules in organic and inorganic bodies.
Philosophical Magazine **4** (21), pp. 161–173, e-print: http://dx.doi.org/10.1080/14786442808674769 .
[Cited on page 2.]

Carbajal-Tinoco, M. D., Lopez-Fernandez, R. & Arauz-Lara, J. L. 2007
Asymmetry in colloidal diffusion near a rigid wall.
Physical Review Letters **99** (13), p. 138303.
[Cited on pages 146 and 153.]

Chavez, I., Huang, R., Henderson, K., Florin, E.-L. & Raizen, M. G. 2008
Development of a fast position-sensitive laser beam detector.
Review of Scientific Instruments **79** (10), p. 105104.
[Cited on pages 63 and 80.]

Cheng, D., Halvorsen, K. & Wong, W. P. 2010
Note: High-precision microsphere sorting using velocity sedimentation.
Review of Scientific Instruments **81** (2), p. 026106, e-print: http://dx.doi.org/10.1063/1.3302828 .
[Cited on page 85.]

Choi, C.-H. & Kim, C.-J. 2006
Large slip of aqueous liquid flow over a nanoengineered superhydrophobic surface.
Physical Review Letters **96** (6), p. 066001.
[Cited on page 112.]

Chow, T. & Hermans, J. 1973
Brownian motion of a spherical particle in a compressible fluid.
Physica **65** (1), pp. 156 – 162.
[Cited on page 25.]

Clarke, R. J., Jensen, O. E., Billingham, J. & Williams, P. M. 2006
Three-dimensional flow due to a microcantilever oscillating near a wall: an unsteady slender-body analysis.
Proceedings of the Royal Society A: Mathematical, Physical and Engineering Sciences **462** (2067), pp. 913–933.
[Cited on page 3.]

Clercx, H. J. H. & Schram, P. P. J. M. 1992
Brownian particles in shear flow and harmonic potentials: A study of long-time tails.
Physical Review A **46** (4), pp. 1942–1950.

[Cited on pages 16, 18, 45, 46, 47, 48, 80, 156, 157, and 160.]

DLMF
NIST Digital Library of Mathematical Functions.
http://dlmf.nist.gov/, Release 1.0.15 of 2017-06-01, f. W. J. Olver, A. B. Olde Daalhuis, D. W. Lozier, B. I. Schneider, R. F. Boisvert, C. W. Clark, B. R. Miller and B. V. Saunders, eds.
[Cited on pages 47 and 149.]

Einstein, A. 1905
Investigations on the theory of the Brownian movement.
Annalen der Physik **17**, p. 549.
[Cited on pages ix and 2.]

Faxén, H. 1921
Einwirkung der Gefässwände auf den Widerstand gegen die Bewegung einer kleinen Kugel in einer zähen Flüssigkeit.
PhD thesis, Uppsala University.
[Cited on pages 32, 113, and 146.]

Felderhof, B. U. 1976
Force density induced on a sphere in linear hydrodynamics: II. Moving sphere, mixed boundary conditions.
Physica A: Statistical Mechanics and its Applications **84** (3), pp. 569 – 576.
[Cited on page 32.]

Felderhof, B. U. 2005
Effect of the wall on the velocity autocorrelation function and long-time tail of Brownian motion.
The Journal of Physical Chemistry B **109** (45), pp. 21406–21412.
[Cited on pages ix, xvi, 6, 28, 91, 93, 94, 95, 96, 98, 106, 126, 134, 140, 141, 142, 144, 145, and 167.]

Felderhof, B. U. 2006*a*
Diffusion and velocity relaxation of a Brownian particle immersed in a viscous compressible fluid confined between two parallel plane walls.
The Journal of Chemical Physics **124** (5), p. 054111.

[Cited on pages 6, 91, and 93.]

Felderhof, B. U. 2006*b*

Errata: Effect of the wall on the velocity autocorrelation function and long-time tail of Brownian motion.

The Journal of Physical Chemistry B **110** (26), p. 13304, e-print: http://dx.doi.org/10.1021/jp0633291 .

[Cited on pages 106, 126, and 140.]

Felderhof, B. U. 2009*a*

Estimating the viscoelastic moduli of a complex fluid from observation of Brownian motion.

The Journal of Chemical Physics **131** (16), p. 164904.

[Cited on pages 3 and 5.]

Felderhof, B. U. 2009*b*

Transient flow of a viscous incompressible fluid in a circular tube after a sudden point impulse.

Journal of Fluid Mechanics **637**, pp. 285–303.

[Cited on pages 91 and 93.]

Felderhof, B. U. 2012

Hydrodynamic force on a particle oscillating in a viscous fluid near a wall with dynamic partial-slip boundary condition.

Physical Review E **85** (4), p. 046303.

[Cited on pages xv, 6, 30, 91, 93, 111, 122, 123, 124, 125, 127, 128, 132, 134, 136, 137, 138, 139, 141, and 142.]

Franosch, T., Grimm, M., Belushkin, M., Mor, F. M., Foffi, G., Forró, L. & Jeney, S. 2011

Resonances arising from hydrodynamic memory in Brownian motion.

Nature **478** (7367), pp. 85–88.

[Cited on pages 3, 4, 15, 45, 80, 120, 158, 159, and 160.]

Franosch, T. & Jeney, S. 2009

Persistent correlation of constrained colloidal motion.

Physical Review E **79** (3), p. 031402.

[Cited on pages 17 and 18.]

Frydel, D. & Rice, S. A. 2006

Lattice–Boltzmann study of the transition from quasi-two-dimensional to three-dimensional one particle hydrodynamics.

Molecular Physics **104** (08), pp. 1283–1297.

[Cited on page 124.]

Gautschi, W. & Slavik, J. 1978

On the computation of modified Bessel function ratios.

Mathematics of Computation **32** (143), pp. 865–875.

[Cited on page 149.]

Grimm, M., Franosch, T. & Jeney, S. 2012

High-resolution detection of Brownian motion for quantitative optical tweezers experiments.

Physical Review E **86** (2), p. 021912.

[Cited on page 3.]

Guazzelli, E. & Morris, J. F. 2011

A physical introduction to suspension dynamics, *Cambridge Texts in Applied Mathematics*, vol. 45.

Cambridge University Press.

[Cited on page 29.]

Hajizadeh, F. & Reihani, S. N. S. 2010

Optimized optical trapping of gold nanoparticles.

Optics Express **18** (2), pp. 551–559.

[Cited on page 140.]

Hänggi, P.

Prof. Peter Hänggi's website on historical aspects of Brownian motion.

https://www.physik.uni-augsburg.de/theo1/hanggi/History/BM-History.html, accessed: 18 June 2017.

[Cited on page 1.]

Hänggi, P. & Marchesoni, F. 2005

Introduction: 100 years of Brownian motion.

Chaos: An Interdisciplinary Journal of Nonlinear Science **15** (2), p. 026101, e-print: http://dx.doi.org/10.1063/1.1895505 .
[Cited on page 1.]

Happel, J. & Brenner, H. 1965
Low Reynolds number hydrodynamics with special applications to particulate media.
Prentice-Hall.
[Cited on pages 28, 91, 112, 127, 134, 137, 147, and 148.]

Harada, Y. & Asakura, T. 1996
Radiation forces on a dielectric sphere in the Rayleigh scattering regime.
Optics Communications **124** (5), pp. 529 – 541.
[Cited on pages 53 and 54.]

Huang, R., Chavez, I., Taute, K. M., Lukić, B., Jeney, S., Raizen, M. G. & Florin, E.-L. 2011
Direct observation of the full transition from ballistic to diffusive Brownian motion in a liquid.
Nature Physics **7** (7), pp. 576–580.
[Cited on pages 4 and 80.]

Ishii, K., Iwai, T. & Xia, H. 2010
Hydrodynamic measurement of Brownian particles at a liquid-solid interface by low-coherence dynamic light scattering.
Optics express **18** (7), pp. 7390–7396.
[Cited on pages 146 and 153.]

Jackson, J. D. 1999
Classical electrodynamics.
Wiley.
[Cited on pages 34, 35, and 108.]

Jeney, S., Lukić, B., Kraus, J. A., Franosch, T. & Forró, L. 2008
Anisotropic memory effects in confined colloidal diffusion.
Physical review letters **100** (24), p. 240604.
[Cited on pages 6 and 93.]

Jones, R. B. 2004
Spherical particle in Poiseuille flow between planar walls.
The Journal of chemical physics **121** (1), pp. 483–500.
[Cited on pages 94 and 167.]

Kheifets, S. 2014
High-sensitivity tracking of optically trapped particles in gases and liquids: observation of Brownian motion in velocity space.
PhD thesis, The University of Texas at Austin.
[Cited on pages xiv, 51, 64, 65, and 83.]

Kheifets, S., Simha, A., Melin, K., Li, T. & Raizen, M. G. 2014
Observation of Brownian motion in liquids at short times: instantaneous velocity and memory loss.
Science **343** (6178), pp. 1493–1496.
[Cited on pages ix, 3, 4, 6, 45, 47, 48, 51, 71, 77, 80, 81, 85, 86, 87, 88, and 126.]

Kim, S. & Karrila, S. J. 2013
Microhydrodynamics: principles and selected applications.
Courier Corporation.
[Cited on pages 29, 30, 91, 93, 96, 112, and 135.]

Lamb, H. 1932
Hydrodynamics.
Cambridge University Press.
[Cited on pages 92, 125, and 127.]

Landau, L. D. & Lifshitz, E. M. 1987
Fluid mechanics.
Pergamon Press.
[Cited on pages 17, 21, 25, 27, 30, 43, 96, 97, 125, 161, and 162.]

Langevin, P. 1908
Sur la théorie du mouvement brownien.
CR Acad. Sci. Paris **146** (530-533), p. 530.
[Cited on pages 2 and 8.]

Lauga, E. & Squires, T. M. 2005
Brownian motion near a partial-slip boundary: A local probe of the no-slip condition.
Physics of Fluids **17** (10), p. 103102.
[Cited on page 3.]

Lemons, D. S. & Gythiel, A. 1997
Paul Langevin's 1908 paper On the theory of Brownian motion [Sur la thorie du mouvement brownien, C. R. Acad. Sci. (Paris) 146, 530533 (1908)].
American Journal of Physics **65** (11), pp. 1079–1081, e-print: http://dx.doi.org/10.1119/1.18725 .
[Cited on page 2.]

Li, T., Kheifets, S., Medellin, D. & Raizen, M. G. 2010
Measurement of the instantaneous velocity of a Brownian particle.
Science **328** (5986), pp. 1673–1675.
[Cited on pages 63 and 80.]

Liu, L., Woolf, A., Rodriguez, A. W. & Capasso, F. 2014
Absolute position total internal reflection microscopy with an optical tweezer.
Proceedings of the National Academy of Sciences **111** (52), pp. E5609–E5615.
[Cited on pages 146 and 153.]

Lorentz, H. A. 1896
Eene algemeene stelling omtrent de beweging eener vloeistof met wrijving en eenige daaruit afgeleide gevolgen.
Zittingsverlag van de Koninklijke Akademie van Wetenschappen te Amsterdam **5**, pp. 168–175.
[Cited on page 91.]

Lorentz, H. A. 1907
Ein allgemeiner Satz, die Bewegung einer reibenden Flüssigkeit betreffend, nebst einigen Anwendungen desselben.
In *Abhandlungen über theoretische Physik*, pp. 23–42.
B. G. Teubner.
[Cited on pages 39, 91, 92, and 146.]

Luke, J. H. C. 1989
Convergence of a multiple reflection method for calculating Stokes flow in a suspension.
SIAM Journal on Applied Mathematics **49** (6), pp. 1635–1651.
[Cited on page 112.]

Mazur, P. & Bedeaux, D. 1974
A generalization of Faxén's theorem to nonsteady motion of a sphere through an incompressible fluid in arbitrary flow.
Physica **76** (2), pp. 235–246.
[Cited on pages 27, 30, 32, 33, 34, 92, 93, 95, and 99.]

Milne-Thomson, L. M. 1968
Theoretical hydrodynamics.
Courier Corporation.
[Cited on pages 92, 125, 127, and 129.]

Mo, J. 2015
Short timescale Brownian motion and applications.
PhD thesis, The University of Texas at Austin.
[Cited on pages 5, 51, and 54.]

Mo, J., Simha, A., Kheifets, S. & Raizen, M. G. 2015*a*
Testing the Maxwell-Boltzmann distribution using Brownian particles.
Optics express **23** (2), pp. 1888–1893.
[Cited on pages ix, 3, 6, 51, 80, 84, 85, 88, 89, and 126.]

Mo, J., Simha, A. & Raizen, M. G. 2015*b*
Broadband boundary effects on Brownian motion.
Physical Review E **92** (6), p. 062106.
[Cited on pages x, 5, 7, 51, 93, 100, 126, 127, 134, 135, 136, 137, 145, 147, 150, 152, 154, 155, 156, 157, 158, 159, and 160.]

Mo, J., Simha, A. & Raizen, M. G. 2017
Brownian motion as a new probe of wettability.
The Journal of Chemical Physics **146** (13), p. 134707.
[Cited on pages 3, 5, and 144.]

Morse, P. M. & Feshbach, H. 1953
Methods of theoretical physics, *International Series in Pure and Applied Physics*, vol. 1.
McGraw-Hill.
[Cited on page 91.]

O'Neill, M. E. 1964
A slow motion of viscous liquid caused by a slowly moving solid sphere.
Mathematika **11** (01), pp. 67–74.
[Cited on page 90.]

O'Neill, M. E. & Stewartson, K. 1967
On the slow motion of a sphere parallel to a nearby plane wall.
Journal of Fluid Mechanics **27** (04), pp. 705–724.
[Cited on pages 28 and 91.]

Oppenheim, A. V., Willsky, A. S. & Nawab, S. H. 1983
Signals and systems, vol. 2.
Prentice-Hall Englewood Cliffs, NJ **6** (7), p. 10.
[Cited on page 74.]

Van der Pas, P. W. 1971
The discovery of the Brownian motion.
Scientiarum Historia: Tijdschrift voor de Geschiedenis van de Wetenschappen en de Geneeskunde **13** (1), pp. 27–35.
[Cited on page 1.]

Paschotta, R.
Article on "Gaussian Beams" in the "Encyclopedia of Laser Physics and Technology".
https://www.rp-photonics.com/gaussian_beams.html, accessed: 5 July 2017.
[Cited on page 54.]

Perrin, J. 1909
Mouvement brownien et réalité moléculaire.
Annales de Chimie et de Physique **18**, pp. 5–104.
[Cited on pages ix and 2.]

Pozrikidis, C. 1992
Boundary integral and singularity methods for linearized viscous flow.
Cambridge University Press.
[Cited on pages 29, 39, 40, 41, 100, and 101.]

Pralle, A., Florin, E. L., Stelzer, E. H. K. & Hörber, J. K. H. 1998
Local viscosity probed by photonic force microscopy.
Applied Physics A: Materials Science and Processing **66**, pp. 71–73.
[Cited on page 153.]

Rahman, A. 1964
Correlations in the motion of atoms in liquid argon.
Physical Review **136** (2A), p. A405.
[Cited on pages 2 and 15.]

Rahman, A. 1966
Liquid structure and self-diffusion.
The Journal of Chemical Physics **45** (7), pp. 2585–2592.
[Cited on pages 2 and 15.]

Saichev, A. I. & Woyczynski, W. 2013
Distributions in the Physical and Engineering Sciences, , vol. 1.
Springer Science & Business Media.
[Cited on pages 16 and 47.]

Sardar, R., Funston, A. M., Mulvaney, P. & Murray, R. W. 2009
Gold nanoparticles: Past, present, and future.
Langmuir **25** (24), pp. 13840–13851, pMID: 19572538, e-print: http://dx.doi.org/10.1021/la9019475 .
[Cited on page 140.]

Schäffer, E., Nørrelykke, S. F. & Howard, J. 2007
Surface forces and drag coefficients of microspheres near a plane surface measured with optical tweezers.
Langmuir **23** (7), pp. 3654–3665.
[Cited on page 127.]

Seol, Y., Carpenter, A. E. & Perkins, T. T. 2006
Gold nanoparticles: enhanced optical trapping and sensitivity coupled with significant heating.
Optics letters **31** (16), pp. 2429–2431.
[Cited on page 140.]

Sharma, P., Ghosh, S. & Bhattacharya, S. 2010
A high-precision study of hindered diffusion near a wall.
Applied Physics Letters **97** (10), p. 104101, e-print: http://dx.doi.org/10.1063/1.3486123 .
[Cited on page 146.]

Shinohara, M. & Hashimoto, H. 1979
The lateral force on a small sphere sedimenting in a viscous fluid bounded by a cylindrical wall.
Journal of the Physical Society of Japan **46** (1), pp. 320–327.
[Cited on page 113.]

Simha, A., Mo, J. & Morrison, P. J. 2017
Unsteady Stokes flow near boundaries: the point-particle approximation and the method of reflections.
Submitted for review to the *Journal of Fluid Mechanics* in July 2017, e-print: https://arxiv.org/abs/1707.03936 .
[Cited on pages ix, 6, 20, 90, 108, 111, 134, 138, 139, and 141.]

Steve Smith, Claudio Rivetti, C. B. & others
Tweezers LAB – All you need to build a miniTweezers.
http://tweezerslab.unipr.it/cgi-bin/mt/home.pl, accessed: 14 July 2017.
[Cited on pages 57 and 60.]

Stokes, G. G. 1851
On the effect of the internal friction of fluids on the motion of pendulums.
Transactions of the Cambridge Philosophical Society **9**, p. 8.
[Cited on pages 2, 17, 30, and 161.]

Svoboda, K. & Block, S. M. 1994
Optical trapping of metallic Rayleigh particles.
Optics letters **19** (13), pp. 930–932.
[Cited on page 137.]

Tuck, E. O. 1967
A simple "Filon-trapezoidal" rule.
Mathematics of Computation **21** (98), pp. 239–241.
[Cited on page 18.]

Uhlenbeck, G. E. & Ornstein, L. S. 1930
On the theory of the Brownian motion.
Physical review **36** (5), p. 823.
[Cited on pages 2, 4, and 9.]

Von Smoluchowski, M. 1906
Zur kinetischen Theorie der Brownschen Molekularbewegung und der Suspensionen.
Annalen der physik **326** (14), pp. 756–780.
[Cited on pages ix and 2.]

Wang, G. M., Prabhakar, R. & Sevick, E. M. 2009
Hydrodynamic mobility of an optically trapped colloidal particle near fluid-fluid interfaces.
Physical Review Letters **103** (24), p. 248303.
[Cited on pages 112 and 124.]

Widom, A. 1971
Velocity fluctuations of a hard-core Brownian particle.
Physical Review A **3** (4), p. 1394.
[Cited on pages 2 and 4.]

Yang, F.-L. 2010
A formula for the wall-amplified added mass coefficient for a solid sphere in normal approach to a wall and its application for such motion at low Reynolds number.
Physics of Fluids **22** (12), p. 123303.
[Cited on page 125.]

Zwanzig, R. & Bixon, M. 1970
Hydrodynamic theory of the velocity correlation function.
Physical Review A **2** (5), pp. 2005–2012.
[Cited on pages 2, 4, 15, 27, 45, 49, and 93.]

Zwanzig, R. & Bixon, M. 1975
Compressibility effects in the hydrodynamic theory of Brownian motion.
Journal of Fluid Mechanics **69** (01), pp. 21–25.
[Cited on pages 47 and 126.]

Vita

Akarsh Simha was born in 1988 in India. He completed his high school education from Poorna Prajna High School, Bangalore and M. E. S. College of Arts, Science and Commerce, Bangalore in 2006. He received a Bachelors of Technology degree in Engineering Physics from the Indian Institute of Technology Madras in 2010. He entered graduate school at the University of Texas at Austin in 2010, where he first took courses in quantum field theory in preparation to be a particle physicist. During the summer of 2011, he had an opportunity to work in Prof. Mark Raizen's group, which he liked and therefore continued. After his qualifier, a course in fluid mechanics by Prof. Philip Morrison made him want to explore the same problems he had been working on from a theoretical side. He has no clue where life will take him next!

This dissertation was typeset with LaTeX[†] by the author.

[†]LaTeX is a document preparation system developed by Leslie Lamport as a special version of Donald Knuth's TeX Program.